

Raising the XUV Intensity towards Attosecond-Attosecond Pump-Probe Experiments

Im Fachbereich der Physik
der Freien Universität Berlin
eingereichte Dissertation

von

Martin Flögel



2016

1. Gutachter: Prof. Dr. Marc J.J. Vrakking
2. Gutachter: Prof. Dr. Maria Krikunova

Tag der Disputation: 29.11.2016

Erklärung der Selbstständigkeit

Hiermit versichere ich, die vorliegende Arbeit selbstständig verfasst und keine anderen als die angegebenen Quellen und Hilfsmittel benutzt sowie die Zitate deutlich kenntlich gemacht zu haben. Die Arbeit ist weder in einem früheren Promotionsverfahren angenommen noch als ungenügend beurteilt worden.

Berlin, den 10. Juni 2016

Martin Flögel

*Hinter jeder neuen Kommastelle kann
sich eine neue Physik verbergen.*
Stephan Mertens

*Man kann das erste Bauteil erst festlegen,
nachdem man das letzte festgelegt hat.*
unbekannt

Contents

Introduction	7
1 Noncollinear Optical Parametric Chirped Pulse Amplification	11
1.1 Theory	12
1.1.1 Ultrashort, Intense Laser Pulses	12
1.1.2 Sum Frequency Generation	14
1.1.3 Second Harmonic Generation	15
1.1.4 Noncollinear Optical Chirped Pulse Amplification	15
1.2 Pump Laser System	19
1.3 Seed Oscillator	21
1.4 Stretcher-Shaper and Compressor	21
1.5 OPA Stages	24
1.6 Synchronization	26
1.7 SPIDER	28
1.8 Summary	31
2 Theoretical Comparison of Different HHG Gating Techniques	33
2.1 Introduction	33
2.2 Theory	35
2.2.1 Corkum's Model	35
2.2.2 Lewensteins's Model	36
2.2.3 Wave Equation	38
2.2.4 General Features of the Atom Response	38
2.2.5 Constant's Model	39
2.2.6 Phase-Matching	41
2.2.7 Gating Techniques	42
2.3 Simulation Techniques	44
2.3.1 IR Pulse Model	45
2.3.2 NOPCPA Spectrum	46
2.3.3 Gating Optics	46
2.3.4 IR Field Propagation	47
2.3.5 Lewenstein Model	49
2.3.6 XUV Propagation	50
2.4 Results	52
2.4.1 No Gating	52
2.4.2 Ionization Gating	56

2.4.3	Polarization Gating	61
2.4.4	DOG	64
2.4.5	Hybrid DOG	69
2.4.6	Comparison	71
2.5	Assumptions and Accuracy	74
2.6	Summary	75
3	High Harmonic Generation Setup, End Stations	77
3.1	IR Preparation	78
3.2	HHG Cell	79
3.3	XUV-IR Station	85
3.4	XUV-XUV Station	88
3.5	Summary	91
4	Multiphoton Sequential XUV Double Ionization of Argon	93
4.1	Introduction	93
4.2	Experimental Setup	95
4.3	Experimental Results	97
4.3.1	Time of Flight and Velocity Map Imaging Experiments	97
4.3.2	Ionization Mechanism	102
4.3.3	Ar^{+*} States	106
4.4	Qualitative Model of Ar^{2+} Generation	110
4.4.1	Fedorov-Kazakov Model	110
4.4.2	Effective State Model	114
4.5	Review of Assumptions	119
4.5.1	First Ionization and States not Modeled	119
4.5.2	XUV Intensity Averaging	125
4.5.3	TDSE Simulations	128
4.5.4	Discussion	132
4.6	Summary	134
	Summary	135
	Outlook	137
	Short Summary	139
	Deutsche Kurzzusammenfassung	140
	Bibliography	141
	Nomenclature	153
	List of Publications	157

Introduction

Around 1873 Ernst Abbe improved the understanding of optics, enhancing the spatial resolution of microscopes. This allowed Robert Koch to identify the relation between bacteria and disease for tuberculosis, cholera and anthrax a few years later [1]. During this time one out of seven Germans died from tuberculosis. Probably, Abbe did not anticipate the impact of the enhanced resolution.

More than 140 years later we are aware of the relation between sophisticated scientific instruments and new, influential discoveries. The current frontier of time resolution is attoseconds. As even light travels only 3 \AA per attosecond and the atomic unit of time equals 24 as , atoms and especially electron dynamics are of major interest to the physics on this timescale. As the daily world consists of atoms organized by electron mediated bonds, pushing the time resolution is very promising. A better understanding of the breaking and creation of chemical bonds is of paramount importance to chemistry. Furthermore, optical properties are defined by the electronic structure of a material.

A conventional approach for time resolved experiments is to trigger a process by a pump pulse and later probe it by a second pulse. The resolution depends on the duration of both pulses so that Ferenc Krausz [2] told the history of time resolution in terms of the development of (laser) sources. He stresses a number of key technologies that provide a powerful IR pulse with only few cycles, which can then be used to create attosecond pulses by the method of high harmonic generation (HHG). Due to the restrictions described by the time-bandwidth product, few cycle IR pulses have a large bandwidth (hundreds of nm), which poses a challenge for the laser: First, the solid state laser medium has to support the bandwidth: Ti:Sa is widely used for this property. Second, the cavity modes have to be phase-locked to produce a pulse: This is typically accomplished by Kerr-lens mode-locking. This effect bases upon a different beam shape of pulses in comparison to continuous laser fields due to an index of refraction depending on intensity via the so-called Kerr effect. Third, pulse intensities are limited by the damage thresholds of the used materials: This restriction was eased by reversible elongation of the pulse during the amplification steps. Forth, the phase of the electric field at the center of the pulse becomes important for few cycle pulses: Techniques to stabilize and set this property were developed.

HHG itself bases upon focusing fs ($1000 \text{ as} = 1 \text{ fs}$) IR laser pulses into a gas [3]. Electrons are then ionized and accelerated by the field. If they recombine with their parent ion, XUV photons are emitted [4]. As the process repeats every half IR cycle, gating techniques were developed that limit the generation to a single half cycle [5, 6, 7].

Plasma mirrors pose the most promising alternative approach to HHG [8] as higher conversion efficiencies and driving intensities are possible [9]: Created by an intense fs laser pulse a plasma can oscillate with relativistic speed, which leads to the conversion

of parts of the fs laser pulse to higher frequencies via the Doppler effect [10]. However, this strategy is still immature [9].

Until today, neither HHG nor plasma mirrors led to pulses sufficiently strong for attosecond pump-probe experiments. The concept of pump-probe experiments implies that the investigated system interacts with both pulses. This interaction requires a sufficient intensity for both pulses. A low interaction probability reduces the signal-to-noise ratio or prevents the identification of signals at all. As attosecond XUV pulses with sufficient strength for XUV-XUV measurements are a current frontier of research [11], most experiments with resolutions in the attosecond regime avoid the XUV-XUV pump-probe scheme using a fs pulse to gain an acceptable signal-to-noise ratio. Experimental approaches exist that use the cycle of a fs IR pulse as clock: E.g. Schultze et al. [12] ionize neon atoms with an attosecond XUV pulse. The IR field increases or decreases the energy of the electrons to assign them a "timestamp". The authors deduced a delay of (21 ± 5) as in the ionization of electrons from 2p orbitals with respect to 2s orbitals. Hentschel et al. [13] introduced this approach and isolated attosecond pulses for pioneering time resolution better than 1 fs in electron dynamic measurements in 2001. Several further schemes were demonstrated as reviewed for example by Calegari et al. [14].

While XUV-IR pump-probe experiments allow first investigations, the capacity to perform XUV-XUV pump-probe would severely widen the range of possible experiments. IR intensities are often not perturbative making their influence on atoms and molecules an object of research itself. E.g. lowering the IR intensity would result in smaller, less resolvable energy differences for the time stamps. Alternatively, FELs provide XUV pulses with sufficient energy but pulse durations are available only down to few fs[15]. E.g. Behrens et al. [16] reconstructed average pulse durations of 3 fs.

No research groups have performed attosecond-attosecond pump-probe experiments so far. Recent publications from the group of D. Charalambidis [17, 18] at FORTH, Crete, introduced pump-probe experiments with almost attosecond pulses: An estimated XUV focus intensity of $1 \times 10^{13} \text{ W/cm}^2$ to $1 \times 10^{14} \text{ W/cm}^2$ was sufficient to measure a pulse duration of $1.5^{+0.2}_{-0.8} \text{ fs}$ in an autocorrelation experiment. The pulses covered a spectrum from 16 to 24 eV and were additionally used to investigate molecular dynamics in H_2 . Takahashi et al. [3] measured an autocorrelation trace indicating a pulse duration of 375 as but did not perform subsequent experiments.

In both groups the creation and characterization of the pulses were important and essential achievements indicating that attosecond-attosecond pump-probe experiments are far from maturity. Consequently, the aim of this thesis is to increase the possible attosecond pulse energy for attosecond-attosecond pump-probe experiments. To that end a design is proposed within the thesis.

The first stage of the setup (Chap. 1) is based upon Noncollinear optical parametric chirped pulse amplification (NOPCPA). It is designed to deliver strong, few-fs IR pulses. The chapter provides a short theory on intense, ultrashort pulses and nonlinear optical processes before describing the components of the NOPCPA in detail.

Chap. 2 theoretically analyses the perspectives of different gating techniques for the XUV pulse generation. A common model suitable for a broad set of attosecond gating techniques is developed and implemented. The chapter describes an optimization to-

wards optimal pulse energies and process parameters for all methods that are used in the technical implementation of the HHG setup.

Chap. 3 discusses further, rather technical aspects of the HHG. The novelty of the considerations is in the large amount of converted energy. Two end stations for pump-probe experiments are available. The XUV-XUV station discards the IR and splits, delays and focuses the XUV pulses into the interaction region, which is situated within a velocity map imaging (VMI) spectrometer. Additionally, either XUV pulse energy, spectrum or spatial shape can be characterized. Alternatively, the IR and XUV are separated, delayed and focused into another interaction region and VMI.

The reason for the existence of the second station is that a high XUV intensity is projected and experimentally interesting even with fs-long XUV pulses. Chap. 4 reports pump-probe experiments with Ar using intense, fs long XUV pulses and IR pulses. The interpretation reveals a process using two XUV and one IR photon to produce Ar^{2+} . A quantum mechanical model attributes features in the measurement to the Stark effect and Rabi oscillations between intermediate states, which have not been time resolved in the XUV regime before. The experiment was conducted at a different setup because the described design is being constructed.

1 Noncollinear Optical Parametric Chirped Pulse Amplification

The aim of the Noncollinear Optical Parametric Chirped Pulse Amplification (NOPCPA) is to generate short, intense IR pulses for the HHG section. This design bases upon the work of Witte and Zinkstok [19] and the main structure is depicted in Fig. 1.1. In the NOPCPA pulses from a seed oscillator are temporally stretched before and compressed after the actual amplification in the optical parametric amplification (OPA) stages. The OPA is pumped by reshaped pump pulses provided by a thin disk laser system. Spectral phase interferometry for direct electric field reconstruction (SPIDER) characterizes the pulses and provides data for the fine tuning of the pulse compression to provide the shortest possible pulses to the HHG section.

The chapter starts with a brief, general theory of ultrashort, intense laser pulses and a treatment of light conversion processes (Sec. 1.1) before going through all components. As they are partly built up but not operational, the current chapter presents a design. The pump and seed sources are outlined in Sec. 1.2 and 1.3. Sec. 1.4 describes the stretcher and compressor. The next sections outlines the actual amplification (Sec. 1.5), the synchronization of pump and seed pulse sources (Sec. 1.6) and the SPIDER (Sec. 1.7). A summary (Sec. 1.8) closes the chapter.

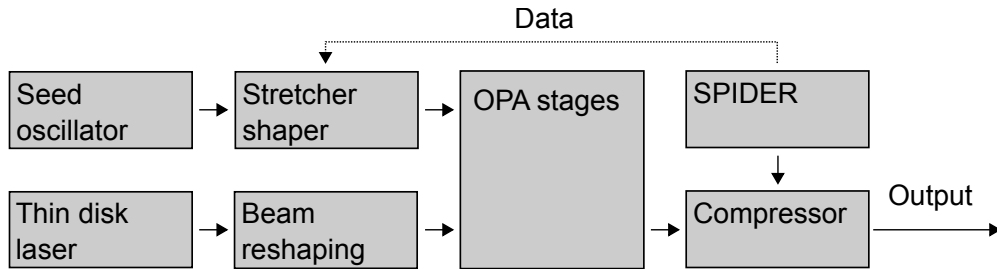


Figure 1.1: Overview of the NOPCPA setup: Before being amplified in the OPA stages the seed is stretched. Recompression is enhanced by SPIDER measurements feed-backing into a shaper within the stretcher. A reshaped pump beam provides the energy for the amplification.

1.1 Theory

1.1.1 Ultrashort, Intense Laser Pulses

The section recalls concepts needed for the understanding of ultrashort, intense laser pulses. This thesis focuses on very high intensities up to $1 \times 10^{16} \text{ W/cm}^2$, where the wave equation

$$\Delta \vec{E} - \frac{1}{c^2} \frac{\partial^2 \vec{E}}{\partial t^2} = \frac{1}{\epsilon_0 c^2} \frac{\partial^2 \vec{P}}{\partial t^2} \quad (1.1)$$

can be deduced from the Maxwell equations in media. \vec{E} is the electric field. c is the vacuum speed of light. t is time. ϵ_0 is the vacuum permittivity and \vec{P} is the polarization.

A simple treatment for the polarization is to develop it in a power series:

$$\vec{P} = \epsilon_0 \sum_k \chi^k \vec{E}^k \quad (1.2)$$

where the tensors χ^k are the (non-linear) electric susceptibilities of the medium.

The polarization is the origin of numerous effects, which are important for the generation and propagation of laser pulses. The refractive index $n = \sqrt{1 + \chi^1}$ is related to the linear term of the polarization:

$$\Delta \vec{E} - \frac{1}{c^2} \frac{\partial^2 \vec{E}}{\partial t^2} = \frac{1}{c^2} \frac{\partial^2}{\partial t^2} (\chi^1 \vec{E}) \quad (1.3a)$$

$$\Delta \vec{E} - \frac{n^2}{c^2} \frac{\partial^2 \vec{E}}{\partial t^2} = 0 \quad (1.3b)$$

In isotropic media χ^n with even n are zero because of the symmetry. Therefore, χ^2 is only non-zero for anisotropic materials. It is essential for second harmonic generation (SHG), optical parametric amplification (OPA) and sum frequency generation (SFG), which will be discussed in the next sections. χ^3 can be different from zero in isotropic media and relates to an index of refraction depending on the intensity via the nonlinear index of refraction n_2 . This dependence of the index of refraction is called Kerr effect and eventually leads to the exponential enhancement of transversal modulations in a beam [20]. This is called light beam modulation or self-focusing instability and can degrade the quality of the beam and potentially split it. The so-called B-integral is calculated along the path of the beam and is a measure for the growth of the modulations. It should be kept low. Typically, the limit is between 2 and 3 [20]:

$$B = \int n_2 k I ds, \quad (1.4)$$

where k is the wavenumber and I intensity. Before introducing the processes in more detail, quantities for the description of pulses are defined. Diels and Rudolph [21] guide this treatment. $E(\omega)$ is the Fourier transform of the electric field:

$$E(\omega) = \int_{-\infty}^{\infty} E(t) \exp(-i\omega t) dt \quad (1.5)$$

where ω is the angular frequency. In order to take advantage of complex notations, the function $\varepsilon(t)$ is defined, which is a complex, analytical function and its real part equals $E(t)$. $\varepsilon(t)$ is called Hilbert transform of $E(t)$ and can be calculated via:

$$\varepsilon(t) = \frac{1}{\pi} \int_0^\infty E(\omega) \exp(i\omega t) d\omega \quad (1.6a)$$

$$= |\varepsilon(t)| \exp(i\phi(t)) \quad (1.6b)$$

$|\varepsilon(t)|$ is called pulse envelop and $\phi(t)$ is the temporal phase. The term carrier envelope phase (CEP) refers to the temporal phase at the maximum of the envelope. The instantaneous frequency is defined as $\omega(t) = d\phi(t)/dt$. A pulse is called chirped unless its $\omega(t)$ is constant.

$\varepsilon(\omega)$ is the Fourier transform of $\varepsilon(t)$. It can also be decomposed into a (spectral) phase $\phi(\omega)$ and an envelope $|\varepsilon(\omega)|$ with $\varepsilon(\omega) = |\varepsilon(\omega)| \exp(i\phi(\omega))$. The spectral and temporal phases of a pulse are related. Assume the development using the constants ϕ_0 , ϕ'_0 and ϕ''_0 :

$$\phi(\omega) = \phi_0 + \phi'_0 \omega + \frac{\phi''_0}{2} \omega^2 \quad (1.7a)$$

$$\varepsilon(t) = \frac{\exp(i\phi_0)}{2\pi} \int_{-\infty}^\infty |\varepsilon(\omega)| \exp\left(i(\phi'_0 + t)\omega + \frac{i\phi''_0}{2} \omega^2\right) d\omega \quad (1.7b)$$

Each of the coefficients represents an aspect of the temporal pulse. ϕ_0 adds to the temporal phase, so it shifts the CEP. ϕ'_0 shifts the pulse in time. The role of ϕ''_0 is not clear from the equation above. It governs the linear chirp. If no higher terms in the spectral phase are present, the instantaneous frequency is

$$\omega(t) \approx \omega_0 - t/\phi'' \quad (1.8)$$

with an offset ω_0 [22]. ϕ'' also affects the pulse length. A pulse centered at time zero obeys

$$\langle t^2 \rangle = \langle t^2 \rangle_0 + \phi''^2 \langle (\omega - \langle \omega \rangle)^2 \rangle, \quad (1.9)$$

where the second order moment of the pulse is $\langle t^2 \rangle$ and a pulse with the same spectrum but no chirp would have a second order moment $\langle t^2 \rangle_0$. It follows that broad band pulses are especially susceptible to elongation by (second order) dispersion.

Generally, second order duration and bandwidth of a pulse obey:

$$\langle t^2 \rangle \langle (\omega - \langle \omega \rangle)^2 \rangle \geq \frac{1}{4} \quad (1.10)$$

Therefore, short pulses have a minimum bandwidth. The smallest product is reached for Gaussian pulses only, whose spectral phase is linear. The Fourier limited duration is the shortest possible pulse duration for a given spectrum. Fig. 1.2 illustrates the effect of additional ϕ'' on a Fourier limited pulse.

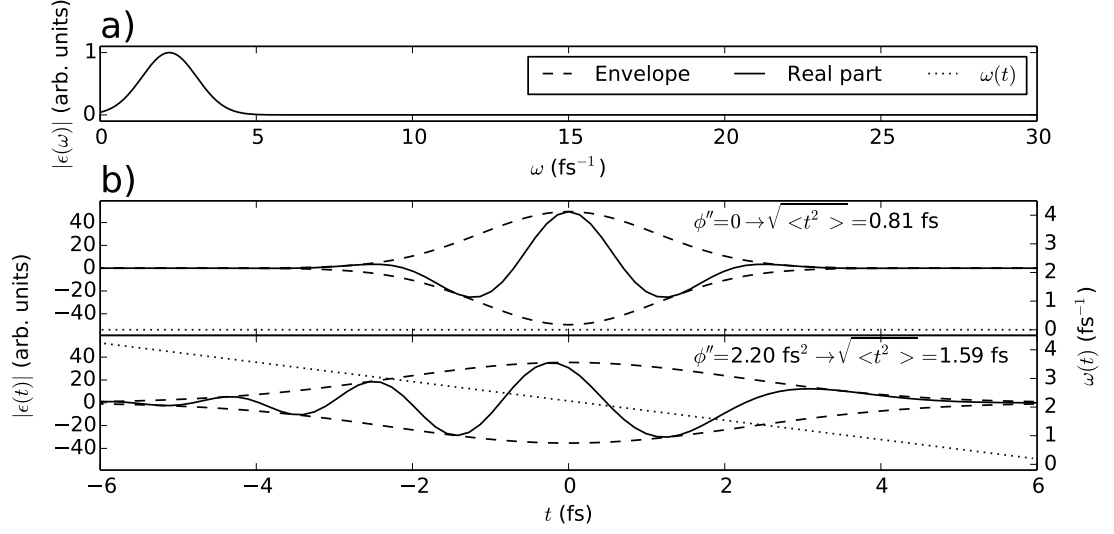


Figure 1.2: Example of pulse elongation and chirp via quadratic dispersion: a) Gaussian spectrum with $\sqrt{\langle(\omega - \langle\omega\rangle)^2}\rangle = 0.62/\text{fs}$ centered at a wavelength of 850 nm b) Time domain representation (Eq. (1.7b)) of the pulse with constant ϕ and ϕ' but different ϕ'' , hence with different durations

1.1.2 Sum Frequency Generation

In a birefringent material with $\chi^2 \neq 0$ the polarization creates a spectral component with an angular frequency ω_1 in the polarization, which is proportional to the product of two spectral components at ω_2 and ω_3 . They can originate from one or two different pulses in the medium. This polarization is the source term for a new pulse and hence energy can be transferred from the incoming, so-called 'fundamental' pulse(s) to the new pulse, effectively merging two photons into one. The relation between the frequencies translates into energy conservation:

$$\hbar\omega_1 = \hbar\omega_2 + \hbar\omega_3 \quad (1.11)$$

Because of different refractive indices the pulses may change their relative phase, which then leads to destructive interference between the new pulse and its generating polarization. The phase mismatch $\Delta\vec{k}$ is defined in terms of the wave vectors \vec{k} belonging to the pulses:

$$\Delta\vec{k} = \vec{k}_2 + \vec{k}_3 - \vec{k}_1 \quad (1.12)$$

If the product of $|\Delta\vec{k}|$ and the interaction length is small, interference between the new pulse and its generating polarization is constructive. As $|\Delta\vec{k}|$ is a function of frequency, phase-matching has a limited bandwidth.

A strategy to minimize $|\Delta\vec{k}|$ is to take advantage of the dependence of the indices of refraction visible to each of the pulses from the ordinary and extraordinary index of

refraction and the angles between the pulses and the optical axis. The two fundamental photons can stem from ordinary or, alternatively, extraordinary waves in case of the so-called type I phase-matching. Both waves contribute as fundamental in case of type II phase-matching.

Sum frequency generation is an instantaneous effect. Therefore, the pulses also have to overlap, which restricts the spatial size of the pulses and also the group velocity mismatch between new and fundamental pulses.

1.1.3 Second Harmonic Generation

Second harmonic generation is a special case of SFG where $\omega_1 = 2\omega_2 = 2\omega_3$. Diels and Rudolph [21] give an analytical expression for the complex electric field after a medium of length L in case of small conversion efficiencies and orthogonal polarization of fundamental and SHG pulse ε_{SHG} . Further, the dispersion is represented only by the group velocities $v_{1,2}$ and phase mismatch Δk at the central angular frequencies $\omega_{1,2}$:

$$\varepsilon_{SHG}(\omega) = -\frac{\chi^2 \omega_1^2}{4c^2 k_1} \frac{\exp(ilL) - 1}{l} \int \varepsilon(\Omega) \varepsilon(\omega - \Omega) d\Omega \quad (1.13a)$$

$$l := (v_1^{-1} - v_2^{-1})(\omega - \omega_1) - \Delta k \quad (1.13b)$$

$$\Delta k = 2k_2(\omega_2) - k_1(\omega_1) \quad (1.13c)$$

It uses a coordinate system moving with the fundamental pulse ε . The quantity l represents the inverse length scale at which phase mismatch and different group velocities play a role.

Fig. 1.3 shows an example of SHG: For short media, an elongation increases the SHG field strength. For sufficiently long media the resulting pulse length is increased at constant field strength.

1.1.4 Noncollinear Optical Chirped Pulse Amplification

OPA also bases on χ^2 but splits one pump photon of frequency ω_p into a signal photon of frequency ω_s and an idler photon of frequency ω_i with

$$\omega_p = \omega_s + \omega_i. \quad (1.14)$$

The signal pulse can be seeded, which means an initially weak pulse containing the frequency ω_s controls the final result of the process. Phase-matching plays the same role as in Sec. 1.1.2 and 1.1.3. The phase mismatch $\Delta \vec{k}$ (Fig. 1.4) depends on the wave vectors of the respective pulses:

$$\Delta \vec{k} = \vec{k}_p - \vec{k}_s - \vec{k}_i. \quad (1.15)$$

θ is called the phase-matching angle and is used in collinear amplification geometries to minimize the phase mismatch for a given wavelength. α was coined the noncollinear angle and is also defined in Fig. 1.4. It allows to increase the bandwidth of the phase-matching. Fig. 1.5 shows both scenarios to illustrate the additional bandwidth.

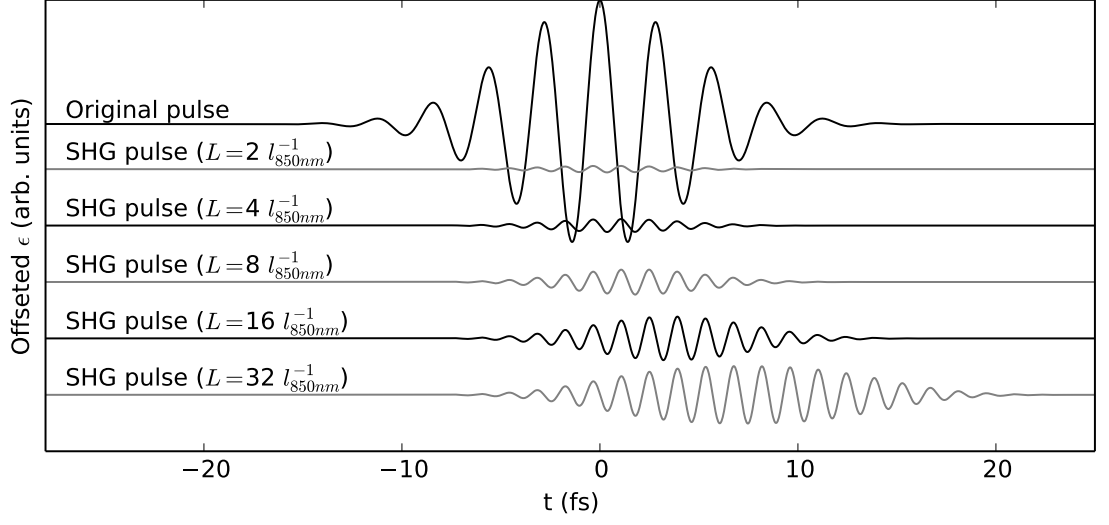


Figure 1.3: Example of SHG, Eq. 1.13: The fundamental pulse and SHG pulses resulting from generation in media of different length L are shown. The length is expressed in units of l_{850nm}^{-1} , the inverse value for l (Eq. (1.13b)) at the central wavelength of 850 nm.

Noncollinear optical chirped pulse amplification (NOPCPA) [24] bases upon this process to amplify a seed pulse with a controlled chirp. As given in Eq. (1.9) the chirp increases the pulse duration so that the intensity is lowered beneath the damage threshold of the interaction material. After the amplification the chirp is compensated to obtain a short and intense pulse.

Baumgartner's Equations Baumgartner et al. [25] give a treatment of optical parametric amplification (OPA). Starting with Eq. (1.1) and (1.2) they neglect the optical density of the interaction medium and take dispersion into account via the index of refraction and the common group velocity v_g . They treat plane waves and hence drop the transversal coordinates and frequency dependences. The resulting system of equations is

$$\frac{du_s}{d\xi} = -u_i u_p \sin \Theta \quad (1.16a)$$

$$\frac{du_i}{d\xi} = -u_s u_p \sin \Theta \quad (1.16b)$$

$$\frac{du_p}{d\xi} = u_s u_i \sin \Theta \quad (1.16c)$$

$$\frac{d\theta}{d\xi} = \frac{\Delta k z}{\xi} + \left(\frac{u_s u_i}{u_p} - \frac{u_i u_p}{u_s} - \frac{u_s u_p}{u_i} \right) \cos \Theta \quad (1.16d)$$

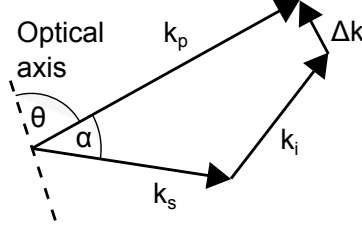


Figure 1.4: The phase-matching angle θ and the noncollinear angle α relate the wave vectors for the pump, \vec{k}_p , and seed pulses, \vec{k}_s , with the optical axes of the crystal. Together with the wave vector of the idler \vec{k}_i the phase mismatch $\Delta\vec{k}$ can be defined.

Where the $u_k = \sqrt{I_k/\omega_k/W}$ represent intensities of signal I_s , idler I_i and pump I_p and $W = I_s(0) + I_i(0) + I_p(0) \cos^2(\beta)$ is the invariant energy flux. A moving coordinate system (r, τ) with

$$r = z \quad (1.17a)$$

$$\tau = t - z/v_g \quad (1.17b)$$

$$\xi = \frac{2\chi^2\pi^{3/2}\sqrt{W}}{\sqrt{\epsilon_0\lambda_i\lambda_s\lambda_p n_i n_s n_p \cos^2 \beta}} r \quad (1.17c)$$

[26] is used. The transformation reduces the dependence on z, t to a dependence on r only and effectively shows the evolution of the pulses while propagating through the medium. $\Theta(r) = \Delta k r + \phi_p(r) - \phi_i(r) - \phi_s(r)$ describes the differences between the phases $\phi_{p,i,s}$ of the electric fields. The angle β represents the difference between phase front direction and energy flow for the pump beam.

Discussion of Numerical and Analytical Solutions Baumgartner et al. [25] further solve the equation for the case of small pump depletion, $u_i(0) = 0$ and $u_s(0) \ll u_p(0)$:

$$I_s(r) = I_s(0) \cosh^2 \left(r \sqrt{\Gamma_0^2 - (\Delta k/2)^2} \right) \quad (1.18a)$$

$$I_i(r) = \frac{\omega_i}{\omega_s} I_s(0) \sinh^2 \left(r \sqrt{\Gamma_0^2 - (\Delta k/2)^2} \right) \quad (1.18b)$$

$$I_p(r) = I_p(0) \quad (1.18c)$$

$$\Gamma_0^2 = \frac{2\pi^2(\chi^2)^2 I_p(0)}{\epsilon_0 \lambda_i \lambda_s n_i n_s n_p c} \quad (1.18d)$$

As $2 \cosh x \approx \exp x$ for large x , Eq. (1.18a) shows that the signal is amplified exponentially (until signal and pump get comparable). The length scale depends on the phase mismatch Δk , the pump intensity $I_p(0)$ and the wavelengths. Fig. 1.6 illustrates the more general equations, Eq. (1.16), by showing a numerical solution and the analytic equations for small depletion, Eq. (1.18).

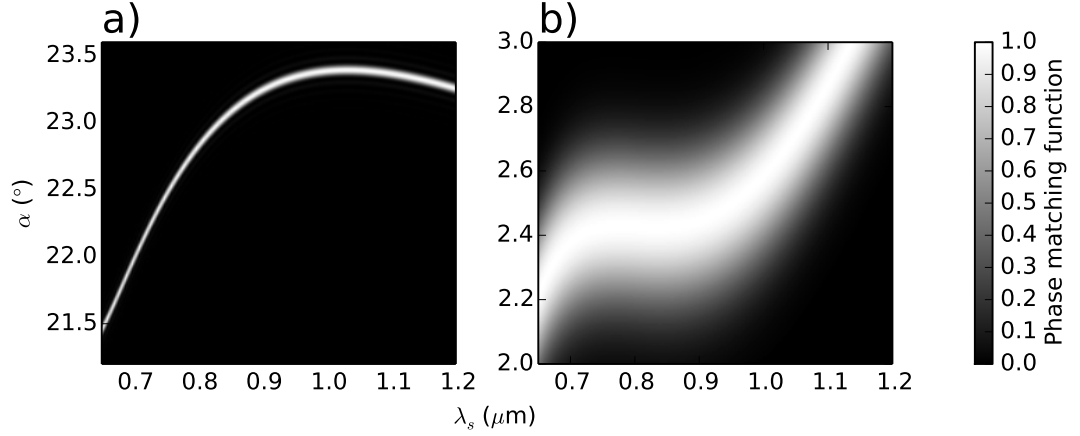


Figure 1.5: Example of phase-matching: The phase-matching function as defined in the publication of Boeuf et al. [23] is a rough measure for phase-matching. It is between one for perfect phase-matching and zero for no phase-matching. a) collinear and b) non-collinear cases for $\theta = 24.45^\circ$ are calculated with the program belonging from Boeuf et al. [23] for a 5 mm long BBO crystal with type I phase-matching at 30°C and a pump wavelength of 515 nm.

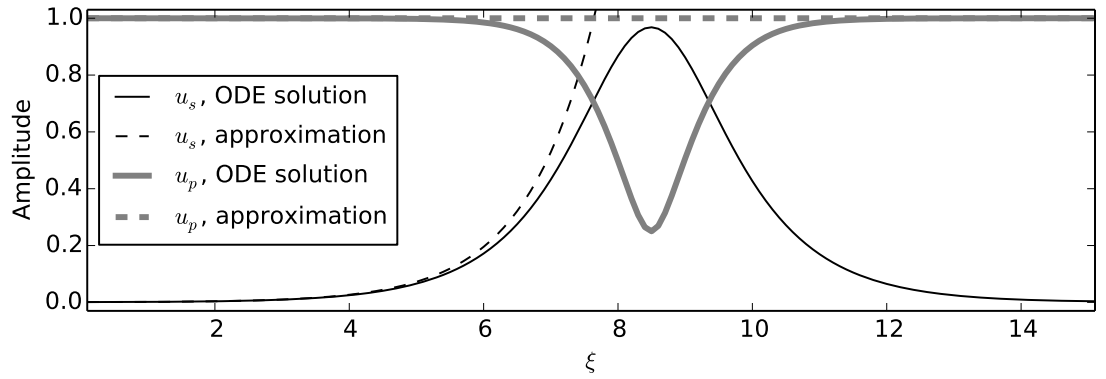


Figure 1.6: Example of OPA described by a numerical solution of the more general ordinary differential equations (ODE), Eq. (1.16), and the analytic solution in the small depletion approximation, Eq. (1.18). The phase mismatch Δk was chosen to be $\xi/2r$. u_i is graphically identical to u_s and therefore not shown.

The figure also shows the typical behavior: Initially, the signal rises exponentially and the pump is almost constant. The approximation and differential equation give the same result until the signal saturates and the assumption of no pump depletion becomes wrong because the pump loses energy. For even longer media, energy is converted back to the pump.

As the seed is chirped, its spectral components are separated in time and coincide with different temporal parts of the pump pulse, which results in different pump intensities relevant for the spectral components of the seed. The length-scale of the gain in Eq. (1.18) is $\sqrt{\Gamma_0^2 - (\Delta k/2)^2}$, which depends on the phase mismatch, the pump intensity and the wavelengths directly or via Γ_0 . As saturation occurs when significant energy is transferred, it is affected by the same quantities. Both influences can be used for spectral shaping, which can adapt the spectrum to support shorter Fourier limited and compressed pulses. Back-converting spectral components reduces the overall energy of the pulse.[27]

Following ideas from Witte [19], the phases of the pump ϕ_p , signal ϕ_s and idler pulses ϕ_i can be calculated from Eq. (1.16) to be

$$\phi_s(r) = \phi_s(0) - \frac{\Delta k}{2} \int_0^r \frac{f(r')}{f(r') + \frac{\omega_p I_s(0)}{\omega_s I_p(0)}} dr' \quad (1.19a)$$

$$\phi_i(r) = \phi_p(0) - \phi_s(0) + \frac{\pi}{2} - \frac{\Delta k r}{2} \quad (1.19b)$$

$$\phi_p(r) = \phi_p(0) - \frac{\Delta k}{2} \int_0^r \frac{f(r')}{1 - f(r')} dr' \quad (1.19c)$$

$$f(r) := 1 - \frac{I_p(r)}{I_p(0)}. \quad (1.19d)$$

Eq. (1.19a) shows that the final phase of the signal is the sum of the initial phase and an intensity-dependent term. This is important for the chirped pulse amplification as the (spectral) phase of the resulting pulse can simply be manipulated via the phase of the seed. Furthermore, changes in the intensity of the pump pulse result in changes of the phase. Changes in the phase of the pump pulse on the other side are projected onto the idler (Eq. (1.19b)).

The remainder of the chapter describes the technical implementation of NOPCPA. Sec. 1.5 discusses the actual OPA process implementation.

1.2 Pump Laser System

The setup provides the pump pulse for the NOPCPA. It is advantageous to use a spatially uniform pump as the amplification factor and phase depend on intensity. Because of to the exponential relation for small pump depletion, slightly lower intensities result in a substantial energy reduction for the resulting pulse, while at pump depletion the influence is lower.

1 Noncollinear Optical Parametric Chirped Pulse Amplification

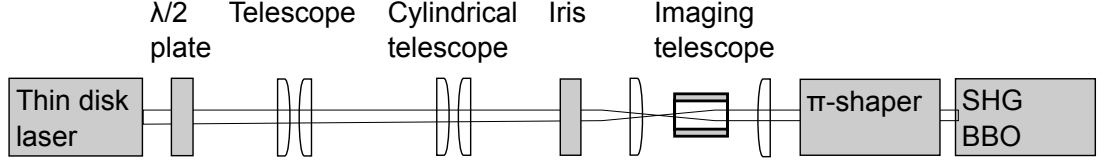


Figure 1.7: Scheme of the pump laser system: Several optics reshape a Gaussian profile with different widths in both dimensions to a flat top with doubled frequency.

A home build diode pumped chirped-pulse-amplification laser system based on Yb:YAG thin-disk technology [28] delivers 50 ps long pulses with an energy of 290 mJ at a wavelength of 1030 nm and a repetition rate of 100 Hz. It is chosen for its high stability and energy at adequate pulse durations. However, the beam shape is elliptic Gaussian, which is a Gaussian function with a different width in each dimension. The beam is reshaped via standard optics and a commercial π -shaper, which converts Gaussian beams of certain size to flat tops. The pump pulse must have a higher frequency than the seed (850 nm, Sec.1.3) in order to split pump photons into signal and idler photons (Eq. (1.14)). Therefore, a SHG process is used to provide 515 nm light.

Several optics (Fig. 1.7) reshape the pump beam to a 515 nm flat top:

1. $\lambda/2$ plate: Turns the polarization for the SHG BBO. Due to phase-matching, the BBO at the end of the pump laser system will only convert one polarization.
2. Spherical and cylindrical telescope: Transforms both axes of the elliptic Gaussian to become a circular Gaussian of the appropriate size for the π -shaper. The spherical part consists of an $f=400$ mm and a $f=-300$ mm lens. The other part is constituted by two cylindrical lenses with $f=-200$ mm and $f=300$ mm.
3. Iris: Cuts the outer part of the beam to protect the π -shaper. Diffraction patterns are controlled by imaging (next point).
4. Imaging telescope: Images the iris onto the SHG BBO to avoid interference patterns from the iris. A vacuum tube prevents self phase modulation (see Eq. (1.4)) and optical breakdown [29] in the focus.
5. π -shaper: converts a Gaussian profile into a flattop profile. It is specified to take TEM₀₀ or multi-mode with Gaussian or similar intensity profile with an $1/e^2$ width of 12.8 mm to 13.0 mm and redistribute the energy to a 12 mm flattop profile with an uniformity $<5\%$ and high edge steepness. Input and output are collimated. It is a field mapping device without internal focus from MolTech of type π -Shaper 12_12.
6. SHG BBO: converts 1030 nm to 515 nm by second harmonic generation. The phase-matching angle (Type I) for this transition is $\theta = 23.4^\circ$ [30]. The crystal has an aperture of 20 x 20 mm at an cutting angle $\theta = 23.4^\circ$ and $\phi = 0^\circ$ and a thickness of 5 mm. The material β -Barium borate (BBO) is chosen to limit the number of

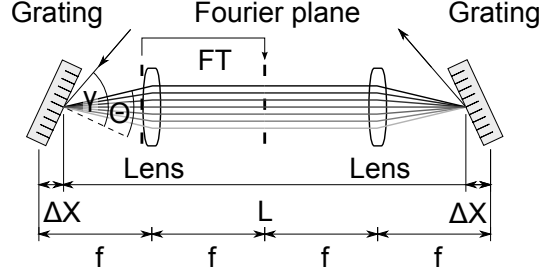


Figure 1.8: Concept of the stretcher-shaper: Light is diffracted at the first grating and follows color-dependent paths (lines in gray) which lead to a spectrally different path length. A Fourier plane is created by the combination of a lens and a grating. The setup is symmetric with respect to the vertical center axis.

crystal materials used in the setup. The crystal is mounted on a heated three-axes rotation stage to adjust the phase-matching angle. The temperature is kept at 30 °C to prevent water from entering the hygroscopic material and sustain a stable temperature without cooling. Changing the temperature would influence the refractive index and thus the phase-matching.

1.3 Seed Oscillator

The purpose of the seed oscillator is to provide spectrally broad, sufficiently strong and CEP-stable pulses as a seed for the NOPCPA.

The seed oscillator is a Rainbow HP from Femtolaser Produktions GmbH, which is specified to produce a 400 mW beam. The pulse duration is <7 fs at a repetition rate of 80 MHz and a spectral width of >260 nm (−10 dB). The central wavelength is 850 nm. It is a Ti:Sapphire oscillator, whose principles of operation are described in [31]. It contains a CEP4 [32] module from Femtolaser Produktions GmbH device to stabilize the CEP. The phase error was measured to be 50 mrad (rms) over 10 h [32].

1.4 Stretcher-Shaper and Compressor

The purpose of the stretcher is to modulate the spectral phase of the pulse to lengthen it for the OPA stages. The aim of the compressor and the shaper inside the stretcher is to ensure minimum pulse duration after amplification.

Stretcher Gratings separate the colors of the pulse such that their geometrical path length is different (Fig. 1.8). Therefore, running through the stretcher as depicted in

Fig. 1.8 adds a phase term ϕ_{st} [21]. It is

$$\phi_{st} = \frac{-2\Delta X\omega}{c \cos(\Theta)}(1 + \cos(\gamma - \Theta)) - \frac{-2\pi\Delta X \tan(\Theta)}{d_{st}} \quad (1.20)$$

$$\Theta = \arcsin\left(\frac{2\pi c}{\omega d_{st}} - \sin(\gamma)\right) \quad (1.21)$$

and depends on the speed of light c , angular frequency ω , the distance of the gratings from the foci ΔX , the angle between the grating's surface normal and the incoming beam γ , the wavelength-dependent angle between the outgoing beam and the normal to the grating Θ and the line spacing of the grating d_{st} .

Shaper Fine-tuning of the spectral phase reduces the final pulse duration. The straightforward approach to modify the compressed pulse would result in too high intensities at the used spatial light modulator (SLM) Jenoptik 640-12. However, the amplification process transfers phase changes from the seed to the signal (Eq. (1.19a)) enabling pre-compensation. The SLM is placed inside the stretcher, where the intensity is low, and the principle of operation can be understood as follows: The electric field of the pulse at the lens and at the focus are related by a Fourier transform with additional phase factors [33]. As the collimated beam in the stretcher was split by a grating before the lens, each color has its unique direction. By virtue of the Fourier transform its direction is mapped to a position. Therefore any color is imaged to a different position in the so-called Fourier plane. This is depicted in the left half of Fig. 1.8. The symmetrical right half is used to reunite the spectral components in one beam.

The 640 transmissive pixels of the SLM are placed into the Fourier plane. Each of them has an effective index of refraction, which can be controlled by a voltage. Therefore, computer control over the optical path length at each position, and hence narrow laser pulse frequency ranges, is available. The maximum phase shift is measured according to the procedure in the SLM manual to be 10.9 rad and 7.7 rad at 700 nm and 1046 nm respectively. The gratings have 600 grooves per mm and are more efficient in s-polarization but the SLM influences only the other polarization. Therefore, two broadband $\lambda/2$ plates surround the modulator.

The actual design is folded and the beam passes twice through the setup including the SLM, such that the phase terms have to be taken into account twice. The resulting path is shown in Fig. 1.9.

Compressor The compressor (Fig. 1.10) is situated after the amplification stages. It resembles the stretcher except that the lenses and SLM are absent. The added phase term reads

$$\phi_{co} = \frac{L_{co}\omega}{c \cos(\Theta)}(1 + \cos(\gamma - \Theta)) - \frac{\pi L_{co} \tan(\Theta)}{d_{co}} \quad (1.22)$$

[21]. The main differences are the change of the sign and that ΔX is replaced by L_{co} , which is the distance between the gratings. Both are the effect of the missing lenses and

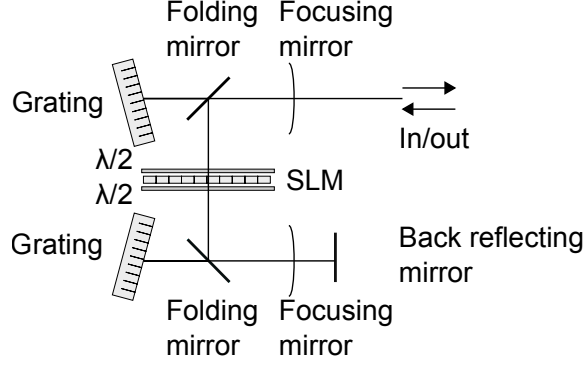


Figure 1.9: Folded design of the shaper-stretcher, Fig. 1.8: The size of the design is reduced by two folding mirrors and the SLM requires $\lambda/2$ plates to affect the right polarization. The pulse runs through the setup twice.

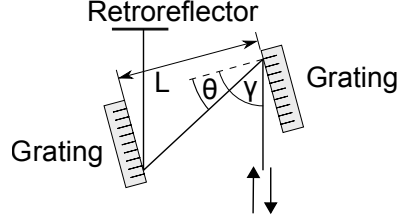


Figure 1.10: Scheme of the compressor consisting of two gratings and a retroreflector

allow to compensate ϕ_{st} by ϕ_{co} by choosing L_{co} and the compressor's γ . It would be experimentally more difficult to change the parameters of the stretcher, as the folded design with an SLM is more sophisticated.

Parameter Choice for Compressor and Stretcher $\Delta X = 14\text{ mm}$ and the stretcher's $\gamma = 14.5^\circ$ are chosen to obtain 15 ps seed pulse duration, which is justified in Sec. 1.6, and reflect the center wavelength back by the used -1st order reflection of the blazed grating to simplify the alignment.

The line spacings are chosen differently, $d_{co} = \frac{1\text{ mm}}{1200}$ and $d_{st} = \frac{1\text{ mm}}{600}$. Therefore, ϕ_{st} and ϕ_{co} do not compensate each other completely and a net phase contribution is available to compensate phase terms from e.g. optics and the NOPCPA process. An example for the compensation of additional phase terms is given in Fig. 1.11: The SLM and the net phase contribution can compensate the dispersion of 40 mm fused silica. Without the net phase contribution the compensation of the fused silica is outside the range of the SLM.

B-Integral Sending the beam from the compressor through ambient air to the next element, the HHG section, is not possible because of a high B-integral (Eq. (1.4)). It equals a few hundred for a 15 mJ pulse with a pulse duration of 7 fs and a diameter of

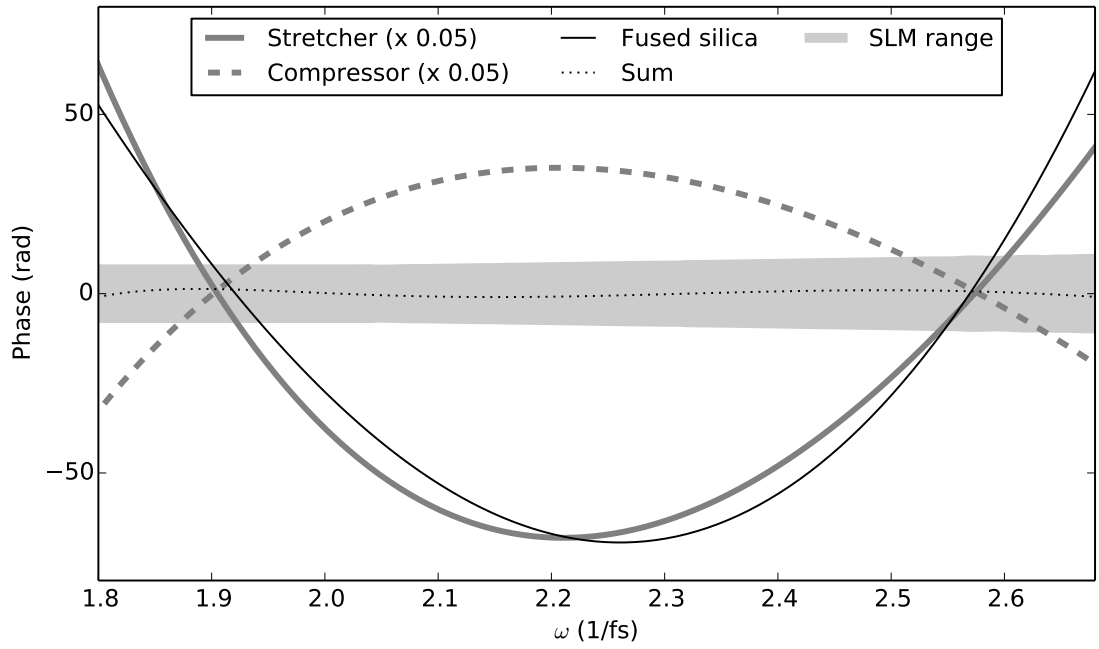


Figure 1.11: Example of compensation of additional phase terms: As only the change of the pulse shape is of interest, linear terms of the form $a\omega + b$ have been added to the shown curves to reduce the absolute phase values without changing the information. The phase term of the stretcher (Eq. (1.20)) is given by the values from the text. As an example, the phase shift of 40 mm fused silica and the contribution from the stretcher are compensated by selecting the adequate the compressor's parameters γ_{co} and L_{co} (Eq. (1.22)). The resulting phase is shown as 'sum' and lies within the range of the phase modulation of the SLM (gray area). Therefore, the remainder phase can be compensated and the pulse duration is Fourier limited. The SLM does not have the capacity to compensate the fused silica alone, so it was necessary to use the difference in the phase curves of stretcher and compressor.

8 mm that travels through 10 m of air, which roughly represent the distance between the compressor and the HHG cell. The nonlinear index of refraction is $\approx 12 \times 10^{-23} \text{ m}^2/\text{W}$ for 1 bar air [34]. The pressure needs to be reduced by a factor of at least 100 to reduce the B-integral sufficiently. Consequently, the beam path is in (rough) vacuum.

1.5 OPA Stages

The purpose of the OPA stages is to transfer energy from the pump pulse (Sec. 1.2) to the seed pulse. There are three amplification stages OPA1, OPA2 and OPA3, which base upon the principle of optical parametric amplification as described in Sec. 1.1.4. They

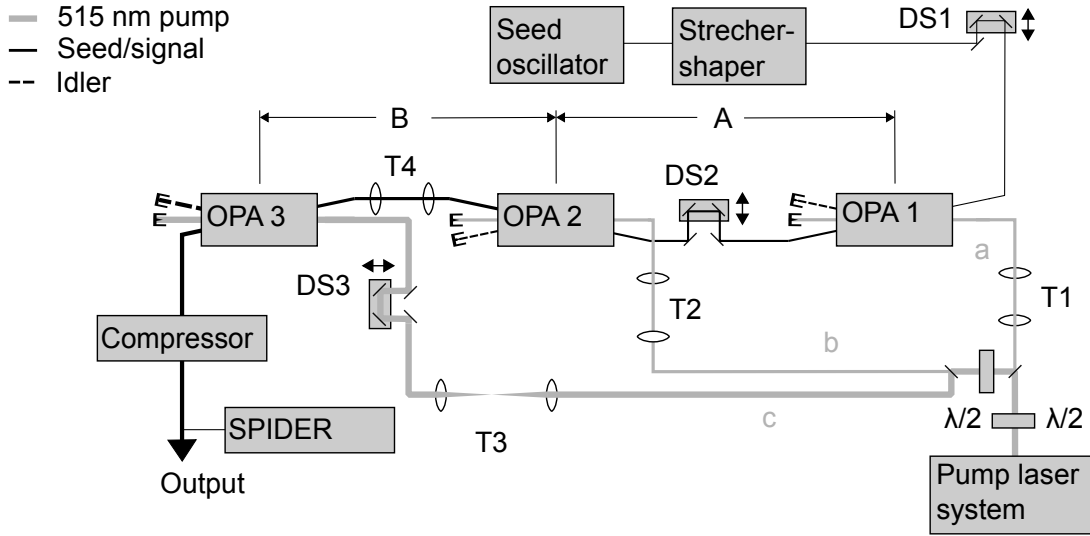


Figure 1.12: Scheme of the amplification: Telescopes T1-3 and $\lambda/2$ plates distribute the pump energy to the OPA stages OPA1-3, where the stretched seed is amplified. The delay stages DS1-3 and the distance A, B, a, b and c enable temporal coincidence of pump and seed pulses. The telescope T4 magnifies the seed for the bigger OPA3. The output of OPA3 is compressed and measured by a SPIDER.

are situated between the stretcher-shaper and the compressor to reduce the intensity under the damage threshold.

BBO was chosen as interaction material for the process because:

- phase-matching is possible over the required bandwidth (700–1000 nm) for the chosen parameters $\alpha = 2.5^\circ$ and $\theta = 24.45^\circ$ [35] in case the seed's polarization is orthogonal to the optical axis and the pump is orthogonal to the seed.
- The damage threshold is high. For 50 ps pulses it is about 20 GW/cm² [36, 37].
- The nonlinearity is high compared to other nonlinear crystals for OPA [38].

The first two OPA stages are intended to amplify 1000 times and OPA3 100 times. The absolute energy transfer in the last stage is by far the biggest. Therefore, a higher pump energy is used in the last stage to allow more conversion. The energy is distributed by a combination of two $\lambda/2$ plates and two polarizing beam splitters as 10 mJ, 10 mJ and 160 mJ, respectively. Pump and seed are magnified for the last pass in order to provide a safe intensity. The BBOs have an aperture of 5 mm \times 5 mm (OPA1-2) and 20 mm \times 20 mm (OPA 3) at a cut angle of $\theta = 21.9^\circ$ and $\phi = 0^\circ$ (Type I phase-matching) and a thickness of 5 mm. They are mounted and temperature-stabilized similar to the SHG BBO in the pump laser system (p. 21).

The constraints for each stage are the same and lead to the setup depicted in Fig. 1.12:

1 Noncollinear Optical Parametric Chirped Pulse Amplification

1. Pump and seed must coincide temporally (and spatially). This is accomplished by the relation of the distances between the OPA stages ($A=120$ cm and $B=140$ cm) and the distances from the SHG BBO to the respective stage ($a=240$ cm, $b=360$ cm and $c=500$ cm) and by synchronizing the pump laser and seed oscillator to be described in the Sec. 1.6. The translation stages DS1-3 can fine-tune the temporal overlaps in their respective OPA stage.
2. The geometry and polarization of pump and seed beam relative to the crystal axis must match broadband phase-matching conditions. The optical axis of the BBO is turned in the horizontal plane. The seed is polarized vertically and the pump horizontally. Because of refraction the phase-matching angle $\alpha = 2.5^\circ$ between pump and seed is 4° in air. Due to the high sensitivity of the phase-matching to the angles, they require fine-tuning to achieve the desired bandwidth of the amplification.
3. Any part of the pump and seed beam must have the same relative angle for phase-matching. Hence the beams have to be collimated.
4. Efficient conversion requires a high pump intensity but the damage threshold limits the possible maximum. Telescopes T1-3 (Fig. 1.12) set the appropriate intensities for the pump in each stage. Their lenses' focal lengths are 20 cm/1 m, 30 cm/1.5 m and 1 m/1.5 m respectively. T4 (Fig. 1.12) magnifies the seed for the bigger OPA3. The assumed pump energies give intensities of 4 (OPA1, 2) and 6 GW/cm² (OPA3), which is under the damage threshold of 20 GW/cm².
5. In order to maintain the flat-top profile of the pump, each crystal has to be in the image plane of the SHG BBO. This is the second purpose of T1-3. In all cases the first lens in the beam images the SHG BBO to infinity and the second images infinity to the OPA stage. A vacuum tube prevents self phase modulation (see Eq. (1.4)) and optical breakdown [29] in the focus.

An estimate of the possible signal pulse energy can be generated by comparison to the similar design from Witte [19]. Their pump laser produces 250 mJ, while the pump laser of the current design returns 290 mJ. Their compressed pulse contained an energy of 15.5 mJ, the spectrum reached from 700 nm to 1000 nm and had a Fourier limited pulse duration of 7.3 fs (FWHM). As the pump power here is slightly higher, further calculations can safely assume 15 mJ in 7 fs.

1.6 Synchronization

Synchronization System The purpose of the synchronization is to ensure that the pump and the seed pulses are coincident in the OPA stages. To this end, the repetition rate and relative phase of seed and pump laser are controlled by a system of five feedback loops (Fig. 1.13), which was developed at the MBI by Ingo Will, Ingo Templin and Mark Fiedler. There are 4 main loops L1-4. Each of them is fed by the signal of a photo diode and changes the length of the respective oscillator cavity by a piezo actuator.

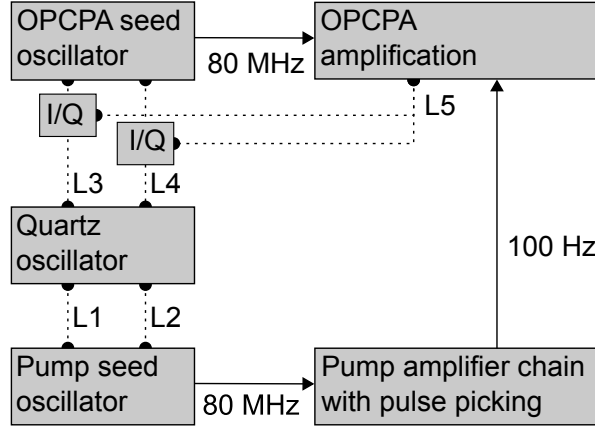


Figure 1.13: Scheme of the synchronization: The pump's seed oscillator and the NOPCPA's seed oscillator are phase locked to a quartz oscillator via the feedback loops L1-4. L5 additionally corrects slow drifts in the pump laser through I/Q modulators.

Initially, the pump seed oscillator and NOPCPA seed oscillator are phase-locked by the loops L1 and L3 to an 80 MHz signal from a clock divider fed by a 1280 MHz quartz oscillator. As the laser oscillators have a repetition rate of 80 MHz controlling their relative phase at the same frequency always allows coincidence at the OPA stages for a phase $0..2\pi$. Control is switched from L1 and L3 to L2 and L4 while maintaining this rough synchronization. Using the 16 times higher frequency of 1280 MHz in L2 and L4 results in smaller temporal fluctuations at the same phase error but depends on the previous synchronization via L1 and L3 as the maximum time shift is now 16 times smaller. The pathway through the pump amplifier chain is on the order of 400 m. To compensate slow (thermal) fluctuations the loop L5 uses I/Q modulators within L3 and L4 to correct the phase of the quartz oscillator. The color of the signal, which depends on the overlap as the pulse is chirped, provides feedback for L5. The pump laser uses a Pockels cell to pick any 800,000th pulse of its oscillator and amplify it. Therefore only any 800,000th seed pulse can be amplified.

Pulse Durations The Jitter of 0.3 ps for the operation of L2 and L4 is the last fact needed for the discussion of the pulse durations of pump (50 ps) and seed (15 ps):

- The compressor and stretcher can elongate the seed pulse to the few ps regime. Much longer pulses would require large setups (Sec. 1.4).
- Damage thresholds must be kept for the pump energy and available crystal aperture sizes (Sec. 1.5).
- The seed is chirped which means that different colors are present at different times. As all colors need to be amplified, a rather constant intensity is favorable. On the

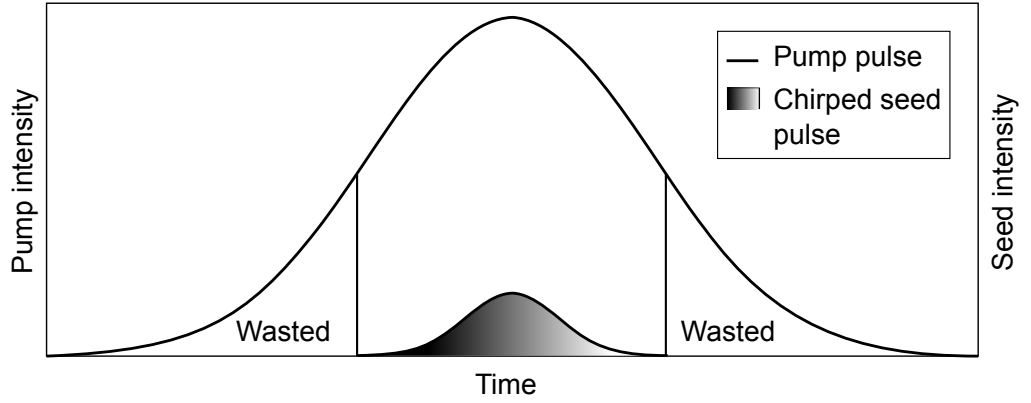


Figure 1.14: Scheme of the relative length of pump and seed: The hue of gray in the seed represents chirp. The pump's energy before and after the seed is lost.

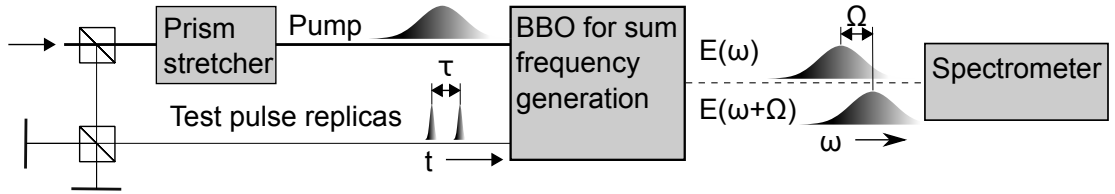


Figure 1.15: Scheme of the SPIDER setup: Beam splitters create 3 replicas of the test pulse. One of them is stretched and pumps the sum frequency generation of the others. As the others are delayed with respect to each other and the pump is chirped, both experience different frequency shifts. A spectrometer records their interference.

other hand, the energy at the ends of the pump pulse is wasted. As a compromise the pump is chosen to be three times longer than the seed. This trade of is illustrated in Fig. 1.14.

- The pump pulse is so long that the synchronization jitter is negligible.

1.7 SPIDER

The SPIDER characterizes the spectral phase of the amplified pulses and provides this information to an algorithm that controls the SLM in the compressor (Sec. 1.4) to reduce the pulse duration to the Fourier limit.

SPIDER stands for spectral phase interferometry for direct electric field reconstruction and is a method to extract the spectral phase $\phi(\omega)$ of a laser pulse by measuring interference patterns between spectrally offset replicas of the pulse. It was developed by Chris Iaconis and Ian Walmsley whose publication [39] guides this description.

The principle is depicted in Fig. 1.15. Two beam splitters generate three pulses: Two

test pulses E , which are delayed by a duration τ with respect to each other, and a pump pulse which chirped by a prism stretcher. A BBO is used for sum frequency generation (refer to Sec. 1.1.2) of both test pulses and the stretched pump pulse. A spectrometer observes the resulting spectrum. Because of the chirp of the pump pulse the test pulses experience pumps with a difference in angular frequency Ω . Therefore, they are spectrally offset with respect to each other after the sum frequency generation in the BBO. This results in a spectral intensity containing a beat term and the phase ϕ of the test pulse:

$$\begin{aligned} I(\omega) &\propto |E(\omega) + E(\omega + \Omega)|^2 \\ &\propto |E(\omega)|^2 + |E(\omega - \Omega)|^2 \\ &\quad + 2|E(\omega)E(\omega - \Omega)| \cos(\phi(\omega - \Omega) - \phi(\omega) - \tau\omega) \end{aligned} \quad (1.23)$$

After a Fourier transformation the first two terms are close to 0 while the last one is centered on $-\tau$ and τ as $\cos \phi = 0.5 \exp(i\phi) + 0.5 \exp(-i\phi)$. Therefore, a Fourier filter can isolate $|E(\omega)E(\omega - \Omega)| \exp(i(\phi(\omega) - \phi(\omega - \Omega) + \tau\omega))$. $\tau\omega$ can be found by setting Ω experimentally to zero or by observing the SHG of the test pulses [19]. After using the complex arg function and subtracting $\omega\tau$, $\theta(\omega) := \phi(\omega) - \phi(\omega - \Omega)$ is known. After setting the phase at frequency ω_0 to zero, the phase can be reconstructed:

$$\begin{aligned} \phi_{recon}(\omega_0 - 2\Omega) &= -\theta(\omega_0 - \Omega) - \theta(\omega_0) \\ \phi_{recon}(\omega_0 - \Omega) &= -\theta(\omega_0) \\ \phi_{recon}(\omega_0) &:= 0 \\ \phi_{recon}(\omega_0 + \Omega) &= \theta(\omega_0 + \Omega) \\ \phi_{recon}(\omega_0 + 2\Omega) &= \theta(\omega_0 + 2\Omega) + \theta(\omega_0 + \Omega) \end{aligned} \quad (1.24)$$

The choice of τ and Ω was discussed by Anderson et al. [40]: Both values have broad optima. A too large delay τ creates a too strongly modulated spectrum which can no longer be sampled by the spectrometer's pixels. According to the Nyquist–Shannon sampling theorem at least two points per fringe are required. In case of too small delays, the Fourier filtering of Eq. (1.23) fails because the contributions of the different terms are not separated. Anderson et al. [40] suggest 15 pixel per fringe. The CCD camera of the spectrometer has 1920 pixels, hence $\tau=900$ fs for the given spectrum¹.

According to the Nyquist–Shannon sampling theorem only pulses up to a duration $T_{max} = 2\pi/\Omega$ can be sampled, which puts a boundary on the choice of Ω . As the phase is reconstructed iteratively on a grid with spacing Ω , a large Ω sacrifices resolution while small Ω lead to the accumulation of large errors Anderson et al. [40] suggest a T_{max} 10 times greater than the pulse duration. This results in $\Omega = 90$ /ps.

Both values determine the second order dispersion ϕ'' of the prism stretcher by their relation (1.8) $\phi'' = -\tau/\Omega$, giving $-10\,000$ fs². As the test pulses are equal the sign of τ is not important and a dispersion of $10\,000$ fs² is appropriate.

¹1920/15 gives 128 fringes. Therefore, $\omega\tau$ should cover $2\pi \cdot 128$, which for the spectrum from 700–1000 nm gives $\tau=900$ fs

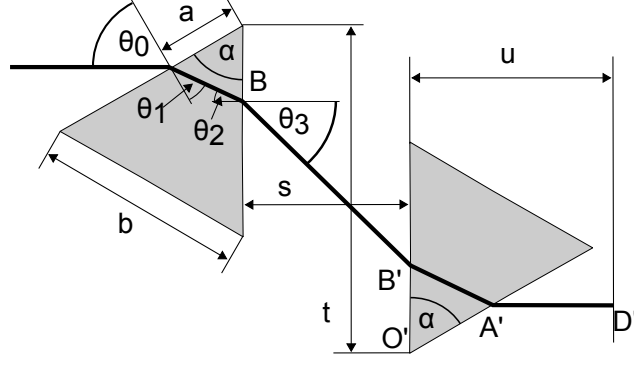


Figure 1.16: Scheme of a stretcher consisting of two prisms and defining geometrical quantities [21]

Fig. 1.16 shows a prism stretcher and the variables defining its geometry. The pump pulse for SFG is running twice through such an stretcher and hence gets an additive phase term ϕ_{prism} :

$$\phi_{prism} = 2 \frac{nL_g + \overline{BB'} + \overline{A'D}}{k} \quad (1.25)$$

The refractive index n for the material of the prism, BK7, can be calculated via Sellmeier coefficients [41]. The lengths a , t and s and the angle θ_0 define the geometry. When also determining the reference plane D by setting u , the variables in Eq. (1.25) can be calculated:

$$n^2 - 1 = \frac{1.03961212\lambda_{\mu m}^2}{\lambda_{\mu m}^2 - 0.00600069867} + \frac{0.231792344\lambda_{\mu m}^2}{\lambda_{\mu m}^2 - 0.0200179144} + \frac{1.01046945\lambda_{\mu m}^2}{\lambda_{\mu m}^2 - 103.560653} \quad (1.26a)$$

$$\theta_1 = \arcsin(\sin(\theta_0)/n) \quad (1.26b)$$

$$\theta_2 = \alpha - \theta_1 \quad (1.26c)$$

$$\theta_3 = \arcsin(\sin(\theta_2)n) \quad (1.26d)$$

$$L_g = (t - s \tan(\theta_3)) \sin(\alpha) / \cos(\theta_1) \quad (1.26e)$$

$$\overline{BB'} = s / \cos(\theta_3) \quad (1.26f)$$

$$\overline{O'A'} = (t - s \tan(\theta_3))(\cos(\alpha) + \sin(\alpha) \tan(\theta_1)) - a \quad (1.26g)$$

$$\overline{A'D} = u - \overline{O'A'} \sin(\theta_0) \quad (1.26h)$$

[21] Taking $a = 10$ mm, $\theta_0 = 60^\circ$, $t = 32$ mm and $s = 20$ mm results in an average dispersion $\frac{d^2\phi}{d\omega^2} = 5000$ fs² for each of the two passes and hence the proposed amount of Ω .

A computer reads the spectrometer and processes the SPIDER measurement. After the voltages required for the correction of the phase at the SLM are calculated and forwarded to the device, the procedure is repeated to keep the pulse duration close to the Fourier limit.

In the course of the thesis the optical setup was constructed. The parameters of the optics were calculated and the actual setup built. Software was written to fine tune the compression of the pulse after the compressor. The implemented steps are

1. Read the CCD camera image and compute $I(\omega)$.
2. Perform the algorithm described above to obtain ϕ_{recon} .
3. Compute a set of voltages for the SLM to minimize the pulse duration.
4. Write the voltages and continue with step 1.

Additionally, the steps are visualized.

1.8 Summary

Due to the prospective to deliver short, multi-TW pulses the chapter proposes an NOPCPA based setup following the work of Witte and Zinkstok [19] but with a stronger pump laser on the basis of thin disk technology. NOPCPA transfers energy from a pump pulse to a seed pulse without storing the energy. The nonlinear nature of the process implies that a constant intensity is highly beneficial. Furthermore, short pulses require a large bandwidth, which must be covered by the amplification process.

These properties lead to a design centered on three BBO crystals, which perform the actual amplification of the CEP stable seed pulses. The large required bandwidth needs a precise tuning of the phase-matching angles. A stretcher before the crystals increases the pulse duration to lower the intensity under the damage threshold. After the amplification a grating compressor reduces the duration. The combination of an SLM and a SPIDER allows automatized fine-tuning of the compression to ensure the lowest possible duration of the resulting pulse. The process benefits from the spatially constant intensity of the pump pulse provided by the pump laser system, which forms a flat top profile from an elliptic Gaussian beam. The influence of intensity gradients in time is reduced by using a pump that is three times longer than the seed. A synchronization scheme and appropriate path lengths for the pump and seed laser forces both pulses to coincide at the BBO crystals, which is required by the instantaneous nature of the amplification process.

The expected pulse parameters, 15 mJ in a 7 fs long pulse, are used in the next chapter, which calculates the optimal conversion to XUV via high harmonic generation.

2 Theoretical Comparison of Different HHG Gating Techniques

2.1 Introduction

The chapter is devoted to the last conversion process of the setup: High harmonic generation. The technical aspects are discussed in Chap. 3. Here, the optimal parameters will be calculated. In order to allow as-as XUV-XUV pump-probe experiments, the intensity should be as high as possible and the pulse duration in the attosecond regime. The parameters for the input pulses are taken from the last chapter (7 fs duration and an energy of 15 mJ). As the XUV pulses without gating techniques are too long for pump-probe attosecond-attosecond experiments, these methods are mandatory. The efficiency of the conversion should be as high as possible.

The simplest explanation of the HHG process is the three step model by Corkum [4]. Within each maximum of a cycle of a laser field atoms are ionized. The electric field accelerates the resulting electron. After the inversion of the direction of the field the electron is accelerated back and electron and parent ion can recombine and emit an XUV photon. This single atom process requires phase-matching to give macroscopic amounts of XUV and repeats at every cycle of the driving IR pulse.

Gating methods reduce the XUV pulse duration by allowing only one cycle to efficiently produce the XUV:

- Polarization gating: Prevents the re-collision for all but one cycle by using an elliptically polarized pulse with only a short time window with linear polarization [5].
- Two-color gating: The HHG process is highly nonlinear [42]. The superposition of two IR laser pulses of different frequencies can result in interference patterns that exhibit only one pronounced peak [43]. As extensive modifications to the NOPCPA setup would be necessary to obtain a second IR pulse with a different spectrum, this approach will not be simulated.
- Double optical gating (DOG): Polarization gating can be assisted by the second harmonic of the fundamental to combine the last two ideas [7].
- Ionization gating: The phase-matching depends on the concentration of electrons which originate from ionization by the driving pulse. The phase-matching can be chosen to be balanced only for a finite concentration and hence a narrow, temporal part of the pulse [6].

2 Theoretical Comparison of Different HHG Gating Techniques

Table 2.1: Overview of the best achieved HHG efficiencies and each gating method

Method	Publication	Efficiency
Ionization gating	Ferrari et al. [6]	2.6×10^{-5}
Polarization gating	Sansone et al. [5]	3.5×10^{-7}
DOG	Mashiko et al. [7]	6×10^{-6}

- Attosecond lighthouse effect [44, 45]: The IR pulse front in the HHG medium can have different directions for different half cycles of the driving IR pulse. The resulting XUV pulses from each cycle propagate into different directions which allows to block all but one by an aperture. This method does not work in the given parameter regime: Following Kim et al. [45], the angle between two XUV bursts from an IR spectrum from 700 nm to 1000 nm and beam waist of 700 μm (see Tab. 2.3) can be at most $\frac{300 \text{ nm}}{2 \cdot 700 \mu\text{m}} = 0.2 \text{ mrad}$. Judging from Midorikawa et al. [42], the beam divergence is about 0.5 mrad. Hence separation is not possible.

High harmonics generation is often done in gaseous media. However, relativistic plasma mirrors are a very promising source for as-as pump-probe experiments [46] as well. Basically, the atom in Corkum's model is replaced by plasma. This new regime is far from the chosen techniques, ionization gating, polarization gating and DOG, and is therefore omitted.

A historical account of achieved parameters is given in the article by Takahashi et al. [3]. Tab. 2.1 lists the selected methods with the publications reporting the highest efficiencies. Ferrari et al. [6] implemented the best efficiency of 2.6×10^{-5} for ionization gating, which cannot easily be compared to the parameters from the NOPCPA chapter as the relation of pulse duration and a single half cycle is a very important parameter. It does not only set requirements for the phase-matching but also directly influences the conversion efficiency as the energy of all but one half cycles is discarded. Therefore, the relation of the fundamental pulse length and half cycle duration ($\approx 1.3 \text{ fs}$) is important. Ferrari et al. work with a 5 fs pulse, which is - in this sense - much shorter than the 7 fs assumed in this chapter. Values from literature for the IR intensity differ by almost an order of magnitude: Ferrari et al. [6] used $2.3 \times 10^{15} \text{ W/cm}^2$, while Abel et al. [47] worked at $5 \times 10^{14} \text{ W/cm}^2$. The difference is unexplained and the pulse durations are similar (5 and 7 fs).

Sansone et al. [5] published the best efficiency for polarization gating. It is markedly lower (3.5×10^{-7}) but comparability for the parameter from the NOPCPA chapter suffers from the short pulse duration of 5 fs as it is not obvious whether the efficiency of both methods scale similar with pulse duration.

Mashiko et al. [7] demonstrated the highest efficiency for DOG, 6×10^{-6} , using an IR pulse duration of 9.1 fs. Their energies are also in a different regime: They are using 150 μJ for the fundamental and 30 μJ for the second harmonic, which is 2 orders of magnitude beneath the given 15 mJ.

No experimental or theoretical work dedicated to the comparison of different gating techniques was found by the author. Composing an experimental comparison from

existing literature would be challenging due to the unknown scaling of the efficiency with the parameters, different objectives of the authors and discrepancies like the mentioned, different intensities for ionization gating.

Calculating HHG is not trivial and an active field of research [48, 49, 50]. Single gating techniques have been reproduced: Ferrari et al. [6] use a numerical computation to understand their ionization gating. Polarization gating was reproduced by Shan et al. [51] numerically and experimentally. Lan et al. [52] demonstrate DOG theoretically. The chapter complements these calculations by a comparison of all techniques with constant input parameters. Furthermore, parameters for the design of the HHG system in the next chapter will be calculated.

To this end, Sec. 2.2 explains the gating techniques in more detail and lays theoretical foundations for the calculation of HHG. The corresponding model is described in Sec. 2.3. Optimal conditions and the corresponding energies and durations of the XUV pulses are presented in Sec. 2.4. A reference optimization without gating and the combination of DOG and ionization gating complements ionization gating, polarization gating and DOG. A review of the assumptions and a summary conclude the chapter.

2.2 Theory

The section introduces the models necessary for the chapter. High Harmonic Generation (HHG) is a nonlinear process that is possible at high intensities (order of magnitude: $1 \times 10^{13} \text{ W/cm}^2$ or above [42]). Therein, single atoms produce XUV radiation. This is described qualitatively by the simple Corkum model [4] (Sec. 2.2.1). The more sophisticated Lewenstein model [53] (Sec. 2.2.2) and the wave equation (Sec. 2.2.3) are used for quantitative calculations in the chapter. The next paragraph observes general features of the HHG radiation of single atoms (Sec. 2.2.4). For a macroscopic effect they have to interfere constructively. Constant's simple model [54] (Sec. 2.2.5) shows the effect of phase mismatch and reabsorption of the XUV in the generating gas. The section concludes with a list of parameters which influence the phase-match (Sec. 2.2.6) and a description of gating methods (Sec. 2.2.7).

2.2.1 Corkum's Model

A simple explanation of laser radiation driven HHG is the three-step model by Corkum [4]. It can be described within the single active electron approximation, where the wave functions of all but one electron are held constant [55]. First, an atom is ionized (modeled by the ADK rate [56]), then the electron is accelerated within the continuum by the laser field. The electron is considered to move on a classical trajectory which neglects the ion's field. Depending on the path it can recombine with the parent ion and emit the gained energy. The trajectories of such a model for a continuous wave are shown in Figure 2.1.

The relevance of a trajectory is given by its population weight (gray level), which is governed by the ionization efficiency. Therefore, trajectories starting when the intensity is low are not important. Most electrons arrive at the core at the second field

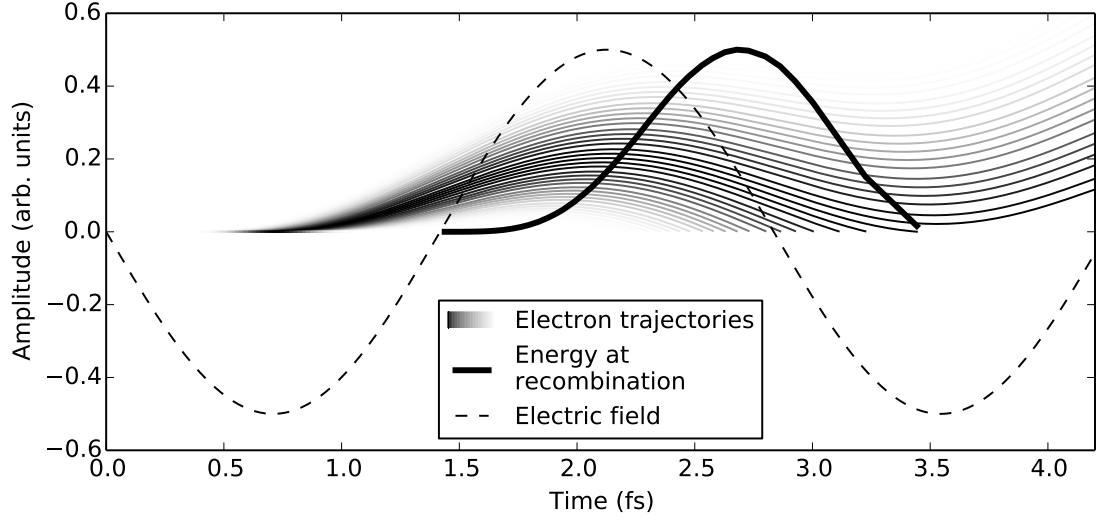


Figure 2.1: Illustration of the electron trajectories in the Corkum model [4]: Calculated classical electron trajectories and impact energies emerging for a continuous, linearly polarized 850 nm wave. The darker the color of the trajectory the higher is the ionization probability (i.e. driving intensity) at the origin of the trajectory. Trajectories from other half cycles than shown are analogous.

reversal after ionization. The most energetic trajectories determine the so-called cut-off energy $E_{\text{cut-off}}$:

$$E_{\text{cut-off}} = IP + 3.17 U_p \quad (2.1)$$

$$U_p = \frac{e^2 \lambda^2 I}{8\pi^2 \epsilon_0 c^3 m_e} \quad (2.2)$$

where IP is the ionization potential of the atom, U_p is the ponderomotive potential (average kinetic energy of a free electron). For monochromatic light it is given by Eq. (2.2) and depends on the wavelength λ , intensity I and the mass of the electron m_e . For example an intensity of $2.3 \times 10^{14} \text{ W/cm}^2$ and a wavelength of 850 nm leads to $U_p = 15.76 \text{ eV}$, the ionization potential of Ar.

2.2.2 Lewensteins's Model

Lewenstein et al. [53] present a quantum mechanical treatment of HHG. They calculate the atomic dipole matrix element \vec{d} , which relates to (the macroscopic) polarization via the particle number density N :

$$\vec{P} = N \vec{d} \quad (2.3)$$

They are assuming that

Table 2.2: Values of the units of Lewenstein et al. [53] in SI units: They are deduced from comparing formulas in the publication with their respective SI versions.

Name	Unit in [53] and Eq. (2.4)
Electric field	$\sqrt{\hbar\omega_0^3 m_e} e^{-2}$
Time	ω_0^{-1}
Energy	$\hbar\omega_0$
Dipole moment	$e\sqrt{\hbar\omega_0^{-1} m_e^{-1}}$

- many photons are necessary to ionize and
- the ponderomotive energy is at least comparable to the ionization potential IP but the corresponding intensity is not sufficient to ionize all atoms during the interaction.

Their conclusions from that are:

- Only the evolution of the ground state of the atom is important, it is not depleted.
- In the continuum, the electron is a free particle in an electric field.
- Their theory does not model slow electrons.

Lewenstein et al. [53] then calculate the dipole moment as their Eq. 13, which can be extended to two dimensions and generalized to the electric field $\vec{E}(t)$:

$$\vec{d}(t) = i \int_0^\infty d\tau \left(\frac{\pi}{\epsilon + i\tau/2} \right)^{3/2} \exp(-iS(\vec{p}_{st}, t, \tau)) \cdot \vec{d}_H^*(\vec{p}_{st}(t, \tau) - \vec{A}(t)) \left[\vec{d}_H(\vec{p}_{st}(t, \tau) - \vec{A}(t - \tau)) \cdot \vec{E}(t - \tau) \right] + c.c. \quad (2.4a)$$

where

$$\vec{d}_H(\vec{p}) = i \frac{2^{7/2} (2IP)^{5/4}}{\pi} \frac{\vec{p}}{(\vec{p}^2 + [2IP])^3} \quad (2.4b)$$

$$\vec{p}_{st}(t, \tau) = \frac{1}{\tau} \int_{t-\tau}^t \vec{A}(t') dt' \quad (2.4c)$$

$$S(p, t, t') = \int_{t'}^t \frac{[\vec{p} - \vec{A}(t'')]^2}{2} + IP dt'' \quad (2.4d)$$

\vec{A} is the vector potential of the laser field. ϵ is a regularization parameter, which is a small number to evade a singularity in the numerical calculation. The expression for the dipole moment \vec{d}_H for hydrogen-like atoms is used as a standard approach. S can be interpreted as quasi-classical action and $\vec{p} = \vec{v} + \vec{A}$ is a canonical momentum depending on the speed of the electron \vec{v} . The stationary momentum \vec{p}_{st} stems from the application of a saddle point method to solve an integral over canonical momentum. It also leads to a

physical interpretation of the equation: \vec{p}_{st} belongs to electrons that are created at time τ and return at time t . The $\vec{d} \cdot \vec{E}$ term hence represents their production, \vec{d}^* the effect of their recombination and $\left(\frac{\pi}{\epsilon + i\tau/2}\right)^{3/2}$ the quantum diffusion in between. All quantities in Eq. (2.4) are in atomic units except the time, which uses the inverted central angular frequency ω_0 of the driving electric field as unit. Tab. 2.2 lists the relevant conversions.

The model is only valid for XUV frequencies beyond the ionization threshold as an electron with less energy cannot be assumed to be a free particle. E.g. An monochromatic E field with a wavelength of 850 nm and an intensity of 2.3×10^{14} W/cm² in Ar ($IP = 15.76$ eV) would result in a XUV spectrum modeled only above 15.76 eV and reaching till $E_{\text{cut-off}} = 66$ eV (Eq. (2.1)).

2.2.3 Wave Equation

Husakou and Herrmann [57] reformulated the wave equation Eq. (1.1). They express the relation between a nonlinear polarization \vec{P}_{NL} and the resulting electric field \vec{E} using a moving frame of reference (ξ, η) :

$$\frac{\partial \vec{E}(\vec{r}, \omega)}{\partial \xi} = -\frac{1}{2L_{abs}} \vec{E}(\vec{r}, \omega) + i \frac{1 - n(\omega)}{c} \omega \vec{E}(\vec{r}, \omega) - \frac{i\omega}{2c\epsilon_0 n(\omega)} P_{NL}(\vec{r}, \omega) \quad (2.5a)$$

$$\xi = z \quad (2.5b)$$

$$\eta = t - z/v_g \quad (2.5c)$$

They neglect back reflection and the term $-\frac{1}{2L_{abs}} \vec{E}(z, \omega)$ was added to account for absorption. As the index of refraction is very close to unity in the XUV [58] the second term on the right side of the main equation is zero for XUV radiation. The source term $-\frac{i\omega}{2c\epsilon_0 n(\omega)} P_{NL}(\vec{r}, \omega)$ is proportional to the number density N and includes the nonlinear polarization P_{NL} from Lewenstein's dipole moment and Eq. (2.3). The quantity A_r is defined as

$$A_r = -\frac{1}{N} \frac{i\omega}{2c\epsilon_0 n(\omega)} P_{NL}(\vec{r}, \omega). \quad (2.6)$$

It is called atomic response because it is only a function of the gas species and the fundamental field and is the source term for the XUV field (Eq. (2.5)).

2.2.4 General Features of the Atom Response

Fig. 2.2 shows examples of single atom HHG radiation for a monochromatic fundamental pulse. The simple model of Corkum predicts the highest frequencies of light to be generated shortly before the fundamental electric field is zero (Fig. 2.1). The same effect is present in Lewenstein's model. Corkum's model also predicts a highest frequency, the cut-off, which is shown in the graph and marks the end of the plateau of the spectral intensity.

The process is periodic in the fundamental's frequency. This translates into a spectrum that consists of contributions around harmonics of the fundamental laser cycle and leads

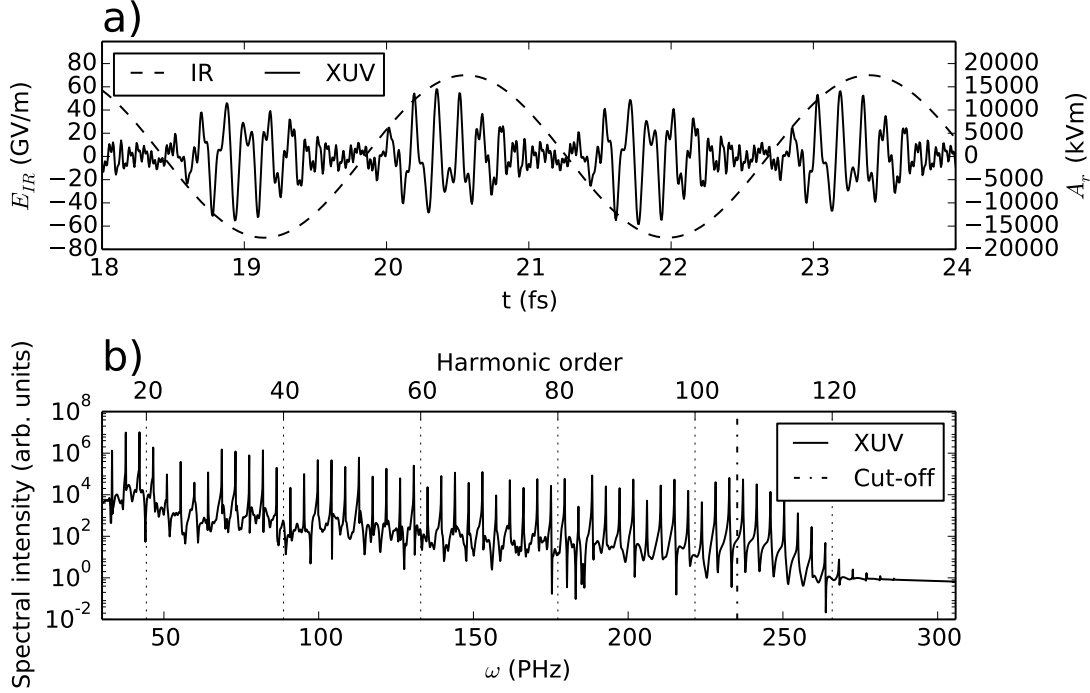


Figure 2.2: Example of the single atom response A_r for a long, monochromatic pulse centered on a wavelength of 850 nm with a peak field strength of 70 GV/m in Ar calculated by Eq. (2.3), (2.4) and (2.6). The cut-off is calculated by Eq. (2.1).

to the term high harmonic generation. Both half cycles of the pulse generate the same radiation but with opposite sign. Spectral components around even multiples of the fundamental frequency would result in identical half cycles and are therefore not present for long pulses. Fig. 2.2b shows the spectrum of the example pulse to consist of odd harmonics.

The spectral contributions broaden with falling periodicity. For few cycle XUV pulses, they merge into a continuum (Fig. 2.3).

2.2.5 Constant's Model

Despite originating in a single atom effect, HHG in a medium is more complicated. phase-matching and reabsorption in the generating gas are important. Analogous to Constant et al. [54] the calculation is restricted to one dimension z and one harmonic, models A_r by $|A_r| \exp(i\phi(z))$, where $\phi(z)$ is governed by a phase mismatch Δk , and

2 Theoretical Comparison of Different HHG Gating Techniques

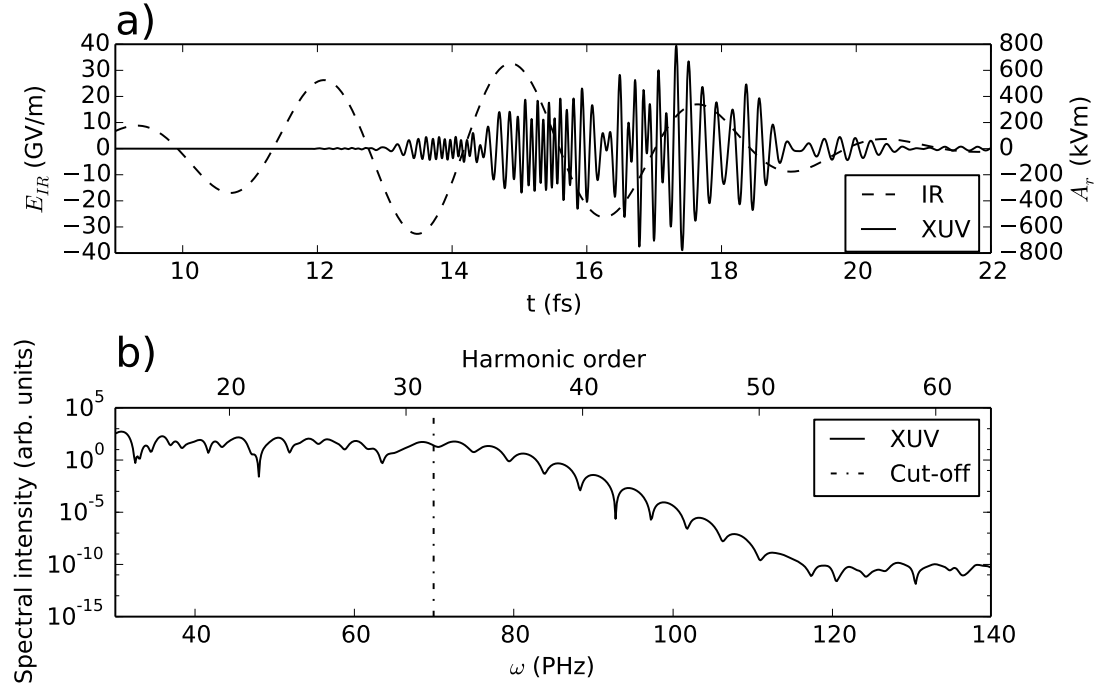


Figure 2.3: As Fig. 2.2 but for a few cycle IR pulse

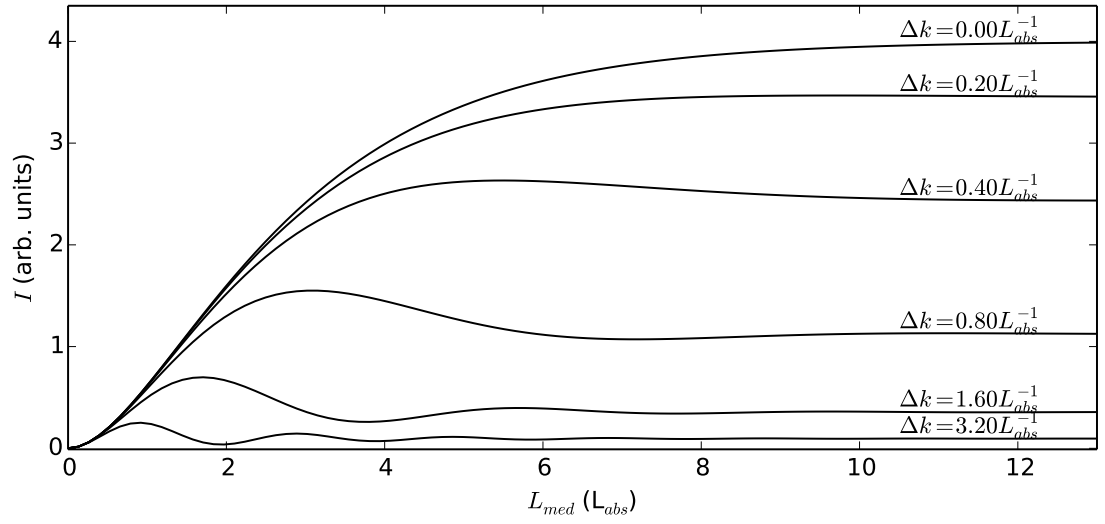


Figure 2.4: Dependence of the on-axis intensity I from medium length in units of the absorption length for different phase-mismatches according to Eq. (2.7b)

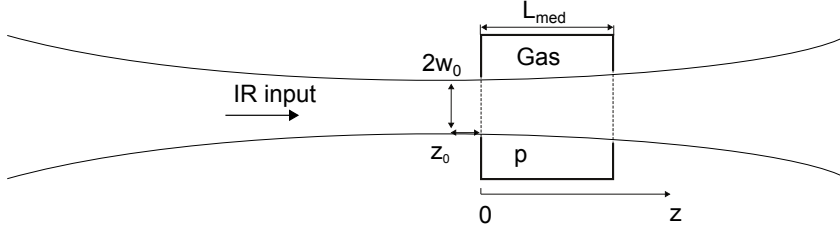


Figure 2.5: Scheme of the geometry for HHG and declaration of the variables beam waist w_0 , focus position z_0 , pressure p , medium length L_{med} and the coordinate z

calculates the intensity on axis I :

$$I \propto \left| \int_0^{L_{med}} N |A_r| \exp\left(-\frac{L_{med}-z}{2L_{abs}}\right) \exp(i\phi(z)) dz \right|^2 \quad (2.7a)$$

$$I \propto N^2 A^2 \frac{4L_{abs}^2}{1 + 4L_{abs}^2 \Delta k^2} \left[1 + \exp\left(-\frac{L_{med}}{L_{abs}}\right) + 2 \cos(L_{med} \Delta k) \exp\left(-\frac{L_{med}}{2L_{abs}}\right) \right] \quad (2.7b)$$

It is depicted in Fig.2.4. The lower the phase mismatch Δk , the higher I at any medium length becomes. For $\Delta k = 0$, I builds up quadratically with medium length until the gas absorption through the longer medium cancels the effect of more contributing atoms. For high phase mismatches back conversion reduces the yield stronger than the gas absorption. Constant et al. conclude that Δk has to be small compared to the inverse absorption length and the medium length has to be long enough compared to the absorption length in order to produce a high yield.

2.2.6 Phase-Matching

To provide high intensities HHG is usually conducted close to the focus of a laser (Fig. 2.5). This results in a strongly position-dependent intensity and influences the phase-matching. There are several effects on the phase-matching between the fundamental and its q th-harmonic:

- Dispersion in Gas
- Kerr effect in Gas: The change in the refractive index due to the intensity is relatively small. For example the n_2 for Ar at 1 bar is in the order of magnitude of $1 \times 10^{-23} \text{ W/cm}^2$ [59].
- Plasma phase: The dispersion due to free electrons is large. Even a small percentage of ionization can break the phase-matching [60]. The ionization depends on the intensity via the ionization rate.
- Dipole phase: The single atom response's phase depends on the intensity. It has been shown to be not important in the regime of this work [47].

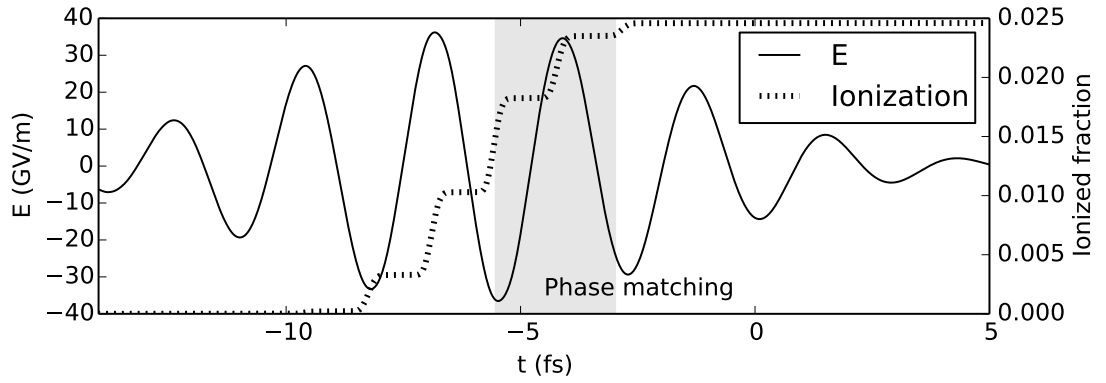


Figure 2.6: Scheme of ionization gating: A laser pulse ionizes the HHG mediums. Only a short time interval has a ionization fraction that allows phase-matching (shaded area). The data stems from an intermediate result from the optimization of ionization gating Sec. 2.4.2.

- Gouy phase: It is a geometrical phase shift within the focus and produces a phase mismatch contribution $\Delta k = q/(b + z^2/b)$ [61], which depends on position z and Rayleigh length $b = \pi w_0^2/\lambda$. It is modeled in the theory of the Gaussian pulse.

Phase-matching requires all these effects to cancel out for the relevant spectral range and volume. According to Constant's model this is crucial for efficient HHG.

2.2.7 Gating Techniques

Gating techniques aim to reduce the duration of the XUV radiation from HHG. This section gives a brief overview. Sec. 2.4 describes the calculations using the techniques and gives more insight.

Ionization Gating Jullien et al. [62] suggest to use the dispersion of the free electrons to gate. The process parameters are chosen such that a certain amount of electrons is required for phase-matching. It is only present during the center of the pulse. Fig. 2.6 illustrates this. The ionization jumps can be controlled by the intensity such that the phase-matching is present long enough for only one half cycle of the driving field.

Polarization Gating According to Corkum's model HHG requires the electron to hit its parent ion. For linear polarized light there are times where the classical electron trajectories approach the ion (refer to Fig. 2.1). The idea of polarization gating is to remove contributions of IR half cycles by adding a second polarization that displaces the electron trajectory in one dimension at these moments. Hence the light should be circular polarized to prevent HHG and linear to allow it [63].

The pulse is prepared by a set of optics: A linear polarized pulse is split into two when propagating through a birefringent material when the polarization of the pulse

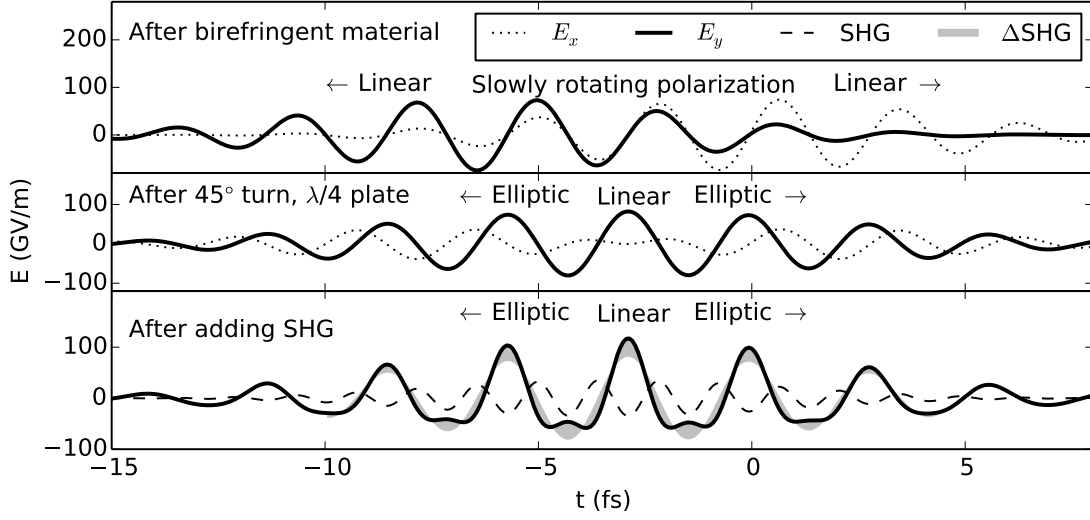


Figure 2.7: Illustration of polarization gating and DOG: Both components of the field are shown at different stages of the DOG optics. The figure reuses the code that will be described in Sec. 2.3.3.

and the optical axis of the material are offset by 45° . The center of gravity of both pulses is displaced because of the different group velocities belonging to the ordinary and extraordinary index of refraction of the material. Fig. 2.7 displays the pulse after this step. In this case the polarization in the front of the pulse points in x direction and the end in y direction. The central part varies between x and y and hence covers any possible angle.

Fig. 2.7 also shows the field after a $\lambda/4$ plate. The polarization in the center of the pulse has to coincide with the direction of the optical axis of the phase plate at one time and is linear at that time after the $\lambda/4$ plate. The outer parts were linearly polarized at an angle of 45° to the $\lambda/4$ plate before it and hence become circular. This leads to a small time window where the pulse performs HHG.

Double Optical Gating (DOG) DOG is an extension to polarization gating. The polarization gating mechanism is used to prevent all but the three highest peaks from producing XUV, which is easier than preventing all but one in the classical polarization gating. Adding a second harmonic to a pulse can increase the maximum field strength of one half cycle while reducing the field strength for its neighboring half cycles (Fig. 2.7). As the XUV intensity resulting from HHG scales with a high power of the driving intensity, small differences are important and can increase the efficiency. Therefore, only the highest of the three remaining peaks is relevant.

When Mashiko et al. [7] suggested this approach, they synthesized the SHG field and recombined it with the main driving IR pulse. Feng et al. [64] replace the $\lambda/4$ wave plate by a combination of a BBO and a quartz plate with the same overall phase shift. This

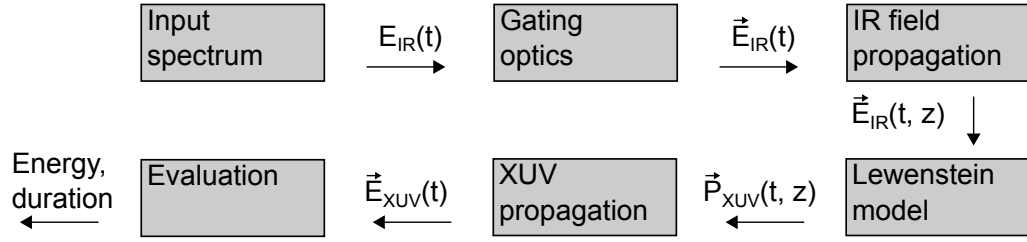


Figure 2.8: Scheme of the calculation approach: See text for an overview and Sec. 2.3 for details.

approach eliminates the need to recombine pulses.

2.3 Simulation Techniques

A method for the evaluation of the three gating techniques is required. This section first describes the requirements and then the general approach and the detailed method.

Requirements The expectation of pulses from the NOPCPA with 15 mJ in 7 fs with a central wavelength of 850 nm sets the input parameters. The resulting XUV pulses should be as energetic as possible to increase the experimental signal strength and short to allow attosecond experiments. Both qualities need to be quantified and compared. The latter favors a common method for all gating techniques. In order to set the parameters of the gating techniques meaningfully, an optimization is necessary. Especially for a high number of parameters, this is only feasible if the computation time is not too long.

The XUV originates from the volume of space that is illuminated by an IR pulse. In the simplest case, no gating, the input pulse is to be calculated from the NOPCPA parameters. Propagation effects and focusing in the medium need to be considered for high intensities to calculate the IR field at any point in space. There, the atomic response needs to be estimated. As the XUV is very weak, it does not influence the IR propagation, which can therefore be treated independently from the HHG. The final XUV pulse can then be calculated from the atomic response and propagation in the entire medium.

Ionization gating requires a model for ionization effects and high intensities. E.g. Ferrari et al. [6] used an IR intensity of $2.3 \times 10^{15} \text{ W/cm}^2$. Polarization gating requires including both transversal dimensions of the electric field. The effect of the corresponding optical elements on the initial pulse needs to be calculated. DOG adds an SHG process to this evaluation.

Approach The approach is the same for all gating techniques and summarized in Fig. 2.8. First, a Gaussian spectrum is calculated. Then different optics affect the pulse. A program of Usman Sapaev [65, 66] is then used to calculate the IR field on

the axis of propagation. The Lewenstein model returns the polarization for all points in space. The XUV propagator converts these into the final XUV pulse, which is then evaluated in terms of energy and duration. The restriction to one spatial dimension greatly reduces the computation time.

2.3.1 IR Pulse Model

The simulation relies on a representation of the IR pulse, which is outlined in this section. The pulse propagates along the z -axis. It is represented by values for the two transversal polarizations at time t on the axis of propagation $\vec{r} = (0, 0, z)$.

$$\vec{E}(t, x, y, z) \rightarrow \vec{e}_x E_x(t, z) + \vec{e}_y E_y(t, z) \quad (2.8)$$

The first part of the simulation calculates the pulse that results from the gating optics. Here, the beam is collimated and hence approximated by a plane wave. Focusing is essential for HHG. To represent the x - and y -dependence of the electric field, the spatial dependence of the pulse is modeled by a monochromatic Gaussian pulse.

The Gaussian beam [67] is a solution of the wave equation Eq. (1.1) in paraxial approximation around the direction z and given by

$$\epsilon(x, y, z) = E_0 \frac{w_0}{w(z)} \exp \left[i \arctan \left(\frac{z}{b} \right) - i\theta + \frac{-ikr^2}{2R(z)} - \frac{r^2}{w(z)^2} + i\omega t - ikz \right] \quad (2.9a)$$

$$b = \frac{\pi w_0^2}{\lambda} \quad (2.9b)$$

$$w(z) = w_0 \sqrt{1 + \left(\frac{z}{b} \right)^2} \quad (2.9c)$$

$$R(z) = z \left(1 + \left(\frac{b}{z} \right)^2 \right) \quad (2.9d)$$

in complex notation (see Eq (1.6a)). E_0 is the amplitude of the electric field, θ is a free phase parameter, w_0 is called beam waist and b was coined Rayleigh length. $r = \sqrt{x^2 + y^2}$ is the transverse coordinate. The term $\arctan(z/b)$ is called Gouy phase. If a collimated Gaussian beam with a beam waist w_1 is focused over a distance f , the Gaussian beam describing the focus has a beam waist w_0 with

$$w_0 = \frac{\lambda f}{\pi w_1}. \quad (2.10)$$

The power P of a Gaussian beam is

$$P(z) = \int \int \frac{\epsilon_0 c}{2} |\epsilon(x, y, z)|^2 dx dy \quad (2.11a)$$

$$= \frac{\epsilon_0 c \pi}{4} w_0^2 E_0^2. \quad (2.11b)$$

The elements of the simulation use moving coordinate systems to reduce the necessary number of points in time. The remainder of the section discusses the elements of the simulation in the order of the computation, which is given in Fig. 2.8.

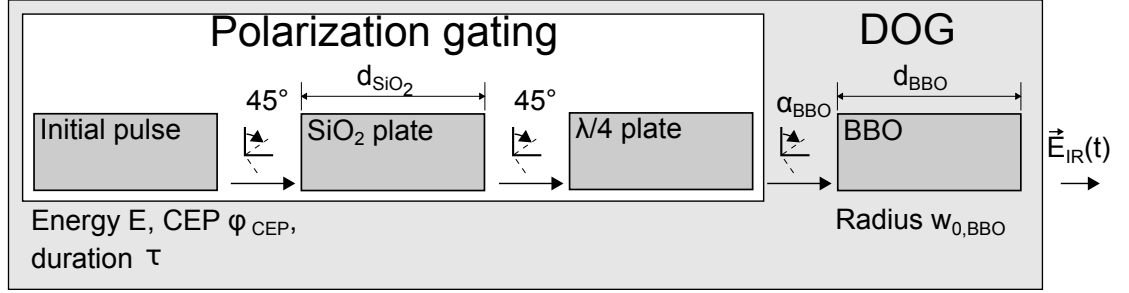


Figure 2.9: Scheme of the gating optics calculation: Several steps require the given parameters and rotations of the coordinate system.

2.3.2 NOPCPA Spectrum

The spectrum is assumed to be Gaussian in frequency. Its FWHM is calculated from the duration of $\tau_{\text{FWHM}} = 7$ fs via Eq. (1.10) and the assumption of being Fourier-limited. The center of the spectrum is 850 nm and the phase is a constant φ_{CEP} . E_0 from the last equation then is time dependent:

$$E_0(t) = E_{00} \exp\left(\frac{-t^2}{4\tau^2}\right) \quad (2.12)$$

$$\tau = \frac{\tau_{\text{FWHM}}}{\sqrt{8 \log 2}} \quad (2.13)$$

The input energy of $E = 15$ mJ relates to the field strength via the integral over the power P of the pulse:

$$E = \int P dt \quad (2.14a)$$

$$= \frac{\epsilon_0 c \pi}{4} w_0^2 E_{00}^2 \sqrt{2\pi} \tau \quad (2.14b)$$

The model uses this relation to initially normalize the pulse. $E_0(t)$ is plotted in the chapter. This is straightforward within the HHG cell where a well-defined beam size $w(z)$ is available. The beam waist of the focus before the HHG cell w_0 is used in the same role within the gating optics before. The advantage of this simple approach is that it produces values close to the situation in the HHG medium.

2.3.3 Gating Optics

No gating and ionization gating require no additional optics. The steps for the other two methods are depicted in Fig. 2.9.

Polarization gating requires a first phase plate to create temporally offset pulses. The thesis follows Feng et al. [64] and uses a Quarz plate of length d_{SiO_2} . The corresponding spectral phase is calculated and applied to the pulse. The refractive index is modeled

by the corresponding Sellmeier coefficients:

$$n_o^2 - 1 = 0.28604141 + \frac{1.07044083\lambda_{\mu\text{m}}^2}{\lambda_{\mu\text{m}}^2 - 1.00585997 \times 10^{-2}} + \frac{1.10202242\lambda_{\mu\text{m}}^2}{\lambda_{\mu\text{m}}^2 - 100} \quad (2.15a)$$

$$n_a^2 - 1 = 0.28851804 + \frac{1.09509924\lambda_{\mu\text{m}}^2}{\lambda_{\mu\text{m}}^2 - 1.02101864 \times 10^{-2}} + \frac{1.15662475\lambda_{\mu\text{m}}^2}{\lambda_{\mu\text{m}}^2 - 100} \quad (2.15b)$$

where $\lambda_{\mu\text{m}}$ is the wavelength in μm [68]. After a rotation of the coordinate system by 45° , an ideal $\lambda/4$ plate is applied. It follows a rotation of the coordinate system by the angle α_{BBO} .

DOG requires an additional SHG of the pulse. It is calculated according to Eq. (1.13). The formula neglects higher order dispersion and assumes phase-matching. In accordance to Feng et al. [64] the crystal with length d_{BBO} consists of BBO. The material parameters are $\chi^2 = 4 \times 10^{-12} \text{ m/V}$ [19] and $v_1^{-1} - v_2^{-1} = 1.644 \times 10^{-10} \text{ s/m}$ [30] for the group velocity mismatch. The process is calculated for the electric field at the center of the pulse, $E_0 \frac{w_0}{w(z)}$. As this is a nonlinear process, the field strength must be controlled. It is parametrized via the beam waist $w_{0,BBO}$. The fundamental of the SHG will be plotted as E_x . The resulting new electric field will be added to E_y . The analytic formula neglects the depletion of the fundamental and is therefore only valid for small total conversion efficiencies and can change the total pulse energy. As later optimizations are intended to use a fixed pulse energy, this gain is compensated.

2.3.4 IR Field Propagation

Model An existing code was modified within the thesis. The author, Usman Sapaev, used it for publications [65, 66].

The code calculates the propagation of an IR field in an Ar medium in one dimension. It effectively calculates the field $E(t, z)|_{x=y=0}$ on the axis of the Gaussian beam (Eq. (2.9)). The method is based on a split-step Fourier algorithm: For each step in the propagation direction effects are calculated in the time domain and in the frequency domain. These are:

Frequency domain:

- Gas dispersion
- Gas absorption
- Gouy phase shift
- Intensity change due to focusing

Time domain:

- Kerr effect
- Ionization loss: The field ionizes atoms (calculated via the ADK rate [56]). The required energy is subtracted from the field.

2 Theoretical Comparison of Different HHG Gating Techniques

- Brunel harmonics and electron plasma dispersion: Tunneling current is localized around the field maxima. The quick oscillations produces low order harmonics [69].

Beam Reshaping Estimation Gouy phase shift and focusing assume a monochromatic Gaussian pulse (Eq. (2.9)). The Kerr effect and the dispersion of the electrons can change the divergence of the beam [21], as they affect the refractive index and are position dependent via the intensity.

The next paragraph will assess the difference: Within the derivation of the Gaussian beam [67, 70], the complex beam parameter

$$q(z) = \left(R(z)^{-1} + -\frac{i\lambda}{\pi w^2(z)} \right)^{-1} \quad (2.16)$$

follows from the differential equation

$$\frac{dq(z)}{dz} = 1. \quad (2.17)$$

The numerical calculation splits the medium into small steps. Each slice will be treated as a lens and follow Eq. (2.17). The effect of a thin lens on a Gaussian beam is described by

$$w_2 = w_1 \quad (2.18a)$$

$$\frac{1}{R_2} = \frac{1}{R_1} - \frac{1}{f} \quad (2.18b)$$

[67] where R_2 is the radius of curvature after the lens and R_1 before and $w_{1,2}$ the beam waists, respectively. After each slice this equation is used to update $q(z)$. The focal length for the Kerr lensing is

$$f_{Kerr} = \frac{w_0^2}{4n_2 dz I_0} \quad (2.19)$$

[21]. The nonlinear index of refraction n_2 is proportional to pressure. At 1 bar Ar it is $1.08 \times 10^{-19} \text{ cm}^2 / \text{W}$ [71]. dz is the length of the step. Eq. (2.19) assumes a constant intensity in time. For simplicity, it is replaced by an effective intensity of the pulse here:

$$I_{eff} = \frac{\int I^2 dt}{\int I dt} \quad (2.20)$$

It is the intensity average over the pulse.

The electron lens is calculated by fitting the electron dispersion's phase change over space with the spatial phase dependence of a thin lens. The phase is modeled via a Gaussian beam, the ADK rate and the dielectric function of the plasma. An effective ionization is defined in analogy to Eq. (2.20).

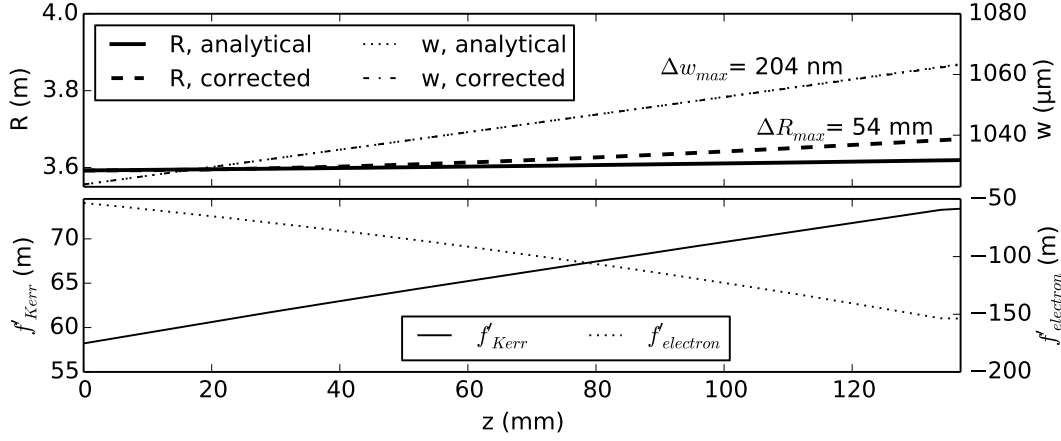


Figure 2.10: Corrections to the Gaussian beam defined by the radius of curvature R and the beam waist w for any point on the propagation axis z by Kerr (f_{Kerr}) and electron lensing ($f_{electron}$): See text for calculation details. The focal lengths vary within the medium. To clarify its importance, the focal length is expressed by the focal length that the entire medium under the local conditions would produce: $f' := fL_{med}/dz$.

It is not necessary to go into detail for those two calculations. As an example for high intensity the focal lengths are shown in Fig. 2.10 anticipating the optimal parameters for ionization gating. The Kerr lens results in focal lengths which are much longer than the medium and hence not important. The electron lens is much weaker. The graph validates this by comparing the analytical solutions (Eq. (2.9)) without corrections with the corrected version. The radius of curvature is reduced by the focusing. The maximum deviation is small, 1 % of the typical values. The difference is even smaller for the beam radius w , 2×10^{-4} of the typical value. As the correction does not matter, it is omitted for the rest of the chapter.

Model Extensions The code was extended for this thesis. The input pulse is arbitrary instead of Gaussian, a second, orthogonal polarization was added and the field within the medium can be saved at a set of points on the propagation axis. Before, output was limited to the end of the medium.

2.3.5 Lewenstein Model

Eq. (2.4) calculates the HHG polarization \vec{P}_{NL} from the IR field at different points on the propagation axis. The conversions from Tab. 2.2 are used.

2.3.6 XUV Propagation

The origin of the XUV field is the HHG polarization. The XUV field can be calculated by the modified Maxwell equation, Eq. (2.5). The changing beam waist of the generating IR must be accounted for. L'Huillier et al. [72] discuss that a power law cannot describe the intensity dependence of HHG. However, they suggest $P_{NL} \propto E^5$ as a simple model for the plateau harmonics.

The effect of driving intensity on the XUV spectrum and phase is neglected. This assumption is supported by the quick decay in conversion efficiency with intensity, which reduces the influence of regions with lower intensities. This approach allows integrating the polarization of areas $z = \text{const.}$:

$$\int P_{NL} \pi r dr = \int P_0 \left(\exp -r^2/w(z)^2 \right)^5 \pi r dr \quad (2.21a)$$

$$= \frac{P_0 \pi}{2} \left(\frac{w(z)}{\sqrt{5}} \right)^2 \quad (2.21b)$$

This statement is compared to the calculation of the power of a Gaussian beam, Eq. (2.11): The only effect of the power 5 is a factor, which can be included as an effective radius $w(z)/\sqrt{5}$ for HHG. To avoid working with such area integrated quantities and compute meaningful XUV fields the XUV field is held to be Gaussian with the constant beam radius w_0 . For the correct energy in terms of Eq. (2.11) a modification of Eq. (2.5) by the factor $\frac{w(z)}{\sqrt{5}w_0}$ to the nonlinear polarization P_{NL} is then necessary:

$$\frac{\partial \vec{E}(z, \omega)}{\partial \xi} = -\frac{1}{2L_{abs}} \vec{E}(z, \omega) - \frac{i\omega}{2c\epsilon_0} \vec{P}_{NL}(z, \omega) \frac{w(z)}{\sqrt{5}w_0} \quad (2.22)$$

The gas absorption length L_{abs} is computed from Henke et al. [73].

The spectral transmission of a thin metal filter [73] is multiplied to the XUV field at the end of the medium as those are typically used to remove the IR from the XUV beam in experiments. Further, the factor

$$F_L = 1 - \exp \left(- \left(\frac{12\lambda}{850 \text{ nm}} \right)^{16} \right) \quad (2.23)$$

removes contributions to the XUV field at frequencies too low to conform to the assumption of the Lewenstein model that electrons are free particles. F_L is chosen because of its step transition at the frequencies belonging to the first calculated harmonic.

Calculation of Energy and Duration As discussed for Eq. (2.22) the calculation of the energy is done via Eq. (2.11).

The evaluation of the pulse duration is less straightforward. The chosen definition should be relevant for pump-probe experiments, which show a signal that is the autocorrelation of the input pulse's intensity in the simplest case. The left part of Fig. 2.11a shows a typical pulse and its autocorrelation $I \otimes I$.

Classical time measures fail to represent the duration of the autocorrelation:

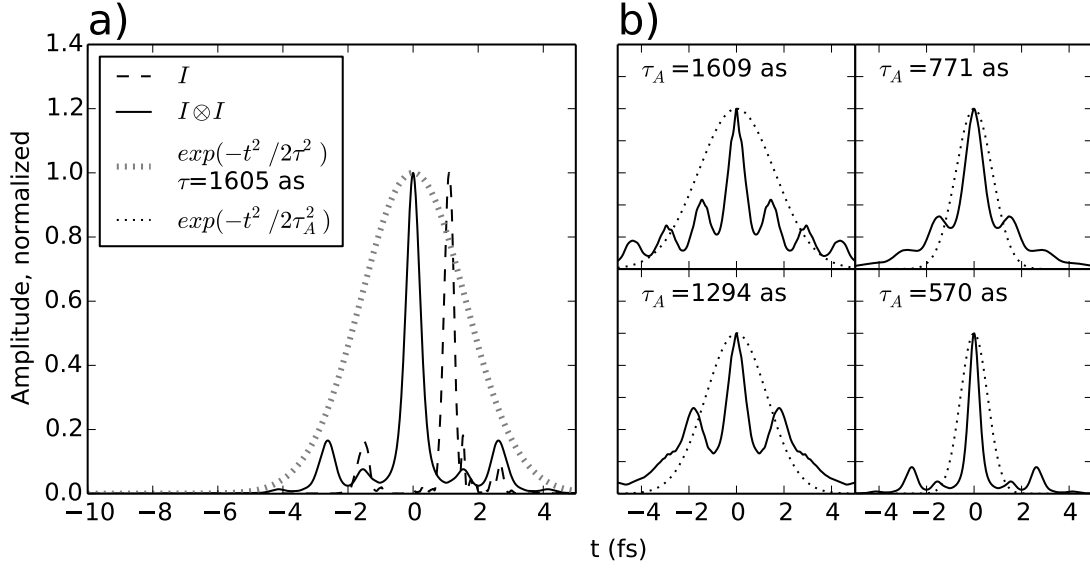


Figure 2.11: Illustration to the justification of τ_A : a) The duration is a function of the autocorrelation $I \otimes I$ of the intensity I to represent the resolution in pump-probe experiments. The standard deviation duration (dotted line) are inadequate for XUV intensity functions typical for the HHG simulation as a Gaussian pulse with the same standard deviation duration is too long. b) consequently a new measure τ_A is defined. The images show autocorrelations of typical XUV intensities encountered during the optimization process and autocorrelations of Gaussian pulses with equal τ_A . The cases are chosen to cover a range of different values for τ_A .

- Full width half maximum (FWHM) neglects pedestals.
- Standard deviation gives inadequate results. As an example the standard deviation duration τ is calculated and a Gaussian pulse with the same τ is drawn in Fig. 2.11a). A reasonable representation should be similar to the main peak and account for the side peaks with additional width. In contrast, the curve is wider than the side peaks. The reason is that the tail of the pulse is not falling fast enough.

Fig. 2.11b shows typical XUV intensities encountered during the optimization process and Gaussian curves with equal τ_A defined by

$$\tau_A := \frac{1}{\sqrt{2}} \frac{\int (I \otimes I)^2(t) t^2 dt}{\int (I \otimes I)^2(t) dt} \quad (2.24)$$

Its only justification is that the Gauss functions are, as judged by eye, adequate representations of the autocorrelations. This is less the case for the example with $\tau_A = 1665$ as,

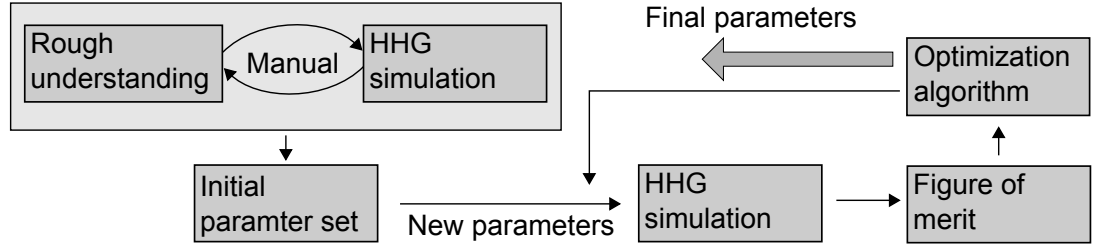


Figure 2.12: Scheme of the optimization approach as described in the text

which can be neglected as the chapter seeks short pulses and the pulse is not short. Instead, it shows considerable side peaks.

Tzallas et al. [74] pioneered pump-probe experiments close to the attosecond regime. Their autocorrelation measurement revealed a pulse length of $\tau = 1.5$ fs. In order to be truly in the as regime the chapter aims for pulses of at most half that length. This corresponds to $\tau_A = 600$ as or less.

2.4 Results

The aim of the section is to find sets of optimal parameters for each gating method and to compare their performance. First, the general optimization approach is described. Then each of the methods is discussed in a similar way. The order is chosen to work with a slowly incrementing number of parameters: No gating, ionization gating, polarization gating, DOG and hybrid DOG. Each discussion starts with the introduction and explanation of the new parameters. Then the optimization strategy is adapted and the result examined. The section concludes with a synopsis of the gating method's parameters.

The approach is depicted in Fig. 2.12. For each parameter a rough understanding is developed to guide a manual optimization of the initial parameters, which are then fine-tuned by an automatic algorithm [75], which tries to maximize a figure of merit (FOM), that is defined for each method. Starting from the initial parameters it runs the simulation, calculates the FOM from the results and varies the parameters and repeats until optimal parameters are found. Typically 1000 steps are necessary.

2.4.1 No Gating

No gating is intended as a reference without any form of gating. It is separated from ionization gating by a lower intensity.

Parameters The initial parameters and their main influences on the simulation are:

- w_0 The beam waist (Fig. 2.5) relates to the focal length of the lens before the HHG focus f and the radius w of a collimated beam as $w_0 = \frac{\lambda f}{w\pi}$ (Eq. (2.10)). Therefore, both experimental parameters are encoded in one relevant parameter.

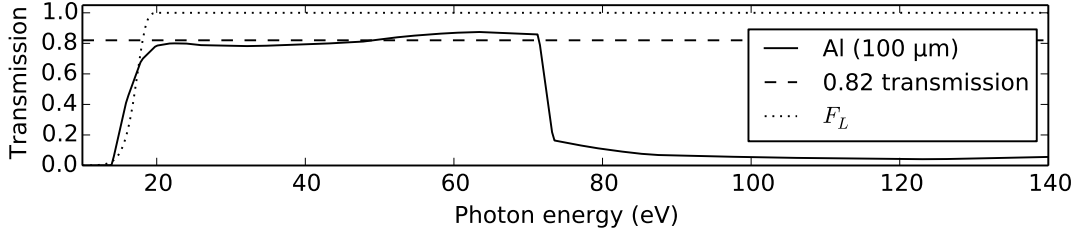


Figure 2.13: Transmissions through 100 μm Al [73] and the filter F_L (Eq. (2.23)), which removes frequencies not modeled by the Lewenstein equations.

z_0 The size of the beam translates the power of the pulse into an intensity. As the energy and duration of the pulse are fixed, w_0 sets the intensity. There are two major restrictions to that statement: First, z_0 , the distance between focus and beginning of the medium (Fig. 2.5), can reduce the intensity by displacing the medium from the focus. Second, the pulse can be deformed during propagation in the medium.

The Gouy phase is $\arctan\left(\frac{z\lambda}{\pi w_0^2}\right)$ and therefore governed by w_0 and z_0 .

L_{med} Increasing the medium length L_{med} (Fig. 2.5) adds XUV contributions from the new volume. If the medium is behind the focus the lower IR intensity reduces the XUV production. Additionally, all XUV contributions from old volumes suffer more absorption due to a longer path through the medium.

p The pressure p sets the amount of IR pulse propagation effects by interaction with the medium like gas dispersion. It governs the number density of atoms and thereby the strength of the generated XUV. The absorption of XUV increases with pressure.

φ_{CEP} The CEP φ_{CEP} of the IR pulse influences the height of the actual electric field peaks within the envelope.

The gas species is Ar as Ar and Xe were used by the most effective gating techniques (Sec. 2.1) and Ar is inexpensive making it a good starting point. However, as the efficiency of HHG in rare gases raises with higher atomic numbers [76], Xe should be investigated at a later stage too.

The metal filter is not optimized but always an Al foil with a thickness of 100 μm , as more filtering will reduce the energy and such a filter worked well in the experiments described in Chap. 4. Thinner filters would be more likely to break. Furthermore the choice of the material Al poses a small restriction: Fig. 2.13 shows the Al transmission curve together with F_L (Eq. (2.23)). The Al filter transmits about 82 % at the frequencies from about 18 eV to 70 eV. The lower border is not relevant because the Lewenstein model is not adequate there. The high harmonics at the upper border are deeper in the plateau and typically not more intense (Sec. 2.2.4).

Rough Understanding Several statements on the position of the optimum are possible. They lead, together with the information of the previous paragraphs to a rough understanding of the parameter space.

- Salières et al. [77] discussed that the focus should be before the medium to create a Gauss like XUV beam.
- As argued for Eq. (2.22), the single atom response efficiency is rising with intensity. So it should be high. Sec. 2.2.7 discuss ionization gating: If the ionization is too high, phase-matching is destroyed. Hence the intensity should be as high as possible without ionizing too much.
- Constant's model (Sec. 2.2.5) discusses that phase-matching is crucial but the medium has to be long enough. Typically a few absorption lengths are sufficient.
- Midorikawa et al. [42] state that the phase-matching is typically achieved by compensating gas dispersion and Gouy phase shift. As the single atom response is proportional to the number density, the pressure should be high. To compensate the resulting high gas dispersion, the Gouy phase shift should be constant and strong. Experimental studies [78, 76] investigate the dependence of HHG yield of z_{waist} . Optimal parameters were in the order of the Rayleigh length.
- The CEP can favor one peak of the electric field by making it higher than its neighbors.
- The pressure is used to fine-tune the phase-match. The alternatives, w_0 and z_0 , would tune the phase-matching via the Gouy phase but also affect the intensity.

FOM and Optimization The figure of merit should represent the quality of the parameter set. As gating is not intended the efficiency η_{HHG} is the only relevant quantity. It is the XUV pulse energy divided by IR pulse energy.

$$FOM_{No\ Gating} := \eta_{HHG} \quad (2.25)$$

The intensity is limited by setting w_0 to a fixed value. The aim is to prevent ionization gating but still work in the same intensity regime as ionization gating. CEP, p , z_0 and L_{med} are optimized by hand and then automatically fine-tuned.

Results Fig. 2.14 shows the driving field and the new quantity \vec{C} for the numerical optimum. \vec{C} is introduced to visualize the contributions along the propagation axis to the XUV field. It is defined as

$$\vec{C} := F(\omega) \left(-\frac{i\omega}{2c\epsilon_0} \vec{P}_{NL}(z, \omega) \frac{w(z)}{\sqrt{5}w_0} \exp\left(-\frac{L_{med} - z}{2L_{abs}}\right) \right). \quad (2.26)$$

The quantity encodes the polarization \vec{P}_{NL} from the Lewenstein model. The factor $F(\omega)$ is the product of F_L (Eq. (2.23)) and the transmission of the Al filter. \vec{C} takes all factors

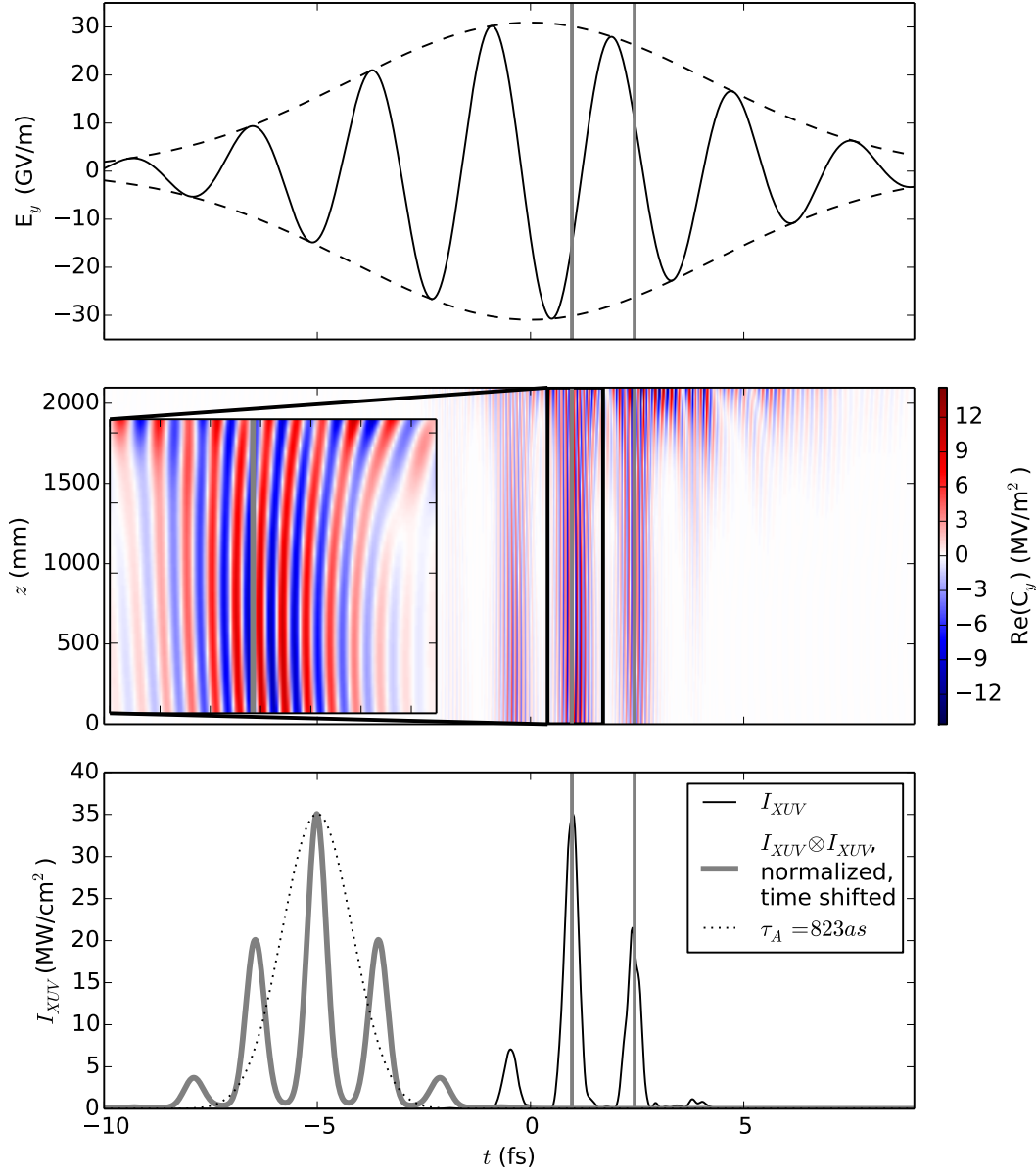


Figure 2.14: Visualization of the calculation for the optimal parameters for no gating: The initial IR pulse E_y results in the contribution C_y , which accumulates over the propagation coordinate z to the final XUV intensity. I_{XUV} 's duration is evaluated via τ_A (see Fig. 2.11). The vertical lines mark the time of the main XUV bursts.

from Eq. (2.22) into account such that the relation of local XUV generation and final pulse becomes as intended:

$$\int \vec{C} dz = \vec{E}_{XUV} \quad (2.27)$$

The image shows three similar, vertical stripes in the time representation of \vec{C} . The strongest is shown as a zoom in the inset. It consists of oscillating contributions changing quickly with time and very slowly with z . As the integration of \vec{C} over z results in the XUV field and different phases would reduce the final field strength the change of \vec{C} over z is a measure of phase-matching. As it is almost constant here phase-matching is present and leads to the three shown XUV bursts. According to Corkum's model the highest E field peaks should result in XUV bursts 3/4 of an IR cycle later. The gray lines mark the times of the strongest two stripes. They agree with Corkum's prediction. Additional structures are present at the end of the cell ($z > 1700$ mm). They are present between the stripes and later. As their accumulated influence on the XUV pulse is small, they will be neglected in the discussion. A possible explanation is that the corresponding polarization is present throughout the medium but they have a spectrum different from the main stripes. The gas attenuates it unless the remaining medium is too short.

As no gating is intended, the pulse's τ_A is longer than the target and the temporal structure of the final XUV intensity contains four XUV bursts. As mentioned for C_y the XUV bursts are present at the expected times and the two largest peaks originate from the two highest peaks of the driving IR field, while the neighboring XUV bursts are much smaller and originate from weaker IR half cycles.

The efficiency of the HHG process is nonlinear in intensity, which is intentionally set to a low value for this reference optimum. Therefore, the efficiency is low, 2.69×10^{-8} , compared to later optimization aiming for efficiency.

Later, a number to quantify phase-matching will be necessary. $\vec{E}_{XUV,pm}$ is used to represents the XUV pulse for ideal phase-matching:

$$\vec{E}_{XUV,pm} := \int |\vec{C}(t)| dz \quad (2.28)$$

The quantity Φ is the actual XUV pulse energy divided by the energy of $\vec{E}_{XUV,pm}$. 0 indicates completely destructive interference and 1 perfect phase-matching. The result is $\Phi = 0.62$ for the given parameters. This relative low value indicates that the optimal solution contains contributions that are close to being out of phase. Such C_y are visible for $z < 200$ mm in the inset in Fig. 2.14. As the solution is optimal the contributions are still slightly beneficial. Otherwise the front of the medium would be removed by increasing z_0 and reducing L_{med} . Another reason is the structure that appears at the end of the medium.

2.4.2 Ionization Gating

The parameters from no gating are sufficient for this method.

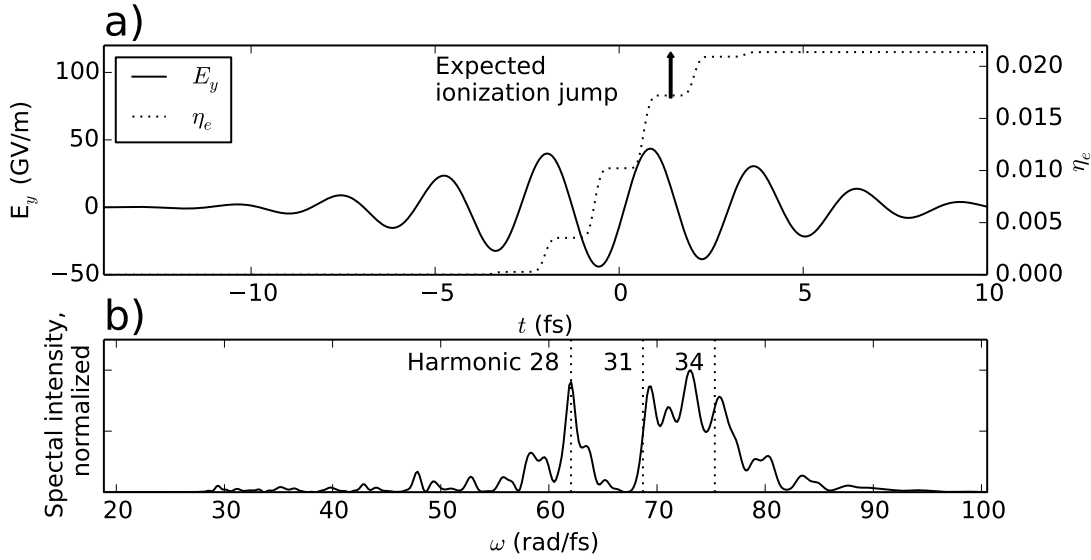


Figure 2.15: Illustration for the required ionization: a) Ionized fraction η_e , and electric field. The expected height for the ionization jump that switches phase-matching is calculated from Eq. (2.29). The base of the arrow is placed arbitrarily. b) Spectrum of the XUV radiation. Harmonic 31 is roughly in the middle. The optimal parameters for ionization gating are used.

Rough Understanding Ionization gating uses the dispersion of the electrons to limit the phase-matching to one cycle. The required extra amount of ionization fraction $\Delta\eta_e$ can be roughly estimated. The problem shall be restricted to one harmonic h : The additional phase mismatch

$$\Delta k = \frac{\pi}{hL_{med}} \quad (2.29a)$$

is required to switch between perfect phase-matching and destructive interference. It translates to refractive index changes Δn as

$$\frac{\Delta n}{c} = \frac{\Delta k}{\omega_{IR}} \quad (2.29b)$$

The electrons cause a change in the refractive index at the IR frequency ω_{IR} according to

$$\Delta n = \Delta\eta_e \left(\frac{\omega_p}{\omega_{IR}} \right)^2 \quad (2.29c)$$

$$\omega_p = \sqrt{\frac{Ne^2}{\epsilon_0 m_e}} \quad (2.29d)$$

[79]. As the XUV has a much higher frequency it is not significantly affected by the plasma. Fig. 2.15 shows an IR pulse, the respective ionization and the expectation

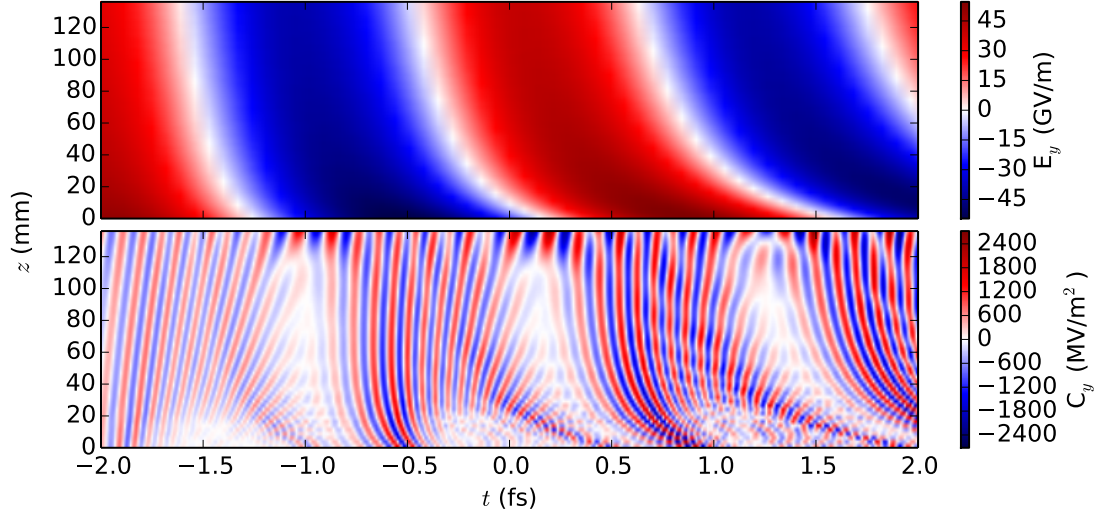


Figure 2.16: Illustration for field (E_y) deformations via high intensities and resulting contributions C_y : The optimal parameters for ionization gating (Tab. 2.3) are used and the normally fixed energy doubled to increase the intensity without additional changes to the phase-matching.

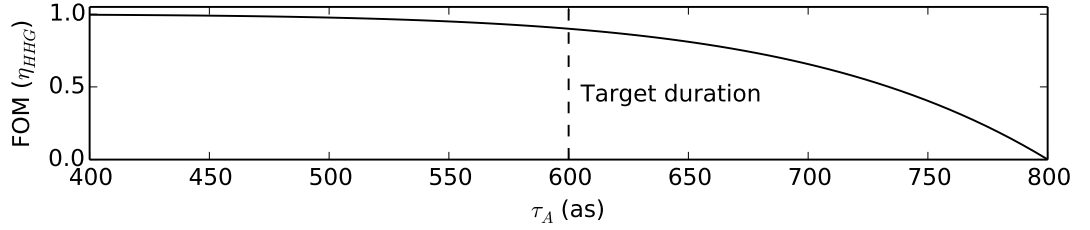


Figure 2.17: Illustration of the FOM, Eq. (2.30)

according to Eq. (2.29), 0.4 %. At each field maximum the ionization is rising. The expectation has a comparable height.

Fig. 2.16 illustrates the effect of very high intensities. At the beginning of the medium the pulse is very strong so that Kerr effect and electron plasma dispersion are important and deform the pulse. These changes translate into a complex pattern in the contribution C_y . They appear to be too unsystematic to be phase-matched, which prevents efficient generation of HHG and the gating mechanism.

This leads to the understanding that the intensity should at least lead to the ionization as expected according to Eq. (2.29) but not much higher as the arising beam distortions are detrimental.

FOM and Optimization The aim of the optimization are intense pulses with a duration of at most $\tau_A = 600$ as. The FOM is therefore chosen to be slightly higher for shorter pulses and to fall quickly for pulses longer than $\tau_{target} = 600$ as:

$$FOM_{Ionization} := \eta_{HHG} \cdot \left(1 - 0.1 \left(\frac{\tau_A}{\tau_{target}} \right)^8 \right) \quad (2.30)$$

The duration dependence of the FOM is depicted in Fig. 2.17.

The rough understanding from no gating and the previous paragraph is used to find parameters that lead to ionization gating. They are then automatically fine-tuned.

Result The gating is reproduced and the pulse duration $\tau_A = 457$ as is under the threshold of 600 as. In contrast to the expectation, the optimization leads to an input parameter of the initial pulse ϕ_{CEP} resulting in two IR peaks of comparable strength in the HHG medium (Fig. 2.18). The main XUV burst is marked by a gray line and is 3/4 of an IR cycle after the second maximum. This indicates phase-matching after the maximum of the IR.

C_y shows the same characteristics as the no gating case (Fig. 2.14) with the exception that the picture is dominated by five stripes, which have an absolute maximum outside the structure at the end of the cell of 150, 450, 600, 550 and 350 MV/m², respectively. The last stripe grows over z more than the others and is therefore overestimated by its maximum. A zoom shows the inner stripes. The first two stripes show significant z dependences of the phase of the contributions. This and the low maximum intensities in I_{XUV} of 1.4, 17, 47, 494 and 78 MW/cm² for the respective burst indicate missing phase-matching. The phase-matching at the marked stripe is confirmed by the resulting peak in I_{XUV} : Despite a comparable magnitude of C_y , the last stripe of C_y results in the by far largest XUV intensity. This can be expressed as the stated peak heights of the intensity divided by the number for the mentioned contributions: 0.009, 0.04, 0.08, 0.9 and 0.2, where the main XUV peak belongs to the highest ratio. $\Phi = 0.25$ also indicates large amounts of non phase-matched contributions. Fig. 2.15 already confirmed that the jumps in the ionization are comparable to the expectation for these parameters.

In contrast to the no gating scenario the beam waist w_0 became a free parameter for this optimization, which reduced w_0 from 1000 to 696 μm in order to increase the maximum IR intensity in the HHG cell from 0.13 to 2.03 W/cm². Consequently, the efficiency is higher by a factor of 6, 1.75×10^{-7} . The phase-matching in ionization gating is of a different nature. Within the no gating solution the phase-matching is provided by a balance of Gouy phase shift and gas dispersion. The electron dispersion is additionally crucial for ionization gating. As the generation of electrons depends on intensity, and phase-matching is necessary in the entire cell, the optimization reduces variations of the IR intensity by a short (137 instead of 2097 mm) cell further away from the focus (1931 instead of 952 mm). The shorter cell allows higher pressures at the same absorption (139.1 instead of 10.4 Pa).

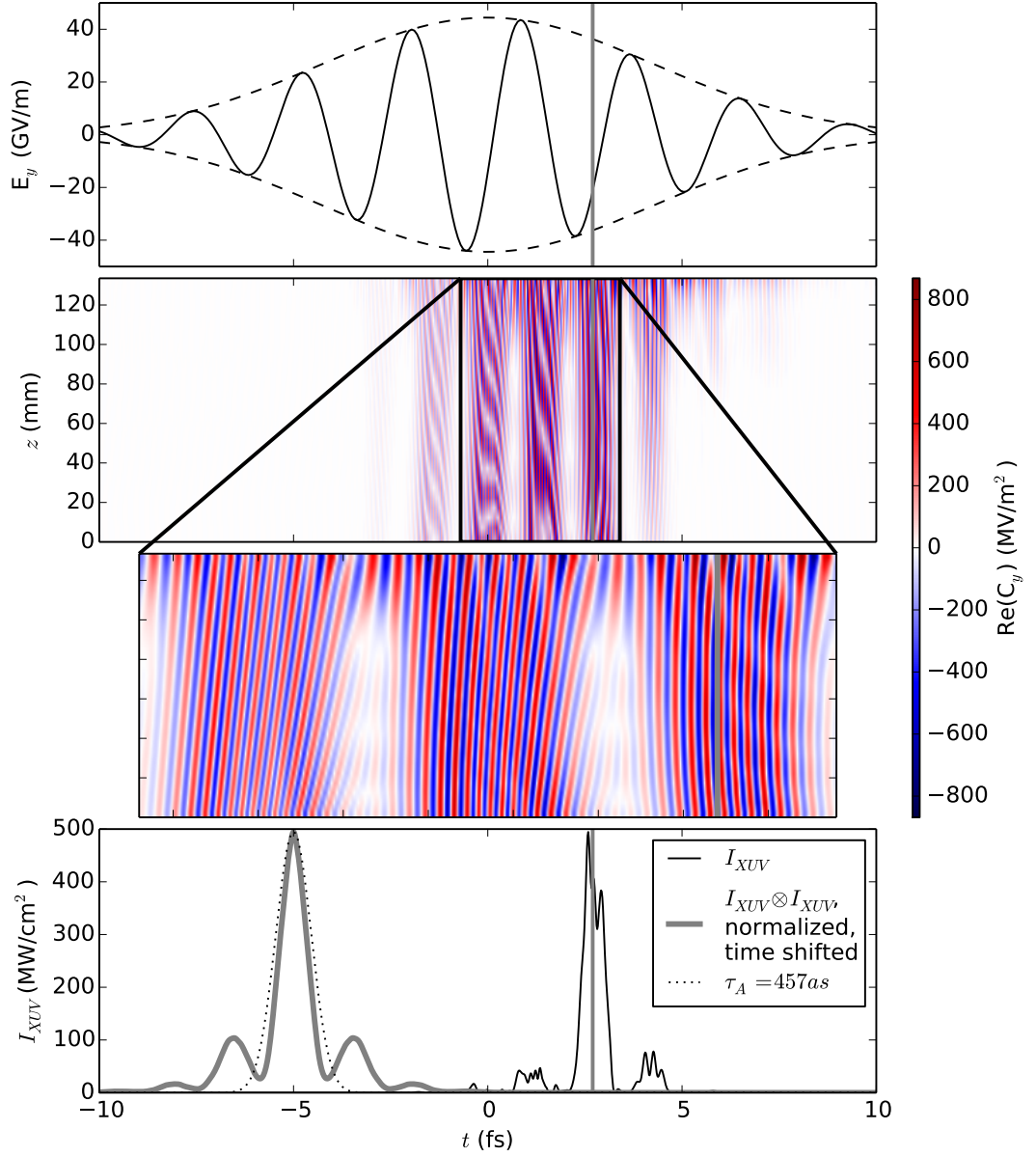


Figure 2.18: Visualization of the calculation for the optimal parameters for ionization gating: The initial IR pulse E_y results in the contribution C_y , which accumulates over the propagation coordinate z to the final XUV intensity. I_{XUV} 's duration is evaluated via τ_A (see Fig. 2.11). The vertical line marks the time of the main XUV burst.

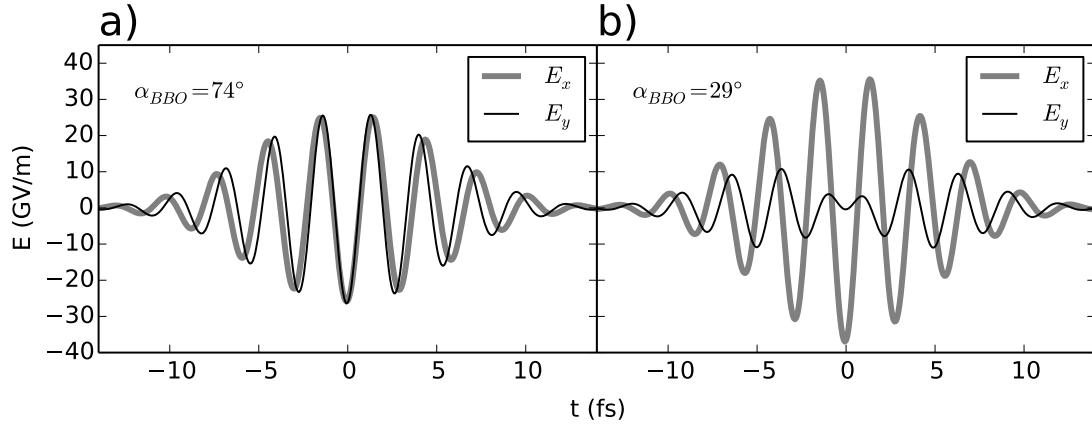


Figure 2.19: The same IR field for polarization gating in two coordinate systems: They are rotated according to α_{BBO} (refer to Fig. 2.9 for definition).

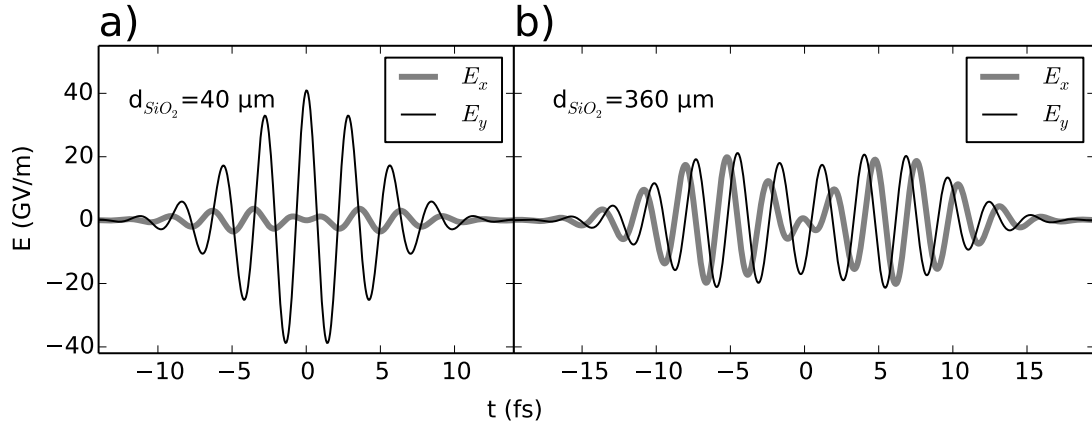
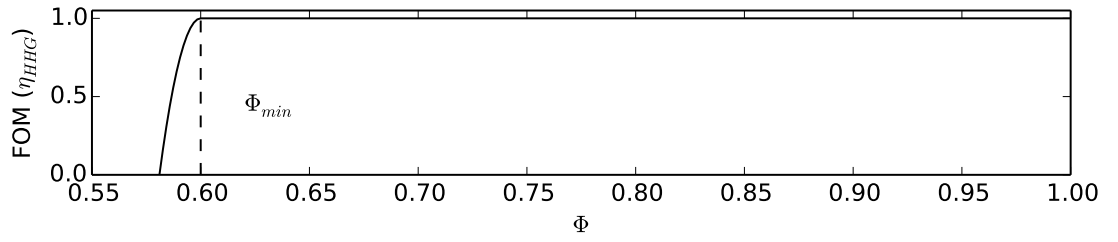


Figure 2.20: The IR field for polarization gating resulting from a thin and a thick SiO_2 plate: The constant α_{BBO} is chosen to show gating and driving fields.

2.4.3 Polarization Gating

Rough Understanding Polarization gating bases upon the use of E_x and E_y of the IR field. To illustrate options for plotting them Fig. 2.19 shows one pulse in two differently rotated coordinate systems. As required by polarization gating the pulses are elliptically polarized except for the linear middle. However, the Fig. 2.19a shows this using both polarizations. They have to be in phase. Fig. 2.19b shows linearity by a vanishing E_y . The latter description is used by Feng et al. [64]. They give the polarizations names according to their function: E_x is driving field and E_y gating field.

This way of presenting the pulses is also chosen in Fig. 2.20. It shows the result of small (Fig. 2.20a) and large values (Fig. 2.20b) of d_{SiO_2} , the thickness of the SiO_2 plate.


 Figure 2.21: Illustration of the FOM, Eq. (2.31) for $\tau_A \rightarrow 0$ and $\Phi_{min} = 0.62$

The first produces a weak gating field and a strong driving field. The second produces almost separate pulses with a lower intensity. The optimum is in between: A parameter set that has a gating field strong enough to reduce the pulse duration but does not waste intensity.

FOM and Optimization In principle the previous figure of merit (Eq. (2.30)) can be used for optimization. However, this will raise the efficiency by increasing the intensity. As demonstrated in the previous section more intensity can lead to shorter pulses. The optimization will either gravitate towards ionization gating without the polarization gating mechanism or into a hybrid of ionization gating and polarization gating.

As this is not the purpose of this section the ionization gating mechanism has to be specifically penalized. Φ measures the average phase-matching, which is beneficial at any position of time for no gating, polarization gating and DOG. The optimal no gating solution achieves $\Phi = 0.62$. For ionization gating the number is lower (optimum: $\Phi = 0.25$) because all but one XUV bursts are suppressed by low phase-matching.

This difference is used to refine the FOM

$$FOM_{Ionization} := \eta_{HHG} \cdot \left(1 - 0.1 \left(\frac{\tau_A}{\tau_{target}} \right)^8 - 1000 \left(\frac{\Phi_{min}}{\Phi} - 1 \right)^2 \chi_{[0, \Phi_{min}]}(\Phi) \right) \quad (2.31)$$

with a term that reduces the FOM severely if Φ is less than Φ_{min} (Fig. 2.21). $\chi_{[0, \Phi_{min}]}(\Phi)$ denotes the characteristic function being one if Φ is in the interval $[0, \Phi_{min}]$ and zero otherwise. Φ_{min} is the lowest accepted Φ . The optimal no gating solution has shown that optimizing for intensity leads to Φ less than 1. Its value is chosen as minimum: $\Phi_{min} = 0.62$. This choice limits the ionization gating mechanism.

A solution with adequate Φ and a SiO_2 thickness that is sufficient to deliver shorter pulses than 600 as is found manually. The result is then automatically optimized.

Result Fig. 2.22 shows the result in a coordinate system chosen such that the gating field is E_y . Its maximum is lower than the driving field's E_x by a factor of three. The main burst (gray line) is 3/4 of an IR cycle after the center of the pulse. As expected

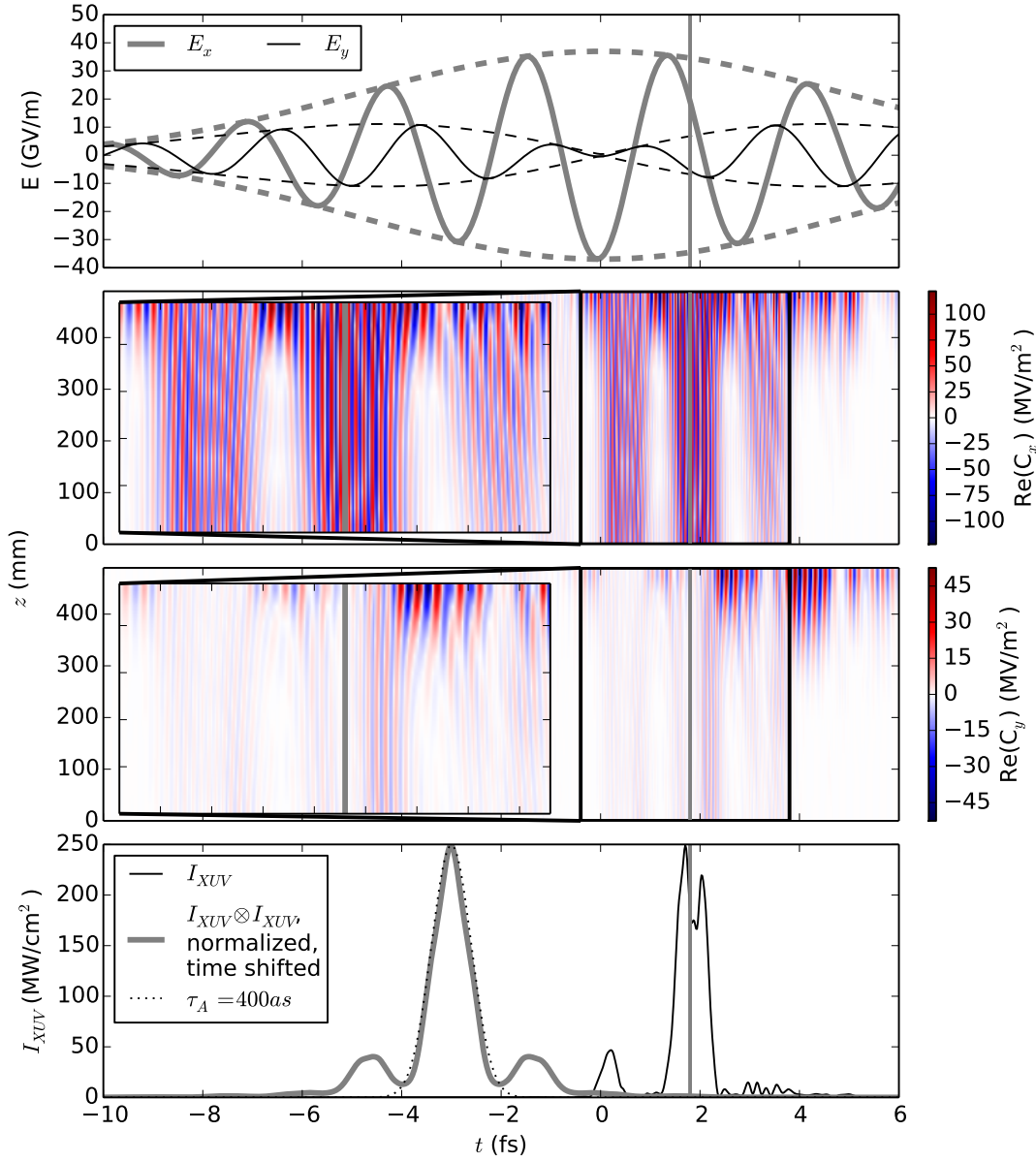


Figure 2.22: Visualization of the calculation for the optimal parameters for polarization gating: The initial IR pulse \vec{E} results in the contributions C_x and C_y , which accumulate over the propagation coordinate z to the final XUV intensity. I_{XUV} 's duration is evaluated via τ_A (see Fig. 2.11). The vertical line marks the time of the main XUV burst.

the CEP is selected in a way that the peak generating the XUV burst is at the center of the pulse. As the pulse is linear only there, all other XUV bursts are suppressed.

In contrast to ionization gating, both polarizations of the driving IR field are present and result in contributions C_x and C_y . C_y belongs to the gating field and is much weaker than C_x , which is dominated by vertical stripes with the same characteristics as in the no gating scenario except that the middle stripe is much stronger than the satellites. This indicates the success of the gating method.

The Gaussian representing the duration τ_A appears to be too short to express the autocorrelation's pedestals. This is not relevant for the validity of the solution as it is short and that is the only purpose of using τ_A in the optimization.

The Φ of the solution is 0.62. This indicates that the anti-ionization gating punishment of the FOM is necessary and effective. As expected the maximum IR intensity is lower than for ionization gating (1.79 instead of 2.03×10^{14} W/cm²), which should contribute to the lower efficiency in comparison to ionization gating (1.08 instead of 1.75×10^{-7}) and is needed to avoid low Φ . The intensity reduction is influenced by the pulse elongation through the gating optics, the large beam waist (746.5 instead of 696.1 μ m) and the smaller distance between focus and cell (749 instead of 1931 mm). As the gating methods base upon different, intensity independent mechanisms, the XUV pulse duration cannot be compared and the HHG cell length can be longer than for ionization gating (502 instead of 137 mm). Correspondingly, the pressure is lower to reduce XUV reabsorption (36.0 instead of 139.1 Pa).

2.4.4 DOG

New Parameters A BBO has to be added to the polarization gating. Its description requires three new parameters (Fig. 2.9):

$w_{0,BBO}$ The SHG field strength is indirectly proportional to the square of the beam waist at the BBO, $w_{0,BBO}$. The damage threshold of a BBO is about 1400 GW/cm² for 10 fs pulses [36, 37] giving a safe diameter of 10 mm.

d_{BBO} Fig. 1.3 discusses that for a small BBO thickness d_{BBO} the conversion efficiency is rising with length. Due to the group velocity mismatch between fundamental and SHG long crystals result in pulse elongation. Additionally, the BBO is a phase plate for the IR pulse. Fig. 2.23 illustrates that. As shown, the gate's position changes with d_{BBO} .

α_{BBO} E_x is the fundamental of SHG (Sec. 2.3.3) and the SHG field is added to E_y . The BBO angle α_{BBO} changes the shape of both fields and thereby the result of the SHG. Fig. 2.24 shows two extreme cases. For $\alpha_{BBO} = 296^\circ$ the SHG fundamental is likely to a Gaussian pulse. The resulting SHG field is also similar to a Gaussian but the lower group velocity of the SHG field displaces it with respect to its fundamental. $\alpha_{BBO} = 255^\circ$ results in a gating field. The central hole of E_x induces a hole in the SHG field, which is blurred by the group velocity mismatch.

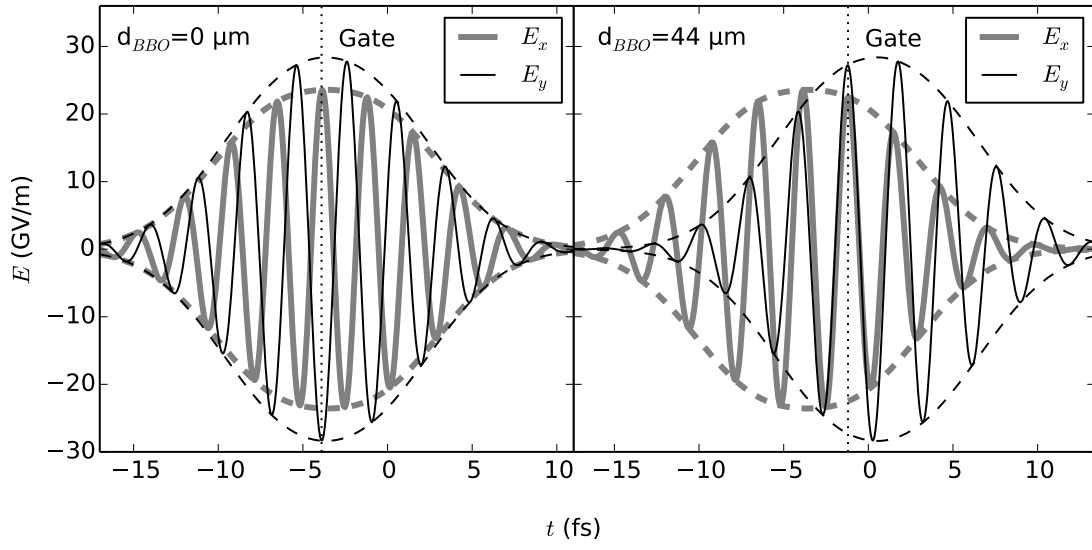


Figure 2.23: Effect of the BBO as phase plate: The electric field of the IR pulse is shown after the BBO for two different d_{BBO} . The SHG is disabled for this picture. All other parameters anticipate the DOG optimum.

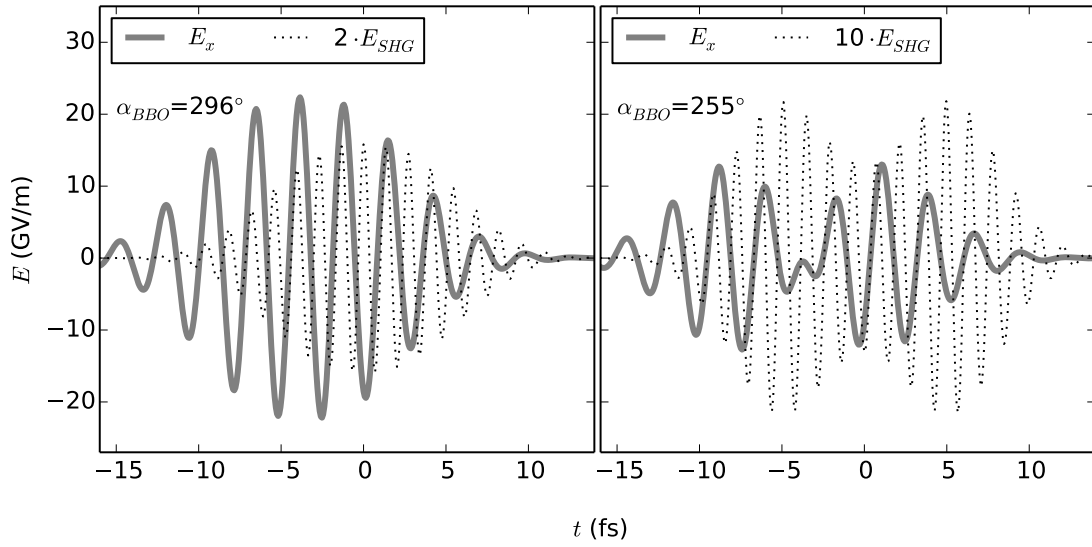


Figure 2.24: Effect of the BBO angle on the shape of the SHG: The driving E_x and the generated SHG pulse E_{SHG} are shown for two different α_{BBO} . All other parameters anticipate the DOG optimum.

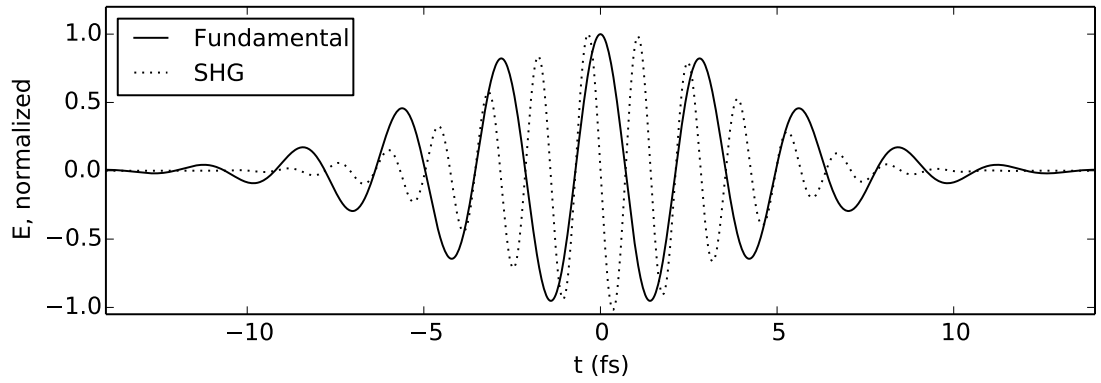


Figure 2.25: Illustration of the phase mismatch of a fundamental and its SHG: Calculated according to Eq. (1.13) for a negligibly thin crystal.

Rough Understanding The SHG should enhance only one polarization-gated IR field peak. The BBO angle is used to prevent a hole at that position. The beam waist at the BBO, $w_{0,BBO}$, controls the strength of the SHG. The BBO thickness fulfills three roles:

- It matches the phase of E_y and the SHG field. Because of the polarization gating E_x and E_y have the same phase in the gated cycles. The SHG and the fundamental E_x have a phase offset of $\lambda_{850\text{nm}}/8$ (refer to Fig. 2.25). Hence E_y and the SHG field have a phase offset. The phase plate property of the BBO is used to match both phases.
- As a side effect the polarization gated time is shifted. This shift must be small in order to gate the most intense part of the pulse.
- The BBO thickness allows sufficient SHG efficiency without forcing to increase the intensity via $w_{0,BBO}$ beyond the damage threshold.

The first argument limits the choice of the thickness to a periodically distributed set of values. The other two arguments result in a minimum and maximum value.

Fig. 2.26 illustrates the understanding of the BBO thickness. The efficiency and the duration are roughly periodic. The peak in efficiency occurs when the BBO compensates the SHG - E_y phase mismatch. The plot anticipates the optimal parameters for DOG. There, the BBO is a multi-order plate. The slightly higher efficiencies for thicker BBOs do not challenge the optimization as the SHG conversion efficiency is too high for larger values and the duration is increasing as well.

FOM and Optimization The SHG is only intended to differentiate the main peak from its neighbors. The chosen calculation method is limited to small conversions. Therefore,

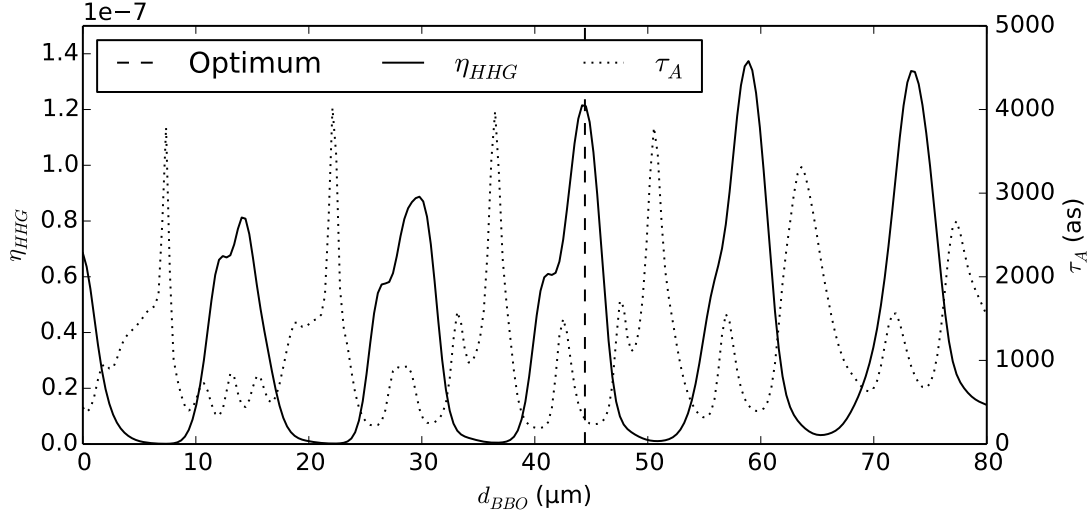


Figure 2.26: Effect of the BBO length d_{BBO} : Efficiency η_{HHG} and pulse duration τ_A for different d_{BBO} . All other parameters use the optimal values for DOG (Tab. 2.3). In the optimization the SHG efficiency is kept at valid values ($<10\%$) via the FOM. This is not enforced in this plot so that the SHG efficiency may be too high.

the FOM receives a new punishment if the SHG conversion is larger than 10 %:

$$FOM_{DOG} := \eta_{HHG} \cdot \left(1 - 0.1 \left(\frac{\tau_A}{\tau_{target}} \right)^8 - 1000 \left(\frac{\Phi_{min}}{\Phi} - 1 \right)^2 \chi_{[0, \Phi_{min}]}(\Phi) - 1000 \left(\frac{\eta_{SHG}}{0.1} - 1 \right)^2 \chi_{[0.1, 1]}(\eta_{SHG}) \right) \quad (2.32)$$

The optimal parameter set for polarization gating is amended with BBO parameters. They are chosen according to the rough understanding and such that the SHG efficiency remains under 10 %. The result is then automatically optimized.

Result DOG is reproduced. Fig. 2.27 illustrates the calculation. It shows that 3/4 of an IR cycle before the main XUV burst the IR pulse is linearly polarized and the SHG interferes constructively. The neighboring half cycles experience destructive interference. \vec{C} shows the same characteristics as the polarization gating except that the middle pulse is even more pronounced and both polarizations of \vec{C} are of comparable strength. The first stripe indicates that the SHG field is working as intended. The Gaussian representation of the duration τ_A is very close to the actual autocorrelation as the pedestals are weak.

The SHG efficiency of the solution is 10 % and $\Phi = 0.62$. This indicates that SHG and the anti-ionization gating punishment of the FOM are necessary and effective.

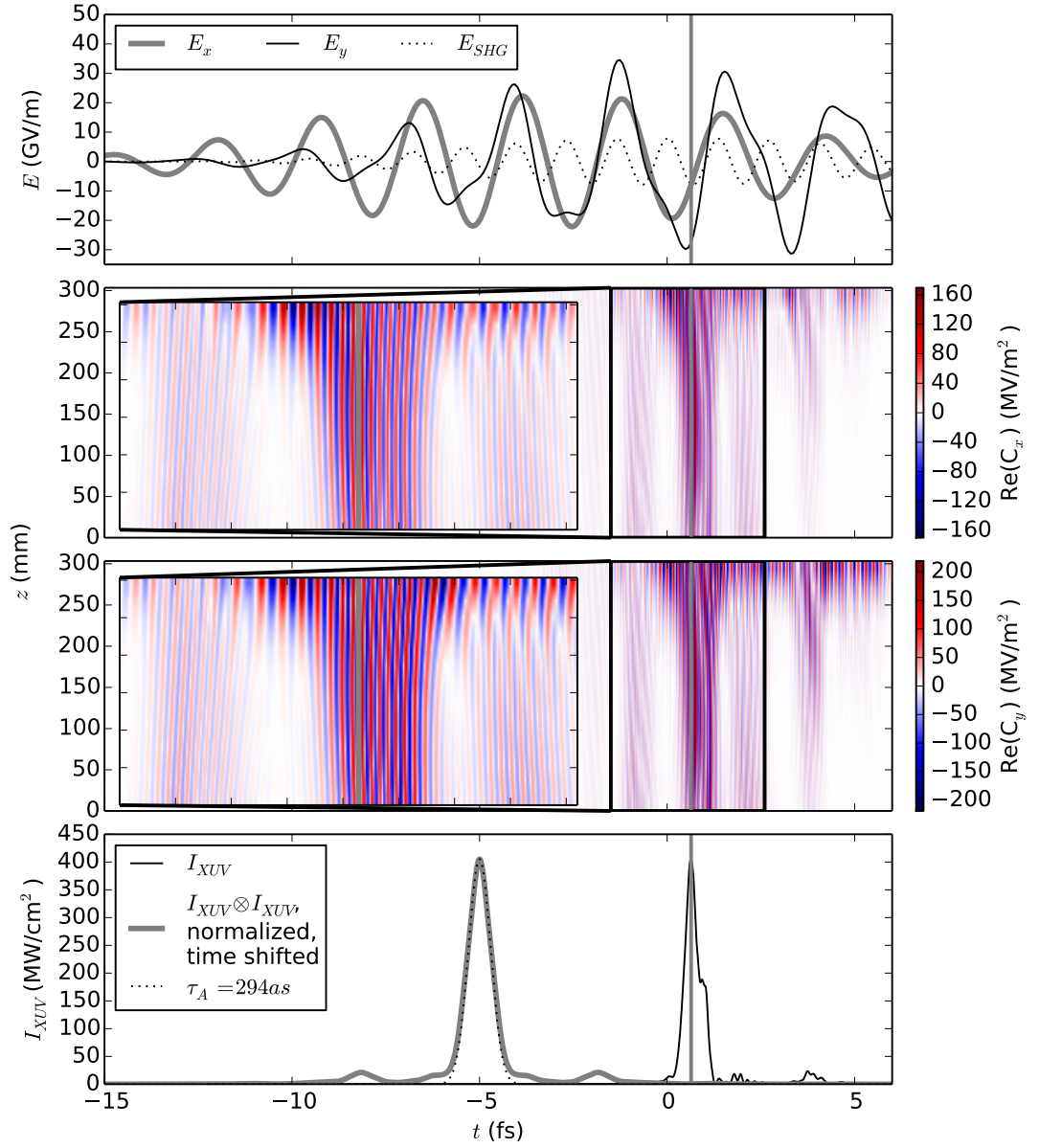


Figure 2.27: Visualization of the calculation for the optimal parameters for DOG: The initial IR pulse \vec{E} results in the contributions C_x and C_y , which accumulate over the propagation coordinate z to the final XUV intensity. I_{XUV} 's duration is evaluated via τ_A (see Fig. 2.11). E_y already contains the SHG amendment. The vertical line marks the time of the main XUV burst.

A smaller ionization gating effect does not necessarily imply that the maximum IR intensity in the HHG cell is less than for ionization gating as the BBO increases the intensity for a short time only. Indeed the maximum intensity is higher (2.16 compared to $2.03 \times 10^{14} \text{ W/cm}^2$ for ionization gating). The thickness of the SiO_2 plate is slightly different from polarization gating because of its new function to assist in the phase-matching of the SHG to E_x . The corresponding loss of intensity due to the longer IR pulse duration is compensated by focusing harder (716.4 instead of 746.5 μm). It is not clear why the medium length is shorter (311 instead of 502 mm) and the cell is farther away from the focus (844 instead of 749 mm) than for polarization gating. However, the relation of pressure (53.2 Pa) and medium length is the same as for all previous methods. The efficiency (1.22×10^{-7}) is lower than for ionization gating (1.75×10^{-7}), which possess an interesting result. The efficiency is higher than the 1.08×10^{-7} of polarization gating. This is necessary as polarization gating is a special case of DOG: If the BBO is not an advantage for the efficiency, the optimization will set the BBO length to zero and achieve the polarization gating efficiency. Because of the presence of two polarizations and the SHG field, it is not straightforward to define whether the CEP resulted in an XUV producing half cycle that is at the center of the pulse. However, the productive peak is the highest (34.5 GV/m).

2.4.5 Hybrid DOG

The previous two sections avoided ionization gating. This can be detrimental for the actual aim to maximize intensity for short pulses. Therefore, this section introduces hybrid DOG, which is a combination of DOG and ionization gating. This solution is of experimental relevance as optimization in the laboratory will optimize for signal and not against ionization gating effects. Investigating hybrid polarization gating is less interesting as the achieved efficiency is slightly lower.

FOM and Optimization The Φ term in DOG's FOM (Eq. (2.32)) is removed to allow ionization gating:

$$FOM_{HybridDOG} := \eta_{HHG} \cdot \left(1 - 0.1 \left(\frac{\tau_A}{\tau_{target}}\right)^8 - 1000 \left(\frac{\eta_{SHG}}{0.1} - 1\right)^2 \chi_{[0.1,1]}(\eta_{SHG})\right) \quad (2.33)$$

The DOG optimum is a sufficient starting point for the automatic optimization. This procedure simply finds ionization gating assisted DOG. It may neglect a parameters set that lead to ionization gating with small contributions from DOG.

Result Fig. 2.28 shows the result of the optimization. The time difference between the XUV burst and the point where E_x , E_y and SHG have the same phase is 3/4 of an IR cycle. In the neighboring peaks the SHG interferes destructively. The following peak shows linear polarization and constructive SHG- E_y interference. \vec{C} shows three stripes. They are present on both dimensions but C_y is much stronger due to a stronger driving

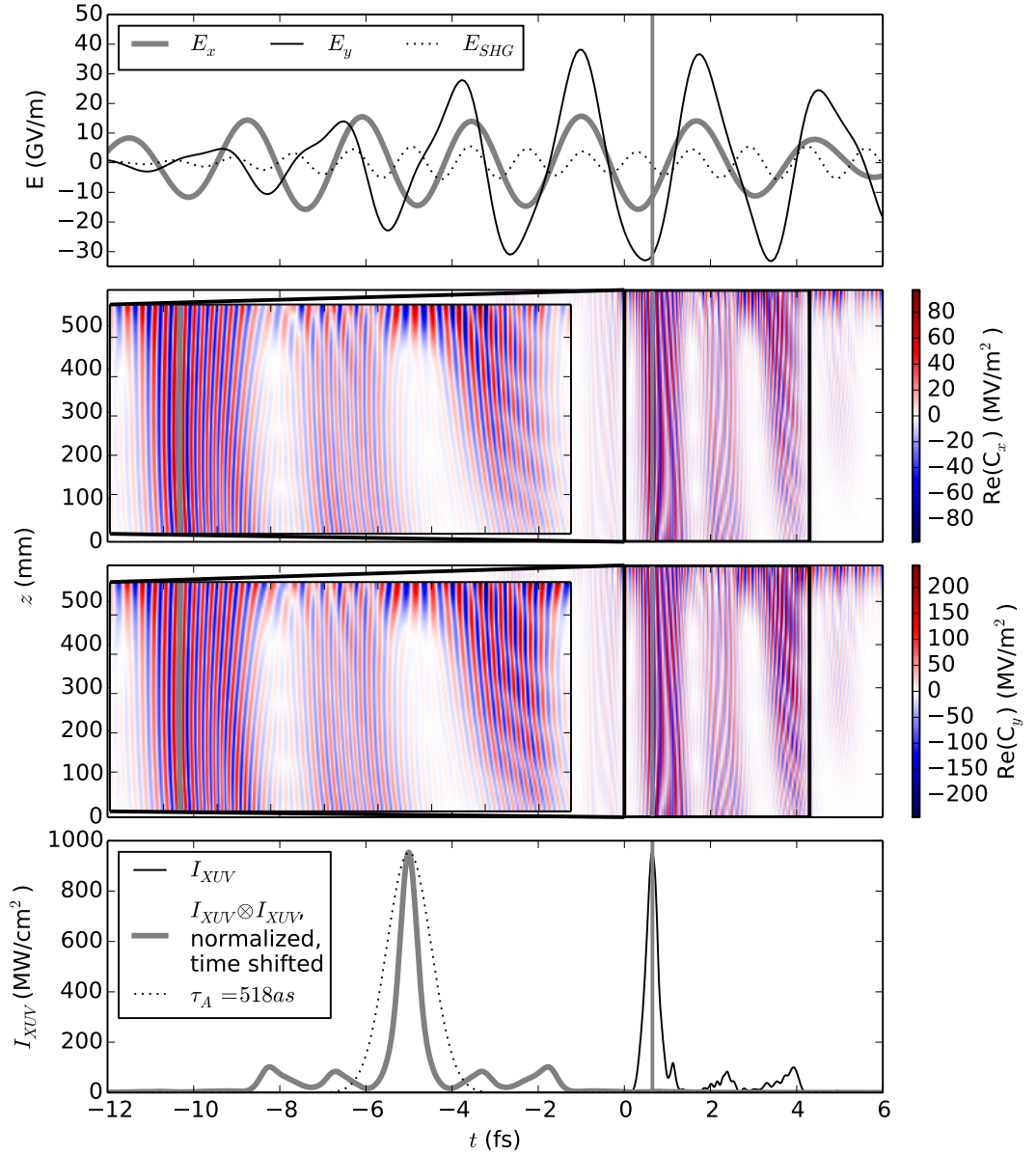


Figure 2.28: Visualization of the calculation for the optimal parameters for hybrid DOG: The initial IR pulse \vec{E} results in the contributions C_x and C_y , which accumulate over the propagation coordinate z to the final XUV intensity. I_{XUV} 's duration is evaluated via τ_A (see Fig. 2.11). E_y already contains the SHG amendment. The vertical line marks the time of the main XUV burst.

field strength in the y -polarization. Only the contributions in the first of the three stripes are phase-matched. The middle stripe is also weak due to the destructive interference of the SHG. $\Phi = 0.33$ is between 0.25 for ionization gating and 0.62 for the no gating optimum. This affirms the hybrid nature of the optimum. $\eta_{SHG} = 0.10$ indicates the necessity for the FOM punishment.

As DOG and ionization gating are special cases of hybrid DOG, it must have the highest efficiency. This is indeed the case (2.25 compared to 1.75 and 1.22×10^{-7} , respectively). As expected from the lower Φ , the maximum IR intensity in the HHG cell is higher than for DOG (2.19 instead of 2.16 W/cm²). Correspondingly, the beam waist is smaller (684.9 instead of 716.4 μm) and the cell is closer to the focus (701 instead of 844 mm) than for DOG. The SiO₂ thickness is almost the same as for DOG (149.9 instead of 151.3 μm). The BBO angle differs by 15°, which results in a different curve shape of E_x and E_y . To compensate the smaller driving field of the SHG the beam size at the BBO is smaller (9.2 instead of 15.5 mm). Pressure (42.3 Pa) and medium length (599 mm) are not between the values for ionization gating (139.1 Pa, 137 mm) and DOG (53.2 Pa, 311 mm). The reason is unknown due to the complexity of this new method originating from the two gating mechanisms and the high number of parameters. Because of the presence of two polarizations and the SHG field, it is not straightforward to define whether the CEP resulted in an XUV producing half cycle that is at the center of the pulse. However, the productive peak is the highest (38.1 GV/m).

2.4.6 Comparison

Tab. 2.3 shows all input parameters and important properties of the calculation results. They will mainly be discussed in the same order as in table.

p, L_{med} Constant's model resulted in the statement that the medium length should be few times the absorption length L_{abs} . Its frequency dependence would complicate the analysis. Instead, it is noted that $L_{abs} \propto p^{-1}$ so that the product pL_{med} should be constant to keep the transmission through the HHG medium constant. It is about 20 Pa m for all parameter sets.

φ_{CEP} φ_{CEP} defines the initial CEP. Because of the influence of the optical elements before the HHG medium, the phase relevant for the medium is discussed along the pictures of each gating method and not via this variable.

w_0, z_0, I_{max}^{IR} The beam waist w_0 for no gating is set to 1000 μm to reduce the intensity. The others have values around 700 μm . w_0 , focus positions z_0 and the IR pulse length in the medium are the main parameters for the intensity. The long z_0 of ionization gating and the increased IR pulse durations of pure and hybrid DOG reduce the IR intensity I_{max}^{IR} .

The highest intensities belong to DOG and hybrid DOG. The value for ionization gating does not need to be higher. Due to the SHG the maximum of DOG is only higher for a single cycle and therefore breaks comparability into two groups. With

2 Theoretical Comparison of Different HHG Gating Techniques

Table 2.3: All input parameters and output quantifiers for the five types of gating. The literature efficiencies stem from [5, 6, 7]. I_{max}^{IR} is the highest intensity occurring in the medium.

Method	No gating	Ionization gating	Polarization gating	DOG	Hybrid DOG
Input					
p (Pa)	10.4	139.1	36.0	53.2	42.3
L_{med} (mm)	2097	137	502	311	599
φ_{CEP} ($^\circ$)	26.4	161.1	85.6	284.2	238.7
w_0 (μm)	1000.0	696.1	746.5	716.4	684.9
z_0 (mm)	952	1931	749	844	701
d_{SiO_2} (μm)			128.7	151.3	149.9
d_{BBO} (μm)				44.4	42.1
$w_{0,BBO}$ (mm)				15.5	9.2
α_{BBO} ($^\circ$)				295.8	281.0
Output					
η_{HHG}	2.69×10^{-8}	1.75×10^{-7}	1.08×10^{-7}	1.22×10^{-7}	2.25×10^{-7}
lit. η_{HHG}		2.6×10^{-5}	3.5×10^{-7}	6×10^{-6}	
τ_A (as)	823	457	400	294	518
I_{max}^{IR} (W/cm 2)	1.25×10^{14}	2.03×10^{14}	1.79×10^{14}	2.16×10^{14}	2.19×10^{14}
η_{SHG}				0.100	0.100
Φ	0.62	0.25	0.62	0.62	0.33

SHG: hybrid DOG is expected and observed to have a higher maximum intensity than pure DOG. Without SHG: ionization gating should have a higher maximum IR intensity than no gating and polarization gating. This is fulfilled too.

A possible reason for the high z_0 for ionization gating is its different kind of phase-matching. Usually, the main contributions stem from the Gouy phase and gas dispersion. The Gouy phase's influence is weaker far from the focus. The phase-matching of ionization gating depends on the intensity via the electron dispersion. As the phase-matching must be present for the entire cell, a rather constant intensity can be beneficial and is achieved by the short cell far from the focus.

d_{SiO_2} The thickness of the birefringent material is similar for all applying methods. The plate fills an additional role, phase-matching for SHG and driving field, for DOG and hybrid DOG, which leads to a new optimum.

BBO d_{BBO} , the thickness of the BBO, is about the same for DOG and hybrid DOG. The beam waist at the BBO, $w_{0,BBO}$, is close to the damage threshold identified to occur around a $w_{0,BBO} = 10$ mm and much smaller for hybrid DOG than for DOG. The reason is a difference in the BBO angle α_{BBO} , which leads to another field strength in the fundamental of the BBO and is compensated. The SHG conversion

efficiency η_{SHG} is always at 10 %.

η_{HHG} The efficiency of the HHG η_{HHG} is lowest for no gating because the intensity is set to a low value. Polarization gating is less efficient than DOG. This is mandatory as DOG contains polarization gating: If the additional BBO would not result in additional benefits, setting the BBO length to zero would increase the FOM and degenerate DOG to polarization gating. For the same reason hybrid DOG is the most efficient method: Ionization gating and DOG cannot be more efficient than hybrid DOG as they are special cases too.

Compared to the literature values the calculated efficiencies are more similar. Their similarity is not astonishing: Basically, the XUV energy stems from the 3/4 of an IR field cycle between the ionization of the electrons and the recombination with its parent ion. The driving IR pulse energy and duration are fixed up to the elongation by the gating optics, which add only a small factor (compare the SiO₂ length to the cases in Fig. 2.20), and the BBO, which does not convert more than 10 % of energy. Therefore, the available energy for conversion is also fixed up to a small factor and large changes in the XUV energy require different conversion efficiencies. As the phase-matching has a similar quality for all productive cycles (refer to the figure showing \vec{C} for each method), only the amount of absorption or nonlinear polarization P_{NL} are left for discussion. As mentioned for the product of p and L_{med} the transmission through the gas is similar for all methods. P_{NL} is calculated via the Lewenstein model from the laser field. The actual dependence is complicated but the field before the emission of the XUV is most important and always roughly similar to a sinus wave. The scaling with the E-field strength is left and simplistically described by $P_{NL} \propto E^5$ in Sec. 2.3.6. This E-field strength is represented by I_{max}^{IR} in Tab 2.3. The values are different, but not enough to change the efficiencies by orders of magnitude.

The difference between the lowest and the highest efficiencies is a factor of 2.1. Therefore, technical difficulties play an important role in the choice of the method. These aspects are discussed in Chap. 3. The comparison between experimental and calculated efficiencies can be found at the end of Sec. 2.5.

τ_A The τ_A durations for all methods except no gating are beneath the targeted duration of 600 as. This indicates the successful reproduction of the gating methods. Optimizing the time resolution would require additional optimizations with a new FOM and benefit from the specification of an experiment, which may led to a new, specialized quantity for the XUV pulse duration.

Φ As expected, the phase-matching parameter Φ is lower for the methods using ionization gating. The polarization gating and DOG are forced to 0.62 using the FOMs. hybrid DOG does - in contrast to ionization gating - not have a large z_0 . Together with the larger Φ this put the influence of ionization gating for hybrid DOG into perspective.

2.5 Assumptions and Accuracy

The section reviews assumptions in order to evaluate the accuracy of the results. There are two groups. The first is concerned with the simulation for a given parameter set:

- The XUV does not influence IR propagation: The low XUV intensities justify this.
- The spectrum of the laser is Gaussian.
- The effect of the gating optics is calculated in plane wave approximation, which includes the SHG. Only the SiO₂ plate's higher moments of dispersion are taken into account: Due to the shortness of the optics this is not important and the SHG is only a small amendment to the pulse.
- The validity of the model belonging to the code of Usman Sapaev is assumed. This is backed by its prior usage including peer reviewed publications. The model's assumption of Gaussian pulses in space was checked by calculating that focusing because of the Kerr effect and electron dispersion are negligible (Sec. 2.3.4).
- The simple Lewenstein model is used. Explicit knowledge on its quantitative accuracy is not available. However, other groups (e.g. [80]) use much slower TDSE calculations, which indicates a limited accuracy. Due to its assumptions it does not correctly predict low XUV frequencies. Experimentally, they are removed by the Al filter and do not matter.
- A simple effective area model is used to take the volume into account that produces XUV: This approach neglects any off-axis propagation effects and bases upon a power law, which is taken from L'Huillier et al. [72]. They discuss the limitations of the power law. According to Platonenko et Strelkov [76] the power law has also been accessed to be 8 and 12 instead of the used 5, which would change the XUV energy by a factor of 1.6 or 2.4 correspondingly.
- The pressure in the HHG cell is assumed to be a constant. Usually, gas is flowing out of the cell through the entry and exit holes. This leads to pressure gradients. HHG cells with a diameter that is much bigger than the hole diameter are better modeled by this assumption.

The second set is concerned with choosing the optimal parameter sets:

- The automatic optimization mimics the fine-tuning of the signal in the lab. All parameters are chosen freely, which is adequate for e.g. p which can be continuously tuned by a valve. It is limited for e.g. the BBO which has a fixed length and can only be tuned by tilting or replacing the crystal.
- A rough understanding guided the manual optimization of parameters. However, for DOG and hybrid DOG there are nine parameters, which may overstretch the concept and lead to initial (and final) parameters in a local optimum.

In summary, the approach is only sufficient to make semiquantitative predictions for the resulting XUV because of the Lewenstein model and the effective area approach. The chosen parameters are justified but not rigorous.

This makes a direct comparison of the efficiency to experimental data difficult. A problem of the optimization for polarization gating and DOG is to avoid the ionization gating mechanism. Only ionization gating is straightforward but the calculated value, 1.75×10^{-7} is much lower than the experimental, 2.6×10^{-5} [6]. This may indicate that the calculated values are generally too low by two orders of magnitude. The shorter pulse duration of 5 instead of 7 fs may contribute to the difference, but it is difficult to believe that simpler gating and less discarded half cycles explain both orders of magnitude. The efficiencies for polarization gating (theory 1.08×10^{-7} , experiment 3.5×10^{-7} [5]) and DOG (theory 1.22×10^{-7} , experiment 6×10^{-6} [7]) are lower by a factor of 3 and 50, respectively. This may have two origins: First, as discussed above experimental setups do not offer the same flexibility as the parameters of the simulation so that the optimal parameters were potentially not reached which causes that the experimental values should be much higher than the actually reported values. Second, as the ionization gating mechanism is intensity susceptible, the effective area approach is coarse.

Nevertheless, the literature values for the efficiencies have the same order as the calculated representations.

Future projects may extend the simulation to calculate the fields over the radial coordinate. The impact of the effective area approach on ionization gating would be accessible by comparing the results from the present and the extended simulation. The extended simulation would be less useful for optimization because of a higher computation time. The presented optimizations typically took about 100 manual and 1000 automatic runs with a duration in the order of one minute each. A pre-optimization using the present simulation would help to identify interesting parameters faster. Additionally, the XUV divergence would become directly accessible.

Another approach to the difference between experiment and theory is to directly reproduce the efficiencies by simulating for the parameters of the experiments.

2.6 Summary

The aim of the chapter is to guide the construction of the high harmonic generation (HHG) cell. It is intended to produce a short XUV pulse with the highest possible energy. To this end, gating techniques are required. Three techniques, ionization gating, polarization gating and double optical gating (DOG) are chosen and complemented with no gating (for reference) and hybrid DOG, which is introduced within this thesis. In order to compare the potential of the gating methods a model is developed that calculates the ratio of resulting XUV energy and initial IR energy and the duration of the XUV pulse for each gating method.

The model assumes the input pulse as expected from the NOPCPA setup in Chap. 1, applies optical components as necessary for the gating technique in plane wave approximation. Then, an upgraded version of a model by Usman Sapaev is used to calculate

2 Theoretical Comparison of Different HHG Gating Techniques

the IR field on the axis of propagation within the HHG cell. A Gaussian beam represents the focusing. The Lewenstein model returns XUV polarizations on the propagation axis, which are converted via an approximation of the Maxwell equations and an effective area approach to the XUV field. The XUV pulse's energy and a measure of duration are calculated. The latter is defined and validated in the thesis.

With respect to the chosen parameters each gating method has a different optimum. Finding it allows to compare the maximum performance of the gating techniques. An understanding of the parameter space is developed and guides a manual search for initial parameters, which are then automatically fine-tuned. All gating methods are reproduced and optimal parameter sets are found. However, a conceptual challenge is identified: High intensities lead to more single atom efficiency and, via the ionization gating mechanism, to shorter pulses. Both features are beneficial in terms of pulse duration and energy for polarization gating and DOG. Therefore, simple optimization leads to a combination of them and ionization gating. Consequently, the concept of hybrid DOG is introduced and evaluated within the thesis. Alternatively, a criterion to limit this effect is found and polarization gating and DOG are optimized. Parameters describing the process and its performance are compared.

Finally, to analyze the accuracy of the numerical approach the assumptions are reviewed.

3 High Harmonic Generation Setup, End Stations

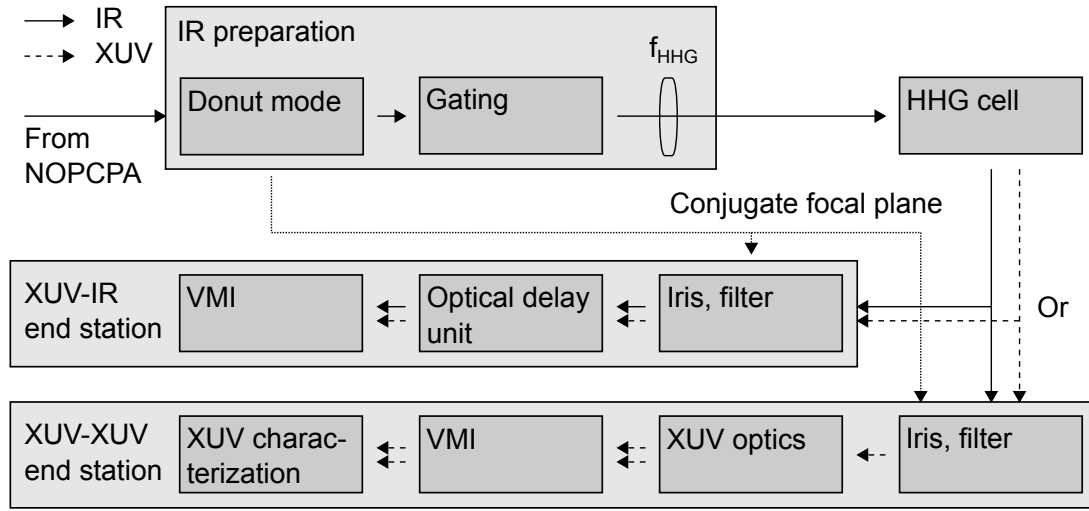


Figure 3.1: Overview of the setup after the NOPCPA

The chapter suggests a setup using the optimization results from Chap. 2 to reach optimal conditions for the HHG. It introduces rather technical aspects for the process and describes the end stations for experiments. Fig. 3.1 summarizes the setup.

Sec. 3.1 introduces a concept for the spatial separation of the IR and the XUV after the HHG cell and discusses technical aspects of the gating optics and focusing. A sophisticated pressure control around the HHG cell is required and designed (Sec. 3.2). Sec. 3.3 describes the XUV-IR end station intended for XUV-IR pump-probe experiments, which reuses the driving pulse of the HHG. An iris and a filter prepare the pulses for the optical delay unit, which delays and focuses them into the interaction region in a VMI. Alternatively, the XUV-XUV end station discards the IR and splits and focuses the XUV pulse into the VMI. A XUV characterization unit is available. Sec. 3.5 summarizes the setup.

Beyond several smaller contributions to other parts the gating and HHG cell including the pressure control system was designed within the thesis. The latter was also built completely.

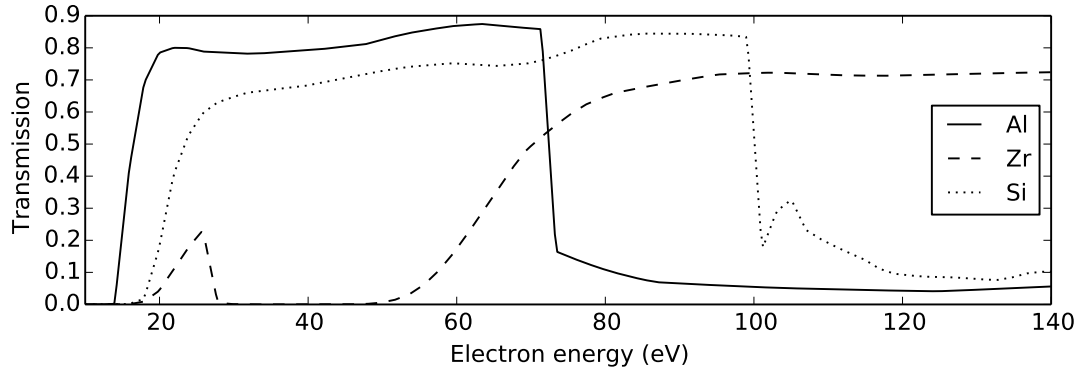


Figure 3.2: Transmission as a function of photon energy for 100 nm thick Zr, Al and Si [73]

3.1 IR Preparation

The HHG produces a weak XUV beam from an IR beam. The end stations use metal filters to isolate the XUV. However, the thermal power of the IR is problematic:

Assuming that the entire power of the NOPCPA (given by a pulse energy of 15 mJ at a repetition rate of 100 Hz) is only dissipated via radiation. According to the Stefan-Boltzmann law, the temperatures would be 1170 K or 641 K for the diameter of 3 mm or 10 mm for the used commercial filters, respectively. The melting points of 933 K (Al), 1687 K (Si) and 2128 K (Zr) are high but the filter lifetime is falling with power.

These materials have been chosen because of their transmission curves (Fig. 3.2).

- Zr: High transmission from 70 eV
- Al: High transmission from 18 eV to 70 eV
- Si: High transmission from 15 eV to 100 eV

Beyond covering different spectral ranges, sharp absorption edges can be used for the calibration of the energy scale of the VML. These filters are mounted in a motorized filter wheel to allow switching in vacuum.

An energy reduction is accomplished by a piece of copper in the beam, which is mounted by thin wires and placed before the compressor to create a hole in the intensity distribution. This donut mode is imaged to the IR filter. The XUV has a lower divergence [42] and is therefore present in the region in the center of the beam. This approach for separation was used for a publication by Peatross et al. [81]. A motorized iris is used to block the IR in the outer region. Another application of this iris is to reduce the amount of IR in the XUV-IR mode. The solution is summarized in Fig. 3.3.

The filter's thicknesses 100, 200 and 300 nm are available to experimentally balance filter lifetime and absorption loss, which both rises with the thickness of the foils.

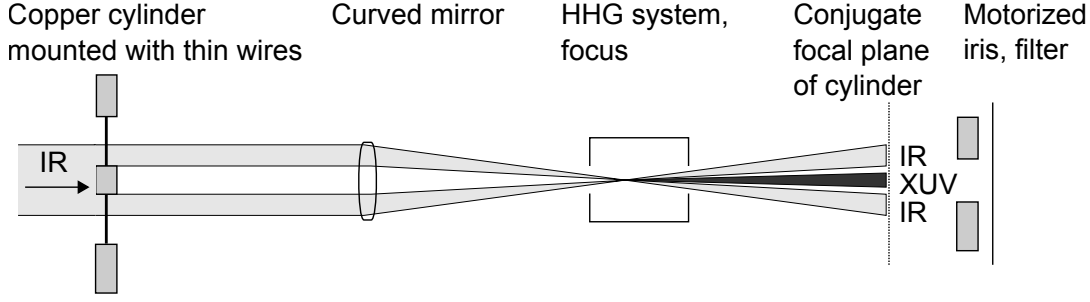


Figure 3.3: Summary of the XUV-IR separation concept: A shadow is created by a piece of copper and imaged through the HHG system with its lens to a thin metal filter. Its central region is illuminated by XUV only, which allows the separation by filters and an iris.

The output of the compressor is sent to the gating optics, which are already described in Fig. 2.9, and then focused. Parts of the design discussed later¹ require a certain polarization of the pulses. As e.g. DOG includes rotations of the polarization the capacity to turn the VMI or the polarization of the pulses is advantageous to match the requirements. The latter is chosen via implementing an additional $\lambda/2$ plate before the gating optics and the option to turn all following gating optics.

The focal length of the curved focusing mirror into the HHG cell relates the collimated beam diameter to the focal beam waist. All gating techniques have an optimal $w_0 \approx 700 \mu\text{m}$ (Tab. 2.3). As the input beam is $2w_1 = 8 \text{ mm}$ in diameter, the focal length is

$$\begin{aligned} f_{HHG} &= \frac{w_0 w_1 \pi}{\lambda} \\ &= 10.3 \text{ m} \end{aligned} \quad (3.1)$$

[67]. Shorter focal lengths, which would reduce lab space constraints, are difficult to reach. The only free parameter is the size of the beam at the curved mirror. Telescoping the beam to half the diameter would reduce the focal length to 5 m. The flux would rise to 0.09 J/cm^2 , which is close to 0.1 J/cm^2 , the damage threshold judged from the focusing mirror's manufacturer's catalog [82]. Therefore, much shorter focal lengths are challenging.

3.2 HHG Cell

Requirements The HHG cell itself is optimized in Chap. 2. Therefore, the resulting parameters (Tab. 2.3) for the beam waist w_0 , the distance from focus to beginning of the cell z_0 , its length L_{med} and pressure p are known. However, the design should be flexible enough to react to changes and differences between experimental and theoretical optima.

¹The VMIs (page 87) and grazing incidence XUV optics (Sec. 3.4)

3 High Harmonic Generation Setup, End Stations

The radiation has to pass the cell. Therefore, holes for entry and exit are necessary and gas can flow out of these holes. Outside the HHG cell the gas has detrimental effects, which are not modeled in Chap. 2. The remainder of the section describes and minimizes them:

- Because of the high intensities close to the focus, the B-integral (Eq. (1.4)) reaches high values. As explained on page 12 the value has to be smaller than 2...3 to prevent the degradation of the IR beam. For simplicity the integral is calculated from infinity.

$$B = \int_{-\infty}^{z_0} n_2 k I dz \quad (3.2a)$$

$$= b n_2 k I_0 [\arctan(z_0/b) + \pi/2] \quad (3.2b)$$

The computation assumes a Gaussian beam (Eq.(2.9)) and the nonlinear index of refraction $n_2 \approx 12 \times 10^{-23} \text{ m}^2/\text{W}$ [34] for a pressure of 1 bar of Ar. B reaches comparable values for the different gating techniques. The highest value of 10,000 belongs to ionization gating. In order to reduce the values, the pressure should be reduced by a factor of 100,000. Therefore, pressure before the cell beneath 1 Pa are safe.

- VMI operation suffers from high pressures, because the measured particles must not collide with ambient gas and the micro channel plates (MCP) experience more noise and faster degradation [83]. The manufacturer of the MCP states a limit of $1.3 \times 10^{-4} \text{ Pa}$ [84], the measurement in Chap. 4 worked at $1 \times 10^{-5} \text{ Pa}$ so that the MCP lifetime can be enhanced by restricting to $1 \times 10^{-6} \text{ Pa}$ as a safe value.
- Any gas after the HHG cell absorbs XUV. The pressure must drop sufficiently fast to limit the energy loss. For reasons stated later in the chapter the relevant path is 25 mm. Fig. 3.4 shows the transmission of XUV through 25 mm of Ar at 150 Pa. For harmonics higher than 29 the transmission is close to 90 %, which is used as the threshold for maximum accepted loss. Therefore, the pressure there must stay lower than 150 Pa to maintain the transmission threshold. The frequency regime beyond harmonic 29 is favorable for its low absorption and it is used in the theoretical calculations (see. Fig. 2.15).

Design In order to maintain a given pressure in the HHG cell and sufficiently low pressures anywhere else constant pumping and gas flow into the cell are necessary. As the large diameter of the beam requires large holes resulting in large flows, an elaborate pumping system is necessary. The corresponding theory of flow in vacuum is given in textbooks [85] and only the required relations will be given. The actual design and variable definitions are given in Fig. 3.5. For better adaptability it is built from pipes with the nominal standard diameter of 100 mm with ISO-K 100 and ISO-CF 100 connectors.

The strategy to bridge the pressure difference from $1 \times 10^2 \text{ Pa}$ in the cell to $1 \times 10^{-6} \text{ Pa}$ in the experimental chamber is to use multiple differential pumping stages. A differential

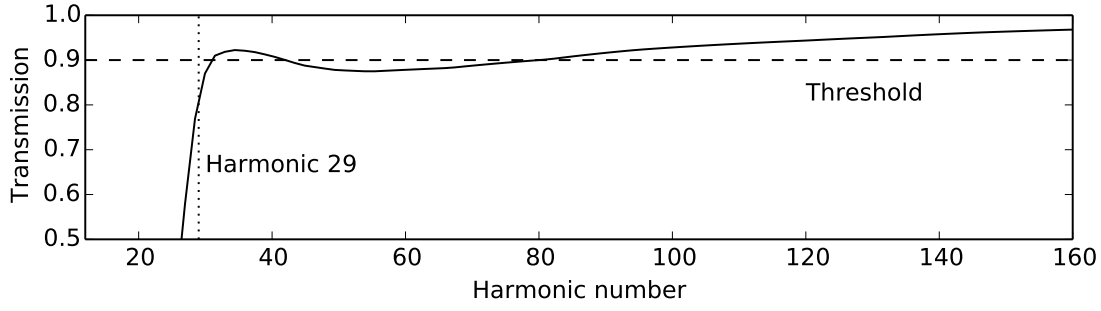


Figure 3.4: Transmission of XUV through 25 mm of Ar at 150 Pa for different energies expressed in harmonic order (multiples of 850 nm) [73]

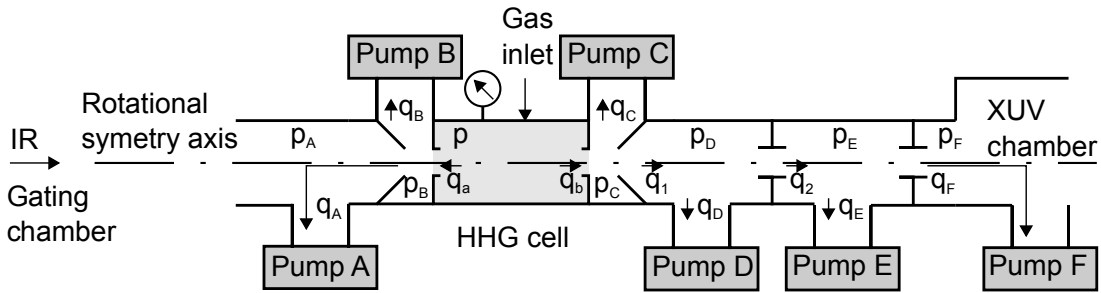


Figure 3.5: Setup of the vacuum system of the HHG cell: All elements inside the horizontal main tubes are rotationally symmetric with respect to the center axis of the tubes. q and p denote flow and pressure. The indices A, B, C, D, E, F are given according to the pumps. a and b refer to choked flows. 1 and 2 label the remnant flows. See text for details on the setup.

pumping stage is a volume with an entrance and an exit (here for the laser beams) and a pump and designed such that most entering gas leaves through the pump and not through the exit. This is achieved by using the smallest exit diameters possible for the beam and a pump with a pumping speed that results in a much larger flow than the exit.

The center of the setup is the HHG cell. Its pressure is maintained by a feedback loop consisting of a pressure gauge and a gas inlet with an electronic valve.

The cell is surrounded by differential pumping stages. The chamber to the right side (in Fig. 3.5) has a special geometry. The laser path is kept to 25 mm to reduce the reabsorption of XUV by the gas. Reducing the length to the order of magnitude of the hole diameter would allow gas particles to simply pass the stage. The volume between the entrance and exit holes must be open towards Pump C. Obstacles would reduce the effective pumping speed.

There are two more differential pumping stages to the right. Both have exits with 60 mm long tubes that reduce the flow despite a relatively large diameter and are pumped

3 High Harmonic Generation Setup, End Stations

by Pump D or E respectively. Behind the stages is the XUV chamber. The VMI inside results in gas load which will require a share of the chamber's pump's pumping speed. It is assumed that 150 l/s are available to keep the pressure p_F at 1×10^{-6} Pa (safe value from above), which defines a maximum flow from the differential pumping chamber of Pump E. More flow results in a higher pressure p_F .

The differential pumping stage of Pump B is symmetric to the stage of Pump C.

Model Checking the above criteria requires calculating all pressures by a system of equations constructed from the equation of choked flow, flow conservation, pumping speeds and conductances. All flows and pressures are defined in Fig. 3.5.

The two holes of the cell results in a flow out of the HHG cell that is choked for the parameters of each gating method as the pressures in the neighboring chambers $p_{B,C}$ is less than $\left(\frac{2}{\kappa+1}\right)^{\frac{\kappa}{\kappa-1}} p$, where κ is the heat capacity ratio and the term equals $0.487p$ for single atomic gases. Therefore, the flows $q_{a,b}$ do not depend on $p_{B,C}$ [85]:

$$q_{a,b} = 0.51p\sqrt{\frac{\pi}{4}}\bar{v}A_{hole\ a,b}\sqrt{\frac{\kappa}{2} \cdot \left(\frac{2}{\kappa+1}\right)^{\frac{\kappa+1}{\kappa-1}}} \quad (3.3)$$

\bar{v} is the average speed of the atoms in the cell and A_{hole} is the area of the hole. The factor 0.51 in the last equation represents the geometry of the hole [86], which is shown in Fig. 3.5. In vacuum technology flow q is formulated with the product of pressure and volume as conserved quantity, which is equivalent to particle number at constant temperature, because of the ideal gas law. If the incoming and outgoing flows a volume V differ by Δq , its pressure is changing as $Vdp/dt = \Delta q$.

The system is intended to work with constant pressures so that the flows are conserved:

$$q_a = q_A + q_B \quad (3.4a)$$

$$q_b = q_C + q_1 \quad (3.4b)$$

$$q_1 = q_D + q_2 \quad (3.4c)$$

$$q_2 = q_E + q_F. \quad (3.4d)$$

As there are no gas sources in the gating chamber and the compressor has its own pump it is assumed that there is no gas flow through the entrance of the setup in Fig. 3.5 and the flow escaping the differential pumping stage of Pump B q_A leaves the system via Pump A. The pumping speed S relates the pressure in front of the pump to the flow through it:

$$q_i = S_i p_i \quad i = A, B, C, D, E, F \quad (3.5)$$

Table 3.1: Calculation of $4w(z)$, the estimation for minimum necessary orifice and tube diameter. The geometry of the beam and HHG cell stems from the theoretical calculation of HHG parameters for different gating methods in Chap. 2 as summarized in Tab. 2.3. The names of the holes match the indices of the flows in Fig. 3.5. A set of rounded, smallest diameters matching all gating methods is given as 'Choice'. Manufactured denotes values describing machined parts that base upon outdated calculations.

Gating technique	Minimum hole diameter (mm)					
	A	a	b	1	2	F
Ionization gating	4.06	4.10	4.25	4.29	4.55	5.14
Polarization gating	3.16	3.18	3.49	3.52	3.69	4.12
DOG	3.12	3.14	3.36	3.38	3.57	4.02
HDOG	2.94	2.95	3.42	3.45	3.67	4.19
Choice	4.10	4.10	4.30	4.30	4.60	5.20
Manufactured	2.00	2.00	2.00	2.00	4.00	5.00

for the respective pump. The conductances relate pressure gradients and flows:

$$q_A = C_A(p_B - p_A) \quad (3.6a)$$

$$q_1 = C_1(p_C - p_D) \quad (3.6b)$$

$$q_2 = C_2(p_D - p_E) \quad (3.6c)$$

$$q_F = C_F(p_E - p_F) \quad (3.6d)$$

[85]. They are calculated from the geometry of the linking orifice and tube. Their naming is according to the affected flow. The conductance C_{hole} of an orifice of diameter D is $D^2\pi\bar{v}/16$. A tube of length L and diameter D provides a conductance $C_{tube} = D^3\bar{v}\pi/12L$. The orifice conductances C_A and C_1 are calculated from the respective diameters. C_2 and C_F additionally take the tubes into account via $C^{-1} = C_{hole}^{-1} + C_{tube}^{-1}$. The tubes of 60 mm length are added to reduce the conductance of the orifices.

The orifices have to be large enough to let the laser pulses pass. The beam parameters from the theoretical optimization define a beam radius $w(z)$ for any hole position. Integrating the equation of the Gaussian pulse, Eq. (2.9), reveals that 99 % of the energy are located within a radius of $1.5w(z)$:

$$\frac{\int_0^{1.5w_0} \exp\left(\frac{-2r^2}{w_0^2}\right) r dr}{\int_0^\infty \exp\left(\frac{-2r^2}{w_0^2}\right) r dr} = 1 - \exp(-2 \cdot 1.5^2) \quad (3.7)$$

$$= 99 \%$$

A diameter of $4w(z)$ is chosen adding a buffer for the alignment of the holes.

Tab. 3.1 shows the required hole sizes. They are calculated from the optimal geometry for each gating method. The table also gives a choice, which is the rounded largest hole diameter and values for manufactured parts.

Table 3.2: Evaluation of the design criteria for three scenarios: The first three double rows evaluate the criteria on page 80 (Low B-integral, low XUV absorption, VMI at safe operation pressure). The high vacuum pressures of the pumps are given too.

All values are pressure in Pa			
Value	Chosen hole size	Double chosen hole size	Manufactured,
Condition	p=139, Ar	p=347, Ar	p=2000, N ₂
p_A	8.6e-03	2.5e-01	1.9e-02
$p_A < 1$	OK	OK	
p_C	3.7e-01	2.9e+00	1.8e+00
$p_C < 150$	OK	OK	
p_F	5.1e-09	8.1e-06	1.6e-08
$p_F < 1e - 6$	OK	Failed	
Pump	Pressure in front of the pump		
Pump A	8.6e-03	2.5e-01	1.9e-02
Pump B	3.4e-01	2.7e+00	1.8e+00
Pump C	3.7e-01	2.9e+00	1.8e+00
Pump D	3.5e-03	1.1e-01	6.3e-03
Pump E	3.5e-06	7.7e-04	7.2e-06

Theoretical and Experimental Evaluation The system of equations is solved for the chosen hole sizes and the optimal pressure for ionization gating. The other methods require less pressure.

By solving the equations for different vacuum pumps from the market and comparing the results to the requirements a set of pumps was chosen and procured. Their pumping speeds are $S_A = 501/\text{s}$, $S_B = S_C = 5001/\text{s}$ and $S_D = S_E = 1511/\text{s}$. Choosing larger pumps presents a reserve for later modifications.

The pressures resulting for these pumps are shown in Tab. 3.2's second column. It passes all criteria. As the hole diameters and the cell pressure are compatible with all gating techniques this design supports all simulated gating methods. The pressures in front of the HHG cell, p_A , after the cell, p_C and in the VMI chamber, p_F , are much lower than required.

However, the solution is not technically exaggerated with respect to the requirements. The next column of Tab. 3.2 uses diameters and a HHG pressure that are larger by a factor of 2. p_A is only a factor of 4 beneath the maximum and the pressure in the VMI chamber is too high by factor of 7.

In both cases the pressure p_C still seems safe regarding XUV reabsorption but the choice of commercially available vacuum pumps in this pressure regime is limited. A few Pa are too low for rough pumps to operate effectively and too high for high vacuum pump operation. The chosen solution is to compose a pumping block of an adapter from 100 to 160 mm nominal tube diameter and a turbomolecular pump. The limited

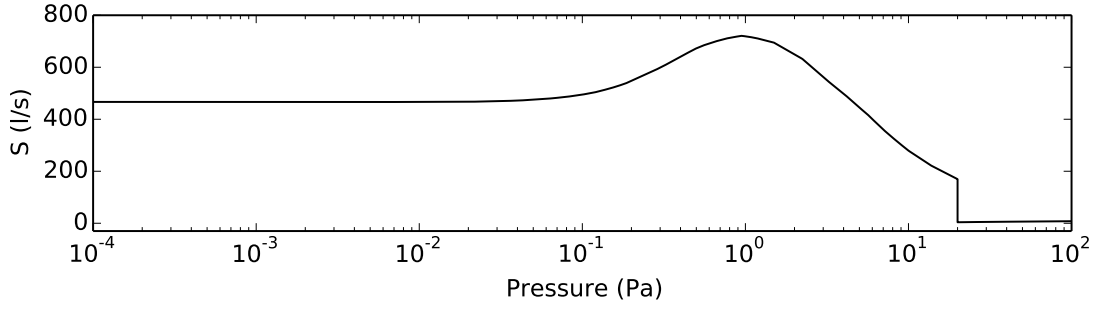


Figure 3.6: Vendor specified pumping speed as a function of high vacuum pressure for the used Leybold MAG W 600 iP (Pump B and C) in connection with its tube diameter reduction and protective mesh

conductance of the adapter reduces the pressure at the inlet of the actual pump. Fig. 3.6 shows that it provides adequate pumping unless the pressure is higher than a few Pa. The graph also shows an instantaneous drop in pumping speed at 20 Pa, which reflects the end of the operation range because of gas friction based heating of the pump. All turbomolecular pumps use water cooling to reduce this effect.

The lower part of the table shows the pressure on the high vacuum side of the pumps. As discussed, pump B and C are close to the highest pressure feasible for operation. All other pumps are safe.

The last column of Tab. 3.2 shows the result of the same calculation but for the manufactured part's hole diameters and 2000 Pa of N_2 in the HHG cell. To validate the model p_E was measured. After 6 h of operation it was 4.0×10^{-5} Pa without gas inlet and increased to 5.8×10^{-5} Pa if the N_2 supply was opened. The calculation does not take the desorption of gas from the surfaces or leakage into account. However, it predicts the effect of the flow from the HHG cell to be 7.2×10^{-6} Pa. The measured difference is 2 times higher, 1.8×10^{-5} Pa. The error is acceptable as the calculation is very simple and the position is far from the HHG cell with a defined pressure. The base pressure and the difference indicate the need for a surplus in pumping capacity.

3.3 XUV-IR Station

This end station uses the driving IR and the generated XUV pulses. Using the spatial separation concept from Sec. 3.1 the pulses are separated, delayed and focused into a spectrometer. Fig. 3.7 illustrates the setup and the section describes it. As the driving IR of the HHG is reused, the section assumes ionization gating. The additional structures in the IR in all other cases elongate the pulse and can influence an experiment.

Filtering The pulses arriving from the HHG are spatially separated: The IR forms a donut mode with the XUV in its center (Sec. 3.1). In order to remove the IR from the XUV beam completely a metal filter is mounted on a 0.15 mm thick cover glass or on

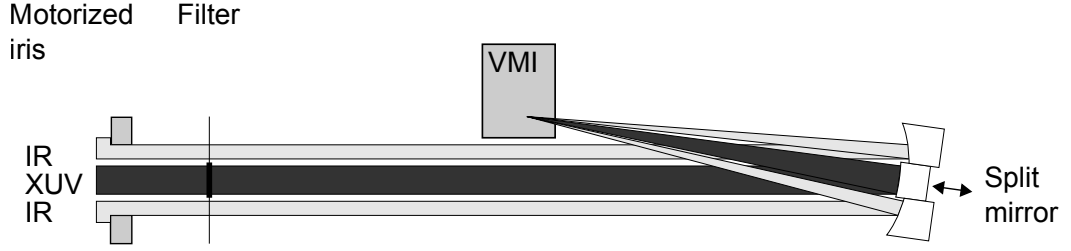


Figure 3.7: XUV-IR station: The metal filter removes the IR from the XUV pulse after a motorized iris reduces the IR intensity. The pulses are then delayed with respect to each other and focused into the interaction region of the schematically depicted VMI.

7.5 μm thick Kapton wires so that the inner part is cleaned from IR but the outer IR can pass. Before the filter, a motorized aperture removes the energy from the IR.

Optical Delay Unit The commercial optical delay unit is designed to mount two concentric on-axis focusing mirrors. The outer annular mirror focuses the IR over 13 cm into the interaction zone of a velocity map imaging spectrometer (VMI). The XUV is focused to the same position by a round mirror set into the center of the IR mirror. These two mirrors are moved by pico-motors, which control the focusing angles as well as the time delay between both pulses, which can be up to 300 fs with a resolution of 3 as.

The maximum delay shifts the focal position by 90 μm in the propagation direction. However, the IR's focus is much longer: Using the NOPCPA beam diameter of 8 mm, the focal length and the position of the mirrors ≈ 2.5 m after the HHG cell the Rayleigh length, b , can be calculated to be 5 mm (Eq. (2.9), (2.10)). Therefore, the shift can be neglected.

Intensity Estimation The theoretical optimization in Sec. 2.4.2 returns an IR and XUV pulse (Fig. 2.18) at the end of the HHG cell for ionization gating. The reflectivity of the mirrors in the optical delay unit and sizes of the focuses are used to rescale the pulse intensities and predict an intensity in the interaction region.

Condensed matter typically has a reflectivity in the XUV below 1×10^{-4} for normal incidence [87]. Exceptions are specially designed multilayer mirrors, which need to be specially designed for each HHG spectrum. The design of multilayer mirrors is still challenging. Bandwidth, added chirp and maximum reflectance must be optimized [88]. The spectrum of the theoretical XUV pulse from ionization gating ranges from harmonic number 28 to 34 (Fig. 2.15). As a rough measure for possible reflectivity the value of 12% for the mirror XUV41BW17 from Ultrafast-Innovations GmbH is taken, because of its bandwidth.

The size of the XUV mirror is assessed from the divergence for the 137 mm long HHG

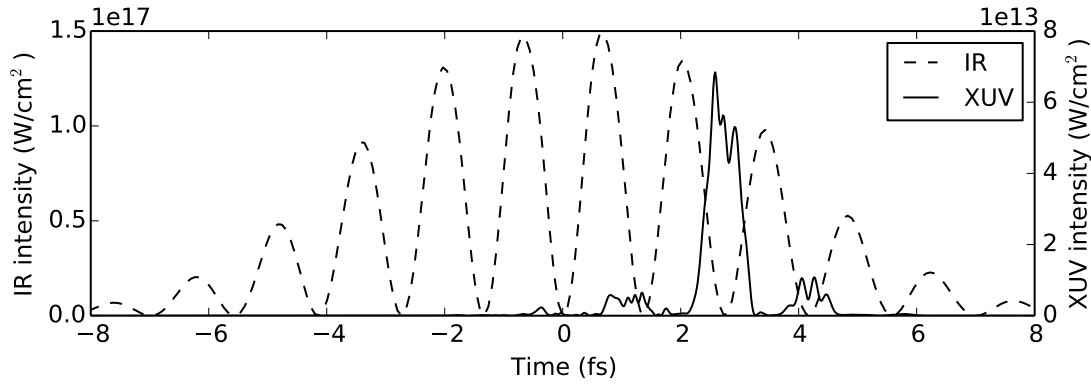


Figure 3.8: XUV and IR intensity as a function of time: Pulses from the theoretical ionization gating (Sec. 2.4.2) at the end of the medium are taken and rescaled for the calculated focal size and loss at the XUV multilayer mirror.

gas cell from Midorikawa et al. [42], 0.7 mrad, the HHG cell-mirror distance of 2.5 m and the mean wavelength of the XUV pulse (harmonic 31, Fig. 2.15). Eq. (2.10) then returns a beam waist of $0.65 \mu\text{m}$. The same formula gives an IR beam waist of $35 \mu\text{m}$. The IR mirror's reflectivity is assumed to be one.

Fig. 3.8, the result of the rescaling, shows the peak XUV and IR intensities to be $7 \times 10^{13} \text{ W/cm}^2$ and $1.5 \times 10^{17} \text{ W/cm}^2$, respectively. Both intensities are the result of a large setup. Consequently, there are many sources for deviations:

- The HHG simulation is semiquantitative and the predicted efficiencies lower than the literature references. Furthermore, it bases upon assumed NOPCPA output specifications.
- The focus is smaller if the beam at the mirror is larger. This can be achieved by a larger distance between HHG cell and mirror.
- The focal size is calculated from the Gaussian beam. Beam distortions increase the size.
- The loss of energy by forming the donut mode of the IR is not included in the calculation but will reduce the intensity.

Velocity Map Imaging The actual experiment takes place in a VMI [89]. This paragraph summarizes its principles as introduced by Eppink and Parker [90]. The device uses an inhomogeneous field from three annular plates: The repeller, extractor and ground electrode. By adjustment of the relative voltages at repeller and extractor the field shape can focus charged particles from an interaction zone to the micro channel plate (MCP). The amplified electrons are observed using an acceleration field, a phosphorus screen and a CCD camera. The position is almost independent of the position of creation and the

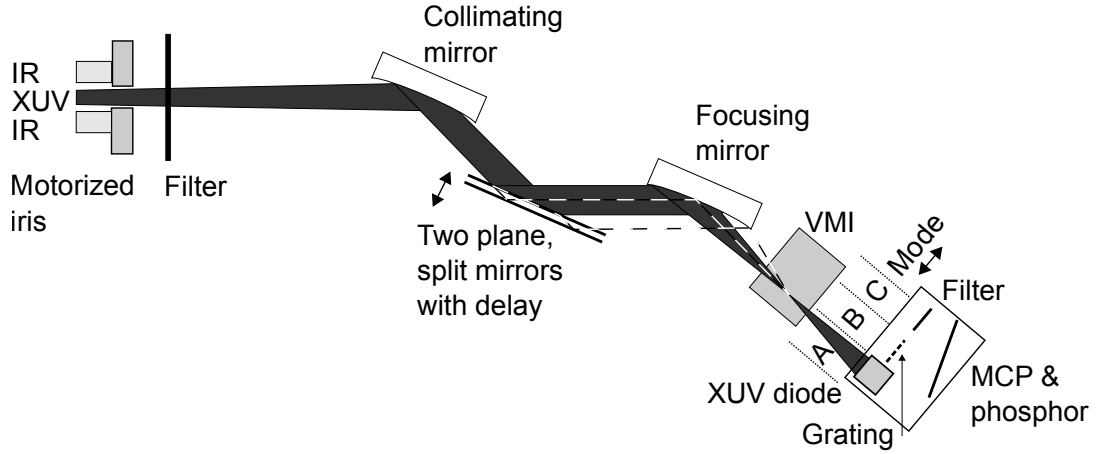


Figure 3.9: Summary of the setup for the XUV-XUV station: The section goes through all details of the image. The dashed lines show the shape of the second XUV pulse.

initial momentum is 'pancaked' along the extraction field. If the velocity distribution of the investigated process is symmetric with respect to an axis perpendicular to the extraction field, the entire 3d velocity distribution can be reconstruction by an inverse Abel transformation [91]. The energy distribution of the particles can be calculated from the result. Alternatively, the same setup is a TOF spectrometer when grounding the extractor electrode. The VMI is linked to the setup only by an ISO-CF 250 flange and can therefore easily be replaced to vary gas source, maximum detectable energy and resolution. The advantage of the current VMI [92] is the integration of the gas source in the repeller, which maximizes the possible gas density in the interaction zone.

3.4 XUV-XUV Station

Alternatively, the XUV and IR pulses can be co-propagated towards the XUV-XUV station, which discards the IR pulse, splits the XUV pulse into two and focuses them into another VMI. Advanced data processing is enabled by the option to record XUV characterization data and VMI images for each laser shot. The steps are described in the following paragraphs and are depicted in Fig. 3.9.

Filtering The first step is to remove the majority of IR with the motorized iris. As the IR is only in the outer parts simple blocking is possible. Metal filters (Sec. 3.1) remove any remaining IR.

XUV Optics Another strategy to circumvent the low reflectance for normal incidence in the XUV regime is using optics in grazing incidence. Fig. 3.10 shows the energy dependence for different grazing incidence angles of B_4C , a material widely used for its

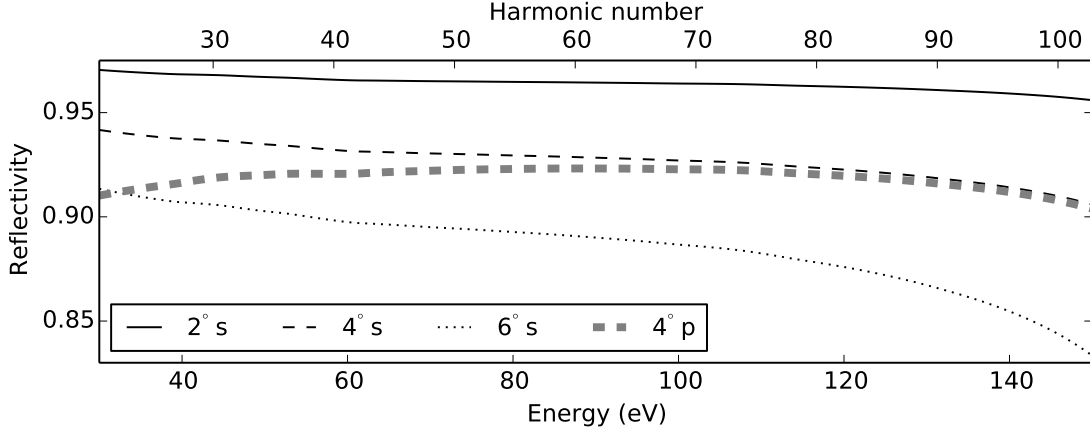


Figure 3.10: Spectral reflectivity of B_4C in s or p-polarization and different grazing incidence angles as a function of photon energy [73]

high reflectance [93]. The smaller the angle is, the higher the reflectivity becomes. On the other hand smaller angle also require larger surfaces for the same beam diameter. Using the 0.7 mrad beam divergence from p. 87, the distance from the HHG cell to the collimation mirror of 3 m and the $3w$ criterion from Eq. (3.7) for the diameter containing 99 % of the energy, the necessary lengths of the mirrors for each angle can be calculated to be 18, 9 or 6 cm for 2, 4 and 6°, respectively. A grazing incidence angle of 4° is chosen as a compromise. s-polarization offers more reflectivity than p-polarization. Consequently, the HHG has to produce vertical polarization and the VMI must be oriented to have a MCP with a vertical surface.

Due to the size of the VMI the focal length is chosen to be 30 cm. Reusing the beam size at the collimation mirror and harmonic 31's wavelength from the previous section, Eq. (2.10) returns a focal beam waist of $1.2 \mu\text{m}$ and a Rayleigh length for the XUV of $180 \mu\text{m}$. $180 \mu\text{m}$ corresponds to a delay of only 600 fs. As the limitation to much smaller delays is not adequate, the moving of the foci is avoided by collimation:

A first toroidal mirror collimates the beam. The mirror has $-86\,020 \text{ mm}$ and -418 mm radii of curvature in the tangential and sagittal plane. The focal length is 3 m. Two plane mirrors, which can be moved independently, split XUV pulse into two delayed pulses. They are as close as possible to each other to minimize the loss of XUV. The last toroidal mirror focuses both pulses over 30 cm into the interaction region of a VMI. The radii of curvature are -8680 mm and -41.97 mm^2 .

Each mirror is mounted on a five axis stage. To enhance the interferometric stability of the two XUV pulses vibrations of the plane mirrors with respect to each other are reduced: The turbo pump of the chamber is not attached directly but via vibration damping. The optical breadboard is decoupled via spacers from the chamber. A heavy

²The relation of radii of curvature for a focal size of 3 m and 30 cm do not follow the simple expectation of the a factor of exactly 10 because they were optimized by the manufacturer.

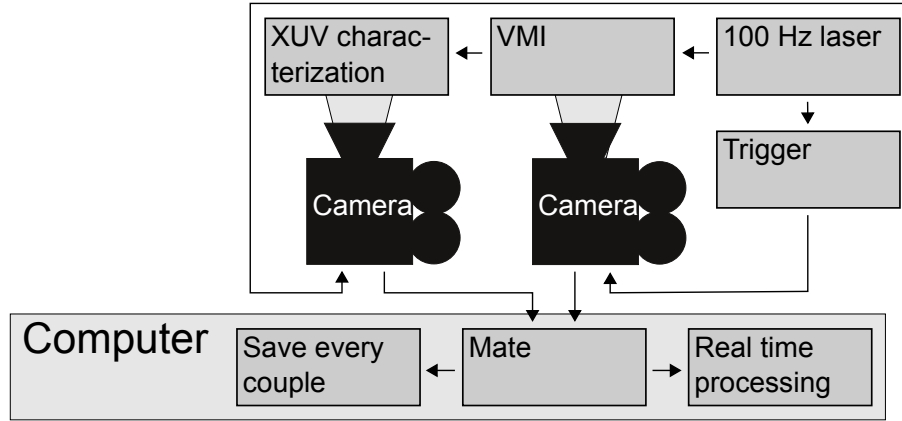


Figure 3.11: Camera setup for synchronized single shot recording of VMI and XUV characterization images: Laser shots at 100 Hz trigger the cameras that record VMI and XUV characterization. Both images are mated in a computer that can save any image or average subsets of them.

metal block is bolted to the bread board and holds a combined optomechanical component mounting both plane XUV mirrors. During his internship Iason Katechis built and described an interferometric setup that confirmed the stability to a level of 30 as over short durations. The maximum XUV-XUV delay is 80 fs.

XUV Characterization The XUV characterization unit (Fig. 3.9) has three modes of operation and bases upon the design from Kornilov et al. [94]. Mode A measures the XUV pulse energy by a calibrated XUV diode. Mode B represents a spectrometer consisting of a 100 nm transmission grating, a camera, a MCP and a phosphorus screen. Mode C attenuates the beam with a filter before it images its spatial properties with the MCP.

Data Acquisition The VMI and gas source are linked only via ISO-CF 160 flanges to easily adapt them to future experimental conditions. The advantage of the current implementation is the presence of a gas source with a supersonic expansion, which cools the gas particles to allow e.g. cluster formation or reduce the internal energy of the particles.

More sophisticated data processing techniques are possible due to the ability of recording synchronized camera images from the VMI and the XUV characterization unit. To this end a computer with a camera for the XUV VMI and for the XUV characterization unit is set up and a program was written within the thesis to synchronize both sources. It is tested to write both images at the full repetition rate of 100 Hz to hard disk. Additionally, real time processing of the images is possible. For example, in case the stability is insufficient for a specific task and an algorithm is known that can select adequate laser shots, the corresponding VMI pictures can be averaged immediately to guide the adjustments. Fig. 3.11 illustrates this concept.

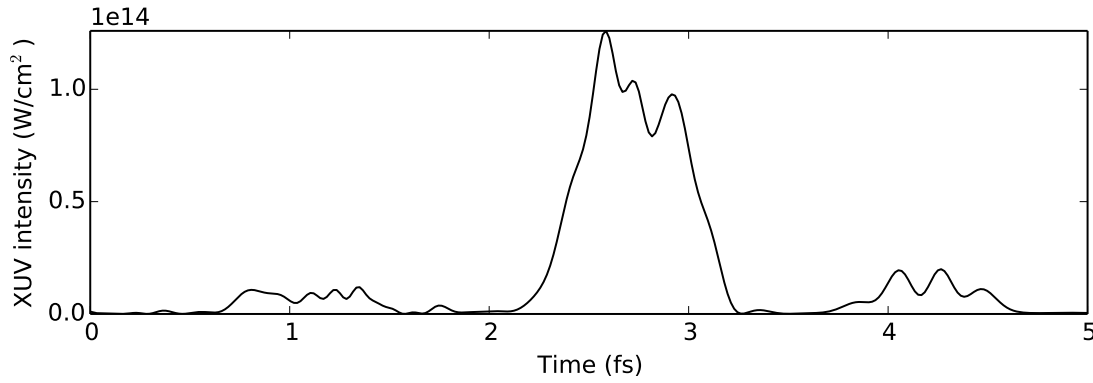


Figure 3.12: XUV intensity as a function of time: Pulses from theoretical ionization gating (Sec. 2.4.2) at the end of the medium are rescaled for the calculated focal size and loss at the three reflections at B₄C mirrors.

Intensity Estimation Finally, the calculated XUV focus size is used to predict an intensity under the assumption of the theoretical intensity from Sec. 2.4.2, the numerical optimization for ionization gating. It is shown in Fig. 3.12 to have a maximum of $1.3 \times 10^{14} \text{ W/cm}^2$. The splitting is not accounted for so that the value reflects the situation without delay. As for the XUV-IR station, the number may deviate:

- An additional uncertainty is the loss of XUV in the region between the plane B₄C mirrors intended for splitting.
- As the end station discards the IR, all gating methods become available. Other methods result in different XUV energies and longer HHG media, which result in lower divergence and large foci in the interaction zone unless the distance between HHG cell and collimation mirror is adapted.

3.5 Summary

The last part of the experimental setup provides the radiation and instruments to conduct pump-probe experiments with intense and short XUV radiation.

To this end, using the results from the theoretical optimization of HHG in Chap. 2 a flexible design is introduced, which covers a strategy to spatially separate the driving IR radiation from the generated XUV by a donut mode in the IR beam and rather technical aspects of the process. The most important solutions are an elaborated, experimentally tested vacuum design to prevent XUV reabsorption, IR beam degradation via the self-focusing instability and a too high pressure in the VMI. The solution enables all simulated gating techniques, which allows to test and compare them experimentally. Alternatively, running hybrid DOG is calculated to yield the highest conversion efficiency.

3 High Harmonic Generation Setup, End Stations

The end stations allows XUV-IR pump-probe experiments in the interaction region of one VMI with a maximum delay of 300 fs. The XUV-XUV station uses another VMI and can observe the pulses through an XUV spectrometer, spatial profiler or measure its energy through a diode. A computer is tested to record synchronized VMI images and XUV characterization data at up to 100 Hz. The XUV intensity of $1 \times 10^{14} \text{ W/cm}^2$ of both setups is about as high as the $1 \times 10^{13} \text{ W/cm}^2$ to $1 \times 10^{14} \text{ W/cm}^2$ successfully used by Tzallas et al. [17] for an autocorrelation with XUV. The maximum delay is 80 fs.

4 Multiphoton Sequential XUV Double Ionization of Argon

4.1 Introduction

This thesis paves the way to as-as XUV-XUV pump-probe-experiments, which are demanding in terms of intensity and pulse duration. High intensities in the XUV alone are interesting even without short pulse durations. The attention is related to the development of ultrashort XUV/X-ray free electron lasers (FELs) in the last decades [95, 96]. FELs produce intense and ultrashort XUV/X-ray pulses. Neutze et al. [97] suggest to use ultrashort pulses to dramatically reduce damage to biological samples and to create a powerful device for diffractive imaging. For the successful development of these methods, it is essential to be able to observe and understand changes of the electronic structure while the sample is illuminated by the FEL pulses. Therefore, it is important to unravel the multi-photon, multi-electron ionization dynamics of model systems in XUV/X-ray laser fields.

Without covering all fields a few example should be given to illustrate the width of systems where multi-photon, multi-electron ionization dynamics occur: Clusters are one interesting model system. They show a complex ionization scheme: Atoms in a cluster are ionized. The escaping electrons create a potential that reduces further ionization. Schütte et al. [98] used the setup described in this chapter to measure energy-resolved photoelectron yields at different cluster sizes and XUV intensities. Their results suggest the excitation of Rydberg states in the plasma. Noble gas atoms provide a well-studied and fundamental model system. Therein, single-electron multi-photon ionization via intermediate states was observed by Hikosaka et al. [99]. The authors analyzed the electron energy resolved photoelectron yield of Ar for different pulse wavelengths to unravel multiple ionization pathways. The studies take advantage of power laws. For example the energy of electrons stemming from autoionization is constant. In contrast, Heissler et al. [100] observed single-electron two-photon ionization without intermediate states. The second ionization of Ar required two of their XUV photons. At intensities of at least $5 \times 10^{11} \text{ W/cm}^2$ the corresponding photoelectrons were measured. Their overall yield was proportional to the approximately second power of the XUV energy, which also indicated a two-photon process. The authors suggested to use this nonlinearity for pulse characterization. Xenakis et al. [101] also investigated a power law using the third harmonic of 248.6 nm light at 15 eV. They used one photon to excite a state in Ar which was then ionized by a further photon. As the third harmonic's energy depends on laser power to the power of three, they expected a power of 6 in laser energy. Their yield was proportional to the third power of the fundamental laser energy because the first step

was saturated, effectively resulting in a single photon process.

Nonlinearities are not limited to simple power laws. Rabi oscillations add a further effect: Stimulated emission. The Rabi oscillation is a general effect and occurs in quantum mechanical two-level systems that are driven by an oscillatory field. Photons are periodically absorbed and emitted so that the system oscillates between both states. The phenomenon is formulated for a general system and the original publication by Rabi [102] covers a general system in a rotating magnetic field. Rabi oscillations are of a fundamental nature in physics and are therefore present in many fields.

Examples include research in quantum computing such as Li et al. [103]. They investigated quantum dots with few states and demonstrated a quantum gate with a quantum dot that contains two electron-hole pairs that exhibited Rabi-like oscillations. They proposed its usage for information processing. Experiments closer to the scope of the thesis were conducted too. Vasa et al. [104] used 700 nm-700 nm pump-probe and found Rabi oscillations in surface plasmons.

Rabi oscillations were not time resolved in the XUV so far. Sato et al. [105] measured the intensity dependence of the two-photon ionization in He at a free electron laser facility. The power law contradicted the lowest-order perturbation theory. Sako et al. [106] identified Rabi oscillations as the reason for the deviation.

Further theoretical studies confirmed promising research opportunities within the XUV regime: Gaarde et al. [107] studied transient absorption and reshaping of XUV pulses in He, which were dressed by a moderately strong IR field. Their cross section was reduced by Rabi oscillations between 2s and 2p states driven by the IR as it periodically removes population from the states responsible for the absorption. Kaiser et al. [108] modeled two states resonantly coupled by an XUV field and a high intensity photo-ionization of one of these states. The resonant coupling lead to Rabi oscillations that changed the relation of XUV intensity and ionization probability, because the state coupled to the continuum has varying populations. Additionally, the model predicts a shift of the Rabi frequency originating in the ionization.

In summary, Rabi oscillations are abundant in a wide range of problems but there is only one, indirect measurement in the XUV range. The aim of this chapter is to add a more direct observation of Rabi oscillations in the XUV to the knowledge about this fundamental phenomenon.

Next, the experimental setup is briefly described (Sec. 4.2). The measured data of pump-probe XUV-IR experiments in Ar reveal the delay dependent presence of Ar^{1+} , Ar^{2+} and electrons. The main ionization process and the relevant states are identified in Sec. 4.3. The following Sec. 4.4 develops a deeper understanding based upon a quantum mechanical model to reproduces non-trivial features in the delay dependences. Sec. 4.5 critically reviews the model. Sec. 4.6 summarizes the chapter.

The measurement were conducted together with Judith Dura, who also participated in discussions on the analysis of the data. The other parts base upon the work of the author. The paper mentioned in the list of publications (page 157) as item no. 2 represents a short version of this chapter.

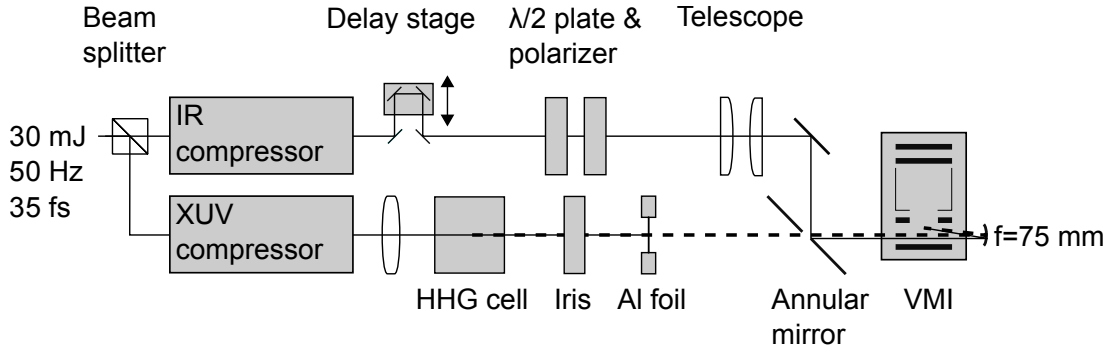


Figure 4.1: Experimental setup: The setup consists of an pump (lower) and probe (upper) arm fed by the same laser. XUV is generated via HHG and the IR is filtered out. The IR in the probe arm is delayed and its intensity attenuated. Both arms are reunited by an annular mirror before being focused into the VMI.

4.2 Experimental Setup

For the experiment a fs laser system, a HHG system and a VMI end station located at the Max-Born-Institute, Berlin were used. This section is dedicated to describe the experimental setup (Fig. 4.1).

A Ti:sapphire laser amplifier delivered pulses centered at 790 nm with 35 fs (FWHM) pulse duration and 35 mJ pulse energy at 50 Hz repetition rate. The output was split into two beams. 90 % of the energy was compressed and loosely focused over 5 m into a 15 cm long HHG cell, which was statically filled with Xe at a pressure of 1.3 mbar. The IR and resulting XUV collinearly propagated until the point where an iris and a 100 nm thick Al foil filtered the IR out. The XUV passed an annular mirror with an open diameter of 6 mm and was focused by a boron carbide coated, on-axis mirror into the interaction region of a VMI over 75 mm. The target was an Ar gas beam formed by expanding 1 bar of Ar into vacuum through a nozzle with a diameter of 500 μm . The other arm of the initial IR received 10 % of the pulse energy. The beam was compressed, sent through a delay stage and attenuated using a $\lambda/2$ plate and a polarizer. After passing a telescope the IR is recombined with the XUV pulse by the annular mirror. In the experiment, the XUV was used as pump pulse and the IR as probe pulse.

The resulting experimental conditions were:

XUV The XUV spectrum in the interaction region consisted of the harmonics 11, 13, 15 and 17 of the 790 nm fundamental pulse. Fig. 4.2 shows a typical photoelectron spectrum of Ar atoms (ionization potential: 15.76 eV) ionized by XUV together with the respective photoionization cross section. The positions of the harmonics were used to calibrate the energy scale, where the energy of a harmonic h was $1.57 \text{ eV} \cdot h$. Their relative intensity could be evaluated by observing how many electrons they generated

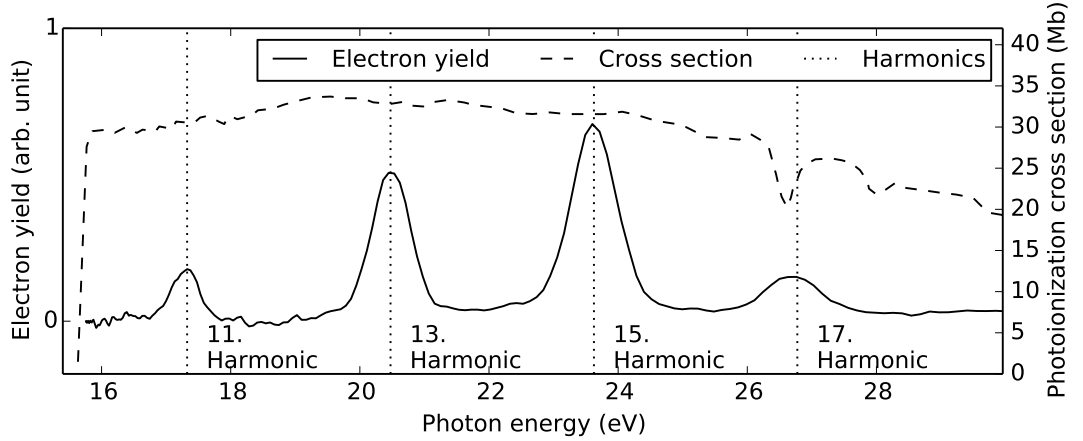


Figure 4.2: Photoionization cross section for the first ionization of Ar [109] (dashed line) and electron yield as a function of photon energy (solid line): Dotted lines mark the center of the harmonics. Harmonic 17's position is slightly off because of imaging aberrations.

by ionization of Ar atoms at a given cross section. In recent experiments, about 10 nJ of XUV were available and a focus intensity of $2 \times 10^{12} \text{ W/cm}^2$ [110]. XUV pulse durations were estimated to be $(20 \pm 3) \text{ fs}$ [111] and the focal size was $3 \mu\text{m}$ [98].

IR The IR intensity was up to $1 \times 10^{14} \text{ W/cm}^2$ and could be selected by the angle of the $\lambda/2$ plate in front of the polarizer in the IR arm. The relation between the angle of the $\lambda/2$ plate and the transmission was calibrated using a power meter and used to access the relative IR intensities in the chapter. The IR focus measured about $10 \mu\text{m}$ in diameter.

The IR pulse duration could be estimated by a so-called sideband scan [112]. When the harmonics of the IR ionize an atom, an additional, temporally overlapping IR pulse can shift the energy of the resulting photoelectrons. The HHG spectrum only contains odd harmonics. The additional photon changes the energy of the original photoelectrons by the energy of one IR photon. Thus the electron yield for energies corresponding to odd harmonics drops and contributions at energies corresponding to even harmonics appear. Fig. 4.3a shows this delay-dependent redistribution. As the energy shift requires the presence of one photon of each pulse, the yield reduction of the harmonics and the yield between the harmonics is proportional to the cross-correlation of both pulses [112].

It was assumed that both pulses have a Gaussian dependence on time. The cross-correlation is then a Gaussian function with the FWHM $\tau_{FWHM,cc}$, which was fitted to the data. The FWHMs fulfill

$$\tau_{FWHM,cc}^2 = \tau_{FWHM,IR}^2 + \tau_{FWHM,XUV}^2. \quad (4.1)$$

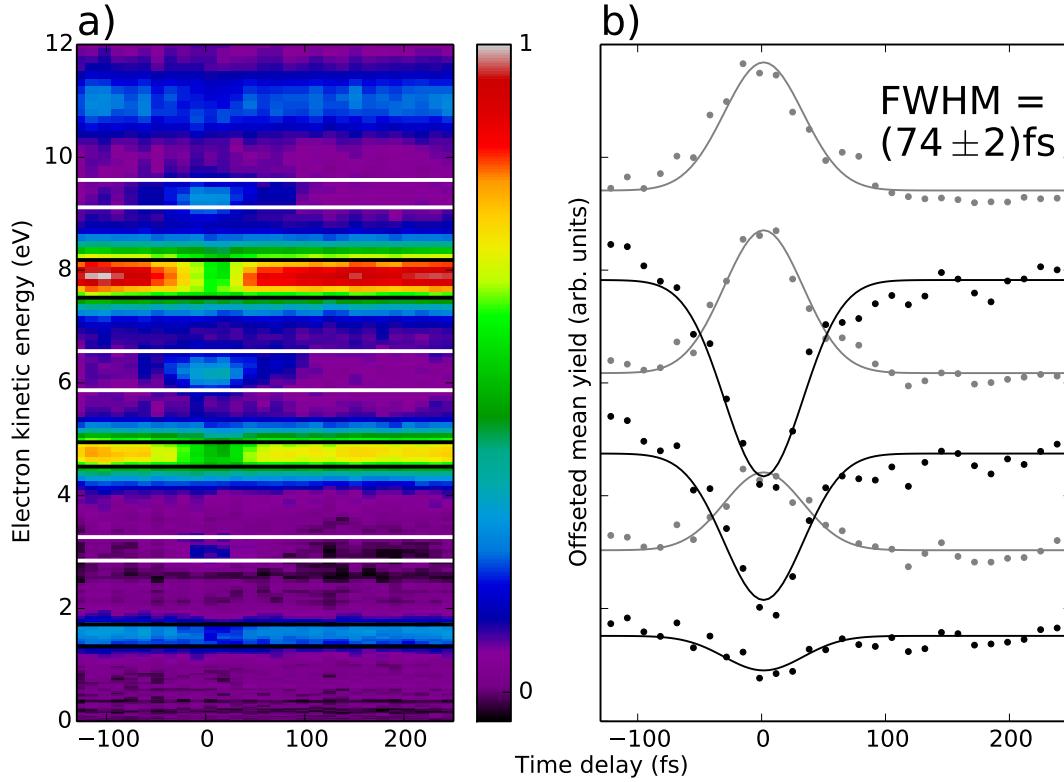


Figure 4.3: Sideband scan (see text for details): a) shows the electron yield as a function of electron energy and delay. Black (white) horizontal lines mark odd (even) harmonics. b) The dots show the average over the energy interval marked in a). They are offset to match the height to the a) side and fitted by Gaussian functions with a common FWHM duration.

Fig. 4.3b presents a Gaussian fit to the averaged electron yields of these features. Using the fitted $\tau_{FWHM,cc}$ and $\tau_{FWHM,XUV} = (20 \pm 3)$ fs Eq. (4.1) predicts an IR duration of (71 ± 3) fs, which is much more than expected from the previous 35 fs pulse duration of the Ti:sapphire amplifier. Optical elements in the probe arm are unlikely to cause the elongation as an independent IR compressor is available. Therefore, the reason for the discrepancy is unknown. The center time was used to define the temporal overlap of the XUV and IR pulse as 0 fs. The fit returns an error of 2 fs for time zero.

4.3 Experimental Results

4.3.1 Time of Flight and Velocity Map Imaging Experiments

This section describes measurements, while the analysis is shown in Sec. 4.3.2.

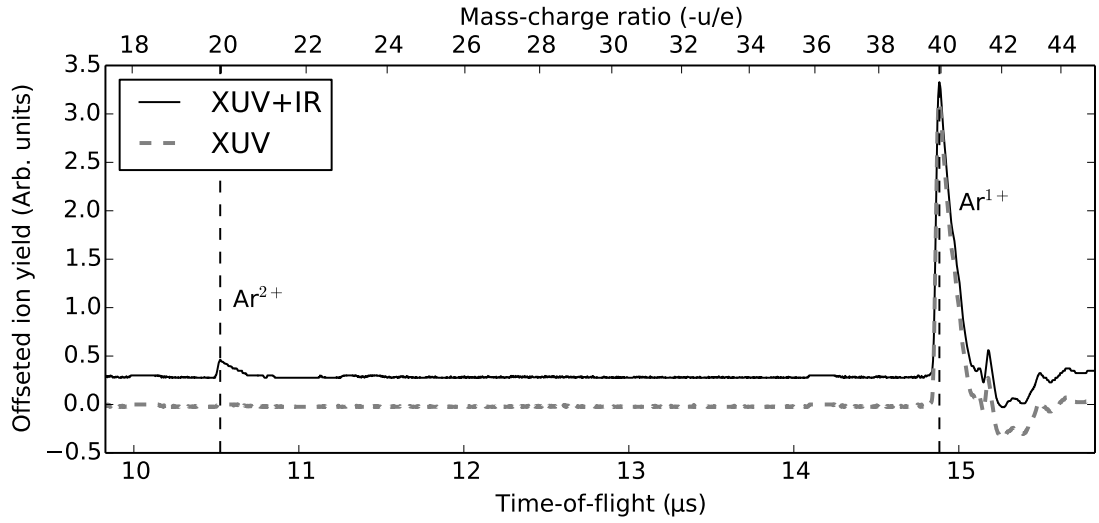


Figure 4.4: Example of the time-of-flight dependence of the ion yield in TOF mode for XUV only and a combination of XUV and IR at a delay of about 800 fs. The abscissae are calibrated using the peaks for Ar^{1+} and Ar^{2+} .

The influence of IR and XUV was investigated using the setup described in Sec. 4.2 with an atomic jet of Ar as target. For this chapter the intensity of the IR was chosen so low that no ionization was detected from IR alone. Fig. 4.4 shows an example of the TOF ion yield measurements. XUV alone resulted in a peak (with electronic ringing) identified as Ar^{1+} . Additional IR lead to a small peak related to Ar^{2+} .

In the course of the chapter only the total amount of both ions is analyzed. It equals the integral over the respective peak and is typically averaged over 256 laser shots.

Fig. 4.5 shows the Ar^{2+} yield as a function of delay between XUV and IR for 6 representative of 16 measured IR intensities. If the IR arrived before the XUV, the Ar^{2+} yield equaled the XUV-only yield. In case the IR arrived after the XUV, the maximum amount of Ar^{2+} was generated. The Ar^{2+} yield for delays with overlapping XUV and IR pulses was generally increasing but its dependence deviated from a simple step function. The difference can be described by a feature at overlap, which reduces the yield for high IR intensities, and a reduction at a delay of 50 fs, which is present for all IR intensities.

Fig. 4.5 uses the sum of a Boltzmann sigmoid

$$Y = B_{BS} + \frac{D_{BS}}{1 + \exp \frac{t_{BS} - t}{\tau_{BS}}} \quad (4.2)$$

and Gaussian functions as an eye guiding fit for this dependence. The Boltzmann sigmoid represents a step function starting from a base value B_{BS} . It increases by D_{BS} over a length given by the slope τ_{BS} . Its center is at t_{BS} .

To eliminate the possibility that the nonmonotonous behavior originated from laser fluctuations a scan with rising delays and a scan with falling delays was conducted

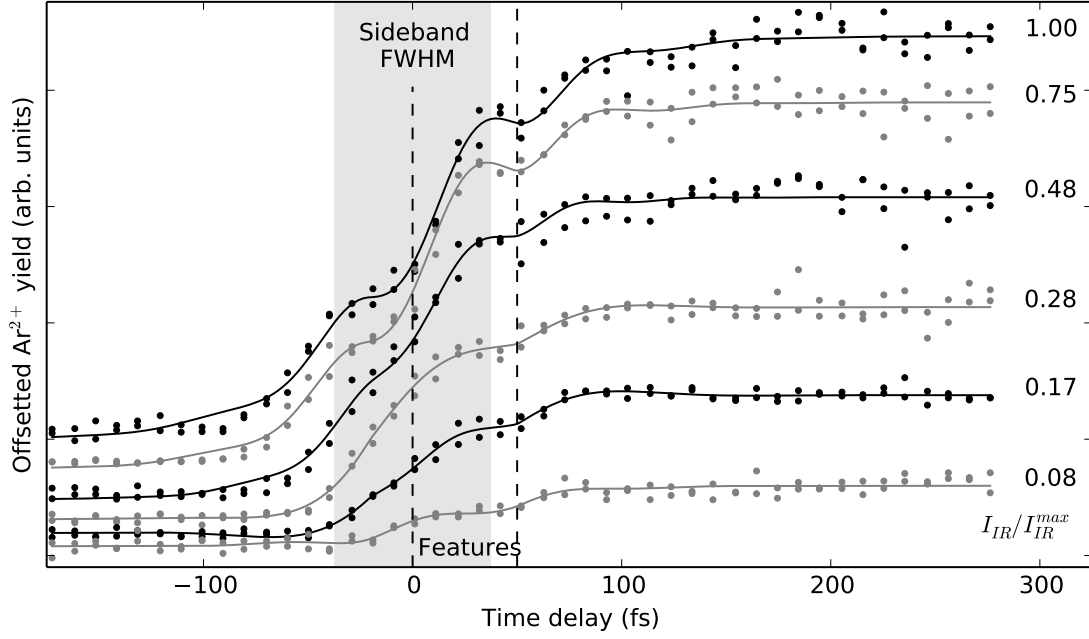


Figure 4.5: Experimental Ar^{2+} yield as a function of pump-probe time delay and calibrated, relative IR intensity $I_{\text{IR}}/I_{\text{IR}}^{\text{max}}$ (dots). The experimental data is fitted with a superposition (continuous lines) of a Boltzmann sigmoid (Eq. (4.2)) and two Gaussian functions. The FWHM of the sidebands (Fig. 4.3) is given (shadow area) as an indication of the temporal overlap of the XUV and IR pulses. Two features at 0 and 50 fs are marked by vertical dashed lines.

at every IR intensity. Additionally, the IR intensities were examined in a randomized order. Further measurements were necessary to understand the underlying process and the nonmonotonous behavior. They are described in the following.

Fig. 4.6 is similar to Fig. 4.5 but shows longer delays. The yield was fitted by an exponential decay with offsets

$$Y = A_k \exp \tau / \tau_{21} + B_k. \quad (4.3)$$

A single decay time of $\tau_{21} = (168 \pm 7)$ ps was applied to fit all IR intensities. Different heights A_k were necessary because the maximum Ar^{2+} yield depended on IR intensity k . The baselines B_k compensated changing baselines, which can originate from fluctuations in the laser leading to different XUV pulses.

Fig. 4.7 and 4.8 compare Ar^{1+} and Ar^{2+} yields as a function of delay. Under the given experimental conditions the yields can be directly compared¹. Fig. 4.7 shows

¹The extractor and repeller voltages were 0 keV and 6 keV. As the interaction zone was in the middle of both electrodes the kinetic energies of Ar^{1+} and Ar^{2+} were 3 and 6 keV respectively. Yagi et al. [113] found that for this regime the detection probability is almost the same for Ar^{1+} and Ar^{2+} . It was assumed that the MCP gain was constant.

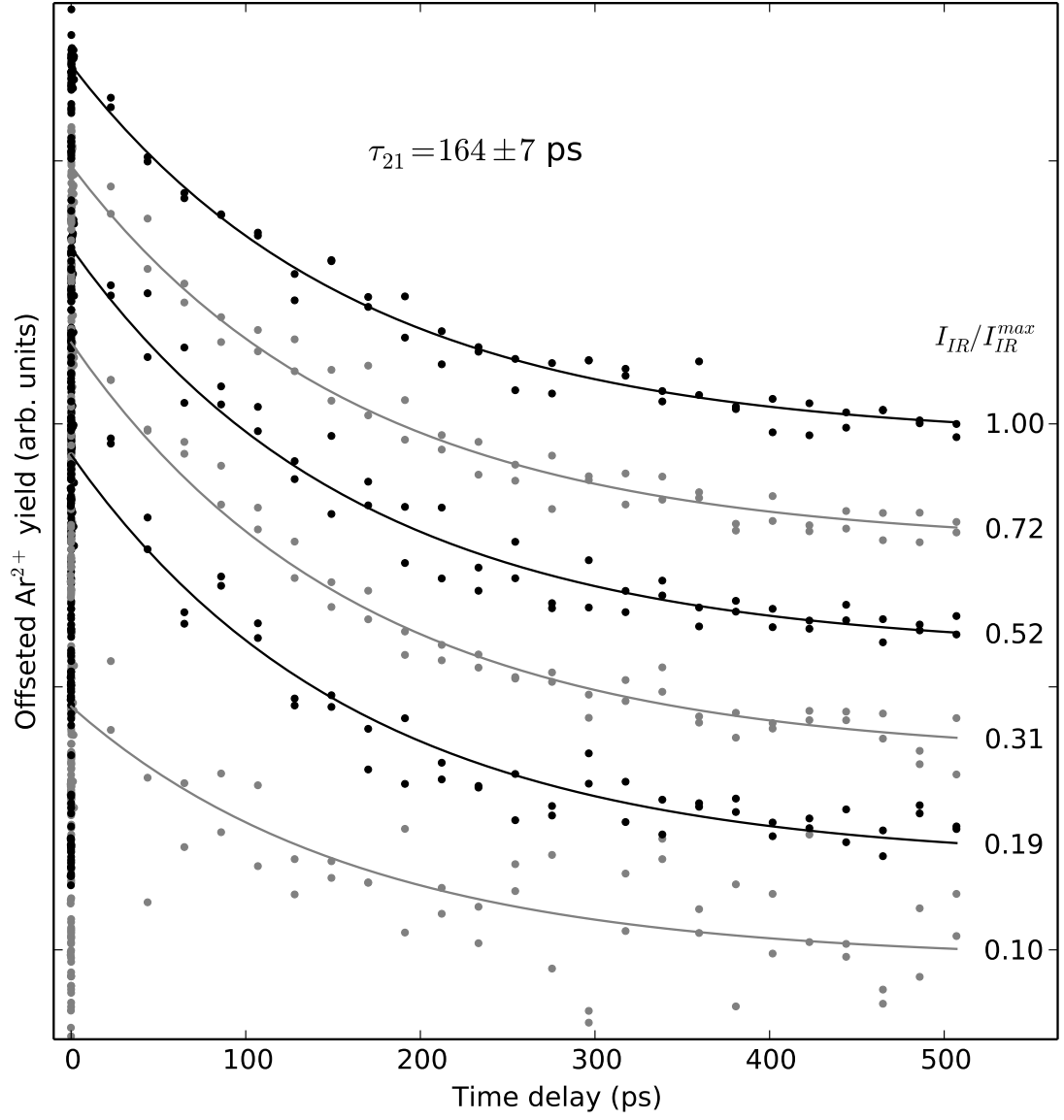


Figure 4.6: Ar²⁺ yield Y as a function of XUV-IR delay τ and IR intensity. The experimental data is normalized independently for each IR intensity. The exponential fit (4.3) uses a common decay time τ_{21} but its height A_k and baseline B_k are independent for each IR intensity.

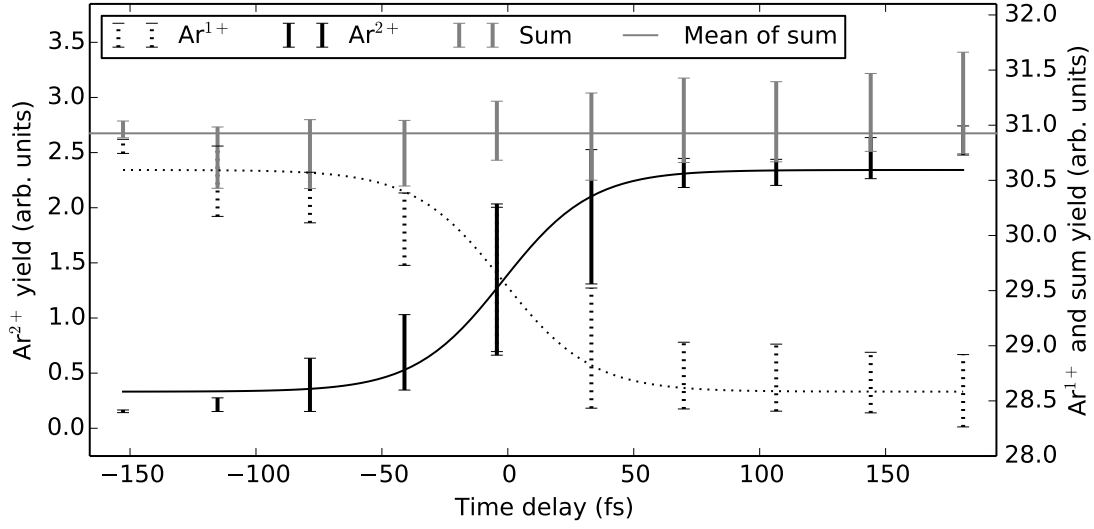


Figure 4.7: Ar^{2+} and Ar^{1+} yield as a function of delay for an IR intensity of $0.46 I_{IR}^{max}$. The error bars represent standard deviations from multiple measurements. The arb. units of both y-axes can be directly compared (see text). The fittings for Ar^{1+} and Ar^{2+} follow a Boltzmann sigmoid (Eq. (4.2)).

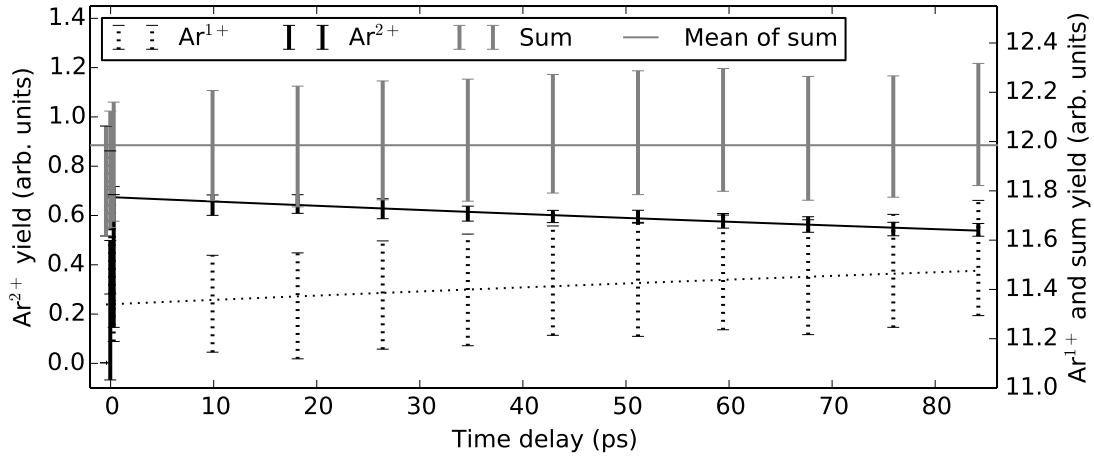


Figure 4.8: Ar^{2+} and Ar^{1+} yield as a function of delay for an IR intensity of $0.46 I_{IR}^{max}$. The error bars represent standard deviations from 9 measurements. The arb. units of both y-axes can be directly compared (see text). The fitting for Ar^{2+} is an exponential decay. The Ar^{1+} yield is fitted by using a single constant. The Ar^{1+} line is the difference of the Ar^{2+} fit and this constant.

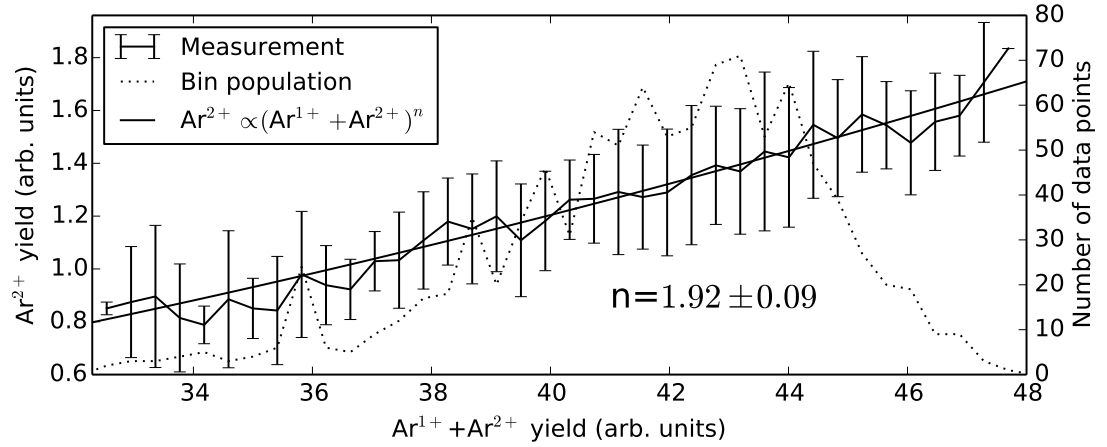


Figure 4.9: Ar^{2+} yield as a function of the sum of the Ar^{1+} and the Ar^{2+} yield: Ar^{1+} and Ar^{2+} were simultaneously measured for single laser shots. 1000 pairs were fitted by a power law using a least square algorithm. The points are grouped according to their yield of Ar^{1+} and Ar^{2+} . For each group, the number of contained points (dotted line), Ar^{2+} yield's mean and standard deviation (error bars) are plotted.

the Ar^{1+} and Ar^{2+} ion yield for short delays. The Ar^{1+} yield declined by 7 % between positive and negative delays. The Ar^{2+} yield rose by the same absolute amount. The plot also shows the sum of both yields to be constant within the error bars. Fig.4.8 is the counterpart of Fig. 4.7 for long delays: The Ar^{1+} yield rose for ps-delay. Again, the sum of the Ar^{1+} and Ar^{2+} yield was constant within error bars.

To find the number of XUV photons involved in the formation of Ar^{2+} the relation between the Ar^{2+} yield and XUV intensity was investigated within single laser shots. The laser and hence the XUV pulses were fluctuating over time resulting in different yields of both ions. The single shot Ar^{2+} yield was shown to be approximately quadratic in the sum yield of Ar^{1+} and Ar^{2+} (Fig. 4.9), which is proportional to the XUV intensity.

VMI measurements complemented the TOF measurements of this section. The VMI recorded a new contribution of electrons at kinetic energies from 0.53 eV to 0.96 eV (Fig. 4.10) when the IR was later than the XUV. At lower kinetic energies weaker contributions emerged at 0 and 0.13 eV (Fig. 4.10b). Their origin is unknown. Fig. 4.11 shows that the delay-dependence of the integrated electron yield from 0.53 to 0.96 eV reproduced the delay dependent Ar^{2+} yield from TOF measurements in shape and duration.

4.3.2 Ionization Mechanism

Using the measurements from Sec. 4.3.1 this section deduces the mechanism behind the ionization. Fig. 4.12 summarizes the resulting process.

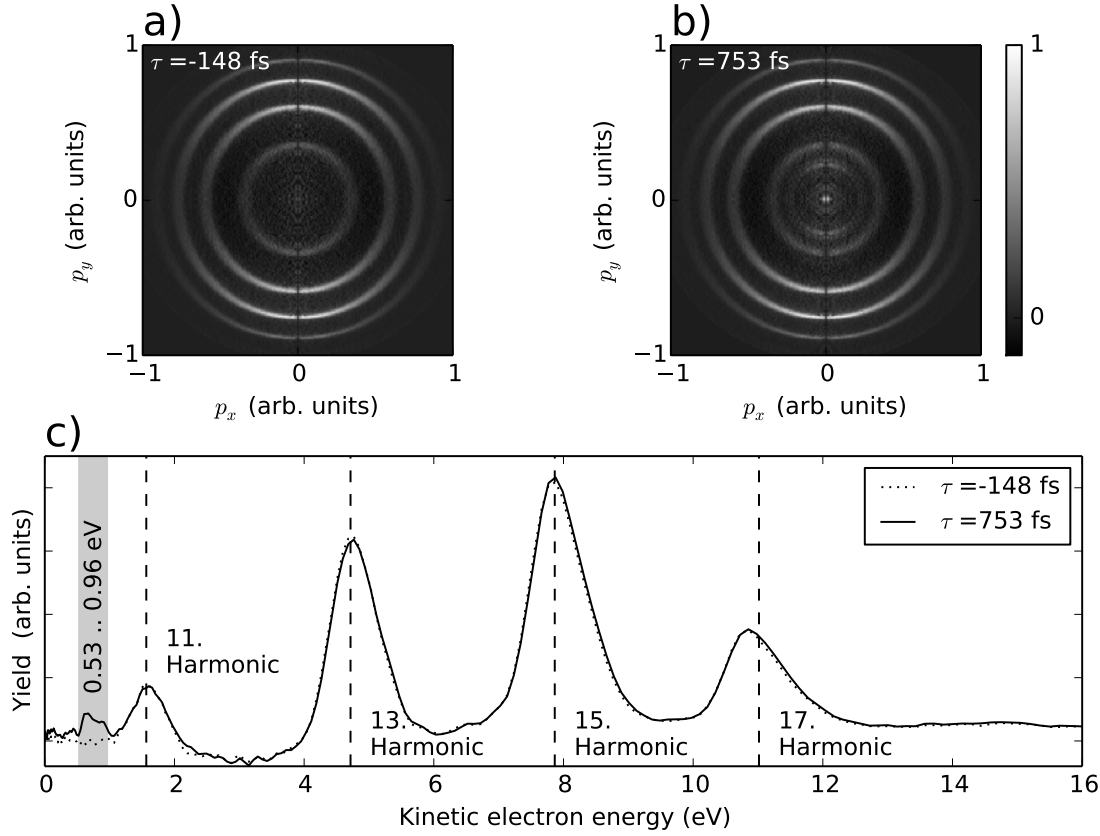


Figure 4.10: a) and b) Normalized 2d photoelectron momentum distributions for ionization of Ar atoms with XUV pump and IR probe at delays of (a) -148 fs and (b) 753 fs; c) Corresponding angle integrated photoelectron spectra

For each IR intensity the Ar^{2+} yield is largest when the IR pulse is coming after the XUV pulse. As the yield decreases again for delays on the ps time scale the XUV pulse must prepare a (set of) state(s) in Ar or Ar^{1+} that can be ionized to Ar^{2+} by the IR and decays otherwise. These states shall be referred to as Ar^{+*} . As the sum of Ar^{1+} and Ar^{2+} is constant for all delays the state decays to Ar^{1+} for ps delays. The identification of Ar^{+*} as a singly ionized state originates from considerations involving energies and the number of XUV and IR photons:

In order to quantify the influence of the IR intensity on the maximum yield of Ar^{2+} , Boltzmann sigmoids are fitted to a series of TOF Ar^{2+} yield measurement as in Fig. 4.7. Each element of the series was recorded at a different IR intensity. Fig. 4.13 shows the dependence of the rise D_{BS} on the IR intensity. It rises linearly for small IR intensities and saturates for larger IR intensities. The dependence of D_{BS} on the IR intensity can be modeled without insight into the influence of the XUV, because for large delays XUV prepares a finite Ar^{+*} population $|C_{\text{Ar}^{+*}}^\infty|^2$, which is independent from the properties of

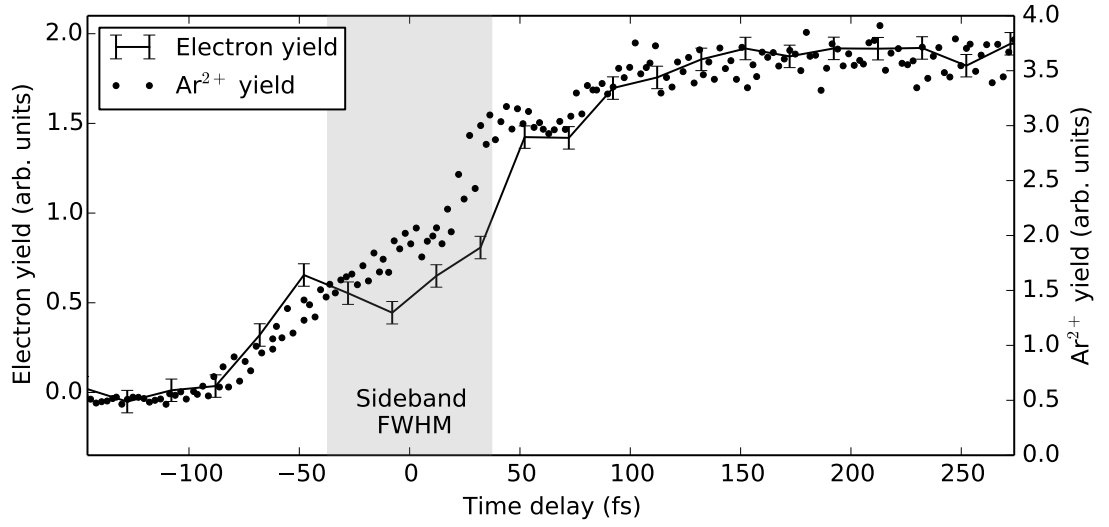


Figure 4.11: Averaged electron yield (solid) between the energies 0.53 eV to 0.96 eV of the VMI electron measurement and Ar^{2+} yield from TOF measurements (dots) as a function of delay. The error bars of the electron measurements show standard deviation and assume that the error is constant and the only source of fluctuations for large positive delays. As a measure for the interaction of XUV and IR the FWHM of the sidebands (Fig. 4.3) is given.

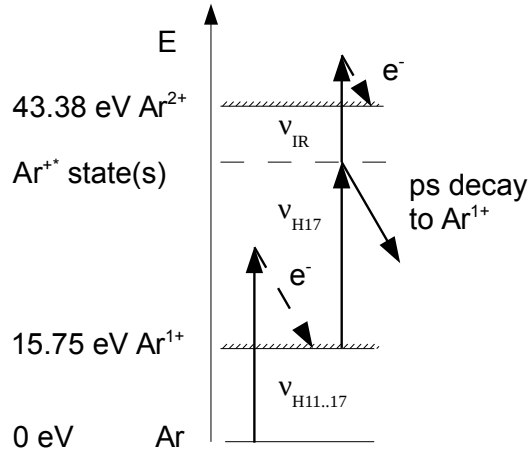


Figure 4.12: Scheme of Ar^{2+} generation: First, an XUV photon ionizes Ar to Ar^{1+} . Then, a second photon from harmonic 17 excites Ar^{1+} to Ar^{++} . Ar^{++} can either decay to Ar^{1+} or is ionized by an IR photon.

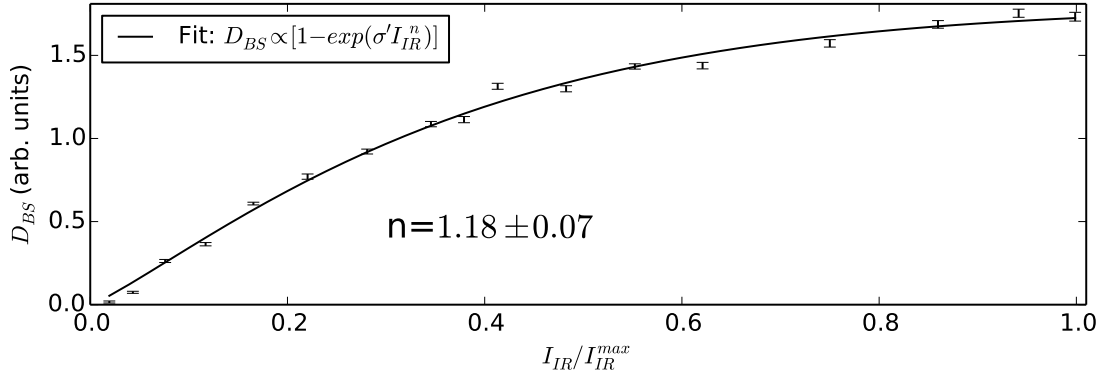


Figure 4.13: D_{BS} , the Ar^{2+} yield difference between large positive and large negative delays, as a function of IR intensity. D_{BS} results from a fit of a Boltzmann sigmoid (Eq. (4.2)) to the experimental data as in Fig. 4.5. The error bars represent fit uncertainties. The fit of D_{BS} follows Eq. (4.5a).

the IR. The ps decay of Ar^{+*} can be neglected on the fs time scale. Then Ar^{+*} is ionized to Ar^{2+} according to

$$\frac{d}{dt}|C_{\text{Ar}^{+*}}|^2 = -\frac{\sigma I_0^n f_{IR}^{2n}}{\hbar\omega_{IR}}|C_{\text{Ar}^{+*}}|^2 \quad (4.4a)$$

$$\frac{d}{dt}|C_{\text{Ar}^{2+}}|^2 = \frac{\sigma I_0^n f_{IR}^{2n}}{\hbar\omega_{IR}}|C_{\text{Ar}^{+*}}|^2 \quad (4.4b)$$

where the Ar^{2+} population $|C_{\text{Ar}^{2+}}|^2$ is 0 before the IR pulse, σ is the IR photoionization cross section, I_0 the maximum IR intensity and f_{IR} the relative field envelope. n is the number of IR photons involved in the process. As D_{BS} is $|C_{\text{Ar}^{2+}}|^2$ for large delays, it satisfies

$$D_{BS} \propto |C_{\text{Ar}^{+*}}^\infty|^2 (1 - \exp(-\sigma' I_0^n)) \quad (4.5a)$$

$$\sigma' := \frac{\sigma}{\hbar\omega_{IR}} \int f_{IR}^{2n} dt \quad (4.5b)$$

Fig.4.13 shows a fit of the experimental data by this equation. As n is close to one, one IR photon is involved in the process.

In order to evaluate the number of involved XUV photons, it is observed that the first ionization energy of Ar is lower than the photon energy of the harmonics. Furthermore, VMI spectra contain electrons with energies corresponding to the difference of the first ionization potential of Ar and the photon energy of the harmonics. Hence, Ar is ionized by them and the Ar^{1+} yield can be used as a measure for the XUV intensity. Fig. 4.2 reads an average cross section σ for this ionization of about 30 Mb. At the assumed XUV intensity of $2 \times 10^{12} \text{ W/cm}^2$ and pulse duration of 20 fs 89 % of the Ar will remain neutral. This shows that the Ar^{1+} yield was far from saturation and linear in XUV intensity. As

later processes can further ionize Ar^{1+} , the sum of Ar^{1+} and Ar^{2+} is proportional to the XUV energy. Fig. 4.9 shows the Ar^{2+} yield to depend approximately quadratic on this sum. Therefore, two XUV photons are involved in the generation of Ar^{2+} .

One of them is already known to ionize Ar so that only one is left to prepare Ar^{+*} . The second ionization energy of Ar is 27.63 eV. The energies of the IR photon plus one photon from the harmonics 11-17 harmonics are 18.9, 22.05, 25.2 and 28.35 eV, respectively. Only harmonic 17 has sufficient energy to lead to ionization. This completes the justification of the ionization process as summarized in Fig. 4.12.

Assuming that the excitation to Ar^{+*} is almost resonant, the model predicts electrons with an energy of 0.7 eV to be produced along with Ar^{2+} . The VMI measurements (see Fig. 4.10 and 4.11) validate the model by showing the correlation between such electrons and the Ar^{2+} yield.

4.3.3 Ar^{+*} States

The last section introduced the Ar^{+*} state(s). To test the above model this section tries to identify them. The second purpose is to provide literature values for the properties of the Ar^{+*} states for later use.

Identification The Ar^{1+} states listed in the NIST atomic database [114] are used as candidates for Ar^{+*} states, which must be accessible from one of the ground states of Ar^{1+} via harmonic 17 and the IR must be able to ionize them. The criteria are represented in Fig. 4.14:

1. The cross section for the ionization of Ar to the lower Ar^{1+} ground state is 21.5 Mb while the higher state has 10.7 Mb [115]. Hence both Ar^{1+} states are expected to be relevant. The highest possible energy of Ar^{+*} is assumed to be the energy of the higher ground state plus the central energy of harmonic 17 plus half its FWHM (0.9 eV) and accordingly for the lower bound.
2. The selection rules for dipole transitions must be obeyed [116].
3. The energy conservation for the ionization of Ar^{+*} by an IR photon must be satisfied. For an energy of an IR photon and Ar^{+*} state the three different Ar^{2+} ground states can lead to three photoelectron energies separated by 195 meV, the maximum energy difference of the Ar^{2+} ground states. The finite IR bandwidth of 60 meV (FWHM) broadens these lines. An Ar^{+*} energy of 730 meV under the ionization potential hence explains electron kinetic energies from 620 meV to 875 meV, which is centered on the broader, measured interval from 530 meV to 960 meV and therefore the most likely binding energy of Ar^{+*} states.

Five different states suit the selection rules and energy conservation. The last criterion favors $3s^2 3p^4(^1D)5d^2 S_{1/2}$. It is also close to the center of the energy interval accessible by harmonic 17. This indicates a higher spectral intensity than the four other possible states.

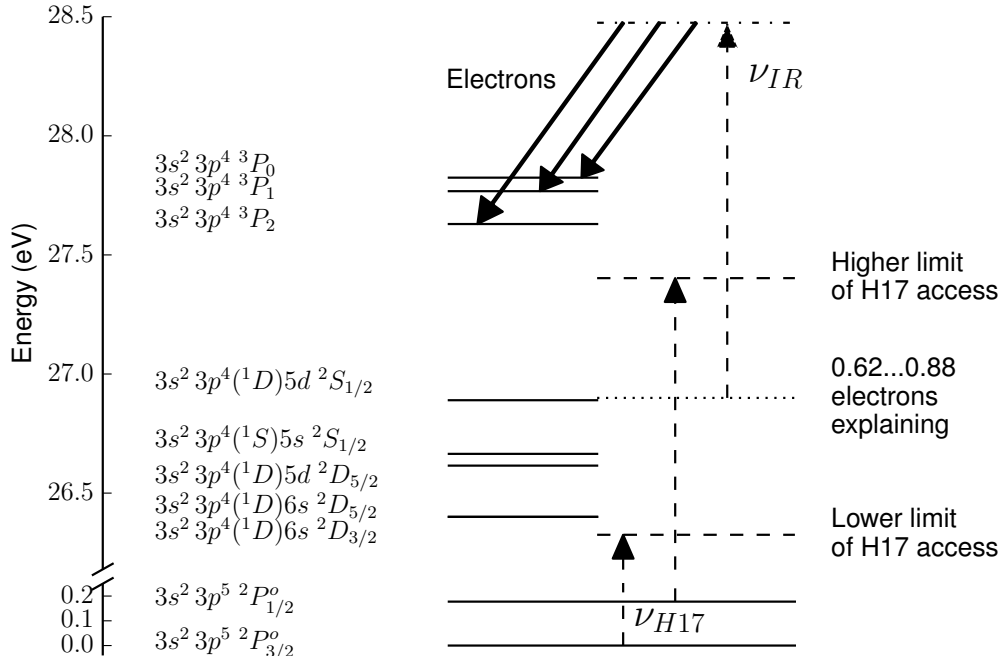


Figure 4.14: Search for Ar^{+*} as described in the text: Criterion 1, being accessible from Ar^{1+} ground states, is represented by dashed horizontal lines. Excited Ar^{1+} states that fail criterion 2, the selection rules, are not drawn. The dotted horizontal line shows the energy that best suits criterion 3, explaining the observed photoelectrons. They are drawn as well.

Table 4.1: Literature values from Verner et al. [117] and Storey and Taylor [118] for weighted oscillator strength for the transition from both Ar^{1+} ground states to the Ar^{+*} states. The additional calculation is described by Eq. (4.7). ‘-’ indicates a forbidden transition. N.A. denotes missing values.

State [114]			Excitation from Ar^{1+} : gf				
Configuration and term	J	Energy (eV)	both	$J=3/2$		$J=1/2$	
			[118]	[117]	calc.	[117]	calc.
$3s^2 3p^4 (1D) 6s \ ^2D$	all		0.132				
	3/2	26.40024		0.00856	0.00857	0.0426	0.0431
	5/2	26.40040		0.0772	0.0772	N.A.	-
$3s^2 3p^4 (1D) 5d \ ^2D$	all		0.0691				
	5/2	26.61537		0.0404	0.0404	N.A.	-
$3s^2 3p^4 (1S) 5s \ ^2S$	1/2	26.66475	0.0601	0.03888	0.0389	0.0193	0.0196
$3s^2 3p^4 (1D) 5d \ ^2S$	1/2	26.88995	0.230	N.A.	0.149	N.A.	0.0749

Table 4.2: Literature values for the Einstein A coefficients: The values are calculated from Tab. 4.1 via Eq. (4.8).

State [114]			Decay to Ar^{1+} : A_{21} (μs^{-1})				
Configuration and term	J	Energy (eV)	$J=3/2$		$J=1/2$		Sum
			[117]	calc.	[117]	calc.	
$3s^2 3p^4(^1D)6s^2 D$	3/2	26.40024	64.7	64.8	318	326	391
	5/2	26.40040	389	388	N.A.	-	388
$3s^2 3p^4(^1D)5d^2 D$	5/2	26.61537	207	206	N.A.	-	206
$3s^2 3p^4(^1S)5s^2 S$	1/2	26.66475	600	601	294	302	903
$3s^2 3p^4(^1D)5d^2 S$	1/2	26.88995	N.A.	2334	N.A.	1175	3509

XUV Excitation to Ar^{+*} The likelihood of transition by excitation or emission can be expressed by weighted oscillator strengths gf . They represent the relation of the absorption/emission rate of the atom to a classical model. Higher values indicate stronger interaction [119].

Verner et al. [117] published extensive data including transitions between the ground states of Ar^{1+} and all except the most important of the five Ar^{+*} states, $3s^2 3p^4(^1D)5d^2 S_{1/2}$. Within the Opacity project Storey and Taylor [118] calculated gf values to all Ar^{+*} candidates' configurations and terms. In order to apply the information to the Ar^{+*} states the gf values for the levels with their specific J quantum number need to be calculated. The relation between dipole moments and gf values is

$$\mu^2 = \frac{3}{2g_2} \frac{\hbar e^2}{m_e \omega_{21}} gf \quad (4.6)$$

[119]. g_2 is the degeneracy of the excited state and ω_{21} is the transition frequency. Within LS coupling the contributions of the states to the overall dipole moments μ of the configuration can be calculated. If the total orbital momentum of the respective states are L and $L-1$ with total spin angular momentum S then the dipole moments of the term μ_{confi} and of the state μ_{state} relate as

$$\mu_{state} = \mu_{confi} \cdot \begin{cases} \frac{(J+L-S-1)(J+L-S)(J+L+S+1)(J+L+S)}{4JL(4L^2-1)(2S+1)} & \text{if } \Delta J = \Delta L \\ \frac{(2J+1)(J+L-S)(J-L+S+1)(J+L+S+1)(-J+L+S)}{4J(J+1)L(4L^2-1)(2S+1)} & \text{if } \Delta J = 0 \\ \frac{(J-L+S+1)(-J+L+S)(J-L+S+2)(-J+L+S-1)}{4(J+1)L(4L^2-1)(2S+1)} & \text{if } \Delta J = -\Delta L \end{cases} \quad (4.7)$$

[120, 121] The respective number from both sources and the result of Eq. (4.7) are given in Tab. 4.1. Verner et al. and the calculation agree in any value given by both sources. As $3s^2 3p^4(^1D)5d^2 S_{1/2}$ has the highest gf value of all states in the table, the previously described ionization model is not challenged.

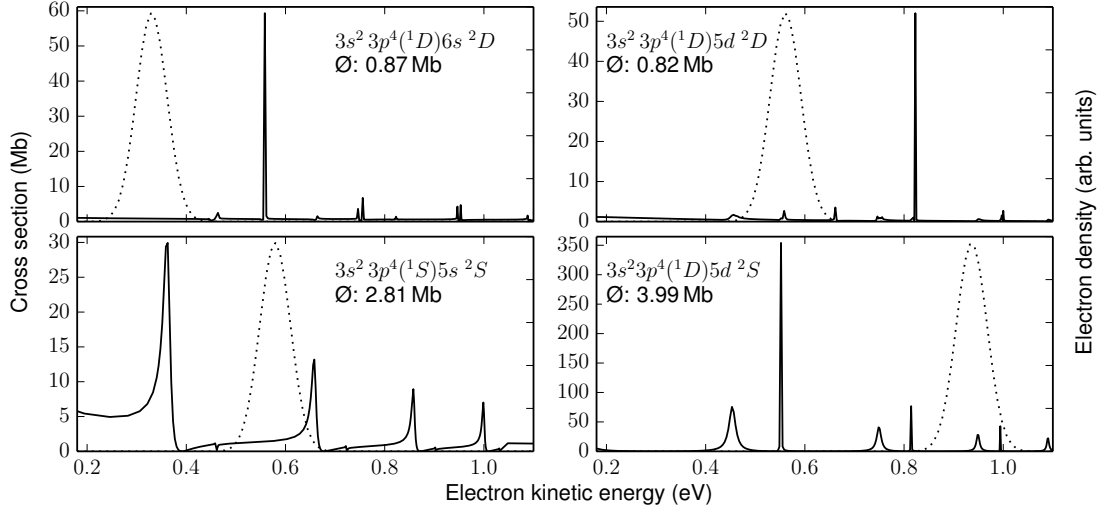


Figure 4.15: Photoionization cross sections [118] (solid line) for the Ar^{+*} states' configurations. Each plot gives the electron energy distribution (dashed line) for the IR spectrum and averages the spectrum over this quantity to generate an effective number for the IR photoionization cross section. Only $3s^2 3p^4(^1D)6s^2D$ represents two Ar^{+*} states.

Decay of Ar^{+*} The next property that is expected from the Ar^{+*} states is spontaneous decay. The Einstein A coefficient of a transition is the probability per time that an electron decays spontaneously from the energetically higher state to the lower state. It can be calculated from the gf values by

$$A_{21} = \frac{gf}{g_2} \frac{\omega_{21}^2 e^2}{2\pi\epsilon_0 m_e c^3} \quad (4.8)$$

[119]. Tab. 4.2 shows the coefficients resulting from the equation and Tab. 4.1.

Generally, the decay time of a state i , τ_{21} , is related to the Einstein coefficients A_{ik} to all accessible states k as

$$\tau_{21}^{-1} = \sum_k A_{ik}. \quad (4.9)$$

For a decay time of (168 ± 6) ps (Fig. 4.6), the Einstein A coefficients have to sum up to $5952 \mu\text{s}^{-1}$. This is larger than the sum of the A_{21} of $3s^2 3p^4(^1D)5d^2S_{1/2}$, $3509 \mu\text{s}^{-1}$. All other Ar^{+*} states are even lower. The difference may be attributed to the contribution of decay channels beyond the available literature data.

IR ionization of Ar^{+*} The last property that presents a test to the Ar^{+*} states is the ionization cross section. Within the Opacity project Storey and Taylor [118] also calculated photoionization cross sections for the configuration belonging to the Ar^{+*} states

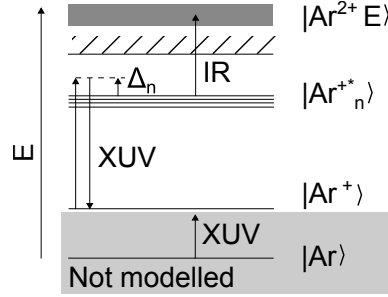


Figure 4.16: Quantum states and interactions involved in the model: One Ar^{1+} state and n Ar^{+*} states are linked via XUV excitation at a detuning of Δ_n . The IR couples each of these states to the continuum of Ar^{2+} and an emitted electron with total energy of E . The ground state of Ar and the first ionization are neglected.

(see Fig. 4.15). The Ar^{+*} states only have one excited electron with a principal quantum number of 5 or 6. This indicates relatively separated cores and valence electrons with low interaction. Assuming that J does not matter is therefore a simple approximation. The calculation also returns energies for the Ar^{+*} states. They differ from the energies from the NIST atomic database. For example the $3s^2 3p^4(^1D)5d\ ^2S_{1/2}$ is 0.740 eV (NIST atomic database) or 0.639 eV (Opacity project) beneath the ionization threshold. This difference of 101 meV is relevant as the cross sections are dominated by a pattern of spikes on the same length scale (Fig. 4.15). For consistency the energy scale of Storey and Taylor is used for this plot. Nevertheless the NIST data is preferred for all other issues as it is experimental.

The favored $3s^2 3p^4(^1D)5d\ ^2S_{1/2}$ state has the highest cross section. Therefore, IR photoionization of this state is more efficient than for the other Ar^{+*} states. A lower value than the other Ar^{+*} candidates would challenge the ionization mechanism.

4.4 Qualitative Model of Ar^{2+} Generation

This section introduces a quantum mechanical model. It bases upon the ionization mechanism from the last section and is intended to shed light on the jet unexplained behavior of the Ar^{2+} yield for fs delays.

4.4.1 Fedorov-Kazakov Model

One of the ground states of Ar^{1+} and an arbitrary number of Ar^{+*} states are included. A continuum of states describes Ar^{2+} and the freed electron. The different ground states and the first ionization of Ar are neglected. The treatment is based upon the work of Fedorov and Kazakov [122] and extensions from [123, 124].

4.4 Qualitative Model of Ar^{2+} Generation

The quantum state of the system can be written as

$$\begin{aligned}
 |\Psi(t)\rangle = & |\text{Ar}^{1+}\rangle C_{\text{Ar}^{1+}}(t) \exp(-i/\hbar E_{\text{Ar}^{1+}} t) \\
 & + \sum_n |\text{Ar}^{+*}_n\rangle C_n(t) \exp\left(-i/\hbar \int_0^t E_{\text{Ar}^{+*}_n}(t') dt'\right) \\
 & + \int |\text{Ar}^{2+}_E\rangle C_{\text{Ar}^{2+}_E}(t) \exp(-i/\hbar Et) dE
 \end{aligned} \quad (4.10)$$

where the E are the respective energies of the states and the functions C describe the evolution of the system.

The Schrödinger equation $(\hat{H} + \hat{V})|\Psi\rangle = i\hbar \frac{\partial}{\partial t} |\Psi\rangle$ uses the Hamilton operator of the unperturbed system \hat{H} and the perturbative contribution from an electric field \hat{V} , which couples Ar^{1+} to the $|\text{Ar}^{+*}_n\rangle$ via the XUV field and $|\text{Ar}^{+*}_n\rangle$ to the continuum states by the IR field. Fig. 4.16 illustrates the states and their interaction.

The assumptions of Fedorov and Kazakov are:

- The electric field envelopes are smooth and the pulses are Fourier-limited. The spectrum is narrow compared to the energy differences of the states.
- The rotating wave approximation is valid.
- There are no transitions within the continuum.
- The continuum states $C_{\text{Ar}^{2+}_E}(t)$ do not have population at the ionization threshold at any time.
- The transition dipole moment is smooth for the ionization of Ar^{+*} .
- The XUV produces a negligible Stark shift.

The model incorporates the IR-induced Stark shift for the energies $E_{\text{Ar}^{+*}_n}$. As these are Rydberg states the effect increases the energy by the ponderomotive energy $U_p = \frac{e^2 \lambda^2 I}{8\pi^2 \epsilon_0 c^3 m_e}$ (Eq. (2.2)) [125]. At an IR intensity of $1 \times 10^{14} \text{ W/cm}^2$ and a wavelength of 790 nm U_p equals 5.7 eV. The Stark shift changes the energy of the Ar^{1+} state by $-1/4\alpha E^2$ where α is the polarizability and E the IR field strength. The reduction of energy is 130 meV at the same IR intensity [126, 127]. The energy shifts for both groups are proportional to the IR intensity and are different by factor of 44. Hence, the field dependence of $E_{\text{Ar}^{1+}}$ is neglected and $E_{\text{Ar}^{+*}_n} =: E_n + U_p(t)$ is set, where E_n is the energy of the state in the absence of the ponderomotive shift. U_p is included via the energy detuning Δ_n :

$$\Delta_n = E_{\text{Ar}^{1+}} + \hbar\omega_{XUV} - E_n - U_p(t) \quad (4.11a)$$

$$= E_{\text{Ar}^{1+}} + \hbar\omega_{XUV} - E_n - \frac{e^2 \lambda^2 I_{IR}}{8\pi^2 \epsilon_0 c^3 m_e} f_{IR}^2(t) \quad (4.11b)$$

where the fields are written with a time dependent function $f(t)$ and the maximum field F . This gives $E = Ff(t)$ for the electric field and is used throughout the model for the IR and XUV field.

4 Multiphoton Sequential XUV Double Ionization of Argon

Evaluation of the Schrödinger equation results in

$$\dot{C}_{\text{Ar}^{1+}}(t) = +if_{XUV}(t) \cdot \sum_n \frac{V_{\text{Ar}^{1+}n}}{\hbar} \cdot \exp\left(\frac{i}{\hbar} \int_0^t \Delta_n(t') dt'\right) \cdot C_n(t) \quad (4.12a)$$

$$\begin{aligned} \dot{C}_n(t) = & -if_{XUV}(t) \cdot \frac{V_{n\text{Ar}^{1+}}}{\hbar} \cdot \exp\left(\frac{-i}{\hbar} \int_0^t \Delta_n(t') dt'\right) \cdot C_{\text{Ar}^{1+}}(t) \\ & - f_{IR}^2(t) \cdot \frac{\pi}{\hbar} V_{nE} \sum_k V_{Ek} \cdot \exp\left(\frac{it}{\hbar} (E_n - E_k)\right) \cdot C_k(t) \end{aligned} \quad (4.12b)$$

[122, 124, 123] The coupling terms V_{mn} of two states coupled by an electric field reduce to $f(t)V_{mn} = -1/2\mu_{mn}f(t)F$ where μ_{mn} is transition dipole moment and ω is the angular frequency of the electric field.

As $\langle \Psi(t) | \Psi(t) \rangle = 1$ the Ar^{2+} population can be calculated from $C_{\text{Ar}^{1+}}$ and C_n . The initial condition is that before XUV interaction all population is in state $|\Psi_{\text{Ar}^{1+}}\rangle$.

The physical quantities can be reformulated into a few rates:

- Ar^{1+} - Ar^{+*} coupling via XUV: $\frac{\mu_{\text{Ar}^{1+}n} F_{XUV}}{\hbar} =: \Omega_n$. Ω_n is the maximum Rabi frequency of the XUV excitations to a state n . This interpretation is discussed later.
- Ar^{1+} - Ar^{+*} energy detuning via constant difference and an U_p dependent term: $\frac{1}{\hbar} \Delta_n(t) =: \Delta e_n - u_p f_{IR}^2(t)$. $\Delta e_n = \frac{1}{\hbar} (E_{\text{Ar}^{1+}} + \hbar\omega_{XUV} - E_n)$ is the detuning rate of the XUV excitation to a state n . $u_p = \frac{1}{\hbar} \frac{e^2 \lambda^2 I_{IR}}{8\pi^2 \epsilon_0 c^3 m_e}$ is the maximum U_p -related detuning rate.
- Ar^{+*} ionization: $|V_{En}|^2/\hbar = \frac{I_{IR} cs_n}{2\pi\omega_{IR}\hbar} =: \Gamma_n$ where cs_n is the cross of state n . Γ_n is IR ionization rate of a state n .

The constants Ω_n , Δe_n , u_p and Γ_n are sufficient to calculate the model for any given envelopes $f_{IR}(t)$ and $f_{XUV}(t)$. The relation $|V_{nE}|^2 = \frac{I_{IR} cs_n}{2\pi\omega_{IR}}$ originates from a comparison of Eq. (4.4), which describes the classical ionization rate, and Eq. (4.12) for $f_{XUV} = 0$.

Using these substitutions Eq. (4.12) simplify² to

$$\dot{C}_{\text{Ar}^{1+}}(t) = +if_{XUV}(t) \cdot \sum_n \Omega_n/2 \cdot \exp\left(i\Delta e_n t - iu_p \int_0^t f_{IR}^2(t') dt'\right) \cdot C_n(t) \quad (4.13a)$$

$$\begin{aligned} \dot{C}_n(t) = & -if_{XUV}(t) \cdot \Omega_n/2 \cdot \exp\left(-i\Delta e_n t + iu_p \int_0^t f_{IR}^2(t') dt'\right) \cdot C_{\text{Ar}^{1+}}(t) \\ & - f_{IR}^2(t) \cdot \pi \sqrt{\Gamma_n} \sum_k \sqrt{\Gamma_k} \cdot \exp(it(\Delta e_k - \Delta e_n)) \cdot C_k(t). \end{aligned} \quad (4.13b)$$

²It is additionally assumed that the V_{nE} are real and positive. The assumption only matters in Sec. 4.5.1 and 4.5.3.

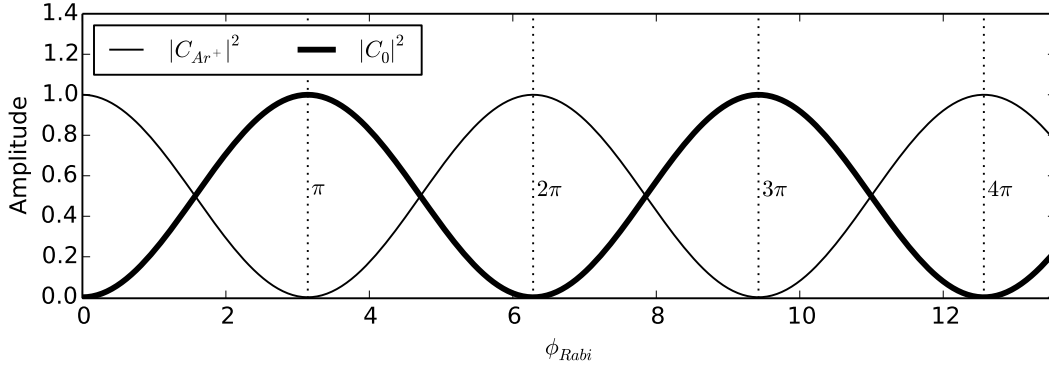


Figure 4.17: Rabi oscillations: Population of $|\text{Ar}^{1+}\rangle$ and $|\text{Ar}^{+*}_0\rangle$ according to Eq. (4.16). Extrema are marked by their ϕ_{Rabi} for later reference.

The calculations take advantage of the finite length of \cos^2 pulses. They are:

$$f_{XUV}(t) := \begin{cases} \cos^2 \frac{t+\tau}{2\tau_{XUV}} \pi & \text{if } -\tau_{XUV} < t + \tau < \tau_{XUV} \\ 0 & \text{else} \end{cases} \quad (4.14a)$$

$$f_{IR}(t) := \begin{cases} \cos^2 \frac{t}{2\tau_{IR}} \pi & \text{if } -\tau_{IR} < t < \tau_{IR} \\ 0 & \text{else} \end{cases} \quad (4.14b)$$

for the respective fields. τ is the delay between the peaks of the relative envelopes. $\tau_{IR/XUV}$ are the corresponding FWHM time durations.

For later reference the simplest solution of this model is calculated analytically. Assuming only two states, $|\text{Ar}^{1+}\rangle$ and $|\text{Ar}^{+*}_0\rangle$, no detuning and no IR field the equations (4.12) reduce to:

$$\dot{C}_{\text{Ar}^{1+}}(t) = +if_{XUV}(t)\Omega_0/2C_0(t) \quad (4.15a)$$

$$\dot{C}_0(t) = -if_{XUV}(t)\Omega_0^*/2C_{\text{Ar}^{1+}}(t) \quad (4.15b)$$

with the solution:

$$C_{\text{Ar}^{1+}}(t) = \cos(\phi_{Rabi}(t)/2) \quad (4.16a)$$

$$C_0(t) = \frac{\Omega_0}{|\Omega_0|} \cdot \sin(\phi_{Rabi}(t)/2) \quad (4.16b)$$

$$\phi_{Rabi}(t) = |\Omega_0| \int_{-\infty}^t f_{XUV}(t') dt' \quad (4.16c)$$

This solution (Fig. 4.17) is the so-called Rabi-oscillation [102] with a maximum Rabi frequency $|\Omega_0|$: The frequency of the change of the populations is $\frac{d\phi_{Rabi}(t)}{dt} = |\Omega_0|f_{XUV}(t)$. The Rabi phase ϕ_{Rabi} governs the number of cycles and its value at the end of the XUV pulse is used throughout the chapter to describe the structure of the time dependence of the population of the Ar^{1+} and Ar^{+*} states.

4.4.2 Effective State Model

The model is first applied to predict the ion yields from the experimental conditions and the literature values for the five Ar^{+*} states. It is then used to fit the experimental Ar^{2+} yield. The model defined in Sec. 4.4.1 is used with the lower ground state of Ar^{1+} and one effective state formulated to represent the five previously discussed Ar^{+*} states. The first paragraph defines the effective state:

Effective State The parameters of the effective state are chosen such that the new state has the same effect on the Ar^{2+} and Ar^{1+} populations as the five Ar^{+*} states together. The values for the properties of the states are taken from Tab. 4.1 and Fig. 4.15. The intensities³ $I_{XUV} = 2 \times 10^{12} \text{ W/cm}^2$ and $I_{IR} = 1 \times 10^{14} \text{ W/cm}^2$ stem from Sec. 4.2:

- Parameter $\Omega_{eff} = 0.132 \text{ fs}^{-1}$: The squared dipole moment of a set of transitions is equal to the sum of the squared dipole moments of the single transitions [119]. As $\frac{\mu_{\text{Ar}^{1+}n} F_{XUV}}{\hbar} = \Omega_n$

$$\Omega_{eff} := \sqrt{\sum_n \Omega_n^2} \quad (4.17)$$

is chosen accordingly.

- Parameter $\Delta_{eff} = 0.0055 \text{ fs}^{-1}$: Average over states' Δ_n , weighted by Ω_n^2 to represent their relevance. The corresponding energy detuning equals 3.6 meV.
- Parameter $u_p = 8.9 \text{ fs}^{-1}$: It only depends on IR intensity and is therefore the same for any state. The maximum ponderomotive energy shift is 5.8 eV.
- Parameter $\Gamma_{eff} = 0.20 \text{ fs}^{-1}$: Average over states' Γ_n , weighted by Ω_n^2 to represent their relevance.

Model with Experimental Parameters Eq. (4.13) is solved numerically for the discussed parameters at the highest IR intensity of $1 \times 10^{14} \text{ W/cm}^2$ and a range of XUV-IR delays. The resulting ionized fraction is plotted together with the corresponding measurement (Fig. 4.18a). First, the section discusses the structure of the Ar^{2+} dependence on delay i.e. the existence of minima and maxima.

The theory reproduces two features of the experimental data: (i) The Ar^{2+} yield rises from one stationary value to a higher one and (ii) the yield decreases around time overlap. However, the decrease is stronger than in the measured data and reduces the yield around temporal overlap to almost zero. In contrast, the measured data shows only a slight reduction. The discrepancy can be decreased by reducing u_p (dashed-dotted line).

The theory fails to reproduce a local maximum and minimum for longer delays (40 and 50 fs respectively). At smaller delays than this minimum lies a maximum, which

³The simplification to attribute all XUV intensity to harmonic 17 is justified on page 133

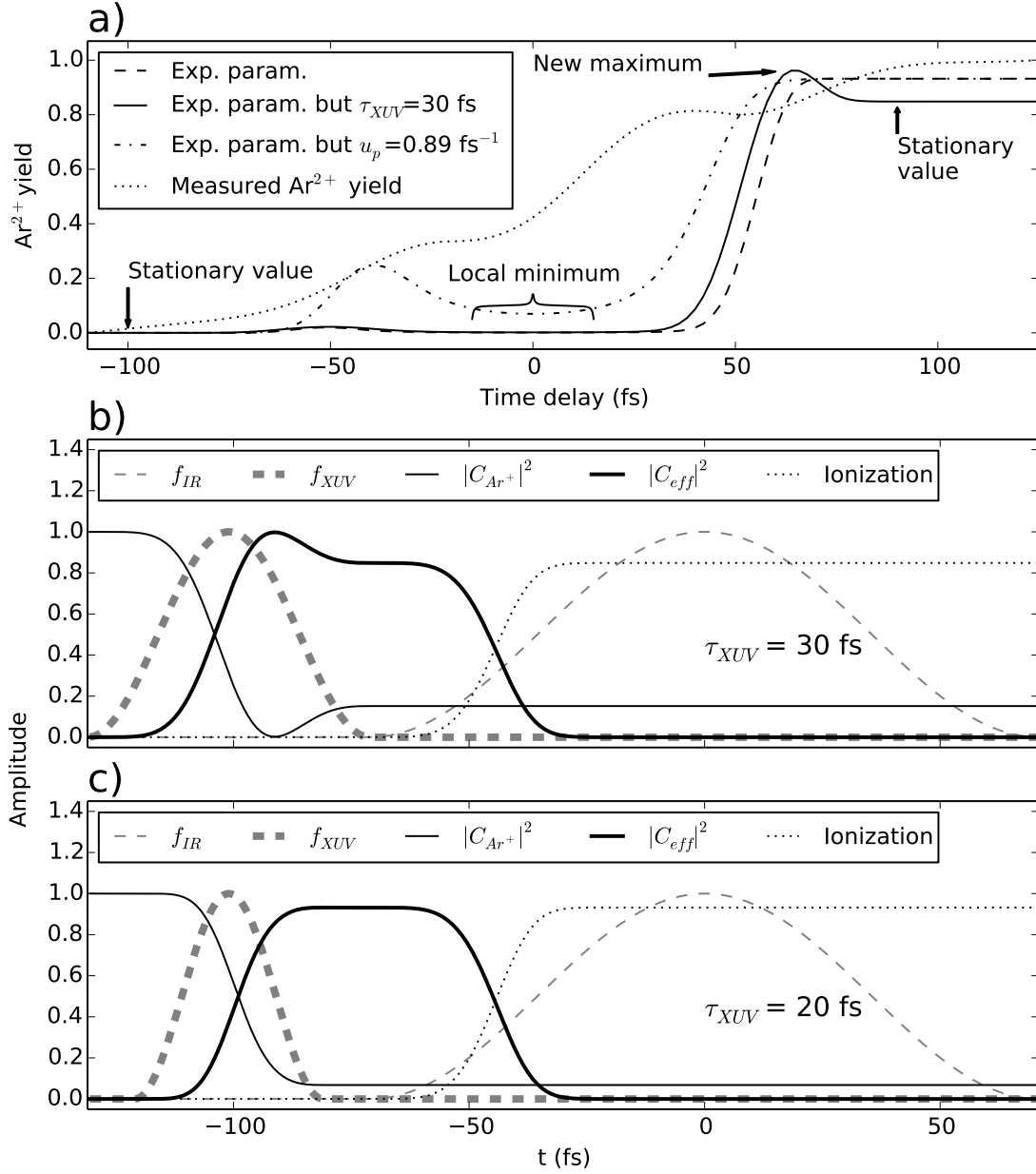


Figure 4.18: Result of Eq. (4.12) for the effective state at the maximum IR intensity 1×10^{14} W/cm 2 : a) shows the Ar^{2+} yield predictions of the model in case of the expected experimental parameters. The solid and the dashed-dotted graph are using the same parameters except that the XUV pulse duration is increased to 30 fs or the u_p is ten times smaller than expected, respectively. For reference, the corresponding experimental Ar^{2+} yield is given as the normalized fit line of Fig. 4.5 (dotted line). b) and c) show for different XUV durations the time developments of the field envelopes, f_{XUV} and f_{IR} , the populations of Ar^{1+} and the effective state, and the amount of ionization at a delay that is large enough to always separate both pulses (101 fs).

can be additionally reproduced by increasing the influence of the XUV by elongating the XUV pulse duration at the same XUV intensity (continuous line).

Fig. 4.18b exhibits why the Ar^{2+} yield at large delays is less than the maximum Ar^{2+} yield at a delay of 65 fs for an XUV pulse duration of $\tau_{XUV} = 30$ fs. It shows the development of the populations for a delay where the IR pulse follows after the XUV pulse. The population is first excited from Ar^{1+} to the effective state by the XUV and then converted partly back creating a maximum in the Ar^{+*} population. The situation is the same as the simple model for Rabi oscillations (Eq. (4.16)). At the end of the XUV pulse the Rabi phase reaches a value slightly higher than π . As Ar^{+*} is ionized by the IR, the Ar^{2+} yield is a measure for the population of the effective state during the IR pulse. The maximum in $|C_{eff}(t)|^2$ translates into a maximum of the Ar^{2+} yield at a certain delay between the XUV and IR. This relation explains why the expected parameter set with $\tau_{XUV} = 20$ fs does not show a local maximum (Fig. 4.18c).

Fit There are several reasons to fit the parameters of the effective state (Ω_{eff} , Δ_{eff} , u_p and Γ_{eff}) and the pulse durations (τ_{XUV} and τ_{IR}):

- The XUV field parameters influence the Ar^{2+} yield structurally. The XUV pulse parameters were not measured but a 50 % difference in τ_{XUV} can change the shape of the delay dependence of the Ar^{2+} yield (Fig. 4.18).
- Sec. 4.5 discusses the limits of the accuracy of the model. As it is only qualitative, all parameters should be interpreted as effective.
- Using calculated values only reproduces basic features hinting that the actual experimental parameters are different from the expected.

The main qualitative difference between the delay dependent Ar^{2+} yields in Fig. 4.18a and the measured equivalent is that the stationary value at long delays is lower than the new maximum (Fig. 4.18b). Following the understanding of the relation between the Ar^{2+} yield and the Ar^{+*} population from the last paragraph, the Ar^{2+} yield as a function of delay should mimic the population of Ar^{+*} as a function of time: It should rise to a local maximum and then fall to have a local minimum and then reach a high value after the XUV pulse. In terms of the Rabi phase this means a final value of $\phi_{Rabi} = 3\pi$ (Refer to Fig. 4.17).

Guided by the desired Rabi phase of 3π and the u_p related quantitative difference of the minimum at overlap the parameters Ω_{eff} , Δ_{eff} , u_p , Γ_{eff} , τ_{XUV} and τ_{IR} are manually chosen to approximately match model and experimental data. A least square algorithm fine-tuned all parameters. Additionally, there are two technical parameters: Y_{coef} , a coefficient to the yield from the model, is applied after measurement and fit data normalization. Another parameter, τ_0 , corrects a possible error in the position of the overlap of XUV and IR.

Fit Quality Fig. 4.19 shows the fit (line) and the data (dots). For the highest intensity the model shows a local minimum at an XUV-IR delay of 50 fs and a reduced yield

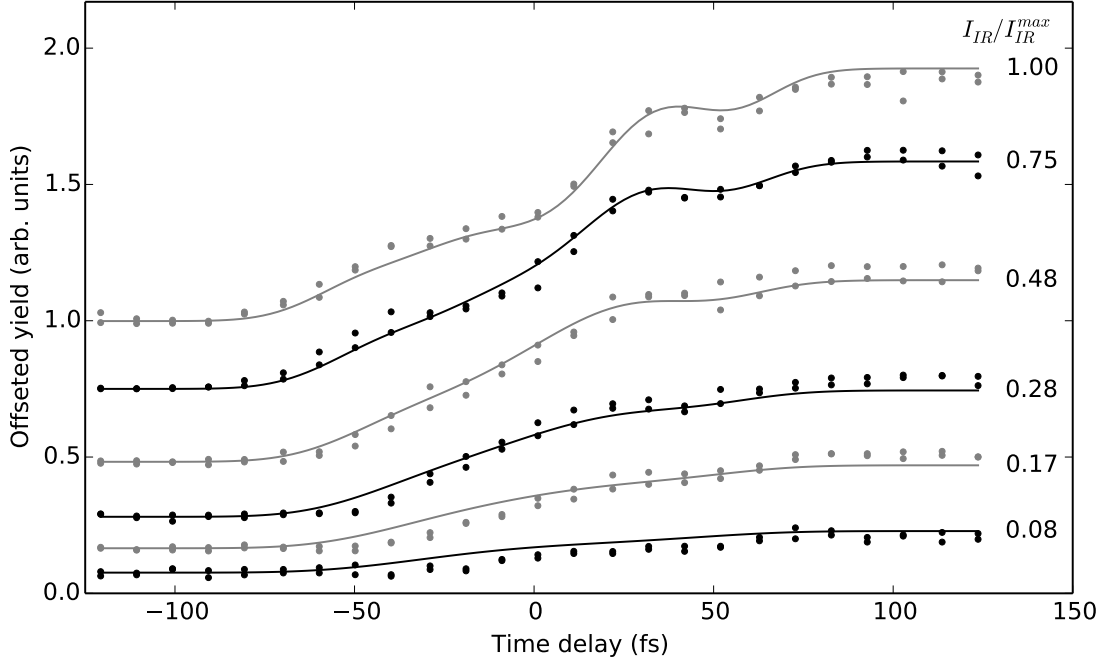


Figure 4.19: Fit (solid line) of the experimental dependence of the Ar^{2+} yield on delay and IR intensity (dots): The fitted parameters are given in Tab. 4.3. Only the IR intensity related values for u_p and Γ_{eff} are far (factor 50) from expectation.

around overlap. Both features and their dependence on IR intensity are reproduced by the model: Experimental and modeled curves for lower IR intensities are more similar to simple step functions around overlap, while the minimum at 50 fs remains. Furthermore, the yield difference between long negative and long positive delays is reproduced for the range of IR intensities.

Fit Quantities Values from the fit and from the calculation based upon experimental conditions are given in Tab. 4.3.

The parameter Ω_{eff} is proportional to the XUV field strength and 33 % higher than expected. τ_{XUV} is larger than expected by a factor of 2.3. Both parameter describe the XUV field but HHG is highly susceptible to daily alignment and the deviations from the expected τ_{XUV} are within reach.

Δ_{eff} describes the detuning between the corresponding photon energy and the transition energy. The model assumes a monochromatic pulse with a constant frequency. For the Ar^{+*} states, $3s^2 3p^4(^1D)6s^2 D_{3/2,5/2}$, $3s^2 3p^4(^1D)5d^2 D_{5/2}$, $3s^2 3p^4(^1S)5s^2 S_{1/2}$ and $3s^2 3p^4(^1D)5d^2 S_{1/2}$, the detunings are 0.37, 0.37, 0.16, 0.11 and -0.11 eV. These values are relative to the central energy of harmonic 17. Its spectral width (FWHM 0.9 eV) is bigger than the energy differences between the states and the center of harmonic 17.

Table 4.3: Comparison of fitted and expected parameters: The expectations for Ω_{eff} , Δe_{eff} , u_p and Γ_{eff} are calculated on page 114. Sec. 4.2 gives τ_{XUV} and τ_{IR} . τ_0 and Y_{coef} are expected to correct only small differences. The error estimations stem from the fit.

Parameter	Fit value	Expected value	Ratio
$\Omega_{eff}(\text{fs}^{-1})$	0.1741884 ± 0.0000060	0.131	1.33
$\Delta e_{eff}(\text{fs}^{-1})$	0.00158 ± 0.00011	0.0055	0.29
$u_p(\text{fs}^{-1})$	0.1732 ± 0.0056	8.9	0.020
$\Gamma_{eff}(\text{fs}^{-1})$	0.00498 ± 0.00021	0.202	0.025
$\tau_{IR}(\text{fs})$	86.4 ± 1.8	71	1.22
$\tau_{XUV}(\text{fs})$	47.44 ± 0.24	20	2.37
$\tau_0(\text{fs})$	0.1130958 ± 0.0000085	0	nan
Y_{coef}	1.079 ± 0.016	1	1.08

Using the central frequency is therefore an important approximation and leads to the reinterpretation of Δe_{eff} : As the detuning reduces the efficiency of a transition, it appears likely that spectral components of the harmonic with a smaller detuning should be weighted more resulting in a smaller, effective Δe_{eff} . As the fitted values are smaller than the expected for monochromatic XUV, the fit may have found this effective value. u_p also describes a detuning and is therefore affected by the same mechanism.

u_p and Γ_{eff} are lower than expected by a comparable number and are both proportional to the IR intensity. This indicates that the IR intensity is not $1 \times 10^{14} \text{ W/cm}^2$ but $2.0 \times 10^{12} \text{ W/cm}^2$ (from u_p) to $2.7 \times 10^{12} \text{ W/cm}^2$ (from Δe_{eff}). The difference is large and established from two independent sources, making it unlikely that the way the quantities are defined is the origin. The accuracy of the IR intensity from Γ_{eff} is limited as (i) The averaging over the Ar^{+*} state's Γ_n is not rigorous. (ii) it bases upon only one (most important state) or two (rest) theoretical calculations of cross sections and (iii) those are reduced to a single number for each state by an average (Fig. 4.15). The accuracy of the IR intensity from u_p is limited by the above mentioned bandwidth of the XUV, which does not comply to the assumptions of the Fedorov-Kazakov model. The experimentally expected intensity of $1 \times 10^{14} \text{ W/cm}^2$ were deduced from the relative yield of Ar^{1+} and Ar^{2+} from IR only ionization. Hence, there must be Ar in a region with such intensity. But this region does not necessarily contain the XUV focus. The foci of XUV and IR are expected to lie at different positions along the propagation axis as multiple checks during the experiments eliminate the possibility of missing lateral overlap.

The IR pulse duration τ_{IR} is 22 % longer than expected. As mentioned before τ_{IR} is only an effective parameter (p. 116). The parameter τ_0 , the time overlap correction, is within the error of the calibration of time overlap of $\pm 2 \text{ fs}$ (Sec. 4.2) and the height correction Y_{coef} is close to 1.

Some of the errors from the least square fit procedure are very small and are only given for completeness. For example t_0 's is $8.5 \times 10^{-6} \text{ fs}$. The 10 fs spacing in the delay

grid and the fit discrepancies deny such small errors. The qualitative accuracy of the model is a greater source of uncertainty. The thesis focuses now on the physical meaning and the approximations in Sec. 4.5.

Quantum Mechanical Detail Fig. 4.20a shows the modeled Ar^{2+} yield fitted to the experimental data at the highest IR intensity as function of XUV-IR delay and the pulse envelopes and populations as functions of time at four different delays (Fig. 4.20b). The lowest part of Fig. 4.20b presents the situation for a delay where the XUV and IR do not overlap. As intended, the maximum Rabi phase is close to 3π . Compared to the expected parameters (Fig. 4.18) the lower Γ_{eff} results only in a partial ionization of the Ar^{+*} state.

Fig. 4.20b also shows the time evolution at the Ar^{2+} yield minimum at the delay of 50 fs (Fig. 4.20a). It was proposed that the Ar^{2+} yield minimum relates to the minimum of the population of the effective state as the IR is ionizing only its population. However, at that time the relative envelope f_{IR} is not close to its maximum. The reason is that the IR pulse is too long to accurately probe the effective state. For shorter IR pulses the delay dependence of the Ar^{2+} yield converges towards a shape that has the same structure as the time dependent population of the effective state (Fig. 4.21).

The Rabi oscillations are affected by the U_p shift. It increases the detuning of the XUV excitation and reduces its efficiency and ability to transfer all population between the effective state and Ar^{1+} . This is most visible at a delay of 0 fs (Fig. 4.20b). Fig. 4.22 shows the effect of the parameter u_p on the delay dependent Ar^{2+} yield by increasing u_p further: Higher values reduce the yield close to overlap. As u_p encodes the Stark effect, the reduced yield at a delay of 0 fs can be attributed to it.

The graph also displays the system evolution for a delay of -60 fs (Fig. 4.20b). The XUV transfers population into the effective state. At that time the IR pulse is already too weak to ionize the majority of the effective state population and the total ionization yield is low.

4.5 Review of Assumptions

This section discusses the approximations made in the quantum mechanical model.

4.5.1 First Ionization and States not Modeled

According to the discussion in Sec. 4.3, the first ionization is caused by the XUV pulse. Fig. 4.23 plots the classical time dependence of the remaining Ar. Most of the Ar remains unionized for both parameter sets, the fitted and the experimentally expected. Therefore, no strong saturation effects complicate the ionization.

The used Fedorov-Kazakov model does not take this first, simple ionization into account. The corresponding extension is unknown to the best of the knowledge of the author. A representation of Ar and a transfer mechanism from Ar to Ar^{1+} are missing for a full model of the ionization process as given in Fig. 4.12. In this model the

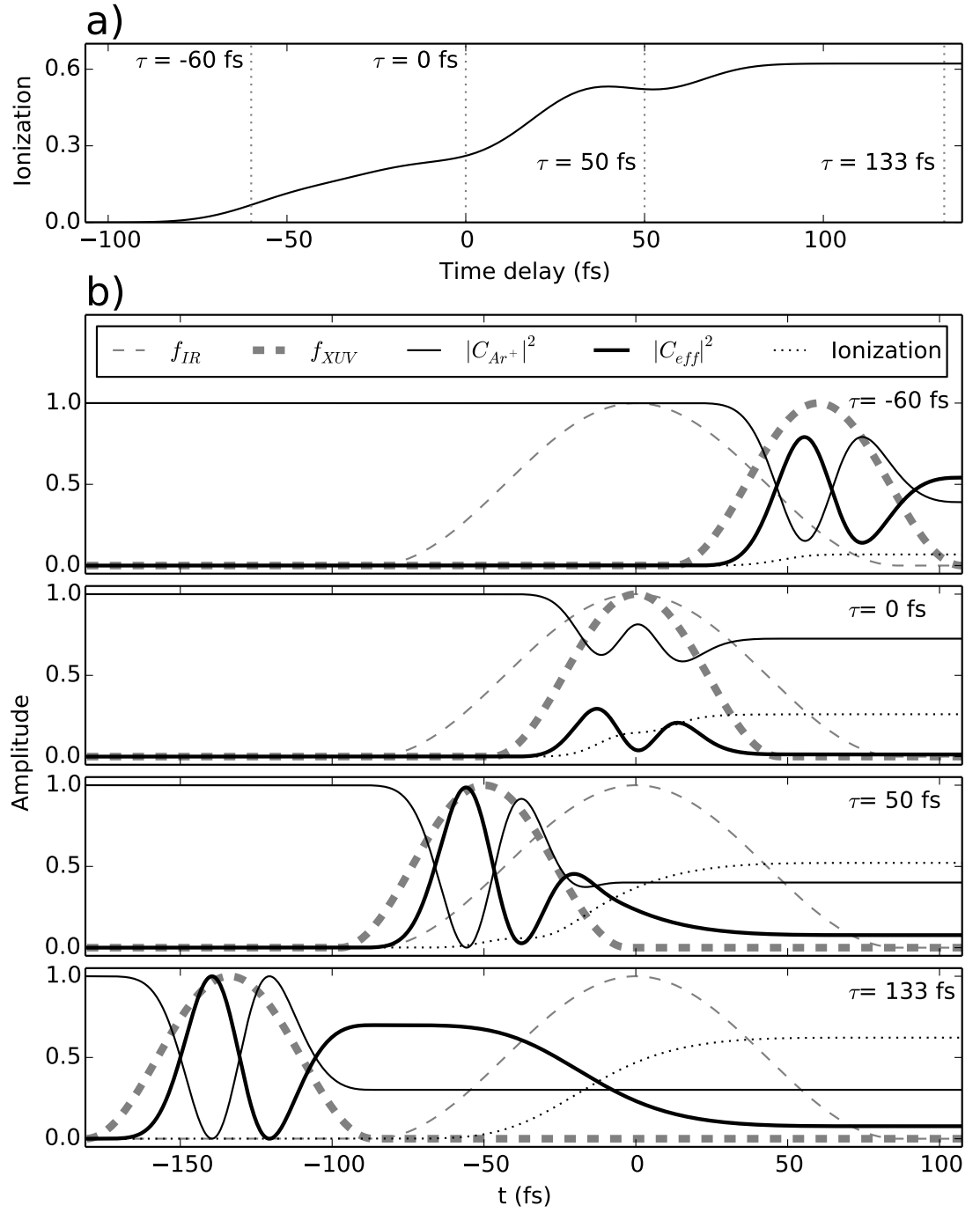


Figure 4.20: a) shows the modeled Ar^{2+} yield fitted to the experimental data at the highest IR intensity as function of XUV-IR delay. b) depicts the pulse envelopes and populations as functions of time at four different delays marked in a)

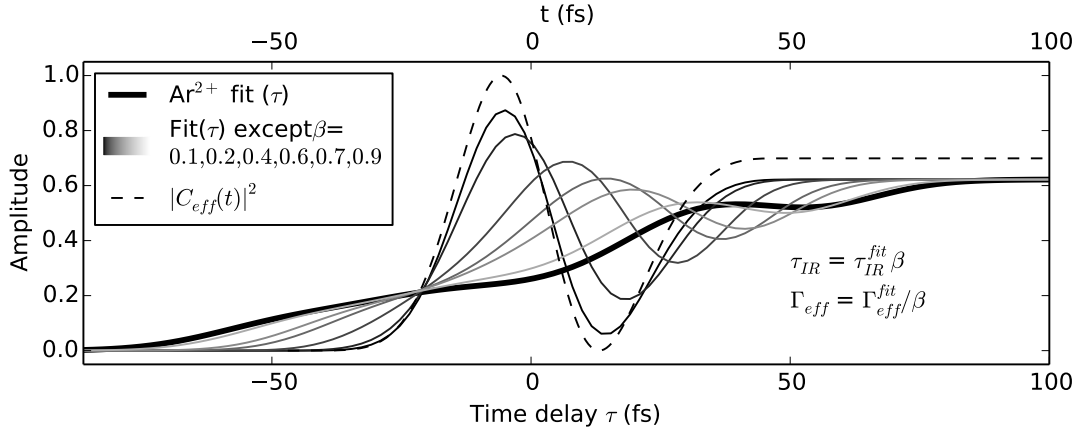


Figure 4.21: Effect of the IR pulse duration on the relation of the Ar^{2+} yield and the Ar^{+*} population: The plot uses one axis for time and another axis for time delay dependences. Time delay axis: Ar^{2+} yield calculated for the fitted parameters and parameters only modified by the factor β . The IR pulse duration is multiplied by the factor β and Γ_{eff} is divided by β to sustain the terminal amount of Ar^{2+} despite the lower amount of time for ionization. The parameters Ω_{eff} , Δ_{eff} , u_p and τ_{XUV} remain. Time axis: $|C_{eff}|^2$ is plotted for the fitted parameters and a delay high enough to separate IR and XUV. Time 0 is set to the center of the XUV pulse.

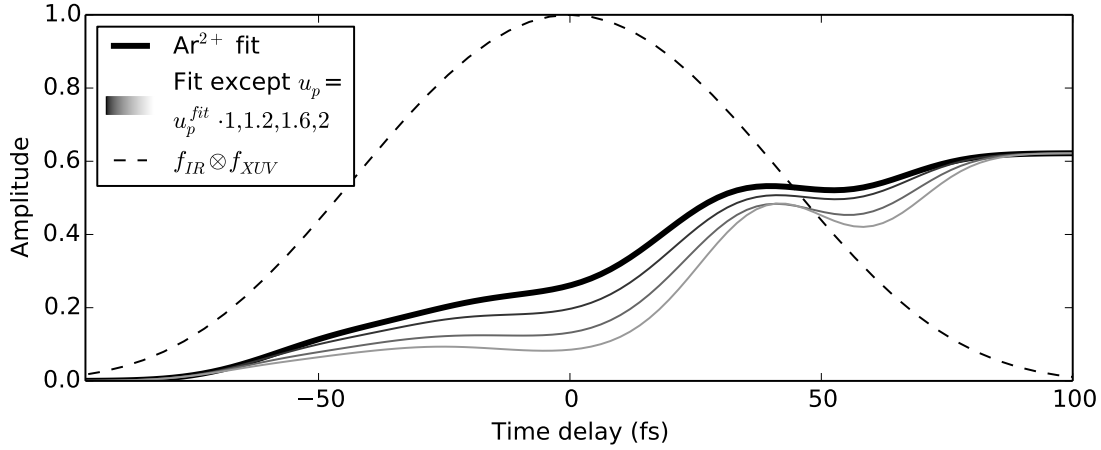


Figure 4.22: Influence of u_p in the model: The Ar^{2+} yield for the fitted parameters and derived parameters are shown. The parameters Ω_{eff} , Δ_{eff} , Γ_{eff} , τ_{IR} and τ_{XUV} remain. Only u_p is increased by a factor. The convolution $f_{IR} \otimes f_{XUV}$ is shown as a reference for IR influence during the Rabi oscillations.

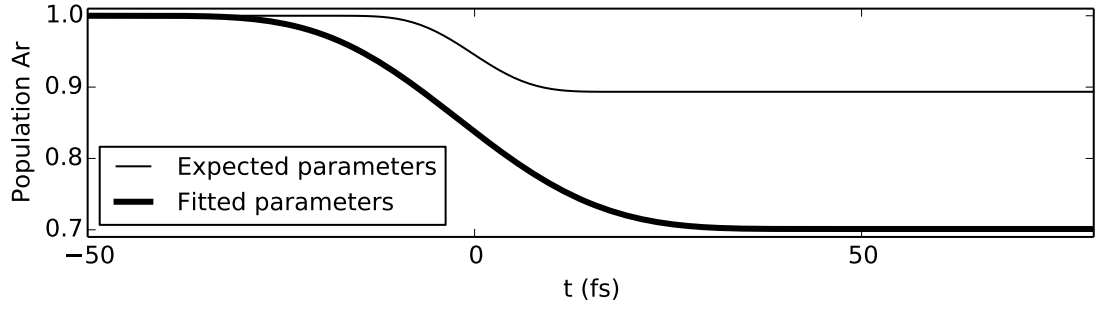


Figure 4.23: Ar atomic populations (Analog to Eq. (4.4)) during the XUV pulse as a function of time for the experimentally expected XUV pulse (thin line) and the fitted XUV parameters (thick line).

sum of the populations in Ar^{1+} , Ar^{+*} and Ar^{2+} would rise from zero to a small number (<0.3 in Fig. 4.23) during the XUV pulse. In contrast, this sum is always 1 in the Fedorov-Kazakov model. Therefore, the sum is more overestimated at the beginning of the XUV pulse than at its end. It appears likely that this trend influences the delay dependent Ar^{2+} yield and that the Fedorov-Kazakov model underestimates the yield at small positive delays in comparison to the yield at small negative delays.

The classical ionization model described in Fig. 4.12 does not cover quantum mechanical phases. The next model also gives an idea of the influence of the phase of the populations resulting from the first ionization:

The used Fedorov-Kazakov model only takes one Ar^{1+} ground state, $3s^2 3p^5 {}^2P_{3/2}^o$, into account. Its cross section for the first ionization is 21.5 Mb [115], which is not large enough to neglect the 10.7 Mb of the other ground state, $3s^2 3p^5 {}^2P_{1/2}^o$. The latter state can only be excited to three of the Ar^{+*} states, as given in Tab. 4.1. The energy difference between both Ar^{1+} states is 177 meV which translates into a period of 23 fs for beatings. As the IR pulse duration is much larger no major influence is expected from the energy difference. The other differences are covered by the next model.

The Fedorov-Kazakov model was originally presented for an arbitrary number of Ar^{+*} states in Sec. 4.4.1. Here all identified Ar^{+*} states will be taken into account.

To test the influence of the two Ar^{1+} ground states, they need to be populated. As the cross sections relate as 2:1 the initial conditions

$$\langle 3s^2 3p^5 {}^2P_{3/2}^o | \Psi(t = -\infty) \rangle = \sqrt{2/3} \quad (4.18a)$$

$$\langle 3s^2 3p^5 {}^2P_{1/2}^o | \Psi(t = -\infty) \rangle = \sqrt{1/3} e^{i\phi_0} \quad (4.18b)$$

with a free relative phase of ϕ_0 are chosen. As the constant phase is not justified more than by being the simplest assumption, the following model will only show the influence of the added states and couplings, while the influence of the first ionization remains unknown. Changing ϕ_0 will only give a very rough idea of relevance of the missing first ionization.

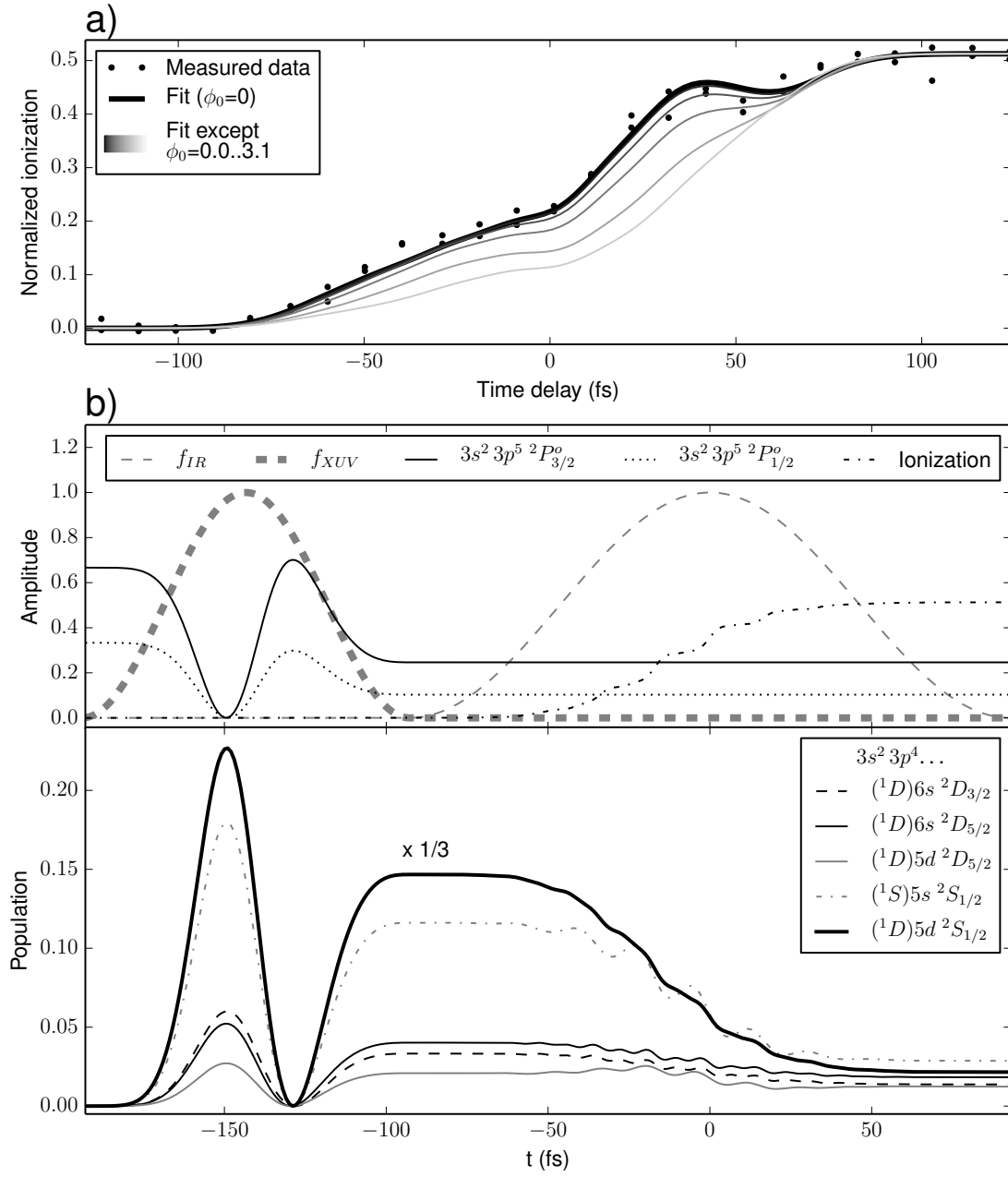


Figure 4.24: Result of a fit of a model with 2 Ar^{1+} states and all 5 Ar^{++} states: a) Fitted ionization for $\phi_0 = 0$ and the corresponding experimental yields. The influence of the initial conditions is shown by plotting the model results for other ϕ_0 but parameters fitted for $\phi_0 = 0$. These curves were normalized to the terminal height of the $\phi_0 = 0$ dependence. b) shows the populations and field envelopes for $\phi_0 = 0$. The high XUV-IR delay avoids overlapping XUV and IR fields.

It is straightforward to add the interaction for another Ar^{1+} state to the model described by Eq. (4.13) and Eq. (4.14). Without using the effective state, the model is parametrized by maximum Rabi frequencies for each allowed XUV excitation (8 constants, see Tab. 4.1), a Δe_n and Γ_n for each of the five states, u_p and the pulse durations τ_{XUV} and τ_{IR} .

The maximum Rabi frequencies encode the excitation dipole moments, which are in principle complex quantities. Their phase is important for the interference effects between contributions from different couplings to the same state. The phases can be chosen such that all dipole moments are real [116] and in this model it is further simplified that they are positive.

The fitting parameters are chosen as follows:

- Using the Rabi frequencies, u_p and ionization rates Γ_n would result in 14 parameters. To reduce the number to two, these values are parametrized by the XUV and IR intensity.
- It was discussed that the detuning rate Δe_{eff} is an effective parameter and much lower than calculated from the central wavelength of the XUV and energies of the states because the spectrum of harmonic 17 is broader than assumed by Fedorov and Kazakov (p. 117). Obtaining effective Δe_n is not feasible here, because 5 additional fit parameters would be introduced. It is chosen to set the Δe_n to 0, instead of the full value as the fitted value for the effective state model was only 29 % of the expected value. Using this percentage as a factor to the five Δe_n is not feasible as the position of the states relative to the harmonic spectrum is not constant.
- The pulse durations τ_{IR} and τ_{XUV} and the parameter Y_{coef} for signal height correction are fitted.

The fit is conducted with $\phi_0 = 0$ and the resulting curve is shown in Fig. 4.24a. The quality of the reproduction of the experimental curve is comparable to the fit's with the effective state. Fig. 4.24b shows the behavior of the Ar^{1+} and Ar^{+*} populations. The populations of both Ar^{1+} ground states maintain a time independent ratio. The majority of the population (maximum: 69 %) of the Ar^{+*} states is in the most important state $3s^2 3p^4(^1D)5d^2 S_{1/2}$ followed by $3s^2 3p^4(^1S)5s^2 S_{1/2}$ (maximum: 18 %). The other states never contain more than 6 %. $3s^2 3p^4(^1D)5d^2 S_{1/2}$ and the other state's population maintain a roughly time independent ratio. $3s^2 3p^4(^1S)5s^2 S_{1/2}$ shows a slower ionization as its cross section is smaller (Fig. 4.15: 2.81 Mb) than $3s^2 3p^4(^1D)5d^2 S_{1/2}$'s cross section (Fig. 4.15: 3.99 Mb). The three other states also have smaller cross sections (Fig. 4.15: <0.87 Mb) and are ionized even slower. The similar behavior among the Ar^{1+} and Ar^{+*} states and the dominance of $3s^2 3p^4(^1D)5d^2 S_{1/2}$ explains why this fitting result is similar to the fitting result of the effective state model and confirms the former merging of the Ar^{+*} state to the effective state and only on Ar^{1+} state.

The fitted parameters are:

- IR intensity: $(1.74 \pm 0.07) \text{ TW/cm}^2$ (result from fit using the effective state: 2.0...2.5 TW/cm^2)

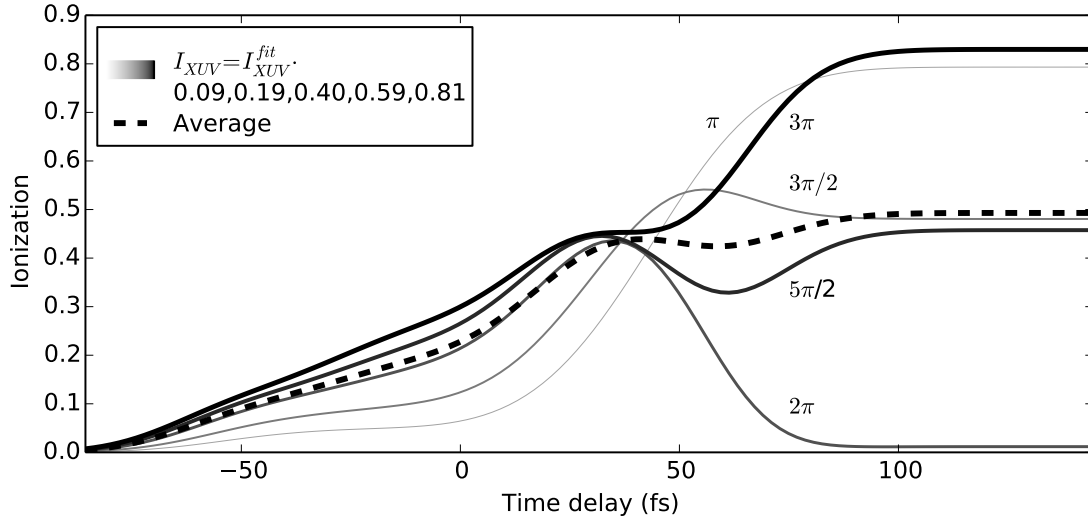


Figure 4.25: Ar^{2+} yield as a function of delay from the effective Ar^{+*} state model for different XUV intensities and a weighted average over them. Each curve is labeled with its Rabi phase. See text for details.

- XUV intensity: $(2.1 \pm 0.1) \text{ TW/cm}^2$ (result from fit using the effective state: 3.5 TW/cm^2)
- τ_{IR} : $(92.8 \pm 0.4) \text{ fs}$ (result from fit using the effective state: 86 fs)
- τ_{XUV} : $(51 \pm 1) \text{ fs}$ (result from fit using the effective state: 47 fs)
- Y_{coef} : 1.12 ± 0.03 (Expected: 1)

The new fitting parameters are similar to those from Sec. 4.4.2. The effective XUV intensity is still comparable with the effective state results but closer to the expectation of 2 TW/cm^2 for the peak intensity.

Modeling of the first ionization would replace the initial conditions by a transfer mechanism from the Ar ground state to the Ar^{1+} ground states. The used cross sections for this transition determine the strength of the mechanism but do not provide any phase information. To gain insight into its importance, Fig. 4.24a changes the phase ϕ_0 . The structure of the dependence changes and the minimum at 50 fs vanishes. Therefore, it appears likely that the missing ionization mechanism influences the shape of the delay dependent Ar^{2+} yield.

4.5.2 XUV Intensity Averaging

According to the Fedorov-Kazakov model the Ar^{2+} yield changes nonlinearly with XUV intensity, which is fluctuating from shot to shot (Fig. 4.9). As the measured Ar^{2+} is an

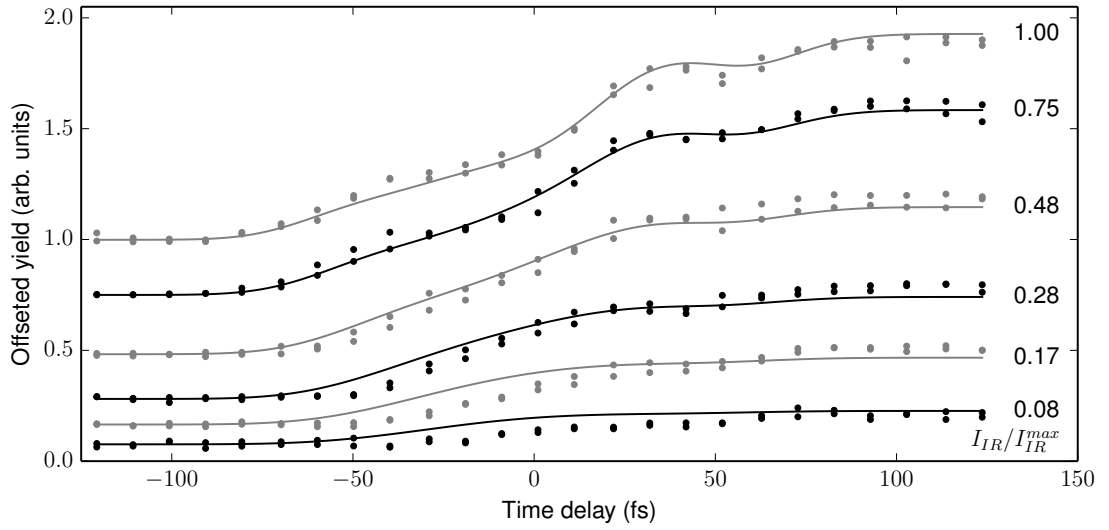


Figure 4.26: Volume averaging fit (solid lines) together with the respective measurement data (dots)

average over typically 256 laser shots, the modeled Ar^{2+} yield should be averaged over XUV laser intensities too.

Another source of differences in the XUV intensity is the spatial distribution in the interaction region. The gas nozzle has a diameter of $500\text{ }\mu\text{m}$ and the IR focus is about $10\text{ }\mu\text{m}$. The XUV focus is much smaller: $3\text{ }\mu\text{m}$ [98]. Hence, it is sufficient to average the Ar^{2+} yield over regions of different XUV intensity but constant IR intensity and gas density.

Finding the distribution of XUV intensities to take both sources of changes into account requires a convolution of the two corresponding distributions. Both contributions are described by Gaussian functions. The convolution of two Gaussian functions is a Gaussian function. As the actual width and origin does not matter for the averaging the section simplifies that volumes and laser shots with different XUV intensities are taken into account by calculating only one average, which will simply be called focal volume averaging.

Fig. 4.25 shows the influence of the Rabi frequency on the structure of the Ar^{2+} yield. As discussed in Sec. 4.4.2 XUV intensities translate into Rabi frequencies. At constant pulse shape and duration they map to specific Rabi oscillations and Ar^{2+} yield curves.

The picture also shows a weighted average. Each of the other curves represents an area of the focus with a different XUV intensity and hence Ar^{1+} fraction. As the model's starting point is Ar^{1+} and its concentration is proportional to XUV intensity, the weights are the product of the corresponding area and XUV intensity.

Despite the different shapes, the average is close to the result of the effective state model (Fig. 4.19). This remains true if the area is split into more and smaller sections than the shown five. The reason can be understood by observing the curve shapes: The

Table 4.4: Comparison of parameters from the intensity averaged and effective state fit (Tab. 4.3). The error estimations stem from the fits.

Parameter	Intensity averaged fit	Effective state fit	Ratio
$\Omega_{eff}(\text{fs}^{-1})$	0.174583 ± 0.000022	0.174188 ± 0.000006	1.00
$\Delta e_{eff}(\text{fs}^{-1})$	-0.01258 ± 0.00042	0.00158 ± 0.00011	-7.94
$u_p(\text{fs}^{-1})$	0.1357 ± 0.0034	0.1732 ± 0.0056	0.78
$\Gamma_{eff}(\text{fs}^{-1})$	0.00492 ± 0.00019	0.00498 ± 0.00021	0.99
$\tau_{IR}(\text{fs})$	85.6 ± 1.0	86.4 ± 1.8	0.99
$\tau_{XUV}(\text{fs})$	58.87 ± 0.72	47.44 ± 0.24	1.24
Y_{coef}	1.077 ± 0.015	1.079 ± 0.016	1.00

curve shapes with high intensities have a maximum around 40 fs. They differ in their final height: $\phi_{Rabi}(t = +\infty) = 2\pi$ like curves end close to zero, $\phi_{Rabi}(t = +\infty) = 3\pi/2$ and $5\pi/2$ like curves stay close to the middle and $\phi_{Rabi}(t = +\infty) = \pi$ and 3π like curves terminate at high values. The average of these final parts of the dependences should be in the middle, which is close to the result of the effective state model ($\phi_{Rabi}(t = +\infty) = 5\pi/2$). The minimum at larger delay can be understood via the weights. The curves with the largest weights are described by $\phi_{Rabi}(t = +\infty) = 3\pi$, which is stationary at 40 fs and rises after the minimum. The curve belonging to $5\pi/2$ already contains the minimum and 2π denotes a curve falling at the beginning of the minimum.

The model parameters for Fig. 4.26 stem from a fit of its average curve to the measurement. The fit is parametrized via the parameters for the effective state model at the highest XUV intensity, Ω_{eff} , Δe_{eff} , u_p , Γ_{eff} , τ_{IR} , τ_{XUV} and Y_{coef} . Fig. 4.26 shows the experimental data together with the fit result. The measurement is reproduced as good as by the effective Ar^{2+} state model fit. Both fitting methods are equal except that the correction for time overlap t_0 was omitted. Ω_{eff} parametrizes the XUV intensity at the center of the focus.

Tab. 4.4 displays the fitted parameters and compares them to values from the effective state fit. Ω_{eff} , u_p , Γ_{eff} and τ_{IR} are the same. Δe_{eff} is smaller. As discussed for the effective state fit, it may be due to the bandwidth of the XUV pulse. τ_{XUV} is bigger than for the effective state fit. This compensates two differences:

- The averaging smears out the minimum at a delay of 50 fs. To compensate that, the minimum is pronounced by reducing the ratio τ_{IR}/τ_{XUV} . As discussed for Fig. 4.21 it increases the visibility of the minimum. As τ_{IR} is fixed by the duration of the slope, only τ_{XUV} can be increased within the fit.
- The effective state model explains the Ar^{2+} yield with a Rabi oscillation described by its maximum Rabi phase $\phi_{Rabi}(t = +\infty)(t) = \int_{-\infty}^{\infty} |\Omega_{eff}(t')| f_{XUV}(t') dt'$ (Eq. (4.16)) of about $5/2\pi$. The average of the curves for the different XUV intensities should be approximately the same. The value for Ω_{eff} stated in Tab. 4.4 is the maximum of all curves. The average Ω_{eff} for all volume average curves will be lower. The given value is equal to the value of the effective state fit and hence

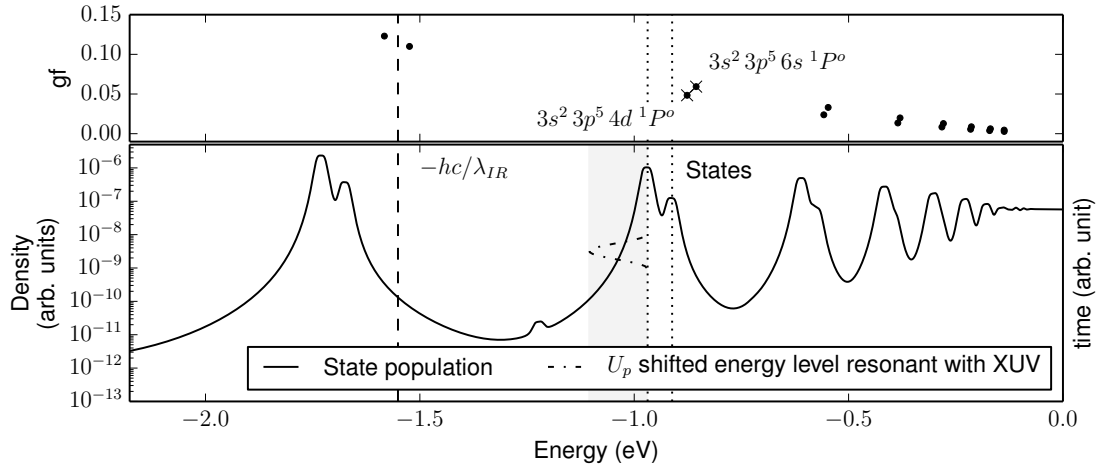


Figure 4.27: Weighted oscillator strength gf for transitions from the ground state [118] to Ar^* states: Their energies are calculated from the transition frequencies and the position of the ground state from the Opacity project. The state population distribution results from a broad band XUV pulse. The other lines are explained in the text.

too low, unless the XUV pulse duration compensates by elongation.

In summary, using an effective XUV intensity instead of volume and fluctuation averaging results in almost the same result and is a valid simplification.

4.5.3 TDSE Simulations

This section complements the evaluation of the assumptions by applying the Fedorov-Kazakov model to a well-defined situation. A code that evaluates the time dependent Schrödinger equation for a single electron in an effective potential, which represents the Ar atom was written by H.G. Muller. In the publication by Nandor et al. [128] it reproduced experimental data with high accuracy. An Ar^{1+} potential is not available.

In the effective state model Ar^{1+} is excited to Ar^{+*} by an XUV pulse and then ionized by an IR pulse. As no specific feature of Ar^{1+} is used, the process can be represented by the TDSE code in Ar: The XUV pulse excites Ar to an excited state, which is then ionized by an IR pulse to Ar^{1+} .

Comparing the yields predicted by the TDSE code and the Fedorov-Kazakov model reveals the importance of the additional assumptions made by Fedorov and Kazakov. This is complementary to the comparison with experimental data as the field parameters are well-defined, without any (volume) averaging effects or the first ionization. On the other hand the parameters of the experiment cannot be used directly. The next paragraph translates the conditions.

Translation of Parameters Fig. 4.27 shows the state population distribution as a function of energy after a single cycle XUV pulse has excited the Ar atom from its ground state. The peaks correspond to the energy of the accessible states. Their energies are negative because the states are bound.

The upper part of the graph shows data from the Opacity project [118]. The states from both sources should be at the same position but differ. They have the same structure of two series converging towards zero. The first ionization energy is

- in NIST database 15.760 eV [129],
- in Opacity project 15.030 eV and
- in TDSE output 15.819 eV.

These deviations suggest a limited comparability of the energy scales solely sufficient to identify the gf values of the states.

The conditions for Ar^{1+} are mapped to Ar by adapting the pulse parameters for IR and XUV. The electric field of the pulses have an \cos^2 envelope.

- The favored Ar^* state should be suitable for the mechanism and have a small binding energy, which is comparable to the binding energy of the Ar^{+*} states (0.9 eV). The Ar states in that region pair. $3s^2 3p^5 6s \ ^1P^o$ and $3s^2 3p^5 4d \ ^1P^o$ are chosen for their similar binding energy (0.91 and 0.97 eV). Additionally, smaller energies would result in energetically even closer states and they are already nearer than within the Ar^{+*} states of the original model, where the energy difference between the most important state and its closest neighbor is 220 meV. The XUV central wavelength is chosen for minimal detuning for the excitation from the ground state to $3s^2 3p^5 4d \ ^1P^o$. It is 83.5 nm.
- The IR central wavelength is left at $\lambda_{IR} = 790$ nm. The energy of one IR is sufficient to ionize the chosen Ar states (Fig. 4.27).
- The number of cycles, 122, of the XUV pulse preserves the relation of the XUV bandwidth (FWHM: Experiment: 700 meV⁴, TDSE: 173 meV) to the energy difference of the most important states to its energetic neighbors (Experiment: 225 meV, TDSE: 57 meV).
- The number of IR cycles, 22, is chosen to preserve the XUV-IR pulse duration ratio.
- The XUV intensities are varied with the objective of observing contrasting shapes explainable by different numbers of Rabi cycles.
- The IR intensities are varied to observe the same minimum around overlap as in the effective state model. Fig. 4.27 shows the energies, that can be resonantly excited by the XUV and the Up shift at different times because of the changing

⁴The calculation uses the outdated value of 700 meV instead of 900 meV.

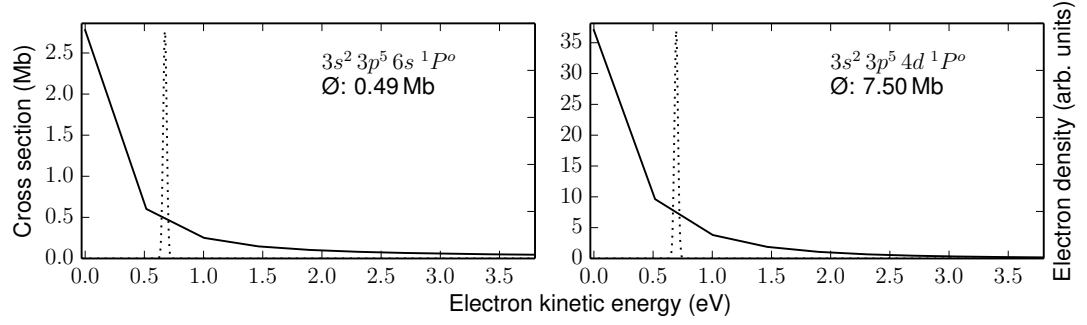


Figure 4.28: Photoionization cross sections [118] (thin line) for the Ar* states' configurations. Each plot gives the electron energy distribution (dashed line) corresponding to the IR spectrum and averages the spectrum over this quantity to generate an effective value for the IR photoionization cross section.

IR intensity (dashed dotted line). As expected, it neither indicates a resonant excitation of the other Ar* state, $3s^2 3p^5 6s ^1P^o$, nor a shift large enough to reach the next pair of Ar states.

Fedorov-Kazakov and TDSE Model Implementation A Fedorov-Kazakov model is implemented for the scenario. It takes only the Ar ground state, the two states $3s^2 3p^5 6s ^1P^o$ and $3s^2 3p^5 4d ^1P^o$ and the Ar^{1+} continuum into account. The weighted oscillator strengths gf are 5.93×10^{-2} and 4.84×10^{-2} (Fig. 4.27). The cross sections for the ionization of the Ar* states by the IR are read from the Opacity project [118] to be 0.60 Mb and 9.63 Mb. Fig. 4.28 shows the cross section data and the electron energy distributions.

The TDSE code is run with different delays between the pulses. It returns the energy distribution of the electron from which the ionization is calculated by integrating over positive energies. Both models use the same fields.

Result of Comparison Both models return delay-dependent Ar^{1+} yields that can be understood in terms of the final Rabi phase (Fig. 4.17, 4.25). However, results for the same IR and XUV intensities suggest different final Rabi phases. The origin of the discrepancy is not known. For comparability, both gf values have been increased by 2.8 and the yields were matched with a constant factor.

Fig. 4.29 compares both models. Fig. 4.29a scans the XUV intensity at an IR intensity of 2.25 TW/cm^2 , which is similar to the parameters of the effective state model. Rabi oscillation with rising frequencies are visible in the TDSE data: The yield at large delays is rising till 5.1 TW/cm^2 ($\phi_{\text{Rabi}}(t = +\infty) = \pi$). 23.7 TW/cm^2 reveals a minimum final yield with a maximum around overlap ($\phi_{\text{Rabi}}(t = +\infty) = 2\pi$). For the highest plotted XUV intensity, 67.9 TW/cm^2 , the yield shows a local maximum and minimum and the yield is high for large delays ($\phi_{\text{Rabi}}(t = +\infty) = 3\pi$). The Fedorov-Kazakov

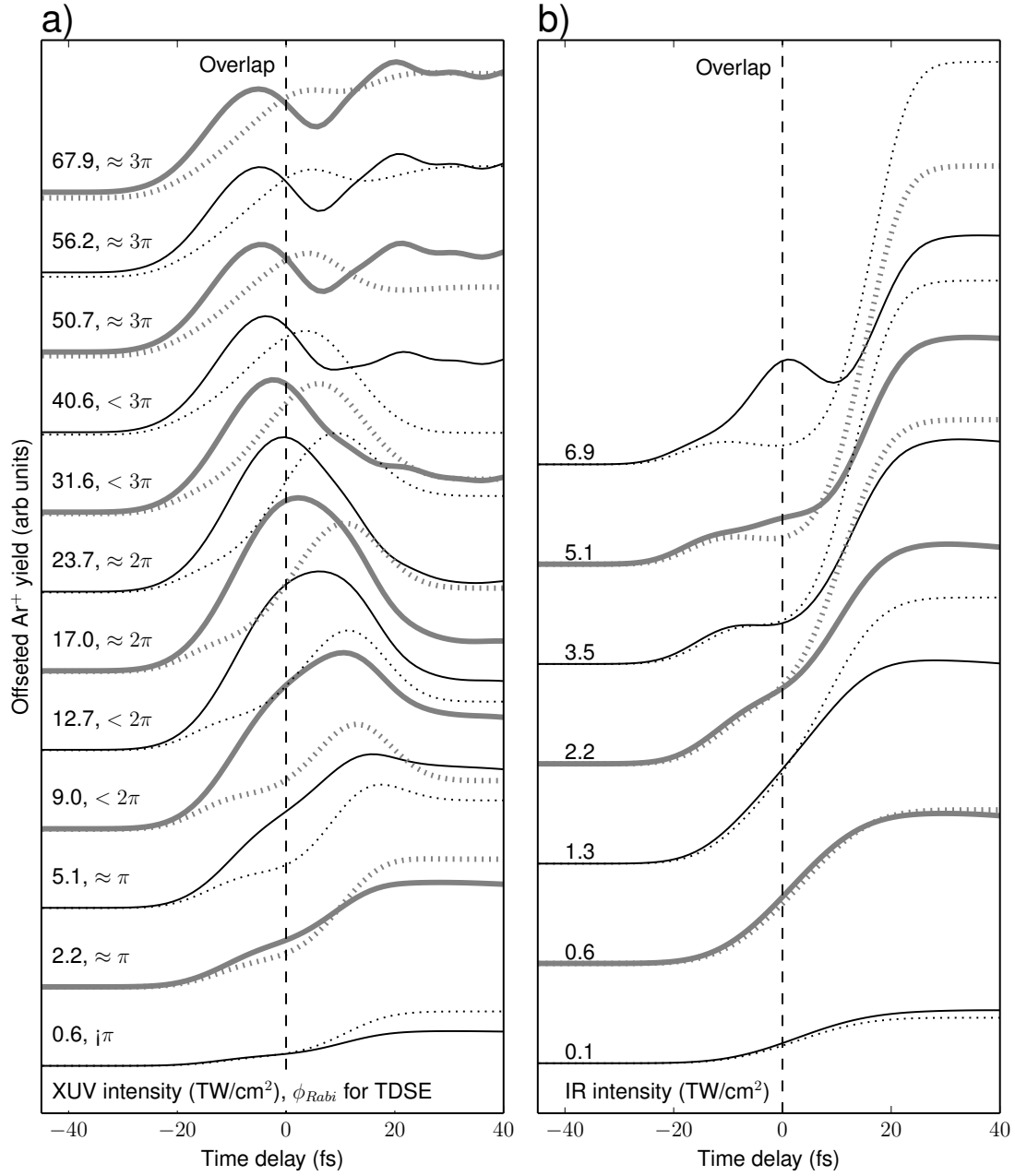


Figure 4.29: Comparison of the Fedorov-Kazakov model (dashed line) and TDSE results (full line). The thickness of the lines alternates to help identifying curves for the same parameters: a) XUV intensity dependence at an IR intensity of 2.25 TW/cm². b) IR intensity dependence at an XUV intensity of 5.62 TW/cm².

model results are structurally identical. The specific relation of Rabi phase and XUV intensity is different. For example at 40.6 TW/cm^2 the Fedorov-Kazakov model results in a $\phi_{Rabi}(t = +\infty) = 2\pi$ shape while the TDSE curve is closer to $\phi_{Rabi}(t = +\infty) = 3\pi$. The detailed curve shapes are different. The TDSE shows the first maximum of the Ar yield at a smaller delay and the reduction of yield at delay zero is only visible at 2.2, and 5.1 TW/cm^2 .

Fig. 4.29b scans IR intensity for an XUV intensity of 5.62 TW/cm^2 , which is chosen to produce a $\phi_{Rabi}(t = +\infty) = \pi$ curve shape. Both models present a reduction of yield around overlap. It is less pronounced in the TDSE. An exception is visible at the highest IR intensity of 6.9 TW/cm^2 : Only the TDSE solution's minimum shifts away from overlap towards higher delays. This is not reproduced in the Fedorov-Kazakov model indicating a new mechanism important at high intensity. The new shape shows a minimum at a positive delay. The yields at large delays and high IR intensities are higher according to the Fedorov-Kazakov model than according to the TDSE solution.

The comparison shows that both features, the Rabi oscillation-dependent shape and the U_p borne minimum at overlap, occur despite the different assumptions of the TDSE calculation and the Fedorov-Kazakov model. The computation time was too long to attempt a fit of the TDSE results to the experimental data.

4.5.4 Discussion

There are two groups of assumptions for the effective state model. The first is inherited from the publication of Fedorov and Kazakov [122]. The second set is specific for the experimental conditions and made to apply the Fedorov-Kazakov model to the experimental situation. This section estimates them as far as possible:

Fedorov-Kazakov Assumptions

- The envelopes of the electric fields are smooth: Structures in the IR pulse envelope would be visible in the sideband scan (Fig. 4.3), as the XUV is much shorter than the IR pulse. The XUV's smoothness is unknown.
- The pulses are Fourier limited: Eq. (1.10) converts the bandwidths to a Fourier limited FWHM pulse duration of 34 fs for the IR, which is much shorter than $(71 \pm 3) \text{ fs}$. The XUV pulse duration of $(20 \pm 3) \text{ fs}$ from Sec. 4.2 and the even greater values from the fit results are longer than the pulse duration of 2 fs supported by only the bandwidth of harmonic 17.
- The transition dipole moment is smooth for the second ionization: Fig. 4.15 shows a proportional quantity, the cross section, as a function of energy. It is dominated by peaks. As Fedorov and Kazakov do not state an exact definition of smooth, it remains unclear whether the assumption is justified.
- The XUV produces a negligible Stark shift: The maximum U_p shift (see Eq. (2.2)) of the XUV at $2 \times 10^{12} \text{ W/cm}^2$ is 0.4 meV. Analogous to the parameter u_p for the

IR, this means a rate for the phase factor of 0.00061 fs^{-1} , which is indeed negligible even at the longest occurring XUV pulse duration of 59 fs.

- The spectrum of harmonic 17 is narrow compared to the energy differences of the states: As discussed on page 117, the FWHM of harmonic 17 is much larger than the energy differences between the Ar^{+*} states.

The last two assumptions, the rotating wave approximation, the perturbation approach, that there are no transitions within the continuum and that $C_{\text{Ar}^{2+} E}(t)$ does not have population at threshold at any time are tested by comparison to the TDSE model. The result is still qualitatively the same concerning the influence of IR and XUV on the structure of the Ar^{2+} yield.

Application Assumptions

- The first ionization is not represented: As discussed in Sec. 4.5.1 this may alter the Ar^{2+} yield and especially the Rabi oscillations.
- One state is used for both Ar^{1+} ground states; The Ar^{+*} states are represented by one effective state: Sec. 4.5.1 implements a model without both simplifications. The states behave equivalent and result in similar fitting parameters.
- Only harmonic 17 is relevant: Even though there are no other states accessible by the harmonics and also ionizable by one IR photon other states are coupled to the Ar^{1+} ground states by the XUV. For example $3s^2 3p^4(^1S)4s^2 S_{1/2}$ is coupled to both ground states of Ar^{1+} by harmonic 13. The other harmonics will cause Rabi oscillations between the Ar^{1+} ground state and other excited Ar^{1+} states. This will increase the rate at which the Ar^{1+} ground states are depopulated. Judging from the model in Sec. 4.5.1, these additional states are expected to behave as the Ar^{+*} states of harmonic 17 only without the second ionization. As a result the effective oscillator strength should take these states into account. On the other hand the calculation assumes that the entire XUV intensity belongs to harmonic 17 despite Fig. 4.2 which shows that harmonic 11, 13 and 15 are present too. If the gf values are the same for the Ar^{+*} states for all harmonics, redistributing the intensity would not change the effective Rabi frequency. As the entire model is qualitative, the chapter simplifies that all XUV intensity is within harmonic 17.
- The measurement averages over laser fluctuations and a volume with different XUV intensities. The existence of an effective XUV intensity is assumed. Sec. 4.5.2 conducts the averaging and thereby shows the existence of such a quantity.
- The initially assumed pulse parameters differ from the parameters used to fit the Ar^{2+} yield. Most notably, as discussed on page 118 the IR intensity is lower than expected by a factor of 50 and the pulse durations (Tab. 4.3) would result in a sideband FWHM of 98.6 fs (Eq. (4.1)) instead of the measured 74 fs. Only the

position of the overlap is clearly an accurate and redundant result of the fit. However, as the pulse parameters are effective only a correct order of magnitude is to be expected.

Conclusion Most of the assumptions could be tested or verified. The three exceptions are the not Fourier limited pulses, the smooth transition dipole moments from the second ionization and the first ionization. These are only covered by the agreement of the fit to the measured data.

In conclusion the model explains the experimental data without being rigorous.

4.6 Summary

XUV-IR pump-probe experiments with an atomic gas jet of Ar showed an enhanced Ar^{2+} production in case the IR arrived after the XUV. The delay dependence of the Ar^{2+} exhibited a region of reduced yield at a delay of 0 fs, which vanished for small IR intensities, and a reduced yield at a delay of 50 fs, which did not depend on the IR intensity. Several time-of-flight measurements of the Ar^{1+} and Ar^{2+} yield for different delays and IR intensities revealed the ionization mechanism: A first XUV photon ionizes Ar to a Ar^{1+} ground state. A second XUV photon from the same pulse excites Ar^{1+} to a Ar^{+*} state, which is finally ionized by the IR. VMI photoelectron spectra confirm the presence of electrons with the corresponding energies for the ionizations and the correlation of the ions and electron originating from the ionization of Ar^{+*} , which is identified with tabulated Ar^{1+} states.

A perturbative quantum mechanical model of the XUV excitation and IR ionization is implemented with a single, effective Ar^{+*} state. Comparison of modeled and measured Ar^{2+} yields suggest that an IR Stark shift of the Ar^{+*} state reduced the Ar^{2+} yield at a delay of 0 fs by moving the state from resonance with the XUV and that the XUV intensity is high enough ($3.5 \times 10^{12} \text{ W/cm}^2$) to excite Ar^{1+} to Ar^{+*} and also stimulate re-emission of the XUV photon. The resulting oscillation of the population between both states is a Rabi oscillation and the first minimum in the population of Ar^{+*} explains the reduction in Ar^{2+} yield at a delay of 50 fs. This is the first time Rabi oscillations are time-resolved in the XUV regime.

The quantum mechanical model adequately fits the measured Ar^{2+} yield as a function of delay and IR intensity. The respective parameters match with the experimental conditions. A review of the assumptions of the model shows that it is qualitative and the identification of the influence of Stark shift and Rabi oscillations is valid.

Summary

This thesis described a design for an attosecond-attosecond pump-probe experimental setup. To date qualified sources of pulses are unavailable but pose a promising way to time resolutions covering the natural time scale of electrons. So far only one group has performed experiments close to the border to attoseconds. Consequently, a design is proposed to maximize the intensity of the attosecond pulses: First, a noncollinear optical parametric chirped pulse amplification (NOPCPA) providing intense and short IR pulses with an expected pulse energy of 15 mJ and duration of 7 fs was built. However, problems with the synchronization of the two involved laser cavities, a breakdown in the pump laser and instabilities in the pump beam delayed the project beyond the frame of the thesis. All further parts of the setup were built and tested to the extend feasible without the NOPCPA. Consequently, the thesis describes a design and not a working setup. A high harmonic generation (HHG) setup was built to create attosecond XUV pulses from this IR. Experimental stations were constructed to prepare the radiation and measure the resulting events.

Different gating techniques are available to reduce the XUV pulse duration. A simulation of them was developed to compare the resulting energy and to choose the most efficient method. Polarization gating, double optical gating (DOG) and ionization gating were discussed to be the most promising gating techniques. To better select the best method and provide experimental parameters such as gas pressure and cell length a simulation was developed and numerically implemented, which attributes a pulse energy and duration to each method and experimental situation. The chosen approach calculated the input spectrum, applied gating optics and estimated the evolution of the IR pulse in the HHG medium considering focusing, gas dispersion and absorption, the Kerr effect, ionization, Brunel harmonics and plasma dispersion. The Lewenstein model returned the polarization, which results in the XUV pulse. As the calculation was limited to the time dependence of the fields on the axis of propagation an effective area approach was used to calculate the XUV field via a modified Maxwell equation.

Using a rough understanding of the parameters developed in this thesis and an algorithm maximizing a figure of merit (FOM) each gating method was reproduced and optimal parameters were found. The FOM was the conversion efficiency modified to fall quickly if the pulse became too long. A conceptual problem arose for polarization gating and DOG: High intensities were beneficial for the conversion efficiency and the pulse duration due to the ionization gating effect. Therefore, the optimizations gravitated towards hybrid solutions using the polarization gating/DOG mechanism and ionization gating. The latter shortened the pulse by limiting the phase-matching to one IR cycle. To enforce the intended mechanisms, Φ , which quantified the phase-matching, was defined

Summary

and used in the FOM. Additionally, hybrid DOG was introduced as a new technique.

The resulting efficiencies were 1.75×10^{-7} (ionization gating) 1.08×10^{-7} (polarization gating) 1.22×10^{-7} (DOG) and 2.25×10^{-7} (hybrid DOG). This is the first comparison of these techniques. The numbers show the same ordering as the best reported cases for each method but smaller ratios.

As the efficiencies and parameters were not too different, a HHG setup flexible enough to allow all methods was outlined. The large IR energy required a long cell with a large hole. A sophisticated vacuum system was designed and experimentally verified to ensure that the large resulting gas flow had no detrimental effects.

The last part of the design focuses the XUV radiation into the interaction region of a VMI. It suffers from the low reflectivity in this frequency regime. The solution for XUV-IR pump-probe experiments is a multilayer mirror. Alternatively, XUV-XUV pump-probe experiments use B_4C mirrors in grazing incidence to collimate, split and focus the XUV radiation. An XUV characterization unit records beam shape, spectrum or total energy. A computer system was tested to record synchronized single shot data from both sources.

Pump-probe XUV-IR experiments with Ar time-resolved Rabi oscillations for the first time in the XUV frequency regime. The investigation benefited from the high XUV intensity of another, HHG-based setup. Time of flight measurements revealed a process starting with the ionization of Ar by one XUV photon and continuing with the excitation of Ar^{1+} by a further XUV photon to a state Ar^{++} , which could then decay on the picosecond time scale or get ionized by an IR photon. Five candidate Ar^{++} states were found in the literature. They had plausible properties in terms of excitation, ionization and decay. VMI measurements validated the model by showing electrons at energies predicted by the binding energy of one state for the IR ionization, which concurred with Ar^{2+} TOF measurements.

This model did not explain deviations in the Ar^{2+} yield as a function of delay from a simple step function. Therefore, a quantum mechanical model was implemented, which started already at Ar^{1+} and merged all five Ar^{++} into an effective state. The Stark shift due to the IR intensity and the final ionization was taken into account together with further assumptions for this perturbative model. The model was fitted to the measured data with plausible parameters. The only two severe exceptions could be explained by proposing a new IR intensity, which may have originated from different XUV and IR focus positions. The quantum mechanical model explained the delay dependence by a combination of (i) the Stark effect, which induced a detuning for the XUV excitation, and (ii) Rabi oscillations between Ar^{1+} and Ar^{++} , which created a minimum in the Ar^{++} population.

The assumptions of the simple model with one effective state were reviewed using TDSE calculations, a quantum mechanical model taking all Ar^{++} states into account and an effective state model, which performed volume and laser shot averaging: The model is valid but not rigorous.

Outlook

This thesis is centered on the construction of a source. It is not complete and therefore followed by a project of a team at the Max-Born-Institute. Therein, an enhanced version of the NOPCPA described in Chap. 1 is developed. The new design is pumped by a stronger, more recent thin disk laser, which already outperformed the pulse energy of 290 mJ stated in Sec. 1.2 by 210 mJ [130].

An operational NOPCPA can therefore provide more energetic pulses to the HHG than anticipated. In this case the theoretical optimization in Chap. 2 would have to be updated using the same strategies and software. The new process parameters can then be used to estimate the need for changes to the existing, highly flexible HHG setup.

The HHG simulation can also be extended. First, it is semiquantitative so that exact quantitative agreement with experiments is not necessarily given. However, checking the qualitative statements might confirm its validity. Of course, using this setup would be promising, as both are designed for the same purpose.

The model can be extended. It would be simple to implement pressure gradients along the propagation axis. This is not important for the present system as the cell has a diameter of 100 mm, which is much bigger than the optimal 4 mm diameter of the orifices, so that the pressure gradients are negligible. However other setups reported gradients [131] and additional control over the related phase matching might enhance efficiency. Another relative simple extension would be the parameters necessary to represent two-color gating (ref. Sec.2.1).

The simulation approach can be extended to a radial dimension within the HHG cell: Currently, the fields on the axis of propagation are used to represent the entire process via an effective area approach based upon the assumption that the IR is a Gaussian beam. Its parameters are known so that a representation of the IR field at any position in the HHG cell is available. Using the radial symmetry of the 3d problem the calculation can be reduced to a radial dimension and the implemented propagation coordinate. Instead of calculating the HHG polarization only on the axis of propagation, the Lewenstein model would then additionally be computed at several points with different distances from the axis of propagation. The new evaluation of the XUV field at the end of the medium then depends on the radial propagation of the XUV. Such a propagator can be implemented in Fourier space. This method would remove the effective area approach and provide the XUV field as a function of time and radius. On the one hand the divergence of the XUV which is invaluable for the estimation of the focus size and focus intensity would become accessible (refer to Sec. 3.3 and 3.4). Additionally, the error induced by the effective area approach becomes visible. On the other hand manual optimization becomes more difficult because the current visualization concepts fail due to the additional dimension and the computation time will rise depending on the number

of radii for the computation, which also impedes the automatic fine tuning.

Chap. 4 describes a pump-probe experiment and explains it using a perturbative quantum mechanical model. An evaluation of the assumptions leads to the conclusion that the model's parameters are only effective. Additional theoretical investigations can result in an enhanced model. A key issue is the missing representation of the first ionization. As then two electrons are involved an analytic treatment may become impossible and TDSE calculations would be necessary.

This would not only enhance the understanding of the process itself but potentially open a new way to measure XUV field strength: The structure of the delay dependent Ar^{2+} yield shows a number of extrema related to the Rabi phase Eq. (4.16) $\phi_{\text{Rabi}}(t) = |\Omega_0| \int_{-\infty}^t f_{\text{XUV}}(t') dt'$. It is therefore possible to 'count' the XUV intensity. Beyond that structural relation, the current model shows features encoding the IR field strength (depth of Stark shift induced yield reduction at overlap and saturation of maximum Ar^{2+} yield), IR pulse duration (main slope of Ar^{2+} production over delay), relation of both pulse durations (width of Rabi-born minimum). Those functions are more subtle pointing at lower accuracy even if an enhanced model can reduce the assumptions and replace the effective quantities. However, even effective quantities would be complementary information for the potential Rabi-born XUV field strength measurement.

An experimental validation of the Rabi-born XUV field strength measurement should start by varying the XUV intensity e.g. with a gas attenuator, which is a volume of gas used to absorb a fraction of the XUV photons. Such devices were already used for fs pulses [132]. Then the structural changes in the Ar^{2+} yield as a function of delay can be compared to the calculations. The chapter also discusses the influence of the IR pulse duration. It shows that a reduction would rise the visibility of the structure stemming from the Rabi oscillations. Fig. 4.21 shows that for the given XUV pulse duration a IR pulse duration of about 9 fs would already be close to optimal. This requirement points at a possible application for the NOPCPA of Chap. 1, which is expected to deliver even shorter pulses. Using an additional laser would require a synchronization. The downside of using a shorter laser pulse would be the lower percentage of ionization, which reduces signal and hides the saturation of the ionization with IR intensity. Thereby, it only leaves the reduced Ar^{2+} yield at overlap as the only feature telling the IR intensity. Increasing the IR intensity is limited because the AC Stark shift can become too strong to see the structure of the Ar^{2+} yield and it will open additional pathways of ionization as the used IR intensity was chosen slightly under the threshold for Ar^{1+} generation by IR only.

The shorter IR pulse which is necessary to measure the XUV field strength in this approach makes it unlikely that this method will become important in the field of attosecond science esp. as FROG-CRAB can retrieve the IR field and the intensity envelope of the XUV [133] and is established in many labs [14].

In summary, the thesis is part of a process towards as-as pump-probe experiments at the Max-Born-Institute and can generally be used for HHG optimization in that errand. It describes experiments and the resulting model, which explains the data using the XUV driven Rabi oscillations. Future experiments have the potential to strengthen the interpretation and lead the way to a novel, complementary XUV field strength measurement.

Short Summary

This thesis described a design for an attosecond-attosecond pump-probe experimental setup. Qualified sources of pulses are unavailable to date. First, a noncollinear optical parametric chirped pulse amplification (NOPCPA) was built. However, problems delayed the project beyond the frame of the thesis. All further parts of the setup were built and tested to the extend feasible without the NOPCPA. Consequently, the thesis describes a design and not working setup. A high harmonic generation (HHG) process was built to create attosecond XUV pulses from this IR. The experimental stations were constructed to prepare the radiation and measure the resulting events.

Different gating techniques are available to reduce the XUV pulse duration. A simulation of them was developed to compare the resulting energies and to choose the most efficient method. It calculated the pulse resulting from the gating optics, the evolution of the fundamental IR pulse on the main axis of propagation in the interaction gas, the XUV polarization via the Lewenstein model and the electric field of the resulting XUV pulse. Polarization gating, double optical gating (DOG) and ionization gating were reproduced and optimized. A conceptual problem arose for polarization gating and DOG: High intensities were beneficial for the conversion efficiency and the pulse duration due to the ionization gating effect. Consequently, a more advanced approach was required for the optimization of pure polarization gating and DOG. Additionally, hybrid DOG was introduced as a new technique. This is the first comparison of the techniques. The efficiencies show the same ordering as the best reported cases for each method but less differences.

As the efficiencies and parameters were not too different a HHG setup flexible enough to allow all was built. Further technical solutions covered vacuum pumping, XUV optics with a high reflectivity and data acquisition.

Pump-probe XUV-IR experiments with Ar time resolved Rabi oscillations for the first time in the XUV frequency regime. The investigation benefited from the high XUV intensity of another, HHG based setup. Measurements showed a process starting with the ionization of Ar by one XUV photon and continuing with the excitation of Ar^{1+} by a further XUV photon to a state Ar^{+*} , which could then decay on the picosecond time scale or get ionized by an IR photon. Ar^{+*} was identified, verified and the properties were used in a quantum mechanical model incorporating the XUV excitation, IR ionization and the Stark shift of Ar^{+*} . The model explained the measured delay dependence of the Ar^{2+} yield by a combination of the Stark effect, which resulted in a reduced yield at the overlap of XUV and IR due to a detuning for the XUV excitation, and Rabi oscillations between Ar^{1+} and Ar^{+*} , which created a minimum in the Ar^{+*} population.

Deutsche Kurzzusammenfassung

Die vorliegende Arbeit beschreibt ein Design für einen Attosekunden-Attosekunden Pump-Probe Versuchsaufbau, da bisher keine geeigneten Quellen existierten. Den ersten Abschnitt stellte eine nicht kollineare, optische, parametrische, gechirpte Pulsverstärkung (NOPCPA) zur Erzeugung kurzer, intensiver IR Pulse dar. Da Probleme im NOPCPA das Projekt über den Rahmen der Promotion hinaus verzögerten, beschreibt die Arbeit ein Design und keinen fertigen Versuchsaufbau. Dennoch wurde das Setup gebaut und soweit möglich getestet. Eine Hohe Harmonischen Erzeugung (HHG) sollte daraus XUV Pulse von Attosekundendauer erzeugen. Im letzten Abschnitt würde die gewonnene Strahlung verwendet und die resultierenden Ereignisse gemessen.

Es existierten verschiedene Techniken zur Verkürzung von Pulsen aus Hoher Harmonischer Erzeugung (Gating). Eine Simulation wurde entwickelt um die resultierenden Pulsenergien zu vergleichen und die effizienteste Methode zu identifizieren. Die Berechnungen beschrieben zunächst das Laserfeld nach den entsprechenden Optiken und innerhalb des HHG-Mediums. Danach wurden die Polarisation mit dem Lewensteinmodell und das elektrische Feld des XUV-Pulses berechnet. Polarization Gating, Double Optical Gating (DOG) und Ionization Gating konnten reproduziert und optimiert werden. Bei der Optimierung von Polarization Gating und DOG wurde ein konzeptionelles Problem offensichtlich: Hohe Intensitäten waren aufgrund des Ionization Gating-Effekts für Dauer und Energie des Pulses vorteilhaft, so dass die Optimierung von reinem Polarization Gating und DOG eine komplexere Strategie erforderte. Zusätzlich wurde Hybrid DOG als neue Methode vorgeschlagen. Dies stellte den bisher ersten Vergleich der Gating-Methoden dar. Die berechneten Umwandlungsraten sind ähnlich und zeigten die gleiche Rangfolge wie die jeweils höchsten aus der Literatur.

Ein HHG-Aufbau mit einer für alle Methoden hinreichenden Flexibilität, wurde gebaut. Weitere technische Lösungen befassten sich mit Vakuumpumpen, XUV-Optiken mit hoher Reflektivität und Messdatenerfassung.

Pump-Probe-XUV-IR-Experimente mit Ar an einem weiteren Versuchsaufbau zeigten erstmals XUV-basierte Rabi-Oszillationen. Der beobachtete Prozess begann mit der Ionisation von Ar durch ein XUV-Photon zu Ar^{1+} und der Anregung zu Ar^{+*} durch ein weiteres XUV-Photon. Der angeregte Zustand Ar^{+*} konnte entweder spontan ein Photon emittieren (ps-Zeitskala) oder durch ein IR Photon ionisiert werden. Ar^{+*} wurde identifiziert, validiert und seine Eigenschaften wurden in einem quantenmechanischen Modell verwendet, das die XUV-Anregung, IR-Ionisation und den IR-Starkeffekt für Ar^{+*} einbezog. Das Modell erklärte die gemessene Abhängigkeit der Menge an Ar^{2+} als Kombination aus dem IR-Starkeffekt, welcher eine Reduktion am XUV-IR-Überlapp durch eine Verstimmung der XUV-Anregung bewirkte, und einer Rabi-Oszillationen zwischen Ar^{1+} und Ar^{+*} , welche ein Minimum in der Ar^{+*} -Population hervorrief.

Bibliography

- [1] Robert Koch. *Untersuchungen über die Ätiologie der Wundinfektionskrankheiten*. Gesammelte Werke von Robert Koch. Robert Koch-Institut, 1878.
- [2] Ferenc Krausz. The birth of attosecond physics and its coming of age. *Physica Scripta, Volume 91, Number 6*, 2016.
- [3] Eiji J. Takahashi, Pengfei Lan, Oliver D. Mücke, Yasuo Nabekawa, and Katsumi Midorikawa. Attosecond nonlinear optics using gigawatt-scale isolated attosecond pulses. *Nat Commun*, 4:–, October 2013.
- [4] P. B. Corkum. Plasma perspective on strong field multiphoton ionization. *Phys. Rev. Lett.*, 71:1994–1997, Sep 1993.
- [5] G. Sansone, E. Benedetti, F. Calegari, C. Vozzi, L. Avaldi, R. Flammini, L. Poletto, P. Villoresi, C. Altucci, R. Velotta, S. Stagira, S. De Silvestri, and M. Nisoli. Isolated single-cycle attosecond pulses. *Science*, 314(5798):443–446, 2006.
- [6] F Ferrari, F. Calegari, M. Lucchini, C. Vozzi, S. Stagira, G. Sansone, and M. Nisoli. High-energy isolated attosecond pulses generated by above-saturation few-cycle fields. *Nat Photon*, 4(12):875–879, dec 2010.
- [7] Hiroki Mashiko, Steve Gilbertson, Chengquan Li, Sabih D. Khan, Mahendra M. Shakya, Eric Moon, and Zenghu Chang. Double optical gating of high-order harmonic generation with carrier-envelope phase stabilized lasers. *Phys. Rev. Lett.*, 100:103906, Mar 2008.
- [8] C. Thaury, F. Quere, J.-P. Geindre, A. Levy, T. Ceccotti, P. Monot, M. Bougeard, F. Reau, P. d’Oliveira, P. Audebert, R. Marjoribanks, and Ph. Martin. Plasma mirrors for ultrahigh-intensity optics. *Nat Phys*, 3(6):424–429, June 2007.
- [9] P. Heissler, A. Barna, J. M. Mikhailova, Guangjin Ma, K. Khrennikov, S. Karsch, L. Veisz, I. B. Földes, and G. D. Tsakiris. Multi- μ J harmonic emission energy from laser-driven plasma. *Applied Physics B*, 118(2):195–201, 2014.
- [10] C Thaury and F Quere. High-order harmonic and attosecond pulse generation on plasma mirrors: basic mechanisms. *Journal of Physics B: Atomic, Molecular and Optical Physics*, 43(21):213001, 2010.
- [11] Maurizio Reduzzi, Paolo Carpeggiani, Sergei KÃ¼hn, Francesca Calegari, Mauro Nisoli, Salvatore Stagira, Caterina Vozzi, Peter Dombi, Subhendu Kahaly, Paris

BIBLIOGRAPHY

- Tzallas, Dimitris Charalambidis, Katalin Varju, Karoly Osvay, and Giuseppe Sansone. Advances in high-order harmonic generation sources for time-resolved investigations. *Journal of Electron Spectroscopy and Related Phenomena*, 204, Part B:257 – 268, 2015. Gas phase spectroscopic and dynamical studies at Free-Electron Lasers and other short wavelength sources.
- [12] M. Schultze, M. Fieß, N. Karpowicz, J. Gagnon, M. Korbman, M. Hofstetter, S. Neppl, A. L. Cavalieri, Y. Komninos, Th. Mercouris, C. A. Nicolaides, R. Pazourek, S. Nagele, J. Feist, J. Burgdörfer, A. M. Azzeer, R. Ernstorfer, R. Kienberger, U. Kleineberg, E. Goulielmakis, F. Krausz, and V. S. Yakovlev. Delay in photoemission. *Science*, 328(5986):1658–1662, 2010.
 - [13] M. Hentschel, R. Kienberger, Ch. Spielmann, G. A. Reider, N. Milosevic, T. Brabec, P. Corkum, U. Heinzmann, M. Drescher, and F. Krausz. Attosecond metrology. *Nature*, 414(6863):509–513, nov 2001.
 - [14] Francesca Calegari, Giuseppe Sansone, Salvatore Stagira, Caterina Vozzi, and Mauro Nisoli. Advances in attosecond science. *Journal of Physics B: Atomic, Molecular and Optical Physics*, 49(6):062001, 2016.
 - [15] Artem Rudenko and Daniel Rolles. Time-resolved studies with {FELs}. *Journal of Electron Spectroscopy and Related Phenomena*, 204, Part B:228 – 236, 2015. Gas phase spectroscopic and dynamical studies at Free-Electron Lasers and other short wavelength sources.
 - [16] C. Behrens, F.-J. Decker, Y. Ding, V. A. Dolgashev, J. Frisch, Z. Huang, P. Krejcik, H. Loos, A. Lutman, T. J. Maxwell, J. Turner, J. Wang, M.-H. Wang, J. Welch, and J. Wu. Few-femtosecond time-resolved measurements of x-ray free-electron lasers. *Nature Communications*, 5:3762–, April 2014.
 - [17] P. Tzallas, E. Skantzakis, L. A. A. Nikolopoulos, G. D. Tsakiris, and D. Charalambidis. Extreme-ultraviolet pump-probe studies of one-femtosecond-scale electron dynamics. *Nat Phys*, 7(10):781–784, oct 2011.
 - [18] P. A. Carpeggiani, P. Tzallas, A. Palacios, D. Gray, F. Martín, and D. Charalambidis. Disclosing intrinsic molecular dynamics on the 1-fs scale through extreme-ultraviolet pump-probe measurements. *Phys. Rev. A*, 89:023420, Feb 2014.
 - [19] S.M. Witte. *Terawatt-intensity few-cycle laser pulses: optical parametric chirped pulse amplification and frequency comb spectroscopy*. PhD thesis, Vrije Universiteit, Amsterdam, 2007.
 - [20] Alexander M. Rubenchik, Sergey K. Turitsyn, and Michail P. Fedoruk. Modulation instability in high power laser amplifiers. *Opt. Express*, 18(2):1380–1388, Jan 2010.
 - [21] J.C. Diels and W. Rudolph. *Ultrashort laser pulse phenomena: fundamentals, techniques, and applications on a femtosecond time scale*. Optics and photonics. Academic Press, 2006.

- [22] C. Iaconis and I. A. Walmsley. Self-referencing spectral interferometry for measuring ultrashort optical pulses. *IEEE Journal of Quantum Electronics*, 35:501–509, apr 1999.
- [23] N. Boeuf, D. Branning, I. Chaperot, E. Dauler, S. Guérin, G. Jaeger, A. Muller, and A. Migdall. *Calculating Characteristics of Non-collinear Phase-matching in Uniaxial and Biaxial Crystals*. National Institute of Standards and Technology, 1999.
- [24] Donna Strickland and Gerard Mourou. Compression of amplified chirped optical pulses. *Optics Communications*, 55(6):447 – 449, 1985.
- [25] Richard A. Baumgartner and R. Byer. Optical parametric amplification. *Quantum Electronics, IEEE Journal of*, 15(6):432–444, Jun 1979.
- [26] D. Haertle, M. Jazbinšek, G. Montemezzani, and P. Günter. Nonlinear optical coefficients and phase-matching conditions in Sn₂P₂S₆. *Opt. Express*, 13(10):3765–3776, May 2005.
- [27] J. Zheng and H. Zacharias. Non-collinear optical parametric chirped-pulse amplifier for few-cycle pulses. *Applied Physics B*, 97(4):765–779, 2009.
- [28] J. Tümmler, R. Jung, H. Stiel, P. V. Nickles, and W. Sandner. High-repetition-rate chirped-pulse-amplification thin-disk laser system with joule-level pulse energy. *Opt. Lett.*, 34(9):1378–1380, May 2009.
- [29] C G Morgan. Laser-induced breakdown of gases. *Reports on Progress in Physics*, 38(5):621, 1975.
- [30] A.V. Smith. SNLO nolinear optics code. Technical report, AS-Photonics, 2011.
- [31] A. Stingl, R. Szipöcs, M. Lenzner, Ch. Spielmann, and F. Krausz. Sub-10-fs mirror-dispersion-controlled ti:sapphire laser. *Opt. Lett.*, 20(6):602–604, Mar 1995.
- [32] FEMTOLASERS, Fernkorngasse 10, 1100 Wien, Austria. *FEMTOSOURCETM rainbowTM CEP₄*, ver 1.13 edition, 2014.
- [33] Joseph W. Goodman. *Introduction to Fourier Optics*. McGraw-Hill, 1996.
- [34] E. T. J. Nibbering, G. Grillon, M. A. Franco, B. S. Prade, and A. Mysyrowicz. Determination of the inertial contribution to the nonlinear refractive index of air, N₂, and O₂ by use of unfocused high-intensity femtosecond laser pulses. *J. Opt. Soc. Am. B*, 14(3):650–660, Mar 1997.
- [35] Freek Kelkensberg. *Capturing atomic and electronic motion with high harmonic generation light pulses*. PhD thesis, Radboud University Nijmegen, June 23rd 2011.

BIBLIOGRAPHY

- [36] X. D. Zhu and L. Deng. Broadly tunable picosecond pulses generated in a β -BaB₂O₄ optical parametric amplifier pumped by 0.532 μ m pulses. *Applied Physics Letters*, 61(13):1490–1492, 1992.
- [37] An-Chun Tien, Sterling Backus, Henry Kapteyn, Margaret Murnane, and Gérard Mourou. Short-pulse laser damage in transparent materials as a function of pulse duration. *Phys. Rev. Lett.*, 82:3883–3886, May 1999.
- [38] D. N. Nikogosyan. Beta barium borate (BBO). *Applied Physics A*, 52(6):359–368, 1991.
- [39] I A Walmsley. Characterization of ultrashort optical pulses in the few-cycle regime using spectral phase interferometry for direct electric-field reconstruction. In *Few-cycle Laser Pulse Generation and its Applications*, volume 95 of *Topics in Applied Physics*, pages 265–291. Springer-Verlag Berlin, Heidelberger Platz 3, D-14197 Berlin, Germany, 2004.
- [40] M.E. Anderson, L.E.E. de Araujo, E.M. Kosik, and I.A. Walmsley. The effects of noise on ultrashort-optical-pulse measurement using SPIDER. *Applied Physics B*, 70(1):S85–S93, 2000.
- [41] Mikhahil N. Polyanskiy. Refractive index database.
- [42] Katsumi Midorikawa, Yasuo Nabekawa, and Akira Suda. XUV multiphoton processes with intense high-order harmonics. *Progress in Quantum Electronics*, 32(2):43 – 88, 2008.
- [43] S. Haessler, T. Balciunas, G. Fan, L. E. Chipperfield, and A. Baltuska. Enhanced multi-colour gating for the generation of high-power isolated attosecond pulses. *Scientific Reports*, 5:10084–, May 2015.
- [44] Jonathan A. Wheeler, Antonin Borot, Sylvain Monchoce, Henri Vincenti, Aurelien Ricci, Arnaud Malvache, Rodrigo Lopez-Martens, and Fabien Quere. Attosecond lighthouses from plasma mirrors. *Nat Photon*, 6(12):829–833, December 2012.
- [45] Kyung Taec Kim, Chunmei Zhang, Thierry Ruchon, Jean-Francois Hergott, Thierry Auguste, Villeneuve D. M., Corkum P. B., and Quere F. Photonic streaking of attosecond pulse trains. *Nat Photon*, 7(8):651–656, August 2013.
- [46] H. Vincenti, S. Monchoce, S. Kahaly, G. Bonnaud, Ph. Martin, and F. Quere. Optical properties of relativistic plasma mirrors. *Nat Commun*, 5:–, March 2014.
- [47] Mark J. Abel, Thomas Pfeifer, Phillip M. Nagel, Willem Boutu, M. Justine Bell, Colby P. Steiner, Daniel M. Neumark, and Stephen R. Leone. Isolated attosecond pulses from ionization gating of high-harmonic emission. *Chemical Physics*, 366(1–3):9 – 14, 2009.

- [48] G. Vampa, C. McDonald, A. Fraser, and T. Brabec. High-harmonic generation in solids: Bridging the gap between attosecond science and condensed matter physics. *Selected Topics in Quantum Electronics, IEEE Journal of*, 21(5):1–10, Sept 2015.
- [49] I. Yavuz, Y. Tikman, and Z. Altun. High-order-harmonic generation from H_2 molecular ions near plasmon-enhanced laser fields. *Phys. Rev. A*, 92:023413, Aug 2015.
- [50] Chao Yu, Jingtao Zhang, Zhi-Wei Sun, Zhenrong Sun, and Dong-Sheng Guo. A nonperturbative quantum electrodynamic approach to the theory of laser induced high harmonic generation. *Frontiers of Physics*, 10(4):1–6, 2015.
- [51] Bing Shan, Shambhu Ghimire, and Zenghu Chang. Generation of the attosecond extreme ultraviolet supercontinuum by a polarization gating. *Journal of Modern Optics*, 52(2-3):277–283, 2005.
- [52] Pengfei Lan, Eiji J. Takahashi, and Katsumi Midorikawa. Isolated-attosecond-pulse generation with infrared double optical gating. *Phys. Rev. A*, 83:063839, Jun 2011.
- [53] M. Lewenstein, Ph. Balcou, M. Yu. Ivanov, Anne L’Huillier, and P. B. Corkum. Theory of high-harmonic generation by low-frequency laser fields. *Phys. Rev. A*, 49:2117–2132, Mar 1994.
- [54] E. Constant, D. Garzella, P. Breger, E. Mével, Ch. Dorrer, C. Le Blanc, F. Salin, and P. Agostini. Optimizing high harmonic generation in absorbing gases: Model and experiment. *Phys. Rev. Lett.*, 82:1668–1671, Feb 1999.
- [55] T. Schultz and M. J.J. Vrakking. Attosecond and XUV science. unpublished version, 09 2012.
- [56] M. V. Ammosov, N. B. Delone, and V. P. Krainov. Tunnel ionization of complex atoms and atomic ions in a varying electromagnetic-field. *Zhurnal Eksperimentalnoi I Teoreticheskoi Fiziki*, 91(6):2008–2013, DEC 1986.
- [57] A. V. Husakou and J. Herrmann. Supercontinuum generation of higher-order solitons by fission in photonic crystal fibers. *Phys. Rev. Lett.*, 87:203901, Oct 2001.
- [58] Martin V. Zombeck. *Handbook of Space Astronomy and Astrophysics*. Cambridge University Press, 3rd edition edition, 2006.
- [59] Charles G. Durfee, Andy R. Rundquist, Sterling Backus, Catherine Herne, Margaret M. Murnane, and Henry C. Kapteyn. Phase matching of high-order harmonics in hollow waveguides. *Phys. Rev. Lett.*, 83:2187–2190, Sep 1999.
- [60] Eiji Takahashi, Yasuo Nabekawa, Tatsuya Otsuka, Minoru Obara, and Katsumi Midorikawa. Generation of highly coherent submicrojoule soft x rays by high-order harmonics. *Phys. Rev. A*, 66:021802, Aug 2002.

BIBLIOGRAPHY

- [61] Eiji Takahashi, Yasuo Nabekawa, Muhammad Nurhuda, and Katsumi Midorikawa. Generation of high-energy high-order harmonics by use of a long interaction medium. *J. Opt. Soc. Am. B*, 20(1):158–165, Jan 2003.
- [62] A. Jullien, T. Pfeifer, M. Abel, P. Nagel, M. Bell, D. Neumark, and S. Leone. Ionization phase-match gating for wavelength-tunable isolated attosecond pulse generation. *Applied Physics B: Lasers and Optics*, 93:433–442, 2008. 10.1007/s00340-008-3187-z.
- [63] Steve Gilbertson. *Double optical gating*. PhD thesis, Kansas State University, 2010.
- [64] Ximao Feng, Steve Gilbertson, Hiroki Mashiko, He Wang, Sabih D. Khan, Michael Chini, Yi Wu, Kun Zhao, and Zenghu Chang. Generation of isolated attosecond pulses with 20 to 28 femtosecond lasers. *Phys. Rev. Lett.*, 103:183901, Oct 2009.
- [65] U. K. Sapaev, I. Babushkin, and J. Herrmann. Quasi-phase-matching for third harmonic generation in noble gases employing ultrasound. *Opt. Express*, 20(20):22753–22762, Sep 2012.
- [66] Usman Sapaev, Anton Husakou, and Joachim Herrmann. Combined action of the bound-electron nonlinearity and the tunnel-ionization current in low-order harmonic generation in noble gases. *Opt. Express*, 21(21):25582–25591, Oct 2013.
- [67] Christopher C. Davies. *Laser and Electro-Optics*. Cambridge University Press, 1996.
- [68] Gorachand Ghosh. Dispersion-equation coefficients for the refractive index and birefringence of calcite and quartz crystals. *Optics Communications*, 163(1-3):95 – 102, 1999. Cited via: M. N. Polyanskiy. Refractive index database. Available at <http://refractiveindex.info>.
- [69] F Brunel. Harmonic-generation due to plasma effects in a gas undergoing multiphoton ionization in the high-intensity limit. *Journal of the Optical Society of America B-optical Physics*, 7(4):521–526, APR 1990.
- [70] Martin Kirchhoff. Assembling of holographic optical tweezers for the study of free standing liquid crystal films. Master’s thesis, Otto-von-Guericke-Universität, 2011.
- [71] Ding Wang, Yuxin Leng, and Zhizhan Xu. Measurement of nonlinear refractive index coefficient of inert gases with hollow-core fiber. *Applied Physics B*, 111(3):447–452, 2013.
- [72] Anne L’Huillier, Philippe Balcou, Sebastien Candel, Kenneth J. Schafer, and Kenneth C. Kulander. Calculations of high-order harmonic-generation processes in xenon at 1064 nm. *Phys. Rev. A*, 46:2778–2790, Sep 1992.

- [73] B.L. Henke, E.M. Gullikson, and J.C. Davis. X-ray interactions: photoabsorption, scattering, transmission, and reflection at $e=50\text{--}30000$ eV, $z=1\text{--}92$. *Atomic Data and Nuclear Data Tables Vol. 54 (no.2)*, 54:181–342, 1993.
- [74] P Tzallas, E Skantzakis, and D Charalambidis. Direct two-XUV-photon double ionization in xenon. *Journal of Physics B: Atomic, Molecular and Optical Physics*, 45(7):074007, 2012.
- [75] J. A. Nelder and R. Mead. A simplex method for function minimization. *The Computer Journal*, 7(4):308–313, 1965.
- [76] Viktor T Platonenko and V V Strelkov. Generation of high-order harmonics in a high-intensity laser radiation field. *Quantum Electronics*, 28(7):564, 1998.
- [77] Pascal Salieres, Anne L’Huillier, and Maciej Lewenstein. Coherence control of high-order harmonics. *Phys. Rev. Lett.*, 74:3776–3779, May 1995.
- [78] Hirofumi Sakai and Kenzo Miyazaki. Effect of multiphoton ionization on high-order harmonic generation and propagation in rare gases with subpicosecond laser pulses. *Phys. Rev. A*, 50:4204–4211, Nov 1994.
- [79] Robert W. Boyd. *Nonlinear Optics, Second Edition*. Academic Press, 2 edition, April 2008.
- [80] Toru Morishita, Anh-Thu Le, Zhangjin Chen, and C. D. Lin. Accurate retrieval of structural information from laser-induced photoelectron and high-order harmonic spectra by few-cycle laser pulses. *Phys. Rev. Lett.*, 100:013903, Jan 2008.
- [81] J. Peatross, J. L. Chaloupka, and D. D. Meyerhofer. High-order harmonic generation with an annular laserbeam. *Opt. Lett.*, 19(13):942–944, Jul 1994.
- [82] LAYERTEC GmbH, Ernst-Abbe-Weg 1 99441 Mellingen GERMANY. *Catalog 2015*. https://www.layertec.de/de/downloads/files/Layertec_Katalog_2015_Femtosecond_Laser.pdf called at 2016-01-14.
- [83] Del Mar Photonics. Microchannel plates. http://www.dmp Photonics.com/MCP_MCPImageIntensifiers/microchannel_plates.htm called at 2016-01-11.
- [84] Hamamatsu photonics K.K. *MCP (Microchannel Plate) and MCP assembly*, 2016.
- [85] Karl Jousten, editor. *Wutz Handbuch Vakuumtechnik*. Springer, 2012.
- [86] McNally Institute. Approximate flow through an orifice. <http://www.mcnallyinstitute.com/13-html/13-12.htm> called at 2016-01-12.
- [87] Pierre Jaegle. Xuv optics. In *Coherent Sources of XUV Radiation*, volume 106 of *Optical Sciences*, pages 23–40. Springer New York, 2006.
- [88] Michael Hofstetter. *Multilayer Mirrors for Attosecond Pulse Shaping between 30 and 200 eV*. PhD thesis, LMU Munich, Juli 2011.

BIBLIOGRAPHY

- [89] Vassilios Papadakis and Theofanis N. Kitsopoulos. Slice imaging and velocity mapping using a single field. *Review of Scientific Instruments*, 77(8), 2006.
- [90] Andre T. J. B. Eppink and David H. Parker. Velocity map imaging of ions and electrons using electrostatic lenses: Application in photoelectron and photofragment ion imaging of molecular oxygen. *Review of Scientific Instruments*, 68(9):3477–3484, 1997.
- [91] Vladimir Dribinski, Alexei Ossadtchi, Vladimir A. Mandelshtam, and Hanna Reisler. Reconstruction of abel-transformable images: The gaussian basis-set expansion abel transform method. *Review of Scientific Instruments*, 73(7):2634–2642, 2002.
- [92] O. Ghafur, W. Siu, P. Johnsson, M. F. Kling, M. Drescher, and M. J. J. Vrakking. A velocity map imaging detector with an integrated gas injection system. *Review of Scientific Instruments*, 80(3), 2009.
- [93] J. F. Seely, M. P. Kowalski, W. R. Hunter, and G. Gutman. Reflectance of a wideband multilayer x-ray mirror at normal and grazing incidences. *Appl. Opt.*, 35(22):4408–4412, Aug 1996.
- [94] Oleg Kornilov, Russell Wilcox, and Oliver Gessner. Nanograting-based compact vacuum ultraviolet spectrometer and beam profiler for in situ characterization of high-order harmonic generation light sources. *Review of Scientific Instruments*, 81(6):063109, 2010.
- [95] W. Ackermann, G. Asova, Ayvazyan V., Azima A., Baboi N., Bahr J., Balandin V., Beutner B., Brandt A., Bolzmann A., Brinkmann R., Brovko O. I., Castellano M., Castro P., Catani L., Chiadroni E., Choroba S., Cianchi A., Costello J. T., Cubaynes D., Dardis J., Decking W., Delsim-Hashemi H., Delserieys A., Di Pirro G., Dohlus M., Dusterer S., Eckhardt A., Edwards H. T., Faatz B., Feldhaus J., Flottmann K., Frisch J., Frohlich L., Garvey T., Gensch U., Gerth C. h., Gorler M., Golubeva N., Grabosch H.-J., Grecki M., Grimm O., Hacker K., Hahn U., Han J. H., Honkavaara K., Hott T., Huning M., Ivanisenko Y., Jaeschke E., Jalmuzna W., Jezynski T., Kammering R., Katalev V., Kavanagh K., Kennedy E. T., Khodyachykh S., Klose K., Kocharyan V., Korfer M., Kollewe M., Koprek W., Korepanov S., Kostin D., Krassilnikov M., Kube G., Kuhlmann M., Lewis C. L. S., Lilje L., Limberg T., Lipka D., Lohl F., Luna H., Luong M., Martins M., Meyer M., Michelato P., Miltchev V., Moller W. D., Monaco L., Muller W. F. O., Napieralski O., Napoly O., Nicolosi P., Nolle D., Nunez T., Oppelt A., Pagani C., Paparella R., Pchalek N., Pedregosa-Gutierrez J., Petersen B., Petrosyan B., Petrosyan G., Petrosyan L., Pfluger J., Plonjes E., Poletto L., Pozniak K., Prat E., Proch D., Pucyk P., Radcliffe P., Redlin H., Rehlich K., Richter M., Roehrs M., Roensch J., Romaniuk R., Ross M., Rossbach J., Rybnikov V., Sachwitz M., Saldin E. L., Sandner W., Schlarb H., Schmidt B., Schmitz M., Schmuser P., Schneider J. R., Schneidmiller E. A., Schnepf S., Schreiber S., Seidel M., Sertore D., Shabunov A.

- V., Simon C., Simrock S., Sombrowski E., Sorokin A. A., Spanknebel P., Spesyvtsev R., Staykov L., Steffen B., Stephan F., Stulle F., Thom H., Tiedtke K., Tischer M., Toleikis S., Treusch R., Trines D., Tsakov I., Vogel E., Weiland T., Weise H., Wellhofer M., Wendt M., Will I., Winter A., Wittenburg K., Wurth W., Yeates P., Yurkov M. V., Zagorodnov I., and Zapfe K. Operation of a free-electron laser from the extreme ultraviolet to the water window. *Nat Photon*, 1(6):336–342, June 2007.
- [96] E. Allaria, R. Appio, L. Badano, W. A. Barletta, S. Bassanese, S. G. Biedron, A. Borga, E. Busetto, D. Castronovo, P. Cinquegrana, S. Cleva, D. Cocco, M. Cornacchia, P. Craievich, I. Cudin, G. D’Auria, M. Dal Forno, M. B. Danailov, R. De Monte, G. De Ninno, P. Delgiusto, A. Demidovich, S. Di Mitri, B. Diviacco, A. Fabris, R. Fabris, W. Fawley, M. Ferianis, E. Ferrari, S. Ferry, L. Froehlich, P. Furlan, G. Gaio, F. Gelmetti, L. Giannessi, M. Giannini, R. Gobessi, R. Ivanov, E. Karantzoulis, M. Lonza, A. Lutman, B. Mahieu, M. Milloch, S. V. Milton, M. Musardo, I. Nikolov, S. Noe, F. Parmigiani, G. Penco, M. Petronio, L. Pivetta, M. Predonzani, F. Rossi, L. Rumiz, A. Salom, C. Scafuri, C. Serpico, P. Sigalotti, S. Spampinati, C. Spezzani, M. Svandrlik, C. Svetina, S. Tazzari, M. Trovo, R. Umer, A. Vascotto, M. Veronese, R. Visintini, M. Zaccaria, D. Zangrando, and M. Zangrando. Highly coherent and stable pulses from the fermi seeded free-electron laser in the extreme ultraviolet. *Nature Photonics*, 6(10):699–704, OCT 2012.
- [97] Richard Neutze, Remco Wouts, David van der Spoel, Edgar Weckert, and Janos Hajdu. Potential for biomolecular imaging with femtosecond x-ray pulses. *Nature*, 406(6797):752–757, August 2000.
- [98] B. Schuette, M. Arbeiter, T. Fennel, M. J. J. Vrakking, and A. Rouzee. Rare-gas clusters in intense extreme-ultraviolet pulses from a high-order harmonic source. *Phys. Rev. Lett.*, 112:073003, 2014.
- [99] Y. Hikosaka, M. Fushitani, A. Matsuda, T. Endo, Y. Toida, E. Shigemasa, M. Nagasono, K. Tono, T. Togashi, M. Yabashi, T. Ishikawa, and A. Hishikawa. Resonances in three-photon double ionization of ar in intense extreme-ultraviolet free-electron laser fields studied by shot-by-shot photoelectron spectroscopy. *Phys. Rev. A*, 88:023421, Aug 2013.
- [100] P Heissler, P Tzallas, J M Mikhailova, K Khrennikov, L Waldecker, F Krausz, S Karsch, D Charalambidis, and G D Tsakiris. Two-photon above-threshold ionization using extreme-ultraviolet harmonic emission from relativistic laser-plasma interaction. *New Journal of Physics*, 14(4):043025, 2012.
- [101] D Xenakis, O Faucher, D Charalambidis, and C Fotakis. Observation of two-xuv-photon ionization using harmonic generation from a short, intense laser pulse. *Journal of Physics B: Atomic, Molecular and Optical Physics*, 29(12):L457, 1996.

BIBLIOGRAPHY

- [102] I. I. Rabi. Space quantization in a gyrating magnetic field. *Phys. Rev.*, 51:652–654, Apr 1937.
- [103] Xiaojin Li, Yanwen Wu, Duncan Steel, D. Gammon, T. H. Stievater, D. S. Katzer, D. Park, C. Piermarocchi, and L. J. Sham. An all-optical quantum gate in a semiconductor quantum dot. *Science*, 301(5634):809–811, 2003.
- [104] Parinda Vasa, Wei Wang, Robert Pomraenke, Melanie Lammers, Margherita Maiuri, Cristian Manzoni, Giulio Cerullo, and Christoph Lienau. Real-time observation of ultrafast rabi oscillations between excitons and plasmons in metal nanostructures with j-aggregates. *Nature Photonics*, 7(2):128–132, 2013.
- [105] Takahiro Sato, Atsushi Iwasaki, Kazuki Ishibashi, Tomoya Okino, Kaoru Yamanouchi, Junichi Adachi, Akira Yagishita, Hiroki Yazawa, Fumihiko Kannari, Makoto Aoyama, Koichi Yamakawa, Katsumi Midorikawa, Hidetoshi Nakano, Makina Yabashi, Mitsuru Nagasono, Atsushi Higashiya, and Tetsuya Ishikawa. Determination of the absolute two-photon ionization cross section of he by an xuv free electron laser. *Journal of Physics B: Atomic, Molecular and Optical Physics*, 44(16):161001, 2011.
- [106] Tokuei Sako, Junichi Adachi, Akira Yagishita, Makina Yabashi, Takashi Tanaka, Mitsuru Nagasono, and Tetsuya Ishikawa. Suppression of ionization probability due to Rabi oscillations in the resonance two-photon ionization of He by EUV free-electron lasers. *Phys. Rev. A*, 84:053419, Nov 2011.
- [107] Mette B. Gaarde, Christian Buth, Jennifer L. Tate, and Kenneth J. Schafer. Transient absorption and reshaping of ultrafast xuv light by laser-dressed helium. *Phys. Rev. A*, 83:013419, Jan 2011.
- [108] B Kaiser, A Brand, M Glässl, A Vagov, V M Axt, and U Pietsch. Photoionization of resonantly driven atomic states by an extreme ultraviolet-free-electron laser: intensity dependence and renormalization of rabi frequencies. *New Journal of Physics*, 15(9):093016, 2013.
- [109] S. L. Sorensen, T. Åberg, J. Tulkki, E. Rachlew-Källne, G. Sundström, and M. Kirm. Argon 3s autoionization resonances. *Phys. Rev. A*, 50:1218–1230, Aug 1994.
- [110] B. Schütte, F. Campi, M. Arbeiter, Th. Fennel, M. J. J. J. Vrakking, and A. Rouzée. Tracing electron-ion recombination in nanoplasmas produced by extreme-ultraviolet irradiation of rare-gas clusters. *Phys. Rev. Lett.*, 112:253401, Jun 2014.
- [111] Bernd Schütte, Tim Oelze, Maria Krikunova, Mathias Arbeiter, Thomas Fennel, Marc J J Vrakking, and Arnaud Rouzée. Recombination dynamics of clusters in intense extreme-ultraviolet and near-infrared fields. *New Journal of Physics*, 17(3):033043, 2015.

- [112] T. E. Glover, R. W. Schoenlein, A. H. Chin, and C. V. Shank. Observation of laser assisted photoelectric effect and femtosecond high order harmonic radiation. *Phys. Rev. Lett.*, 76:2468–2471, Apr 1996.
- [113] S. Yagi, T. Nagata, M. Koide, Y. Itoh, T. Koizumi, and Y. Azuma. Relative counting efficiencies of ion charge-states by microchannel plate. *Nuclear Instruments and Methods in Physics Research Section B: Beam Interactions with Materials and Atoms*, 183(3-4):476 – 486, 2001.
- [114] E. B. Saloman. Energy levels and observed spectral lines of ionized argon, arii through arxviii. *Journal of Physical and Chemical Reference Data*, 39(3):–, 2010. NIST Atomic Spectra Database (ver. 5.1), [Online]. Available: <http://physics.nist.gov/asd> [2014, July 24]. National Institute of Standards and Technology, Gaithersburg, MD.
- [115] M J Seaton. Atomic data for opacity calculations. i. general description. *Journal of Physics B: Atomic and Molecular Physics*, 20(23):6363, 1987. Via universal atomic Database (NASA).
- [116] E.M. Landau, L.D.and Lifshitz. *Quantum Mechanics*, volume 3. Pergamon Press, 1965.
- [117] D.A. Verner, E.M. Verner, and G.J. Ferland. Atomic data for permitted resonance lines of atoms and ions from h to si, and s, ar, ca, and fe. *Atomic Data and Nuclear Data Tables*, 64(1):1 – 180, 1996.
- [118] PJ Storey and KT Taylor. Topbase, the opacity project on-line atomic database. <http://cdsweb.u-strasbg.fr/topbase/topbase.html>, April 2009. Accessed: 2015-06.
- [119] Robert C. Hilborn. Einstein coefficients, cross sections, f values, dipole moments, and all that. *Am. J. Phys.*, 50:982–986, 2002. arXiv:physics/0202029.
- [120] J. Tatum. Oscillator strengths and related topics. astrowww.phys.uvic.ca/~tatum/stellatm/atm9.pdf accessed 2016-01-22, 2011.
- [121] A. R. Edmonds. *Angular Momentum in Quantum Mechanics*. Princeton, New Jerseyprinceton University Press, 1957.
- [122] M.V. Fedorov and A.E. Kazakov. Resonances and saturation in multiphoton bound-free transitions. *Progress in Quantum Electronics*, 13(1):1 – 106, 1989.
- [123] M. Yu. Ivanov. Suppression of resonant multiphoton ionization via rydberg states. *Phys. Rev. A*, 49:1165–1170, Feb 1994.
- [124] Jonathan Parker and C. R. Stroud. Population trapping in short-pulse laser ionization. *Phys. Rev. A*, 41:1602–1608, Feb 1990.

BIBLIOGRAPHY

- [125] T. R. O'Brian, J.-B. Kim, G. Lan, T. J. McIlrath, and T. B. Lucatorto. Verification of the ponderomotive approximation for the ac stark shift in xe rydberg levels. *Phys. Rev. A*, 49:R649–R652, Feb 1994.
- [126] T. K. Ghosh, A. K. Das, Marcos Castro, Sylvio Canuto, and P. K. Mukherjee. Dynamic polarizabilities and rydberg states of the argon isoelectronic sequence. *Phys. Rev. A*, 48:2686–2695, Oct 1993.
- [127] S. H. Patil. Susceptibility and polarizability of atoms and ions. *The Journal of Chemical Physics*, 83(11):5764–5771, 1985.
- [128] M. J. Nandor, M. A. Walker, L. D. Van Woerkom, and H. G. Muller. Detailed comparison of above-threshold-ionization spectra from accurate numerical integrations and high-resolution measurements. *Phys. Rev. A*, 60:R1771–R1774, Sep 1999.
- [129] I Velchev, W Hogervorst, and W Ubachs. Precision VUV spectroscopy of Ar I at 105 nm. *Journal of Physics B: Atomic, Molecular and Optical Physics*, 32(17):L511, 1999. NIST Atomic Spectra Database (ver. 5.2), [Online]. Available: <http://physics.nist.gov/asd> [2015, September 23]. National Institute of Standards and Technology, Gaithersburg, MD.
- [130] Robert Jung, Johannes Tümmler, Thomas Nubbemeyer, and Ingo Will. Thin-disk ring amplifier for high pulse energy. *Opt. Express*, 24(5):4375–4381, Mar 2016.
- [131] P. Rudawski, C. M. Heyl, F. Brizuela, J. Schwenke, A. Persson, E. Mansten, R. Rakowski, L. Rading, F. Campi, B. Kim, P. Johnsson, and A. L'Huillier. A high-flux high-order harmonic source. *Review of Scientific Instruments*, 84(7):073103, 2013.
- [132] Ulrich Hahn and Kai Tiedtke. The gas attenuator of flash at desy. *AIP Conference Proceedings*, 879(1):276–282, 2007.
- [133] Y. Mairesse and F. Quéré. Frequency-resolved optical gating for complete reconstruction of attosecond bursts. *Phys. Rev. A*, 71:011401, Jan 2005.

Nomenclature

\vec{A}	Vector potential
A_r	Atomic response (Eq. (2.6))
A_{21}	Einstein A coefficient
C	Conductance (of a connection in vacuum)
\vec{C}	Contribution to the XUV field, Eq. (2.26)
E	Electric field
E	Energy
\vec{E}	Electric field
F	Maximum field strength
I	Intensity
IP	Ionization potential
L	Total orbital momentum
L_{abs}	Absorption length
L_{med}	Length of medium
N	Number density
\vec{P}	Polarization
\vec{P}_{NL1}	Nonlinear polarization
S	Pumping speed (of a vacuum pump)
S	Total spin angular momentum
T	Transmission (of IR through polarizer and $\lambda/2$ plate)
U_p	Ponderomotive potential
Y	Yield
Y_{coef}	Fit parameter for height matching

Nomenclature

Δe_n	Effective detuning of the XUV excitation in Chap. 4
Γ_n	Effective cross section of the IR ionization in Chap. 4
Ω_n	Maximum, angular Rabi frequency of the XUV excitations in Chap. 4
Φ	Phase-matching number (page 56)
α_{BBO}	Angle of rotation before BBO
χ	Characteristic function
$\chi^{(k)}$	Electric susceptibilities
ϵ_0	Vacuum permittivity, $8.854187817 \cdot 10^{12} \frac{F}{m}$
η	Coordinate in moving reference frame
η_e	Ionized fraction
η_{HHG}	Efficiency from IR to XUV pulse energy
η_{SHG}	Efficiency of SHG
λ	Wavelength
gf	Weighted oscillator strengths
μ	Transition dipole moment
ω	Angular frequency
ω_{21}	Transition frequency
\otimes	Convolution (of two functions)
ϕ	Phase
ϕ_0	Relative phase
ϕ_{Rabi}	Rabi phase
\square_{BS}	Parameter for the Boltzmann sigmoid (see Eq. (4.2))
τ	Time delay (of XUV and IR pulse)
τ	Time duration (standard deviation)
τ_0	Fit parameter for overlap correction
τ_{21}	Decay time of a state
$\varepsilon(t)$	Complex representation of the electric field

φ_{CEP}	Carrier envelope phase (CEP)
$\vec{\Delta}k$	Phase mismatch
ξ	Coordinate in moving reference frame
b	Rayleigh length
c	Vacuum speed of light, $299\,792\,458 \frac{m}{s}$
d_{BBO}	BBO length
d_{SiO_2}	Length of the SiO ₂ plate
f	Focal length
$f(t)$	Relative field envelope
g_2	Degeneracy of the higher state of a transition
k	(Angular) wavenumber
m_e	Mass of the electron, $9.109382 \cdot 10^{-31} kg$
n	Index of refraction
n_2	Nonlinear index of refraction
p	Pressure
q	Flow (of a gas in vacuum)
t	Time
u_p	Effective, maximum U_p shift in Chap. 4
$w_k(\vec{r})$	$1/e^2$ radius of (Gaussian) intensity profile at waist/ \vec{r}
$w_{0,BBO}$	Beam waist at BBO
z_0	Distance from focus to the beginning of the HHG medium
ADK (rate)	Tunnelionization rate according to the Ammosov-Delone-Krainov tunneling model [56]
B4C	Boron carbide
BBO	β -Barium borate
CEP	Carrier envelope phase
FK (model)	Model of Fedorov an Kazakov, see Sec .4.4.1

Nomenclature

FOM	Figure of merit
FWHM	Full width half maximum
HHG	High harmonic generation
MCP	Micro channel plate
NOPCPA	Noncollinear optical chirped pulse amplification
ODE	Ordinary differential equation
OPA	Optical parametric amplification, see section 1.1.4
OPA1-3	Specific stages/crystals for OPA
OPCPA	Optical chirped pulse amplification
SFG	Sum frequency generation
SHG	Second harmonic generation
SLM	Spatial light modulator
SPIDER	Spectral phase interferometry for direct electric field reconstruction
TDSE	Time dependent Schrödinger equation
\bar{v}	Pumping speed (of a vacuum pump)
VMI	Velocity map imaging (spectrometer)
XUV	Extreme ultra violet (light)

List of Publications

1. Martin Floegel, Dominik Z. Kandula, Marc J.J. Vrakking. Laser Source for XUV-XUV Attosecond Pump-Probe Experiments, *Ultrafast Laser Science Applications Summer School (SAUUL Consolider Ingenio 2010)*, 2012, Poster presentation
2. Martin Floegel, Judith Durá, Bernd Schütte, Misha Ivanov, Arnaud Rouzée and Marc J. J. Vrakking. Rabi oscillations in extreme ultraviolet ionization of atomic argon, *Phys. Rev. A* , Accepted: 21 December 2016 (© 2017 American Physical Society)
3. Martin Floegel, Anton Husakou, Usman Sapaev, and Marc J. J. Vrakking. Theoretical Comparison of Different HHG Gating Techniques, in preparation